Synthesis, Characterization and Field Emission Properties of Rare-Earth Hexaboride Nanowires

Han Zhang

A dissertation submitted to the faculty of the University of North Carolina at Chapel Hill in partial fulfillment of the requirements for the degree of Doctor of Philosophy in the Curriculum in Applied and Materials Sciences.

Chapel Hill
2006

Approved by:

Professor Lu-Chang Qin

Professor Jianping Lu

Professor Richard Superfine

Professor Sean Washburn

Professor Otto Zhou

ABSTRACT

Han Zhang: Synthesis, Characterization and Field Emission Properties of Rare-Earth Hexaboride Nanowires
(Under the direction of Prof. Lu-Chang Qin)

Rare-earth hexaborides are a family of compounds which have low work function, high melting point, and high mechanical strength. These properties are highly suitable for electron field emission applications. To explore this possibility, we developed a chemical vapor deposition method and produced three different types of 1D nano-structures, which include single crystalline nanowires of LaB_6, CeB_6, and GdB_6; polycrystalline nanowires of YB_{12}, LaB_{12}, MgO, and Mg_3N_2; core-shell nanocables of MgB_2-in-MgO and LaB_6-in-CNT. TEM, SEM, EELS and EDX techniques were applied to characterize structural and chemical information about the synthesized nano-structures. Vapor-solid growth, catalyst-assisted vapor-liquid-solid growth and CNT-assisted template growth are proposed to be accounted for the formation mechanisms of these 1D nano-structures and the theoretical predictions match the experimental observations quantitatively. To fabricate a single nanowire field emitter, direct contact, electron beam lithography and focused ion beam welding techniques were used to attach a single LaB_6 nanowire to the tip of a tungsten wire. Cold field emission properties were measured from such made single nanowire emitters. Work function values of 2.6 eV and 1.5 eV were obtained from a LaB_6 nanowire emitter and GdB_6 nanowire emitter

respectively. An Emission Current density as high as 5×10^5 A/cm^2 was obtained from a single LaB_6 nanowire emitter, under an extraction voltage of 800 V. Emission current stability was also studied for the nanowire emitter and the results indicate surface-contamination induced emission current fluctuations. A home-designed TEM in-situ field emission measurement holder was fabricated for a JEOL 2010F HRTEM. Field electron emission was performed on a single LaB_6 nanowire field electron emitter simultaneously with high resolution TEM imaging. Image contrast changes were observed at under-focus imaging conditions when a series of negative biases were applied to the nanowire emitter. Such contrast changes can be used to qualitatively image the charge density distribution on the nanowire emitter tip during field electron emission.

To my dearest parents, grandma and grandpa.

ACKNOWLEDGEMENTS

The author wants to give special acknowledgements to his PhD research supervisor, Prof. Lu-Chang Qin, for his academic directing, valuable discussions, and his always kind and gentle attitude whenever the author needs help regarding different issues during his PhD study and the preparation of this dissertation. The author also feels deeply appreciated for the research support and cooperation opportunities provided by Dr. Jie Tang. Special thanks should also be given to the Curriculum in Applied and Materials Sciences and the Department of Physics and Astronomy of the University of North Carolina for all the education and financial support that the author received during his stay in Chapel Hill. The author also thanks the National Institute for Materials Science in Tsukuba, Japan for all the research opportunities. Special acknowledgements are also given to all the author's co-workers and many friends, who offered invaluable helps not only in the author's research, but also in his life during his stay in Chapel Hill and Tsukuba. These special people are Michael Kavic, Joseph Newton, Dr. Qi Zhang, Dr. Gongpu Zhao, Dr. Zejian Liu, Roger Wendell, Douglas King, Dmitry Spivak, Kazumi Pritchett and many others whose names are not listed here only because of the space limit. Lastly, the author wants to give his sincere thanks to all the committee members, Prof. Lu-Chang Qin, Prof. Jianping Lu, Prof. Richard Superfine, Prof. Sean Washburn, and Prof. Otto Zhou, for all their helps during the author's research and the defense of this dissertation.

TABLE OF CONTENTS

LIST OF FIGURES

LIST OF ABBREVIATIONS

CNT……... Carbon Nanotube

CVD ……..Chemical Vapor Deposition

EBL ……...Electron Beam Lithography

EDX ……...Energy Dispersive X-ray

EELS ……Electron Energy Loss Spectrometry

FE ……..Field Emission

FEA ……Field Emission Array

FED ……..Field Emission Display

F-N ……Fowler-Nordheim

MWCNT ……Multi-Walled Carbon Nanotube

NT/NW ……Nanotube/Nanowire

SAED ……Selected Area Electron Diffraction

SEM ……Scanning Electron Microscope

SWCNT ……Single-Walled Carbon Nanotube

TEM ……...Transmission Electron Microscope

VLS ……Vapor Liquid Solid

VS ……...Vapor Solid

LIST OF SYMBOLS

A ……...Ampere/Emission Area

B_{max} …….Maximum Brightness

h …….Plank Constant

I_c …….Charge Density Contrast

I_t ……..Thickness Contrast

J ……Current Density

$\boldsymbol{\phi}$ ……..Work Function

$\boldsymbol{\sigma}$ …….Surface Energy

$\boldsymbol{\varepsilon}$ ……Degree of Defocus

$\boldsymbol{\mu}$ ……Fermi Energy

E……Electric Field

ε_p…….....Dielectric Constant of Cylinder

ε_m.....Dielectric Constant of Media

L_s……Sublimation Energy

k……...Boltzmann's Constant

T……Temperature

R……...…Gas Constant

β……Field Enhancement Factor

b……..…….F-N Formula y-intercept

ΔG.....Gibbs Free Energy

Δg……Gibbs Free Energy Per Volume

v……..……..Volume Density

Chapter 1 Introduction

1.1. Motivation

The extensive research on one-dimensional nano-materials can be traced back to the discovery of carbon nanotubes in 1991 by Dr. Sumio Iijima.(Iijima, 1991) The hollow tube configuration, very tiny size and almost perfect crystallinity of the material triggered great interests in the scientific community, including physicists, chemists, biologists, drug engineers and materials scientists. Exceptional scientific imaginations have been demonstrated in their proposed applications for this novel nano-scale material. Just to name a few, such as the electronic devices and transporting interconnects in microelectronic industry, nano-capsules in drug delivery, biological probes in bimolecular experiments, hydrogen storage fuel cells, enforcement frameworks in composite materials and numerous other emerging potential applications.

We noticed that many of these applications are trying to use carbon nanotubes to substitute the conventional materials that have been proven working the best among all others. A advantage of carbon nanotubes over these conventional materials is sometimes purely from the small size and long aspect ratio that a carbon nanotube bears. In other words, it is better to be smaller, but not necessarily carbon. By using a carbon nanotube, we sometimes have to sacrifice some other favorable properties that the original material possesses because of a certain chemical composition. They were chosen over the graphite material for a reason and it will be so much better if we can make those materials just as small as the carbon nanotube or even in the same morphology shape, if of course, being too big is their only reason to be substituted by carbon nanotubes.

One of the biggest potential applications of carbon nanotubes is to use them as a electron field emission source of high emission density. It is believed that the very sharp tip of a carbon nanotube offers great field enhancement and thus leads to a high emission current density. Conventional emission materials are refractory metals, such as W, Mo, and rare-earth hexaborides, such as LaB_6, CeB_6 and some metal oxides. Metal oxides are not suitable for high current emission, because they have too high electrical resistivity and cause serious joule heating which quickly damage the emitter when operating at high current density. Rare-earth hexaborides are superior to the refractory metals, because their work functions are nearly half of that of refractory metals, and offer a much higher current density at the same extraction conditions, as the current density increases exponentially as the work functions decrease. Carbon materials, on the other hand, have a work function twice as large as that of LaB_6. Therefore, it would be ideal to make one-dimensional single crystalline rare-earth hexaboride nanowires for field emission applications.

The rapid development in nanostructure synthesis, stimulated by the carbon nanotube research, has offered a wonderful opportunity. The chemical vapor deposition method has been successfully applied in making a large variety of nanotubes and nanowires. It is almost safe to believe that any simple binary compound can be made into one-dimensional nanostructures by choosing an appropriate precursor gas and catalysts. This motivates us into the efforts of designing an approach to synthesize rare-earth hexaboride nanowires and perform of measurements on these materials to explore the potential of using them as a new generation field emission electron sources.

1.2. Chemical Vapor Deposition (CVD) Synthesis of Nanostructures

Chemical vapor deposition (CVD) is a method developed to make thin films and

surface structures on substrates where coating is desired. It involves passing a precursor gas through the reaction chamber where the precursor either reacts with or deposits onto the substrate after decomposition. The residual gas is conducted away with a continuous gas flow. One of its advantages is the flexibility in controlling various properties of the deposited film, such as the thickness, uniformity, crystallinity and crystallographic orientation, through adjusting the reaction parameters such as the flow rate, pressure, substrate temperature, catalyst, reaction time, and nature of substrate materials. While one application of this technique is directed towards making uniform smooth films, including epitaxial atomic layers, another major use of the technique is to fabricate rough surfaces, such as diamond films for field emission purpose.

The extremity to a rough film is a forest of free-standing one-dimensional nano-entities. The adoption of the CVD approach in making whisker structures from a few tens of nanometer to more than a 100 μm in diameter started from 1960s (Levitt, 1970). At the time, people found that, at a certain precursor gas density, rod-shaped single crystals were always obtained. The observed phenomena followed the trend that following: when the precursor pressure is the lowest, uniform smooth thin films are made; when it is the highest, isotropically structured powders are the result; in between, whiskers, 2-D diskettes and 3-D bulk crystals are harvested in a sequence of precursor density from lower to higher. It was also found that the presence of metal impurities is often crucial in obtaining a whisker structure and this observation led to the emergence of the vapor-liquid-solid growth mechanism (Wagner, 1964). In the described picture by Wagner, the metal impurity present on the substrate forms a small droplet which size depends on the concentration of impurities. For example, the thickness of the film if the impurity is deliberately introduced in form of a thin film. The droplet keeps absorbing the precursor gas till it reaches over the equilibrium saturation point. Then this

supersaturation initializes and maintains the deposition of the final product in form of one-dimensional crystals. It was also found in the mean time that nanowire growth of some materials does not require the existence of impurity; and therefore, they can not be explained by the VLS mechanism. One of the examples is the use of aluminum halide precursor to react with carbon dioxide and hydrogen gas in the production of alumina whiskers, where no catalyst is used. The term VS growth is used to describe such non-catalyst whisker growth. A generally accepted growth mechanism is a screw dislocation driven growth proposed by Sears (Sears, 1955). However, failure to find these dislocations in most of the whiskers grown through the VS process makes the general growth picture still unclear. Particular intrinsic features of each material and particular experiment conditions such as the gas flow, precursor density distribution, seem to trigger one-dimensional growth in each particular case.

CVD systems are different from one another depending on the particular chemical reaction required. The ones to synthesize nanostructures are in principle similar. A typical tube furnace CVD, which is the one used in the author's synthesis of rare-earth hexaboride nanowires is illustrated in figure 1.1. The reaction chamber is a quartz tube placed inside a tube furnace. A bow of rare-earth trichloride is placed in the center zone as the precursor vapor source. The whole reaction is conducted with a hydrogen flow. A conductance tube is used to deliver to the reaction zone boron, in this case, boron trichloride gas. A deposition substrate is placed against the direction of the gas flow for product collection. The substrate can either be catalyst-coated or clean, depending on the particular reaction desired.

To date, by the CVD method, a large number of nanostructures have been fabricated. One elegant example is a series of work published by Wang's group on the synthesis of ZnO nanostructures. Those nanostructures are termed with nano-propeller

arrays, nano-helixes, nano-springs and nano-rings, respectively (Gao & Wang, 2005; Gao et al, 2004; Kong & Wang, 2003; Kong et al., 2004). The complexity is believed to have originated from a series of special features of the ZnO crystal structure. ZnO crystal has a wurtzite structure with three easy growth directions <0001>, <1210> and <1010>. The anisotropic crystallographic growth energy makes ZnO nanobelts, which has rectangular cross-sections with wider side surfaces and narrower top/bottom surfaces. (Pan et al., 2001) The (0001) plane can be with either Zn termination of positive polarization or O termination with negative polarization. Such electrostatic charges increase the surface energy and therefore, the (0001) planes tend to interface one another in order to neutralize charges. If the nanobelts' top/bottom surfaces are (0001) planes, they tend to coil up forming ring structures, in which the top surface of Zn termination neutralizes itself with the O terminated bottom surfaces. The coil shape is further fixed by forming chemical bonding between the top and bottom surfaces. If side surfaces happen to be (0001) surfaces, then it will cost too much crystal deformation to interface the two side surfaces. In that case, the nanobelts coil up along the axis of <1010> direction, by which manner, the negative charges center in the same line as positive charges to reduce total electrostatic energy. This is the nano-springs. If a nanobelt is composed of superlattice of non-polar and polar surfaces, a wider nano-springs are formed, as the case of nano-helixes. By performing a 2-stage heating process, 3-D arrays of nano-propeller structures can also be produced. The structure's formation is the direct result of competition among the 5 factors influencing the crystal growth habit: 3 easy growth directions and 2 oppositely charged polar surfaces. The control of different morphologies can be simply realized by slight changes of evaporation temperature and substrate temperature of the same synthesis CVD system. The work clearly demonstrates the flexibility and power of using CVD in synthesizing nanostructures.

Another representative example is the CVD synthesis of single wall carbon nanotubes (SWCNTs). Each SWCNT only has one single layer of graphite carbon. Its diameter is within 1-4 nanometers. The synthesis is usually through catalyst-assisted decomposition of carbon precursors, such as methane or ethylene. Though CVD synthesis has the potential to scale-up the production and lower down the cost, it always suffers from the impurities such as the catalyst particles and amorphous carbon. A recent report from Iijima's group announced the successful large-scale synthesis of SWCNTs with the help of an appropriate amount of water vapor addition. Water was a soft oxidizer that selectively etched away amorphous carbon, but kept SWCNTs below a certain temperature. The removal of amorphous carbon not only purifies the yield, but also keeps the active time of the catalyst longer, thus enables ultra-long growth of uniform SWCNTs. SWCNT forest with a height as tall as 2.5 mm is synthesized on top of a deposition substrate. The black soot-looking substance is composed of well-aligned bundles of SWCNT as revealed by SEM images. The purity of the SWCNTs grown by this method can be clearly seen from a low magnification TEM image where no catalyst particles or amorphous carbon is present. A high resolution TEM image further confirming the nanotubes are indeed only composed one layer of carbon atoms. With the many folds application promises of carbon nanotubes, this progress on the mass production will certainly push it closer to industrial applications.

1.3. Rare-earth Hexaborides as Electron Emission Sources

As illustrated in figure 1.2, all hexaborides of rare-earth metals have the same crystal structure, which can be described by a cubic lattice with boron octahedra located at each of the eight corners and one rare-earth atom at the center of the cube. The lattice constant of the compounds, about 4 angstroms, is mainly determined by the boron frame

work, therefore varies only slightly among different rare-earth comporals. Such an arrangement makes the compound similar to pure boron in some aspects of stability, such as the high melting point and high mechanical strength. Besides the covalent bonding, the bonding nature inside a rare-earth hexaboride has metallic bonds, which also render a high conductivity in the compounds. Another amazing nature of this structure is the low work function at their surface. It is believed that the rare-earth hexaboride surface is terminated with rare-earth atoms. This active layer thus enables electrons to escape from the surface over a low energy barrier. The continuous rare-earth atom supply from the body framework maintains this metal atom layer through diffusion, thus keeps the low work function. These properties are perfect for the use of the material as an electron emission source and this opportunity was first brought up by Lafferty in 1951(Lafferty, 1951).

In the work of Lafferty's, he systematically studied the thermionic emission properties of several metal hexaboride materials, which include ThB_6, BaB_6, SrB_6, CaB_6, LaB_6 and CeB_6. Emission results showed that, among the borides tested, CeB_6 and LaB_6 have the lowest work function of around 2.6 eV. LaB_6 has a higher emission constant than CeB_6, therefore is considered the best candidate for a thermionic emission source. A series of comparisons between LaB_6 and conventional emission materials, such as W, Mo, and BaO, were made subsequently. It showed that under the same emission current density, LaB_6 needs a heating temperature 600-800^oC lower than the Mo or W filament. The emission density could go as high as 10 A/cm^2 without degradation, while BaO emitter failed below 1 A/cm^2, likely due to its high resistance. Evaporation rate data showed that, comparing to the refractory metals, LaB_6 weight loss rate due to evaporation is more than 100 times lower than the least evaporation rate from the Ta metal, under the same emission current density. After showing the great advantage of using LaB_6 as a

thermionic emission source material, Lafferty also searched the proper heating material for this compound, since boron was found tending to diffuse into the holding material if a conventional metal holder was used. Graphite was found to be the most proper choice.

Lafferty's work set a solid foundation for using LaB_6 as a superior thermionic emission source. The rare-earth hexaboride he used in the test was a sintered polycrystalline rod. After him, a series of extensive studies were done on single crystals of rare-earth hexaboride by Swanson and his group. Several important facts were found. CeB_6 has comparative emission properties with LaB_6. It has a slightly lower work function of 2.4 eV compared to 2.6 eV of LaB_6. Its evaporation rate is lower than LaB_6 at temperature above 1600^{o}C (Swanson & McNeely, 1979; Davis et al., 1989). Among the low index crystal planes, the (100) surface of LaB_6 and CeB_6 has the lowest work function and therefore is most suitable as the electron emission surface (Swanson et al., 1981). A. N. Broers of IBM reported the first electron gun using LaB_6 as a cathode in 1967 and subsequently the first SEM using a LaB_6 thermionic electron gun (Broers, 1967 & 1969). Today, LaB_6 and CeB_6 thermionic guns are widely used in electron microscopes and electron lithography systems. It usually has a truncated emission plane of (100). The advantage of the truncated shape over conical shape was studied with an electron beam lithography system (Tennant & Swanson, 1989).

The field emission properties of LaB_6 were also studied in the 1970's and 1980's followed by its successful use as a thermionic emission source. A representative work was done by Windsor (year?) . In his work, he used an electrochemically etched polycrystalline LaB_6 rod as the field emitter. An emission current of 1-2 mA was maintained for more than 1000 hours without any observed degradation. Fluctuations in current were believed to be caused by contamination adsorptions which migrate on the emitter surface (Windsor & Eng, 1969). In order to suppress the current fluctuations

caused by surface adsorption, Shimizu's group at Osaka university operated the LaB_6 emitter at elevated temperature. The thermal field emission current density was proven to be higher than that of the tungsten emitter (Nagata et al., 1990). A LaB_6 thermal field emission gun was built by the same group and was installed in a transmission electron microscope (Harada et al., 1991). The thermionic emission from the emitter side surfaces seemed to cause vacuum problems despite of the high current density they achieved. All the LaB_6 field emission studies then were based on conical shaped electrochemically etched LaB_6 needles.

1.4. Nanotube/Nanowire (NT/NW) Field Emission

Field emission is the process of electrons escaping from the emitter surface into vacuum after overcoming a surface energy barrier φ with the help from an externally applied electric field E. At normal temperature, the field emission current is insensitive to temperature changes. Therefore, within a wide range of temperature, the emission current density is well described by the famous zero temperature Fowler-Nordheim (F-N) formula originally invented by Fowler and Nordheim (Fowler & Nordheim, 1928).

$$J = 6.2 \times 10^{-6} \frac{2.2}{(5+\phi)\sqrt{\phi}} E^2 \cdot \exp(-6.8 \times 10^7 \frac{\phi^{1.5}}{E}) A/cm^2$$

taking the Fermi energy level to be 5 eV. From the formula, we see that the emission current is only significantly affected by two variables, the work function φ and electric field strength E. The work function, depending on the specific material, ranges from 1-5 eV. Giving a certain applied voltage, the local electric field E depends on the field enhancement of the emitter geometry, which in general, the sharper the emitter is, the stronger electric field be expected.

Electrochemical etching techniques can make metal needles as sharp as 100 nm in apex radius of curvature with ease. By field emission, for example, the current density

one can attain at room temperature from a sharp tungsten needle, is over 1000 times higher than that from a high temperature thermionic emission mechanism. Therefore, it is highly suitable for making point electron sources where high brightness is demanded. Electron microscopes, such as the TEM and SEM, is a direct application for such bright electron sources. The direct consequence of using a high-brightness electron source is the improved special resolution of the electron microscope. On the other hand, because the work function exponentially affects the emission current density, slight changes in work function can cause large current fluctuations. Even in an ultra-high vacuum, inevitable adsorptions tend to change the emitter's work function, thus cause instability in the beam current. Another problem that a field emitter suffers from is short service life. The high emission current density causes serious joule heating that raises the tip's local temperature, which increases the atomic mobility at the tip. Normal field emission requires field strength of about 10^7 V/cm at the tip of the emitter, which tends to form local protrusions through a field build-up. The sharp protrusion causes a larger emission current, which raise the temperature even more. This cycle usually leads to vacuum arcing and destroys the emitter structure (Furcey, 2005).

Carbon nanotube (CNT) is believed to have the potential in solving these above mentioned problems. Frist of all, carbon nanotube, especially single wall carbon nanotube, has atomically sharp tip and long aspect ratio, therefore naturally has the ideal shape of a field emitter; secondly, it is empirically believed that field emission from a carbon material is insensitive to adsorption. Lastly, the covalent bonding in a carbon nanotube is multiple times stronger than the metallic bonding of tungsten; therefore carbon nanotube field emitter is expected to have a longer service life. A noise ratio as small as 0.08% for a single CNT field emitter was obtained by de Jonge. (de Jonge et al., 2005). He also found that the brightness of the CNT emitter is one order of magnitude higher than the

conventional tungsten field emitter. (de Jonge, 2004)

Another application of field emission sources is to attain electron emission from arrays of emitters evenly distributed on a planer surface. Emission current is collected over a certain area as a sum of more than one emitter. This way, the current fluctuations due to each individual emitter cancel out with one another and give an overall stable performance. Such a structure can directly be used as a field emission display screen. Field emission vacuum devices can be built on the basis of such emitter arrays as well. The usual method to fabricate such arrays is through expensive semiconductor processing. As synthesized nanotube/nanowires are naturally in the form of massive free-standing entities on a flat substrate, such structure may also be directly used as field emission arrays. A more controlled way is to make CNT pastes, a mixture with other organic mixers for adhesion and photolithographic purposes. Such a paste is then printed onto a photolithographically-defined structure and eventually adheres to the desired gated sites. Such a paste layer has a many CNTs and some of the CNTs have their tips protruded from the paste, which can still enhance greatly the local electric field when a driving voltage is applied. A 5-inch color display was made with this technique (Chung et al., 2002).

1.5. In-situ Measurements in a Transmission Electron Microscope (TEM)

Transmission electron microscope (TEM) is a powerful tool in studying the structure of materials. Modern medium-voltage TEM (200-300 kV) can achieve a point resolution better than 1 angstrom with the help of newly developed Cs-correction technique. Seeing individual atoms becomes standard. With the help of spectrosc-pic techniques, such as EELS, EDX, chemical compositions can also be analyzed at the nanometer scale with a TEM The direct observation of the material's structure and the knowledge of its chemical composition help us in predicting its various types of

properties, such as the mechanical strength, conductivity, magnetism and ferroelectrics. Since the materials' functionalities strongly depend on these properties, it has always been a microscopist's task to correlate the materials' structure with their corresponding properties. Conventional ways are that materials are tested for their properties either before or after being put into the TEM for structural characterization, and then ideas will be raised to explain what has been obtained through testing with the structural information we obtained from the TEM observations. However, this process always involves uncertainties. For example, if a certain dislocations was observed in a sample after the tensile loading at its bulk form before making into a TEM sample, it is hard to judge whether the dislocation induced by the loading or simply a result of the sample preparation, no mention to get detailed information about the formation mechanism and dislocation movement. An ideal approach will be observing the sample in TEM while applying tensile loading to it at the same time. The type of holder designed for this purpose is a stretching stage. Another early prototype of in-situ TEM holders is a heating stage, which is capable of heating the sample while imaging it in TEM at the same time.

Nanomaterials, especially one dimensional nanotubes and nanowires have received considerable research interests for the recent 15 years. Newly proposed applications for nanotubes/nanowires such as chemical/biological sensors, electronic devices, structural enforcements, nano-scale lasers, thermal barriers, field emitters, keep occurring in the literatures. Just like other materials, the applications of one dimensional nanomaterials' to a large extent depend on their unique physical properties and these properties are closely related to their crystal structures and chemical compositions. It is especially helpful to study nanotubes/nanowires using the TEM. Nanotubes/nanowires have a high surface-to-body ratio, therefore their properties depend on both the surface and the body structures. TEM is capable of studying these two aspects at the same time.

These materials are also fairly convenient for TEM study, because their dimensions (below 100 nm in width) are within the transparent range for the incident electron beam. We can simply treat nanotubes/nanowires as fine powders when measuring their properties. However, to measure the physical properties of an individual nanotube/nanowire is a formidable task. This is because of the very tiny size of these materials we can not even see them with a conventional optical microscope, not to mention to manipulate and to perform the measurement. To correlate their properties with microstructure is even harder, since the translation of them in and out of the TEM usually introduces damage, modifications and contaminants to their surface, which are probably the very part that determines their properties. In-situ study of nanotubes/nanowires is therefore highly necessary. The high vacuum of the TEM chamber itself also offers a clean environment for a lot of surface-sensitive properties to be studied, for example, field emission and conductance measurement.

The first in-situ field emission and conductance measurement on one dimensional nanomaterials was done by Wang etc. using a home designed TEM holder that enables a voltage been applied between an electrode containing CNT and a counter electrode (Wang et al., 2000). The CNT containing electrode can also be moved in one dimension to and away from the other fixed electrode. This configuration enabled a series of measurements on individual nanotube/nanowires, such as the field emission, bending modulus and conductivity. A more delicate holder installed in an ultra-high vacuum transmission electron microscope was built in Tokyo Institute of Technology. Their manipulation tip enables 3-D fine movements inside the TEM sample chamber. TEM images have been taken when a thin gold nanowire of 1 nm in diameter was gradually stretched along the axial direction. (Kondo & Takayanagi, 2000) The thinning process was monitored at the atomic scale. Since then, more in-situ holders for nano-scale

manipulation and measurements have been reported, including commercialized products, such as the STM holder, nanoindenter by Nanofactory Inc. (Svensson et al., 2003).

1.6. Overview of Thesis

This will be constructed following the sequence of our actual experiments. In chapter 2, the synthesis and characterization of several one-dimensional nanostructures are presented; after that, chapter 3 is dedicated to discussing the growth mechanism accounting for our synthesized nano-materials. Chapter 4 present field emission measurement studies we performed on the fabricated nanowire field emitters using the synthesized LaB_6 nanowires. It is divided into two major parts; the ex-situ measurement and in-situ measurement.

REFRENCES

Broers, A. N. (1969). A new high resolution reflectrion scanning electron microscope. Review of Scientific Instrument, 40(8), 1040-1045.

Broers, A.N. (1967). Electron gun using long-life lanthanum hexaboride cathode. Journal of Applied Physics, 38(4), 1991-1996.

Chung, D., Park, S., Lee, H., Choi, J., Cha, S., Kim, J., Jang, J., Min, K., Cho, H., Yoon, M., Lee, J., Lee, C., Yoo, J., Kim, J., Jung, J., Jin, Y., Park, J., & You, J. (2002). Carbon nanotube electron emitters with a gated structure using backside exposure processes. Applied Physics Letters, 80(21), 4045-4047.

Davis, P. R., Gesley, M. A., Schwind, G. A., Swanson, L. W., & Hutta, J. J. (1989). Comparison of thermionic cathode parameters of low index single crystal faces of LaB_6, CeB_6 and PrB_6. Applied Surface Science, 37, 381-394.

De Jonge, N. (2004). Brightness of carbon nanotube electron sources. Journal of Applied Physics, 95(2), 673-681.

De Jonge, N., Allioux, M., Oostveen, J. T., Teo, K. B. T., & Milne, W. I. (2005II). Low noise and stable emission from nanotube electron sources. Applied Physics Letters, 87(13), 133118.

Fowler, R. H., & Nordheim, L. (1928). Electron emission in intense electric field. Proceedings of Royal Society of London, 119, 173-181.

Gao, P. X. & Wang, Z. L. (2004). Nanopropeller arrays of zinc oxide. Applied Physics Letters, 84(15), 2883-2885.

Gao, P. X., Ding, Y., Mai, W. J., Hughes, W. L., Lao, C. S. & Wang Z. L. (2005). Conversion of zinc oxide nanobelts into superlattice-structured nanohelices. Science, 309, 1700-1704.

Harada, K., Nagata, H. & Shimizu, R. (1991). <310> single-crystal LaB_6 as thermal field emitter of high brightness electron source. Journal of Electron Microscopy, 40, 1-4.

Hata, K., Futaba, D. N., Mizuno, K., Namai, T., Yumura, M., & Iijima, S. (2004). Water-assisted highly efficient synthesis of impurity-free single-walled carbon nanotubes. Science, 306, 1362-1364.

Iijima, S. (1991). Helical microtubules of graphitic carbon. Nature, 354, 56-58.

Kondo, Y. & Takayanagi, K. (2000). Synthesis and characterization of helical multi-shell gold nanowires. Science, 289, 606-608.

Kong, X. Y. & Wang, Z. L. (2003). Spontaneous polarization-induced nanohelixes, nanosprings, and nanorings of piezoelectric nanobelts. Nano Letters, 3(12), 1625-1631.

Kong, X. Y., Ding, Y., Yang, R. & Wang, Z. L. (2004). Single-crystal nanorings formed by epitaxial self-coiling of polar nanobelts. Science, 303, 1348-1351.

Lafferty, J.M. (1951). Boride cathodes. Journal of Applied Physics, 22(3), 299-306.

Levitt, A. P. (1970). Whisker technology. New York: Wiley-Interscience.

Nagata, H., Harada, K. & Shimizu, R. (1990). Thermal field emission observation of single-crystal LaB_6. Journal of Applied Physics, 68(7), 3614-3618.

Pan, Z. W., Dai, Z. R., & Wang, Z. L. (2001). Nanobelts of semiconducting oxides. Science, 291, 1947-1949.

Sears, G. W. (1955). A growth mechanism for mercury whiskers. Acta Metallurgica, 3, 361-369.

Svensson, K., Jompol, Y., Olin, H., & Olsson, E. (2003). Compact design of a transmission electron microscope-scanning tunneling microscope holder with three-dimensional coarse motion. Review of Scientific Instruments, 74(11), 4945-4947.

Swanson, L. W., Gesley, M. A., & Davis, P. R. (1981). Crystallographic dependence of the work function and volatility of LaB_6. Surface Science, 107, 263.

Swanson, L.W., McNeely, D.R. (1979). Work functions of the (001) face of the hexaborides of BA, LA, CE and SM. Surface Science, 83(1), 11-28.

Tennant, D. M. & Swanson, L. W. (1989). The effect of LaB_6 cathode shape on its performance in a JBX 5DII electron beam lithography system. Journal of Vacuum Science and Technology B, 7(1), 93-97.

Wagner, R. S. & Ellis, W. C. (1964). Vapor-liquid-solid mechanism of single crystal growth. Applied Physics Letters, 4(5), 89-90.

Wang, Z. L., Poncharal, P. & de Heer W. A. (2000). Nanomeasurements of individual carbon nanotubes by in situ TEM. Pure and Applied Chemistry, 72(1-2), 209-219.

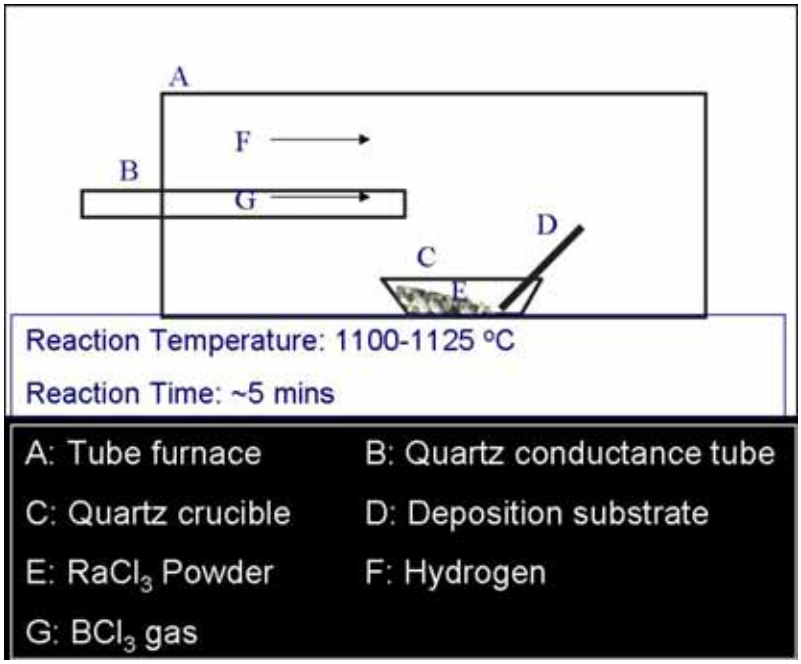

Figure 1.1. Illustration of the chemical vapor deposition system used in the production of rare-earth (Ra) hexaboride nanowires.

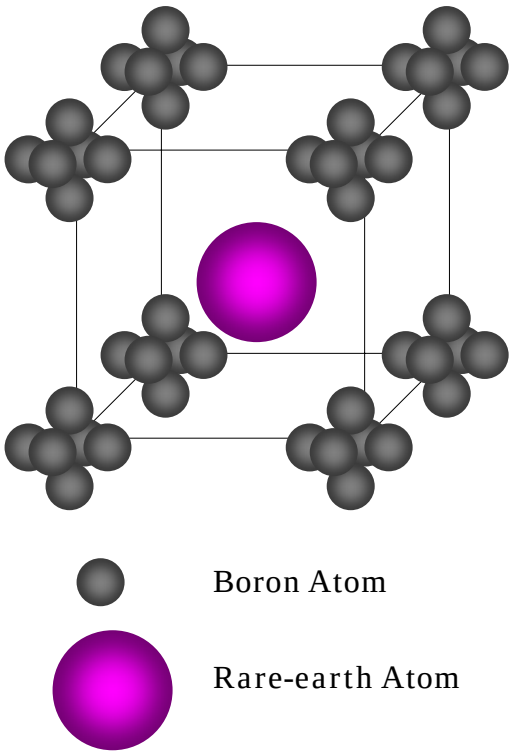

Figure 1.2. Crystal structure of rare-earth hexaboride. A cubic lattice with boron octahedra at each of the eight corners and rare-earth metal atom in the center.

Chapter 2 Synthesis of Rare-Earth Boride Nanowires

2.1. Introduction

2.1.1. Background

One dimensional nanostructures, such as nanotubes and nanowires, are a brand new scientific research area that has attracted a lot of attentions in the past 15 years, ever since the discovery of carbon naotubes in 1991 (Iijima, 1991). The discovery of small one-dimensional inorganic structures can be traced back to 400 years ago, when L. Erker noticed hair-like whiskers grown from copper sulfide ores (Levitt, 1970). In the 1940's, metal whiskers formed from metal surfaces were seriously studied because they were believed to be the cause of short-cut in electric circuitry. The main interest of the study at that time was to avoid the formation of whiskers rather than to grow it. It wasn't till the 1950's that researchers started efforts in making them intentionally, mainly due to the Bell Lab's discovery that metal whiskers were free of defects and could achieve the mechanical strength that approaches the materials' theoretical limit. With their apparent applications in reducing weight and enhancing strength for structural materials, those whiskers attracted much research attentions since then. It was soon well demonstrated that composite materials with whiskers mixed in their matrix have higher strength and stiffness compared to their pure form. To realize this application, the efforts in the whisker synthesis then were directed to produce in larger quantities and at lower costs. Vapor phase synthesis was proven to be the most efficient. Other methods which were hard to guarantee productivity received little attention

due to the fact that only feasible applications then were to make bulk composite materials and that required large quantities. Mercury whiskers as small as 10 nm were carefully studied in the 1950's, mostly out of laboratory curiosity. Such small whiskers actually belong to one of our hottest research categories today, the nanowires. Today, with the fast development in microelectronics industry, the scale we used to look at materials is greatly changed compared to 50 years ago. For example, copper interconnects below 100 nm in integrated circuits are already one of the "standard". Therefore, the need to synthesize materials in nano-scale, to study their emerging new properties relating to size, to utilize their electrical, optical, and magnetic properties in all other fields has re-raised huge interests in whisker materials, which are a group of materials that naturally bear the small dimension. We define the whiskers with size below 100 nm as nanowires and those as nanotubes if they have hollow stems. On the other hand, the advancements in material characterization, material measurement and manipulation have enabled us to "use" or at least test the possibility of using these nanotubes/nanowires (NT/NWs) individually as various types of miniature devices. Each NT/NW's functionality after all mostly depends on its chemical composition. Therefore, as for the synthesis of materials, quantity is not the only important factor now, the variety together with quality is more important than ever.

As for the chemical composition, major elements, most functional oxides, nitrides, carbides, some borides, ternary compounds and even quaternary compounds have all been reported grown into NT/NWs using various approaches (Xia et al., 2003; Rao et al., 2003). As for physical properties, metallic, semiconducting, insulating, magnetic, ferromagnetic, ferroelectric and supeconducting NT/NWs have all been synthesized. The synthesis techniques have almost developed to the stage that we are able to synthesize NT/NWs out of

most of the materials' bulk form counterparts. Lots of times, for one specific NT/NW, there is more than one route to apply. The general strategies can be divided into the following categories: using the materials' structural anisotropy; vapor-liquid-solid growth; vapor-solid growth and template-assisted growth. Among these strategies, some reactions take place in vapor phase and some in solution.

The crystal structure of some materials can be characterized as chain structures. Between molecules, there is only one direction that is easy to form covalent bonding. Therefore, when it crystallizes, one-dimensional growth takes place naturally. The Van der Waals interactions connect different chains side by side. Therefore, the nanowires formed by this manner tend to aggregate into bundles. Examples of materials with this type of structure are: $M_2Mo_6X_6$ (M= Li, Na; X= Se, Te), $(SN)_x$, Se, Te, $K_2[Pt(CN)_4]$, MX_3 (M= transition metal; X= Se, Te). The reduction of selenious acid with hydrazine is one typical reaction to synthesize Se nanowires. After mixing the two reactants in hot water, following reaction take place: $H_2SeO_3 + N_2H_4 = Se + N_2 + 3H_2O$. The precipitates Se is in the form of α-Se colloid. After being left aging for several days, the α-Se is converted into crystalline t-Se and the t-Se self-organizes into nanowires between 10 nm-100 nm in diameter and over microns in length. Alcohol can be used to facilitate the aging process and reduces the processing time from several days into several hours.

The most applied vapor phase method to synthesize NT/NWs is the famous vapor-liquid-solid route developed by Wagner in the 1960's (Wager, 1964). In his model, he utilizes metal liquid droplets' ability to absorb molecules from the vapor phase. When the absorbed composition reaches a eutectic point with the metal catalyst, precipitation takes place on one side of the catalyst droplet. As the droplet keeps collecting vapor molecules,

supersaturation causes more materials to precipitate on the previously formed nuclei, thus realizes one dimensional growth of the materials. At the end of the growth, the metal droplet catalyst usually appears as a particle either at the root or on the tip of the grown whiskers. A classical example is the growth of silicon nanowires. The size of the nanowires is proportional to the size of the gold catalyst. The silicon vapor can either be created by thermal reduction of silane or laser ablation of a silicon target. By laser ablating the catalyst metal with silicon source, Morales have made Si nanowires with uniform diameters of about 20 nm (Morales and Lieber, 1998).

The vapor-solid method is the simplest approach among all. It involves the introduction of the desired vapor phase and the subsequent solidification of the vapor into nanowires. The driving force for the solidification is usually a temperature gradient which is hotter in the evaporation zone and cooler in the deposition zone in order to create supersaturation. Generally speaking, if the supersaturation is low, nanowires are formed; if it is medium, diskettes are formed; intermediate supersaturation produces 3 D blocks and high supersaturation produces isotropic powders. This method is catalyst free, and therefore is a clean and simple approach. However, the lack of control in the NT/NWs' size distribution is its drawback. A series of oxide nanowires, including ZnO, SnO_2, Al_2O_3, have been produced with good quantity. Since the nanowire formation by this method is usually driven by crystallographic surface energy differences, it usually results in good crystallinity in the synthesized nanowires.

Finally, the template-assisted method: the deposition of desired materials into the nano-scale pores naturally formed on the substrate surface and the subsequent procedure of removing the templates. The most commonly used templates are anodized aluminum oxide

(AAO) membranes, which have channels packed in a hexagonal order. Depending on the anodizing parameters, the channel sizes have a range from 30 nm to 100 nm in diameter. The desired materials can be either electrochemically plated into the channels or can be introduced through the vapor phase. After reaction, the AAO membrane can be dissolved by Na(OH) solution. Pre-formed nanowires of other materials can also be used as templates. In this route, desired materials are coated on the outmost wall of the pre-formed nanowires and it is followed by the removal of the template nanowires. By this way, nanotubes can be formed. Technically, any materials can be made into nanotubes by this method. The drawback of the template approach is the poor crystallinity.

Solid-state synthesis strategy has also been reported by several groups in making ternary salts. The advantage of using the solid-state reaction is the high yield. However, it is usually hard to control the product, because of the complexity of the elements involved in those reactions.

Generally speaking, to choose a proper synthesis method, one needs to first find the proper chemical reactions to produce such substance. It is preferred to be an either solution based or vapor phase based reaction. Then within each NT/NW synthesis category, one needs to choose the type of method suitable for the desired materials' crystallographic nature. For example, if the crystal is highly anisotropic, then self-assembly is possible without the need for much external help. If the crystal is highly isotropic, then the catalyst assisted reaction is probably more suitable. If the uniformity in size distribution is preferred over crystallinity, template method might be chosen over crystallization-driven vapor-solid method. Yield and reaction time span should also be considered if more than one option is available.

2.1.2. Motivation

Lanthanum hexaboride (LaB_6) and cerium hexaboride (CeB_6) single crystals have been one of the most widely used thermionic electron sources in a large variety of devices utilizing electron emission. The low work function (Gesley & Swanson, 1984) together with low vapor pressure at high temperature (Swanson et al., 1981) makes LaB_6 a superior thermionic electron cathode material over conventional filamentous tungsten in electron optical instruments such as the transmission electron microscope (TEM) and the scanning electron microscope (SEM). Compared to LaB_6, CeB_6 is believed to have even lower work function and lower volatility, which mean lower operation temperature and longer service life for a thermionic electron emitter. (Swanson & McNeely, 1979; Davis et al., 1989) To pursue higher performance in these microscopy applications, field emission (FE) electron sources have been introduced to achieve an even higher brightness and lower energy spread. W or W/ZrO based field emission gun (FEG) is now commercially available and can offer a brightness two orders of magnitude higher than the LaB_6 thermionic electron gun (Williams & Carter, 1996). The brightness of an FEG is proportional to the current density of electrons emitted from the cathode surface, which can be described by the zero-temperature Fowler-Nordheim (F-N) equation (Brodie & Spindt, 1992).

$$J = 1.5\times10^{-6}\frac{E^2}{\phi}\frac{10.4}{\phi^{1/2}}\exp(-\frac{6.44\times10^7\phi^{3/2}}{E})\ A/cm^2, \quad (2.1)$$

where ϕ is the work function of cathode material and E is the local electric field applied on the cathode tip, which can be expressed as

$$E = V/5r, \quad (2.2)$$

with V being the applied voltage and r being the radius of the cathode tip.

The above relations show that a lower work function and a smaller tip radius of the cathode result in a higher emission current density. Being stimulated by the fact that LaB_6

has a much lower work function than W or W/ZrO and that it offers excellent performance as a thermionic electron source, extensive field emission studies have been carried out on the electro-etched LaB_6 and CeB_6 needles with tip radii ranging from 100 nm to 300 nm, in the search of a brighter field emission electron source. (Shimizu et al., 1975; Futamoto et al., 1977; Nagata et al., 1990; Harada et al., 1991; Zaima et al., 1980; Okano et al., 1977) High temperature field emission studies showed that a brightness of at least two orders of magnitude higher than that of LaB_6 thermionic emitter could be achieved with good stability and that only half of the local electric field was necessary to draw substantial current from the LaB_6 needles compared to thermal assisted W/ZrO FEG, which was attributed to the lower work function of LaB_6. However, when the electron emission is operated at high temperature, it would require higher vacuum and have larger energy spread in the electron beam, which will result in larger chromatic aberration in electron coherence. In their cold field emission studies, a high temperature flashing procedure and a high vacuum of at least 10^{-9} torr were required throughout the measurement in order to obtain field emission. These limitations have held the FE electron source applications below a practical level for this type of electro-etched LaB_6 needles.

In the rare-earth hexaboride (ReB_6) family, GdB_6 is believed to have the lowest work function (~1.5 eV).(Kudintseva et al., 1967) However, satisfactory thermionic emission has not been achieved with this material, likely due to the relatively poor stability of GdB_6 at high working temperature around 1500^{o}C. (Kudintseva et al., 1967; Tanaka et al., 1980; Storms & Mueller, 1981) Nevertheless, the extremely low work function of GdB_6 offers a great opportunity for making this material room temperature field emitters that put less stringency on the high temperature stability.

One-dimensional NT/NWs have very sharp tips with diameter ranging from over a hundred to a few nanometers. Their properties in field emission were first demonstrated in CNTs. (Chernozatonskii et al., 1995; Rinzler et al., 1995; Deheer et al., 1995) The nanometric tip geometry of CNTs enhanced greatly the local electric field and allowed stable field emission of high current density under much more practical experimental conditions such as low applied voltage, low vacuum, room temperature, and even without the need for the flashing procedure. These attractive features have aroused tremendous amount of scientific interest in this field and today, its advantage over conventional field emission electron sources has been well demonstrated. (Bonard et al., 2001; deJonge et al., 2002; Zhang et al., 2004) In the meantime, nanowires of many other materials have also been reported to show low turn-on voltage field emission phenomena which were believed originated from their small tip dimension. (Wong et al., 1999; Chen et al., 2002; Lee et al., 2002; Li et al., 2002; Yin et al., 2005) However, the large work functions of these materials including CNTs still impose tough working conditions under which these materials are utilized. To find a high performance NT/NW field emission cathode material, LaB_6 nanowires, CeB_6 nanowires, and GdB_6 nanowires which have low work function and good electrical conductance, offers a better chance and this possibility has not been well explored yet. Among all the crystal lattice planes of ReB_6, the {001} planes have both low work function and low volatility and therefore it is commonly preferred as the emission plane for commercialized ReB_6 thermionic electron guns. Therefore, it is possible that ReB_6 nanowires orientated in <001> lattice direction are also more preferable for field emission applications than those of other orientations.

In this chapter, the synthesis of <001> oriented ReB_6 nanowires will be reported (Zhang et al., 2005II; Zhang et al., 2005III; Zhang et al., 2006).

In the same time, by introducing carbon in the reactants, we have succeeded in producing a LaB_6-in-CNT structure. Since CNT, especially SWCNT, has extremely small diameter in the range of a few nanometers and carbon material was observed to has the best resistance to chemical etching, this unique structure has the potential to combine these advantages from CNT side with the low work function from the LaB_6 side. (Zhang et al., 2005I;)

The family of ReB_6 can be constructed by placing rare-earth atoms inside vacancies of a 3-D primitive cubic (PC) framework formed by boron octahedron clusters. Rare-earth dedocaboride (ReB_{12}) can be constructed by changing the PC lattice of the ReB_6 into a face-centered-cubic (FCC) structure and replacing the octahedral boron clusters with icosahedra clusters. This type of atomic arrangement is believed to induce superconductivity phenomenon in several metal dedocaboride compounds with the same structure, such as YB_{12}, ZrB_6, LuB_6, ScB_{12} and ThB_{12}. (Matthias et al., 1968)

Nanowires of several metal borides have been successfully grown by various different methods in recent years, such as MgB_2 nanowires synthesized by post-reacting B nanowires with Mg vapor or direct pyrolysis,(Wu et al., 2001; Ma et al., 2003) CrB nanowires by a solid state reaction,(Ma et al., 2003) CaB_6 nanowires by flowing B_2H_6 gas over a Ni covered CaO layer.(Xu et al., 2004) ReB_{12} superconducting nanowires, such as YB_{12} nanowires, provide a perfect model to study size effect of superconductivity on a nanometer scale.(Bezryadin et al., 2000) Therefore, producing single crystalline ReB_{12} nanowires are of great scientific and industrial interests.

Conventionally, Single crystals of eReB_6 and ReB_{12} are prepared by floating zone melting method or aluminum flux methods by sintering pure rare-earth metals with boron powders. (Davis et al., 1986) The specific composition, ReB_6 or ReB_{12}, is controlled by the ratio of rare-earth metal to boron in the starting mixture before sintering. Micron sized LaB_6 whiskers were also reported grown by a chemical vapor deposition (CVD) method. (Motojima et al., 1978; Givargizov & Obolenskaya, 1981; Kher & Spencer, 1998) Superconducting YB_{12} nanowires and LaB_{12} nanowires haven't been reported to be synthesized and LaB_{12} is a new phase in Lanthanum and boron system which hasn't been reported so far.

Besides ReB_6 and ReB_{12} nanowires, it is also important to synthesize some other useful one dimensional nano-structures by using the same CVD system. Examples are MgB_2/MgO nanocables, MgO nanowires and Mg_3N_2 nanowires.

Since Nagamatsu *et al*. discovered that MgB_2 is a superconductor with a transition temperature at 39 K, (Nagamatsu et al., 2001) many research efforts have been focused on MgB_2 due to the excellent properties of this material relating to superconductivity such as high critical current density, high irreversibility field and strong linkage between grain boundaries.(Eom et al., 2001; Larbalestier et al., 2001) Besides the bulk form, other forms of MgB_2 have also been fabricated, including thin films and dense wires.(Eom et al., 2001; Canfield et al., 2001) Motivated by interests in fundamental physics such as the dimensionality dependence of superconductivity and potential applications such as quantum interference devices,(Bezryadin et al., 2000; Burnell et al., 2002) researchers have also reported the synthesis of polycrystalline as well as single crystalline MgB_2 nanowires, (Wu et al., 2001; Ma et al., 2003) which all involve a two-step procedure, either through the

synthesis of Boron nanowire or synthesis of MgB_2 bulk form. However, due to the high volatility of magnesium and its high reactivity with oxygen, B-Mg-O system usually favors the formation of MgO nanowires more than that of MgB_2 nanowires. (Yin et al., 2002; Klug & Dravid, 2002) Here we present a one-step approach to make MgB_2/MgO nanocable structures by reacting B_2H_6 gas with Mg vapor in a tube furnace using Pt wires as catalyst. The characterization of such produced structures using selected-area electron diffraction (SAED) and diffraction contrast electron microscopy is also described.

Magnesium oxide (MgO) is also a widely used important material. Its application covers a wide range from thermal insulation, additives in refractory, paint manufacturing, catalyst, toxic waste remediation, to substrate materials for electronic/magnetic devices .(Ma & Bando, 2003; Smith et al., 2001; Yang et al., 2001) MgO one-dimensional nanostructures were found to have even more intriguing properties. MgO nanowires were successfully incorporated into high Tc superconductors to generate column defects which in turn pin the magnetic flux lines within the superconductor and improve its performance at high temperature and intensive magnetic field.(Yang et al., 1996) Recently, MgO nanowires were used as deposition substrate to synthesize nanocables of various functional oxides materials which are otherwise very difficult to form into one-dimensional nanostructures.(Han et al., 2005; Zhang et al., 2004)

The synthesis of MgO nanowires has drawn intensive research interests during the past few years and various types of single-crystalline MgO one-dimensional nanostructures were produced.(Ma & Bando, 2003; 1,Yin et al., 2002; Zhao et al., 2004; Zhang & 2001; Klug & Dravid, 2002; Li et al., 2002) It was found that a slow reaction rate between Mg vapor and O_2 is very crucial in forming MgO nanowires. In order to get lower Mg vapor

pressure which will in turn lead to slower reaction rate, $MgCl_2$, MgB_2, Mg_3N_2 or Mg/Al mixture were usually preferred as Mg vapor source rather than pure Mg metal which often results in the formation of MgO cubes rather than MgO nanowires. However, we recently discovered that, by direct evaporation of Mg metal in an atmosphere of N_2/H_2, a mass production of polycrystalline MgO nanowires could be achieved and Mg_3N_2 nanowires were also produced during the process. Being an important starting material in manufacturing functional nitrides, ternary rare-earth nitrides and new semiconductor, Mg_3N_2 has been made into ultra-dispersed nanometric powders.(Vissokov & Pirgov, 1996; Cui et al., 1999) However, it is the first time that the synthesis of Mg_3N_2 nanowires being reported. Our successful synthesis of the polycrystalline MgO and Mg_3N_2 nanowires offers some new clues in seeking out the nanowire growth mechanism in Mg-O-N system.

The current only available method to produce nanometer sized LaB_6 single crystalline rods is through a chemical vapor deposition procedure (Zhang et al., 2005I, II, III & 2006). Nanowires with a high growth density appeared on small spots of size around one centimeter square on the catalyst-coated silicon substrate after the deposition. While the yield is sufficient for the fabrication of single-nanowire based field emitters for electron optical instruments, for large area applications such as flat panel displays, field emission x-ray tubes, field emission lamination lamps, a mass production with a high yield is needed. Molten aluminum flux method uses aluminum as a media to bring boron and lanthanum together to form LaB_6 at a temperature much lower than the melting point of LaB_6 (Lundstrom, 1984; Gurin et al., 1979; Aita et al., 1974; Futamoto et al., 1975). Due to crystallization inhomogeneity, LaB_6 needle-shaped single crystals with diameters about several hundreds of micron meters and length of several millimeters are usually produced with large quantities.

Part of the goal of our research is to explore the possibility of utilizing this aluminum flux method to produce large quantities of LaB_6 single crystalline nanowires.

2.1.3. Overview of Chapter 2

Since similar CVD synthesis approaches were used in producing different nano-structures, we will first introduce our synthesis system and procedures at the beginning of the chapter. The rest of the chapter will be divided into seven parts with each part centering on the microscopy characterization of a different nanowire synthesized. They will be about the following topics: LaB_6 nanowires, CeB_6 nanowires, GdB_6 nanowires, LaB_6-CNT nanocables; LaB_{12} and YB_{12} nanowires and two types of magnesium based nanowires, MgO and Mg_2N_3. Lastly, the solid synthesis of LaB_6 micron size semi one-dimensional crystals will be introduced. The chapter will be ended after a brief summary and conclusions. Detailed growth mechanism of these nanostructures will be addressed in the next chapter.

2.2 Synthesis System and Procedures

The CVD synthesis was carried out inside a quartz tube furnace. (Figure 1.1) A quartz boat holding $ReCl_3$ powders was placed at the center of the quartz tube, an arch shaped quartz cover was also put on top of the boat in order to concentrate $ReCl_3$ vapor at high temperature. $LaCl_3$, $CeCl_3$, $GdCl_3$ and YCl_3 powders were used one at a time as rare-earth source. Substrates of different materials were also put inside the boat downstream to the evaporation powders to serve as nanowires deposition sites. BCl_3 gas is used as boron source and is conducted to the quartz boat area by a quartz tube. The system was evacuated to 10^{-3} torr and then filled with hydrogen gas (99.9%) before heating up to get rid of oxygen. At ambient pressure of 1 atm and furnace temperature of 1125^{o}C, the BCl_3 gas is then allowed

into the chamber at a flow rate of 5 ml/min for five minutes. In the same time, hydrogen gas was flushed through the chamber at a flow rate of 1600 ml/min to serve three purposes: first to protect the reactants from residue oxygen, second to decompose BCl_3 into elemental boron through the chemical reaction: $2BCl_3 + 3H_2 = 2B + 6HCl$ and third to mix the generated elemental B well with evaporated $ReCl_3$ vapor for better reaction. The ReB_6 nanowires formation is based on the chemical reactions: $ReCl_3 + 6B + 3/2H_2$ (flowing) = $RaB_6 + 3HCl$; and the RaB_{12} nanowires formation is based on the reaction: $ReCl_3 + 12B + 3/2H_2$ (stationary) = $ReB_{12} + 3HCl$. Hydrogen flow rate was set to be 1600 ml/min and 0 ml/min for each reaction respectively and was found crucial in determining between ReB_6 and ReB_{12} phases. A 5% H_2 in N_2 mixture gas was then used to substitute for pure hydrogen gas in order to study effect from hydrogen concentration on the boride nanowire growth. Different substrates, such as platinum coated silicon wafer, quartz plate, 316-stainless steal piece and iron coated silicon substrate were all tested to study the effect on LaB_6 nanowire growth from different catalyst metals. Similar to the CVD approaches that have also been used to produce ReB_6 whiskers with diameters over 1 μm.(Hagimura & Kato, 1980; Givargizov & Obolenskaya, 1986; Motojima et al., 1978; Givargizov & Obolenskaya, 1981; Kher & Spencer, 1998)

Our MgB_2 nanowire synthesis is similar to the hybrid physical-chemical vapor deposition (HPCVD) method used to fabricate MgB_2 thin films described by Zeng et al. (Zeng et al.,2002) A tube furnace is used as reaction chamber. A tantalum bowl is placed inside the furnace tube to hold magnesium chips (99.98%, by Sigma-Aldrich Co.) which serve as Mg vapor source and a platinum wire (by Ted Pella Inc.) is tied above the chips to later catalyze nanowire growth. After the furnace being heated to 650^{o}C in an atmosphere of

Argon mixed with Hydrogen (5% balanced in Nitrogen), magnesium started to evaporate and, in the mean while, B_2H_6 gas (10% mixed in Helium, by Sigma-Aldrich Co.) was introduced into the tube furnace at a flow rate of 75 std. ml/min. Then the furnace was kept at 900^oC for 10 mins before cooling down to room temperature. After the reaction, a layer of yellow/white wool like substance was found covering the Pt wire surface and was sonicated off for structure characterization on a JEOL 100CX transmission electron microscope (TEM) operated at 100KV.

The synthesis procedure for MgO and Mg_3N_2 nanowires is fairly simple: Mg powders (99% Sigma-Aldrich Co.) was held in an alumina crucible as Mg vapor source and a platinum wire was tied above the Mg powders both to catalyze the nanowire growth and to serve as a deposition substrate. The crucible was placed inside a horizontal tube furnace which was evacuated to 3 mtorr and was then flushed with a mixture of Ar, N_2 and H_2 (Ar: N_2: H_2 = 1:1:0.05) at the pressure of 1atm. The system was then heated to 850^oC and held for 10 minutes before cooling down to room temperature. After the reaction, the platinum wire was found to be covered by a layer of white substance which was subsequently studied by scanning electron microscope (SEM, Hitachi-S4700) and transmission electron microscope (TEM, Jeol-100CX).

For solid state synthesis of LaB_6 nanowires, the starting material is a mixture of 1.2g of Lanthanum metal (99.9%, 40 mesh powders, Sigma-Aldrich Inc.), 0.5g of boron powders (practical grade, Sigma-Aldrich) and 45g of aluminum metal. The lanthanum to boron ratio is nearly equal to the stoichiometry of LaB_6. The La/Al and B/Al weight ratios are about 2.5% and 1% and the corresponding solidification points are around 660^oC and 1000^oC respectively according to La and B elements' binary phase diagram with aluminum

(Massalski et al., 1986). The mixture then was put inside an alumina crucible, which was then placed inside a tube furnace for reaction under 1atm atmosphere of Ar gas. Different settings of temperature and reaction time were tried one at a time to study their influence on the growth of LaB_6 crystals. This includes 1000^oC for 10 minutes, 1100^oC for 10 minutes, 1200^oC for 10 minutes, 1200^oC for 30minutes and 1200^oC for 30 minutes followed by 1100^oC for 30 minutes. After heating at the set temperature for the set time of each setting, the furnace was all cooled down to room temperature at a rate of about 500^oC/hr.

After the reaction, the aluminum melt was found melted with the crucible. The whole crucible was then immersed in hydrochloride acid to separate out the product and resolve aluminum melt. LaB_6 Red-purple powders were found precipitated at the bottom of the beaker with gray powders substance which is believed to be un-reacted boron. The powders was then sucked into a centrifuge tube which was loaded into a centrifuge machine to separate LaB_6 from excessive boron, based on the fact that LaB_6 has a higher density than B. After several purifications, the final pure LaB_6 powders was deposited onto a silicon substrate for scanning electron microscope examinations.

For electron microscopy observations, the produced nanowires were first dispersed in ethanol and then collected onto a TEM grid which is coated with a holey carbon film. Transmission electron microscope (JEM-2010F equipped with a field-emission gun) operated at 200 kV was used in the electron diffraction and electron microscopy examination, electron energy loss spectroscopy was applied for chemical composition analysis.

2.3. LaB_6 Nanowires

Figure 2.1 is a typical scanning electron microscope (SEM) image of the synthesized LaB_6 nanowires on silicon substrate. Similar yield density was found covered most of the substrate area. The nanowires are with lateral dimensions from below a few tens of nanometers to over 100 nanometers and lengths extended to over microns. Nanometer and micron sized cubes and rectangular plates were found grow along with the nanowires, which geometries reveal the crystallographic symmetries of cubic LaB_6 single crystals. These cubes and plates sometimes form a right angle joint to connect two nanowires as marked by the arrow in Figure 2.1.

A typical low magnification transmission electron microscope (TEM) image of the produced LaB_6 nanowires is shown in Figure 2.2a. The nanowires are about 40 nm in lateral dimension and extend to over several microns in length. The nanowires have smooth surfaces and their tips, marked by the bright arrows in the image, are always terminated with a flat surface and form a right angle with their side surfaces. Selected-area electron diffraction (SAED) was used to determine the lattice structure of the nanowires. An electron diffraction pattern of the nanowire A indicated in Figure 2.2a is shown in Figure 2.2b, showing that this nanowire was grown in the [001] crystallographic direction of the cubic LaB_6 with lattice constant a = 4.153 Å. It was also noticed that all the diffraction spots are elongated into streaks perpendicular to the [001] lattice direction, indicating that the nanowire axis is parallel to [001] direction of the LaB_6 crystal. The diffraction pattern appeared identical as we moved the SAED aperture along the entire nanowire, suggesting that the LaB_6 nanowire is single-crystalline. To elucidate more details of the atomic structure of the LaB_6 nanowires, high-resolution transmission electron microscopy (HRTEM) was also employed as shown in Figure 2.2c. The atomic resolution image confirms that the nanowire is parallel to [001]

crystallographic direction of the LaB_6 crystal and also reveals that a right angle was formed between the side surfaces and the tip even at the atomic scale. It should also be pointed out that the HRTEM image contrast near the edge of the nanowire is uniform, unlike to the diminishing image contrast observed in cylindrical nanowires, suggesting that the cross-section of the LaB_6 nanowire were more likely to be square, which was also observed in the case of LaB_6 micron-sized whiskers (Hagimura & Kato, 1980; Givargizov & Obolenskaya, 1986) To determine the chemical composition of the amorphous layer wrapping the nanowire, a small electron beam probe was focused on the amorphous layer and electron energy loss spectrum (EELS) was acquired. The fact that only boron and lanthanum elements were detected suggests that the layer is composed of amorphous boron, since it is the only feasible amorphous phase among the combinations of the two elements and the lanthanum signals were speculated to be caused by the electron scattering from the crystalline part of the nanowire.

LaB_6 nanowires with lateral dimensions below 20 nm were also fabricated. Figure 2.3 shows an HRTEM image of a LaB_6 nanowire of about 15 nm in width. The growth direction of the nanowire is also parallel to its <001> lattice direction and its surfaces are all terminated with the {001} lattice planes. This thin LaB_6 nanowire is also single-crystalline. The <001> direction growth of these LaB_6 nanowires are speculated to be rooted from the fact that LaB_6 {001} lattice planes have the highest atomic density and therefore, it would minimize the total energy for the crystal to grow in this lattice direction. However, the cause of the thickness and length variations among the nanowires is still unknown and detailed growth mechanism still needs further investigations.

In summary, straight single-crystalline <001> oriented LaB_6 nanowires with width ranged from 15 nm to over 100 nm were successfully synthesized by a CVD method. These nanowires are terminated with {001} surfaces and offer a promising structure as point electron sources.

2.4. CeB_6 Nanowires

A representative morphological study and structure determination of the nanowires are presented in Figure 2.4. Figure 2.4a is a typical TEM image at low magnification showing a straight nanowire with smooth surfaces of lateral dimension around 50 nm and length extending over ten microns. Figures 2.4b-d are three electron diffraction patterns taken from three different crystal zone axes of the same nanowire to identify the CeB_6 crystal lattice, which has a primitive cubic structure of space group *Pm3m* and has lattice constant *a* = 0.4129 nm. The three zone axes are [100] (Figure 1b), $[2\bar{1}0]$ (Figure 1c), and $[1\bar{1}0]$ (Figure 2.4d), respectively. The relative orientational relationship between the three electron diffraction patterns are also given in the figures. For example, the $[1\bar{1}0]$ zone axis electron diffraction pattern (Figure 2.4d) was obtained by rotating 45° the nanowire about its [001] direction (illustrated in Figure 2.4b)

Due to the important role of emitter tip in the field emission property of the emitter, a careful study about the CeB_6 nanowire tip area was also conducted with results presented in Figure 2.5. Figure 2.5a is a morphological image showing that the CeB_6 nanowire has a flat tip and its lateral dimension is measured to be 52 nm along this image projection angle. An HRTEM image about the tip left corner is displayed as insertion, where the nanowire growth direction is identified to be along the [001] direction of the crystal and both the flat ending of

the tip and the nanowire walls are found terminated with {100} lattice planes. Figure 2.5b is the image about the same tip after a 45^{o} tilting along the nanowire axis was performed from the previous image projection angle. The new projection direction was identified to be along the [1-10] direction of the crystal as shown in the right image of Figure 2.5b. It's very interesting to notice that the lateral dimension of the nanowire at this new projection angle is 73 nm, which makes a ratio of 2^1/2 with that we previously obtained in Figure 2.5a. By noticing that the tiling angle coincides with the angle between a diagonal and its neighboring side of a square and the ratio 2^1/2 also matches that of a diagonal length divided by its neighboring side length, it can be deduced that the nanowire has a square cross-section. This geometry can also be implied from the left image of Figure 2.5b where a darker contrast line is shown in the middle of the nanowire and this might be due to the largest thickness along the diagonal direction of the nanowire. A summary of the nanowire tip geometry is illustrated in Figure 2.5c: both the nanowire tip and walls are terminated with {100} crystal planes as labelded in the illustration; the dashed arrows represent TEM electron beam with the projections labeled underneath using letter A and B, which correspond to the images shown in Figure 2.5a and Figure 2.5b respectively.

In conclusion, we have developed a CVD method that has been able to produce successfully CeB_6 nanowires of well characterized morphology. The nanowires have a square cross-section with sides of around 50 nm and have a length extending over 10 microns. The growth direction of the nanowires is its <001> lattice direction and they have flat tips and walls which are all terminated by {100} lattice planes. The CeB_6 nanowires' potential applications include providing thermionic emission, field-induced emission and thermal

field-induced emission of electrons for TEM, SEM, flat panel displays as well as other electronic devices that require high-performance electron sources.

2.5. GdB_6 Nanowires

The GdB_6 nanowires were also examined in a transmission electron microscope (TEM, JEM-2010F equipped with a Shottky field-emission gun) operated at 200 kV. Figure 2.6a is a morphological image of the grown GdB_6 nanowires. They are typically 50 – 60 nm in lateral dimensions and are more than several microns in length. The nanowires' tip-top surfaces are flat and form a right angle with side surfaces as can be clearly seen in the inserted high resolution image of the area marked by an arrow. The nanowires were found to grow along their <001> lattice directions and both the tip-top and the side surfaces are terminated with {100} lattice planes. Figures 2.6b and 1c are the TEM images together with their corresponding selected-area electron diffraction patterns taken from a single GdB_6 nanowire along its [100] and [2-10] lattice directions, respectively. A simple geometric calculation was performed as illustrated in Figure 2.6d in order to obtain the morphology of the nanowire tip. By using B = 56 nm measured from Figure 2.6b, C = 68 nm from Figure 2.6c, and $\theta = 26.6^o$ determined from the two diffraction patterns, we obtained the other side length A of the nanowire from the equation: $A = (C-B\cos\theta)/\sin\theta = 40$ nm.

In conclusion, we have developed a CVD process that is able to produce GdB_6 nanowires of well characterized morphology. The nanowires have a rectangular cross-section with width of about 50 nm and have length extending to more than several microns. The growth direction of the nanowires is its <001> lattice direction and they have flat tips and walls which are all terminated by the {100} lattice planes.

2.6. LaB_6-Carbon Nanotube (CNT) Nanocables

A representative morphological study of the nanowires is presented in Figure 2.7. The nanowires with smooth surfaces of diameter around 100 nm and length extending over a few tens of microns were observed and measured using both electron imaging and selected-area electron diffraction. Figure 2.7a is a typical TEM image at low magnification where the dimensional morphology is displayed. Figures 2.7b-d are three electron diffraction patterns taken from three different crystal zone axes of the same nanowire to identify the LaB_6 crystal lattice, which has a primitive cubic structure of space group *Pm3m* and has lattice constant *a* = 0.4153 nm. The three zone axes are [0 1 -1] (Figure 2.7b), [-1 2 -1] (Figure 2.7c), and [-1 4 -2] (Figure 2.7d), respectively. The relative orientational relationship between the three electron diffraction patterns are also given in the figures. For example, the [-1 2 -1] zone axis electron diffraction pattern (Figure 2.7c) was obtained by rotating 30° the nanowire about its [111] direction (illustrated in Figure 1b). It can also be seen from the diffraction patterns that all reflection spots are elongated to become streaks and these streaks are always perpendicular to the [111] lattice direction, indicating that the nanowire axis is parallel to the [111] direction of the LaB_6 crystal. This result was further confirmed by high-resolution transmission electron microscopy (HRTEM).

HRTEM was applied to analyze the detailed atomic structure around the nanowire tip. Figure 2.8a is an electron microscope image of the nanowire tip. The tip is hemispherical and it is terminated by several different lattice planes which are labeled with letters B through G on the image. The HRTEM images characterizing these faceted lattice planes are displayed in Figures 2.8b-g in corresponding sequence. Figure 2.8b shows the lattice image of the stem

area (marked B in Figure 2.8a) of the LaB_6 nanowire. The axial direction, [111], which is the same of the growth direction, of the nanowire has also been indicated in the figure. Figure 2.8c shows the lattice image near facet al of Figure 2.8a, whose surface is terminated with the (1 1 -1) lattice plane. Figure 2.8d shows the area marked with letter D in Figure 2.8a, which has a (110) facet. Figure 2.8e shows a (111) facet, which is equivalent to Figure 2.8c in atomic structure with the same surface energy and is perpendicular to the nanowire axis [111]. Figure 2.8f shows (211) facet alorresponding to the area marked with F in Figure 2.8a. It is interesting to note that facet F is the smallest comparing with others shown in Figure 2.8a. Area G, shown in Figure 2.8g, is a facet of (100) which is a low index lattice plane. By examining the areas covered by the various facets characterized, we found that the (100), (110) and (111) planes are the dominant terminating facets. Lattice planes of higher indices appeared only as transitions between the above dominant facet planes of low indices. This result agrees with the lowest surface energy principle in crystal growth.

Though commercial LaB_6 electron gun filaments are usually made along the <100> direction of the crystal lattice due to the lower work function of the {100} plane and higher symmetry, it has been suggested that the <111> oriented LaB_6 single-crystalline tips might be an even better alternative since they offer better stability. (Takigawa et al., 1982) Electric-field induced electron emission measurements on the LaB_6 nanowires are in progress.

On the 316- stainless steal substrate, a special type of LaB_6-in-CNT core-shell nanocable was collected. TEM was also employed to study its atomic structure with the results presented in Figure 2.9. Figure 2.9a is a typical low magnification image showing a multi-walled carbon nanotube with a darker contrast LaB_6 crystal core in the center. Unlike the flat tip top surface of [001] oriented LaB_6 nanowire, the crystal core of LaB_6-in-CNT

nanocable is continuous and has a hemispherical tip. The diameter of the nanocable is about 100nm. The open end of the out layer CNT is clearly shown in the inset of Figure 2.9a. HRTEM study was conducted on the LaB_6 core tip area with lattice images presented through Figure 2.9b to d. The images show that the tip is terminated with three different lattice planes of cubic LaB_6 crystal which are (100) plane, (111) plane and (011) plane respectively. A high resolution image was also taken at the joint area between the LaB_6 core and the out layer CNT with result shown in Figure 2.9e. The out layer CNT has 17 walls and at the end of the LaB_6 core, 4 out of the 17 walls split from the side surface to grow along the core top surface. In the meantime, some graphitic layers on the top surface expand to the side surface and join together with the side walls graphitic layers. These graphitic layers appear an interesting triangle shape near the LaB_6 core top surface and form a donut shaped graphic tube in the 3-D dimension. The inset of Figure 2.9e shows a magnified image of the CNT walls which reveals the graphite (001) plane spacing of 3.43Å.

However, [111] oriented LaB_6-in-CNT nanocables seem to have a different growth mechanism and this is supported by the fact that [111] growth of LaB_6-in-CNT nanocables only occurs on 316-stainless steal pieces with carbon contents, but not on iron/silicon substrate, which doesn't contain carbon. We speculate the preference of LaB_6 molecules to deposit on the (111) plane instead of (100) plane, which has a higher surface energy, is caused by some poisoning effect from graphitic layer to prohibit the LaB_6 deposition on the (100) planes of the crystal. Since no gaseous phase of carbon is introduced, we believe that the CNT formation is caused by the diffusion of carbon from the 316-stainless steal substrate.

In conclusion, we have developed a CVD method that has been able to produce successfully LaB_6 nanowires of well characterized morphology. The nanowires have

diameter around and smaller than 100 nm and length extending to a few tens of microns. The growth direction of the nanowires is its <111> lattice direction and they have hemispherical tips which are terminated by lattice planes of low indices such as {100}, {110} and {111}. The LaB_6 nanowires' potential applications include providing thermionic emission, field-induced emission and thermal field-induced emission of electrons for TEM, SEM, flat panel displays as well as other electronic devices that require high-performance electron sources.

2.7. LaB_{12} Nanowires and YB_{12} Nanowires

When YCl_3 vapor reacts with BCl_3 gas in a stationary hydrogen atmosphere, Yttrium dedocaboride nanowires were formed. Figure 4 is a set of the structure determination of the YB_{12} nanowire using HRTEM. The typical morphology of an yttrium dedocaboride nanowire is shown in Figure 2.10a. The nanowire is usually around 100nm in diameter and over ten micron meters long. The surface is rather rough and the nanowire is usually seen broken with irregular ends. The body of the nanowire is composed of parallel grains showing different contrasts and those grains are marked by letters B, C, D and E respectively in Figure 2.10a. Figure 2.10b, 2.10c, 2.10d and 2.10e are corresponding high resolution lattice images of the grain B, C, D and E. All these lattice images match with YB_{12} FCC crystal structure with a lattice constant equaling 7.50Å. It is shown in all these lattice contrast images that all four grains share [220] lattice direction as their growth axis and they are tilted along the axis with some angle relative to each other except grains B and C. Though grain B and C have different image contrasts as shown in Figure 2.10a, they have actually the same crystal orientation with [1-10] as normal direction. The darker contrast in grain C is probably due to the larger thickness of grain C as compared to grain B. Between grain C and grain D, a light

contrast line can be seen from Figure 2.10a and this region appears to be lack of clear lattice contrast as can be seen on the right hand side of Figure 2.10c. This is speculated to be the crystal lattice mismatch zone between grain C and Grain D. Figure 2.10d shows the high resolution image of grain D with [1-1-1] lattice direction normal to the projection plane. Grain E, as presented in Figure 2.10e, has its [1-1-2] lattice direction normal to the projection plane. All four co-axial grains have [220] growth direction, but no epitaxial interfaces are observed at the grain boundaries between adjacent grains.

In YCl_3/BCl_3 system, with hydrogen flow rate being 1600ml/min, only amorphous boron nanowires were produced. This might be due to that the high hydrogen supply decompose BCl_3 dramatically and generate too much elemental boron, which grows into amorphous boron nanowires on the substrate surface. When hydrogen is kept stationary without flowing, YB_{12} is formed from the reaction between elemental B and YCl_3 vapor with a mole ratio of 12:1. However, further lowering the Boron supply rate by either using lower flow rate of BCl_3 or by reducing the hydrogen concentration, doesn't help to form any lower boride phase of yttrium. YB_{12} nanowires are still the only product only with a poorer yield. These phenomena suggest that YB_{12} is the most preferred phase in Y/B system at this synthesis temperature.

When using stationary hydrogen during the reaction between $LaCl_3$ and BCl_3, a different type of lanthanum borides nanowires, LaB_{12} nanowires, were produced and the results are presented in Figure 2.11. Figure 2.11a shows a representative low magnification TEM image of the LaB_{12} nanowire. The nanowires' wall is smoother than YB_{12} and the whole nanowire body is a single crystal, which suggests better crystalinity than YB_{12} nanowires. HRTEM characterization was performed on the nanowire and atomic resolution

images taken at two crystal orientations are presented in Figure 2.11b and 5c respectively. Using these two 2-D lattice images and knowledge that the tilting angle between the two orientations is 35^{o}, we are able to reconstruct the 3-D crystal lattice to be a FCC lattice type with lattice constant equal to 7.57Å. Since the crystal structure is identical to that of YB_{12} and knowing the fact that only Lanthanum and Boron elements are present, we believed the crystal is LaB_{12} which is isostructural to YB_{12} phase. The fact that the lattice constant of LaB_{12} is slightly larger than YB_{12} is likely due to the slight larger ionic radius that La^{3+} has compared to Y^{3+}. Similar to YB_{12} nanowire, the growth direction of the LaB_{12} nanowire is also identified to be [220] as shown in Figure 2.11b before tilting the sample.

However, hydrogen flow rate does have a crucial role in determining the phase formation in La/B system. Using a hydrogen flow rate of 1600 ml/min leads to the formation of LaB_6 nanowires, while applying a zero hydrogen flow rate results in the formation of LaB_{12} nanowires. This phenomenon seems to be contradictory with the fact that higher hydrogen flow rate generates more elemental boron, therefore should have led to the formation of higher boride phase. A possible explanation is that the slower hydrogen flow transfers little kinetic energy to the La/B system and thus causes to form a less stable intermediate phase LaB_{12}. The reason that this phase was not observed before by using conventional sintering method could be due to that these rare-earth boride intermediate phases usually decompose into more stable borides before melting, as in the case of newly discovered YB_{50} and YB_{25}.

A CVD method was developed as a general approach to synthesize rare-earth boride nanowires by using $RaCl_3$ powders and BCl_3 gas as reagents. By adjusting experimental conditions, such as catalyst type and hydrogen flow rate, we are able to control the

nanowires' crystal orientation and tune the specific phase of the rare-earth boride nanowires from amorphous boron, RaB_6 to RaB_{12}. Different growth mechanisms are believed to be account for the formation of these different nanostructures. LaB_{12} is discovered as a new compound in La-B binary diagram. More work on this compound is undergoing towards bulk single crystal growth and physical property measurements. The synthesis of this family of rare-earth borides nanowires not only has the application in producing low work function nano-scale field electron emitters but also has fundamental scientific significance such as studying size effect of superconducting nanowires.

2.8. Other Nanostructures Synthesized By This CVD System

2.8.1. MgB_2/MgO Nanocables

The wool like material was found to be nanowires of diameter around 100nm. A typical TEM image is shown in Figure 2.12a, which reveals fine crystallites features inside the wire. The polycrystalline structure of the wire was further confirmed by the reflection rings of SAED pattern taken from the wire as shown in Figure 2.12b. A good match with MgO plane spacings suggests that the wire is polycrystalline magnesium oxide.

An interesting shell-core cable structure was also found among the same sample. Figure 2.13a is a bright field TEM image where a darker contrast core is buried inside a lighter contrast shell which has the same fine crystallites features as in Figure 2.12a. Electron diffraction pattern, given in Figure 2.13b, showed that, in addition to the same diffraction rings as those displayed in Figure 2.12b from MgO, a set of extra single crystalline reflections corresponding to the (001) and (002) lattice planes of MgB_2 crystal is also present. Based on the knowledge that MgB_2 has a hexagonal crystal structure with a = 3.086 Å, c =

3.524 Å and MgO has a face-centered cubic crystal structure with a = 4.213 Å, we simulated electron powders diffraction profiles for MgB_2 and MgO respectively with the results shown in Figure 2(d). By comparing the first five possible lattice reflections from MgB_2 with those from MgO, we found that except those of {001} and {002} from MgB_2, the other three planes {100}, {101} and {110} all have very close spacing values to those of {111}, {200} and {220} planes from MgO. Since these small deviations can be easily covered by measurement uncertainty of the diffraction pattern, it indicates that (001) and (002) lattice reflections are characteristic features to tell MgB_2 phase from MgO phase which is almost inevitable during the synthesis of MgB_2.(Lee, 2003) By taking the dark-field diffraction contrast image with the MgB_2 (002) reflection as marked by a white arrow on Figure 2.13b, we found out that these reflections were from the darker single core of the nanowire and it is single crystalline, based on the fact that the core is the only part of the wire that gives bright contrast which is shown in Figure 2.13c. The diameter of the MgB_2 single crystal nanowire is about 10 nm.

Since no oxygen gas was introduced into the furnace on purpose, the oxidation of the wires could be due to the oxygen residue inside the furnace. Upon evaporation of the magnesium chips, two reactions took place simultaneously: $2B + Mg = MgB_2$ and $O_2 + 2Mg = 2MgO$, through which both pure MgO nanowires and MgB_2/MgO nanocables were formed. The fact that no pure MgB_2 nanowires have been observed in our sample might suggest the high reactivity of MgB_2 with oxygen when its dimension goes down to nano-scale. However, the mechanism of the formation of these nano-structures still remains unclear and needs further investigation.

2.8.2. MgO and Mg_3N_2 Nanowires

A thick layer of nanowires with length over tens of microns was found to cover the platinum wire surface and a typical SEM image is shown in Figure 2.14a. The nanowires were then scraped down to make TEM samples for structure study and a typical TEM image is presented in Figure 2.14b. The nanowires are about 80nm in diameter and have rough surfaces. Dark crystallites about 10-20nm in size appear inside the nanowires, suggesting a polycrystalline structure. Selected Area Electron Diffraction (SAED) was applied on the nanowire to determine its atomic structure with result shown in Figure 2.14c. The reflection rings confirmed that the nanowire is polycrystalline and they match well with cubic MgO structure with lattice constant a = 4.213Å.

Another type of thinner nanowires was also found among the same TEM sample and its typical TEM image was shown in Figure 2.15a. The nanowire is about 40nm in diameter and a consecutive core with darker contrast can be seen wrapped inside a lighter contrast shell. To determine the atomic structure of the nanowire, SAED was again applied and the area selected by the diffraction aperture is indicated by the white circle in Figure 2.15a. Its corresponding diffraction pattern was presented in Figure 2.15b. It is very interesting to notice that the diffraction pattern consists of a set of seemingly 6-fold symmetry reflection dots and some reflection rings. In order to determine whether the reflection dots are truly one set of single-crystalline reflections with a 6-fold symmetry or an overlap of several sets of reflections with a 2-fold symmetry, we applied dark field contrast image technique to form image contrast only with crystals which give selected reflections in the diffraction pattern. The reflection dots selected to form dark field contrast images were marked by C-E in Figure 2.15b and their corresponding dark field contrast images were presented respectively in

Figure 2.15c-e. The fact that when selecting different reflection dot, different parts of the nanowire give contrast suggests that the 6-fold symmetry diffraction pattern is actually an overlap of 3 sets of equivalent 2-fold symmetry diffraction patterns with 120^o orientation angles relative to each other. These 2-fold symmetry diffraction patterns are found to match well with <112> zone diffractions of cubic Mg_3N_2 structure with lattice constant a = 9.95Å and their corresponding computer simulated diffraction patterns are presented as the insertions in Figure 2.15c-e. A sample indexation was given in the insertion of Figure 2.15c and the pattern is indexed as [1 -1 -2] lattice zone diffraction of Mg_3N_2 crystal. The reflection rings are indexed with MgO polycrystalline structure and part of the reflection rings as marked by F in Figure 2.15b was also selected to form dark field contrast image with result shown in Figure 2.15f. It was noticed that the MgO polycrystalline phase was only distributed on the side of the nanowire. It might be due to the partial oxidation of the Mg_3N_2 nanowires during the synthesis process.

Since no oxygen gas was introduced into the system on purpose, the oxidation of the Mg vapor must be from the oxygen residue remained in the reaction chamber. This dilute concentration of oxygen gas was proved to be very crucial in forming MgO nanowires as we tried another experiment by adding air into the chamber while having the other experimental conditions remained the same. This time, we got mostly MgO single-crystalline cubes as shown in Figure 2.16 and didn't observe any nanowires formation. Similar results have also been reported by X. Yin et al. and M. Zhao et al. when applying high oxygen concentration instead of trace oxygen remained in the vacuum system.(Yin et al., 2002; Zhao et al., 2004) We also noticed that some groups have used very similar experimental conditions as we did, but didn't observe MgO polycrystalline nanowires or Mg_3N_2 nanowires. For instance, in X.

Yin's work, they also tried direct evaporating of Mg metal in trace oxygen and barely produced any nanowires(Yin, 2002); in another work by R.Z. Ma, they reacted Mg metal with N_2 and no Mg_3N_2 nanowires were reported.(Ma & Bando, 2003) We speculate that what enabled us to get the high yield of polycrystalline MgO nanowires and Mg_3N_2 nanowires might be the H_2 usage in our reaction atmosphere. It is believed that slow reaction rate allows crystal growth to happen only along the most preferred direction and thus form one-dimensional nanowires, and the H_2 gas in our system might further slow down the reaction rate at high temperature by reducing MgO and Mg_3N_2 to Mg. Experiments without Pt catalyst were also carried out and similar nanowires product was obtained only with much less yield. Although it seems that Pt greatly enhances the yield of the nanowires, yet since no catalyst balls were observed at the ends of the produced nanowires, detailed picture of the catalyst mechanism is still unclear.

2.9. Solid State Synthesis of LaB_6 Nanowires

It was found that when reacting for 10 minutes, at different temperature from 1000^{o}C to 1200^{o}C, the products in each setting are all LaB_6 cubes with side lengths of 1-2 microns. The higher temperature, the higher ratio of LaB_6 to excessive boron in the product mixture was obtained. Very little LaB_6 was produced at 1000^{o}C, which is believed to be the temperature lower limit for Lanthanum metal to react with boron. This limit could be due to the insolubility of boron in aluminum at temperatures below 1000^{o}C, which cuts off the reaction by stopping the boron atoms supply, even though La atoms supply is still abundant since the solidification line of La/Al is below 700^{o}C. An SEM image of the LaB_6 cubes grown at 1200^{o}C was shown in Figure 2.17a. We found that, when extending the reaction

time to 30 minutes at 1200^{o}C, a better yield of LaB_6 was obtained as compared to 10 minutes reaction time at the same temperature, however, the size of the cubes didn't change much. This suggests that at 1200^{o}C, nucleation overruns crystal growth at least for the first 30 minutes, therefore longer time duration only results in more nuclei formations. In the next experiment, another 30 minutes was allowed for crystal growth following the initial 30 minutes nucleation at 1200^{o}C. In order to have rod shaped crystals, inhomogeneous growth should be preferred to cause atom adsorption only at one particular crystal plane that happens to be at an advantageous position. This position could be the relative orientation of the crytal plane to local liquid vortex motion or its closeness to supplying La or B atoms at random moments. However, since no mechanism was intentionally introduced to keep this random inhomogeneous condition, the favored crystal plane could change with time and homogeneity would be reached over a long period of time from a statistical point of view. Therefore, a short growth time should favor for one-dimensional growth in this type of random system. Since the reacting temperature is well below the solidification temperature of LaB_6, 2715^{o}C, a lower crystal growth temperature will result in an even deeper supersaturation, which will in turn generate a faster reaction speed. Therefore, we tested this hypothesis by allowing another 30 minutes growth time at 1100^{o}C following the initial 30 minutes of 1200^{o}C nucleation. The results are presented in Figure 2.17b and 2.17c. It clearly shows that the LaB_6 crystals have grown into rods with rectangular or square cross-sections. The thickness of the rods is around 2 microns and length sometimes exceeds 10 microns. Noting that the thickness of the rod is about the same as that of the cubes in Figure 2.17a with only the nucleation process, we confirmed that the 30 minutes reaction at 1100^{o}C did cause inhomogeneous growth which leads to rod growth at only one crystal plane. However, no

cubes or rods with size smaller than one micron were found under any of these reaction conditions. We speculate this is because the nuclei size has a lower limit which is set to be the size of the smallest particle of the starting material, in this case, the boron particle size which is around 1 micron. Therefore, in order to reduce the LaB_6 rods diameter into nano-scale, boron nano particles would offer a better chance.

In conclusion, an aluminum flux method is modified in order to produce LaB_6 nanowires. It was found higher reaction temperature has better yield of LaB_6 single crystals. A lower temperature crystal growth followed by a higher temperature nucleation process was found effective in growing rod shaped LaB_6 crystals. The thickness of the produced rod is above 1 micron due to the micron size boron particles in the starting material.

2.10 Summary and conclusions:

In this chapter, we described a series of chemical-vapor-deposition experiments in synthesizing various types of rare-earth boride nanowires and two types of magnesium based nanowires. In the synthesis of rare-earth hexaboride nanowires, the chemical reaction of boron trichloride and rare-earth trichloride in the atmosphere of hydrogen was found fairly effective in producing corresponding rare-earth hexaboride nanowires. Platinum catalyst or carbon contained iron catalyst are used to change the so-made nanowires' crystallographic orientation. LaB_6, CeB_6 and GdB_6 nanowires all have the same morphology and very close crystal structures. When the reaction conditions are changed, for example, the hydrogen flow rate, nanowires of different structures were produced. According to the structural analysis, they were speculated to be LaB_{12} and YB_{12} nanowires with FCC crystal lattice. The developed CVD system was proven effective in making nanowires of other chemical

compositions as well. Examples of MgO nanowires and Mg_3N_2 nanowires are given. Lastly, a solid-state reaction was introduced with elemental boron, lanthanum and aluminum as starting materials. LaB_6 single crystals with different size and aspect ratio were observed. Potential of using this method in making large quantity of LaB_6 nanowires was implied.

REFERENCES:

Bezryadin, A., Lau, C.N. & Tinkham, M. (2000). Quantum suppression of superconductivity in ultrathin nanowires. Nature, 404(6781), 971-974.

Bonard, J. M., Dean, K. A., Coll, B. F., & Klinke, C. (2002). Field emission of individual carbon nanotubes in the scanning electron microscope. Physical Review Letters, 89(19), 197602.

Bonard, J. M., Kind, H., Stockli, T. & Nilsson, L. O. (2001). Field emission from carbon nanotubes: the first five years. Solid-state electronics, 45(6), 893-914.

Brodie, I. & Spindt, C. A. (1992). Advances in electronics and electron physics Vol.83. San Diego: Academic Press.

Burnell, G., Kang, D., Ansell, D. A., Lee, H. N., Moon, S. H., Tarte, E. J., & Blamire, M. G. (2002). Directly coupled superconducting quantum interference device magnetometer fabricated in magnesium diboride by focused ion beam. Applied Physics Letters, 81(1), 102-104.

Canfield, P. C., Kinnemore, D. K., Bud'ko, S. L., Ostenson, J. E., Lapertot, G., Cunningham, C. E., & Petrovic, C. (2001). Superconductivity in dense MgB_2 wires. Physical Review Letters, 86(11), 2423-2426.

Chen, J., Deng, S. Z., Xu, N. S., Wang, S., Wen, X., Yang, S., Yang. C., Wang, J. & Ge, W. (2002). Field emission from crystalline copper sulphide nanowire arrays. Applied Physics Letters, 80(19), 3620-3622.

Chernozatonskii, L.A., Gulyaev, Y. V., Kosakovslaja, Z. J., Sinitsyn, N. I., Torgashov, G. V., Zakharchenki, Y. F., Fedorov, E. A. & Val'chuk, V. P. (1995). Electron field-emission from nanofilament carbon-films. Chemical Physics Letters, 233, 63.

Cui, S., Liao, S., Zhang, Y., Xu, Y., & Miao, Y. (1999). Synthesis of nanometric-size magnesium nitride by the nitriding of pre-activated magnesium powder. Journal of Materials Science, 34(x), 5601-5604.

Davis, P. R., Gesley, M. A., Schwind, G. A., Swanson, L. W., & Hutta, J. J. (1989). Comparison of thermionic cathode parameters of low index single crystal faces of LaB_6, CeB_6 and PrB_6. Applied Surface Science, 37(x), 381-394.

Davis, P.R., Swanson, L.W., Hutta, J.J. & Jones, D.L. (1986). Fabrication and characterization of rare-earth hexaboride single-crystal materials. Journal of Materials Science, 21(3), 825-836.

de Jonge, N., Allioux, M., Oostveen, J. T., Teo, K. B. K. & Milne, W. I. (2005). Optical performance of carbon-nanotube electron sources. Physical Review Letters, 94(x), 186807.

de Jonge, N., Lamy, Y., Schoots, K. & Oosterkamp, T.H. (2002). High brightness electron beam from a multi-walled carbon nanotube. Nature, 420 (6914), 393-395.

Deheer W. A., Chatelain, A., & Ugarte D. (1995). A carbon nanotube field-emission electron source. Science, 270(5239), 1179-1180.

Doy, T. K., Kasai, T. & Ohmori, H. (1999). New precision contouring process of lanthanum hexaboride (LaB6) crystals used for electron guns. Journal of the Ceramic Society of Japan, 107(6), 502-509.

Eom, C. B., Lee, M. K., Choi, J. H., Belenky, L. J., Song, X., Cooley, L. D., Naus, M. T., Patnaik, S., Jiang, J., Rkkel, M., Polyanskii, A., Gurevich, A., Cai, X.Y., Bu., S.D., Babcock. S.E., Hellstrom, E.. E., Larbalestier, D. C., Rogado, N., Regan, K. A., Hayward, M. A., He, T., Slusky, J. S., Inumaru, K., Haas, M., & Cava, R. J. (2001). High critical current density and enhanced irreversibility field in superconducting MgB_2 thin films. Nature, 411(x), 558-560.

Fowler, R. H., & Nordheim, L. (1928). Electron emission in intense electric field. Proceedings of Royal Society of London, 119(x), 173-181.

Futamoto, M., Hosoki, S.,Okano H.& Kawabe U. (1977). Field-emission and field-ion microscopy of lanthanum hexaboride. Journal of Applied of Physics, 48(8), 3541-3546.

Gesley, M., & Swanson L.W. (1984). A determination of the low work function planes of LaB_6. Surface Science, 146(x), 583-599.

Givargizov, E.I. & Obolenskaya, L.N. (1981). Controlled growth of LaB_6 whiskers by the vapor-liquid-solid mechanism. Journal of Crystal Growth, 51(2), 190-194.

Givargizov, E.I. & Obolenskaya, L.N. (1986). Regular arrays of LaB_6 whiskers grown on single-crystal substrates by the vapor liquid solid method. Journal of the Less-Common Metals, 117(1-2), 97-103.

Hagimura, A. & Kato, A. (1980). Catalyst effects of various materials on the growth of lanthanum hexaboride whiskers by chemical vapor deposition. Journal of the chemical society of Japan, 7, 1108-1113.

Han, S., Li, c., Liu, Z., Lei, B., Zhang, D., Jin, W., Liu, X., Tang, T., & Zhou, C. (2004). Transition metal oxide core-shell nanowires: Generic synthesis and transport studies. Nano Letters, 4(7), 1241-1246.

Harada, K., Nagata, H. & Shimizu, R. (1991). <310> single-crystal LaB_6 as thermal field emitter of high brightness electron source. Journal of Electron Microscopy, 40, 1-4.

Iijima, S. (1991). Helical microtubules of graphitic carbon. Nature, 354(6348), 56-58.

Kher, S. S. & Spencer, J. T. (1997). Chemical vapor deposition of metal borides 7. the relatively low temperature formation of crystalline lanthanum hexaboride thin films from boron hydride cluster compounds by chemical vapor deposition. Journal of physics and chemistry of solids, 59(8), 1343-1351.

Klug, K, & Dravid, V. (2002). Observation of two- and three-dimensional oxide nanostructures formed by thermal treatment of magnesium diboride powder. Applied Physics Letters, 81(9), 1687-1689.

Kudintseva, G.A., Kuznetsova, G.M., Bondarenko, V.P., Selivanova, F.N. & Shlyuko, V.Y. (1968). Preparation and emissive properties of some yttrium and gadolinium borides. Proshkovaya Metallurgiya, 2(x), 45-53.

Kuno, M., Oku, T. & Suganuma, K. (2001). Synthesis of boron nitride nanotubes and nanocapsules with LaB6. Diamond and Related Materials, 10(3-7), 1231-1234.

Lafferty, J.M. (1951). Boride cathodes. Journal of Applied Physics, 22(3), 299-306.

Larbalesteir, D. C., Cooley, L. D., Rikel, M. O., Polyanskii, A. A., Jiang, J., Patnaik, S., Cai, X. Y., Feldmann, D. M., Gurevich, A., Squitieri, A. A., Maus, M. T., Eom, C. B., Hellstrom, E. E., Cava, R. J., Regan, K. A., Rogado, N., Hayward, M. A., He, T., Slusky, J. S., Khalifah, P., & Haas, M. (2001). Strongly linked current flow in polycrystalline forms of the superconductor MgB_2. Nature, 410(x), 186-189.

Lee, Y. H. Choi, C. H., Jang, Y. T., Kim, E. K., Ju, B. K., Min, N. K. & Ahn, J. H. (2002). Tungsten nanowires and their field electron emission properties. Applied Physics Letters, 81(4), 745-747.

Levitt, A. P. (1970). Whisker technology. New York: Wiley-Interscience.

Li, Y. B., Bando, Y., Golberg, D., Kurashima, K. (2002). Field emission from MoO3 nanobelts. Applied Physics Letters, 81(26), 5048-5050.

Li, Y., Bando, Y. & Sato, T. (2002). Preperation of network-like MgO nanobelts on Si substrate. Chemical Physics Letters, 359(x), 141-145.

Ma R. & Bando, Y. (2003). Uniform MgO nanobelts formed from in situ Mg_3N_2 precursor. Chemical Physics Letters, 370(x), 770-773.

Ma, J.H., Gu, Y.L., Shi, L., Chen, L.Y., Yang, Z.H. & Qian, Y.T. (2003). Reduction-boronation route to chromium boride (CrB) nanorods. Chemical Physics Letters, 381(1-2), 194-198.

Ma, R.Z., Bando, Y., Mori, T. & Golberg, D. (2003). Direct pyrolysis method for superconducting crystalline MgB2 nanowires. Chemistry of Materials, 15(16), 3194-3197.

Matthias, B.T., Geballe, T.H., Andres, K., Corenzwit, E., Hull, G.W., Maita, J.P. (1968). Magnatic ordering in rare-earth hexaborides. Science, 159, 530.

Morales, A. M., Lieber, C. M. (1998). A laser ablation method for the synthesis of semiconductor nanowires. Science, 279(5348), 208-211.

Motojima, S., Takahashi, Y. & Sugiyama, K. (1978). Chemical vapor growth of LaB_6 whiskers and crystals having a sharp tip. Journal of Crystal Growth, 44(1), 106-109.

Nagamatsu, J., Nakagawa, N., Muranaka, T., Zenitani, Y., & Akimitsu, J. (2001). Superconductivity at 39K in magnesium diboride. Nature, 410(x), 63-64.

Nagata, H., Harada, K. & Shimizu, R. (1990). Thermal field emission observation of single-crystal LaB_6. Journal of Applied Physics, 68(7), 3614-3618.

Nakamoto, M. & Fukuda. K. (2002). Field electron emission from LaB6 and TiN emitter arrays fabricated by transfer mold technique. Applied Surface Science, 202(3-4), 289-294.

Rao, C. N. R., Deepak, F. L., Gundiah, G., & Govindaraj, A. (2003). Inorganic nanowires. Progress in Solid State Chemistry, 31, 5-147.

Rinzler, A.G., Hafner, J.H., Nikolaev, P., Lou, L., Kim, S.G., Tamanek, D., Nordiander, P., Colbert, D.T. & Smalley, R.E. (1995). Unraveling nanotubes–field-emission from an atomic wire. Science, 269(5230), 1550-1553.

Shimizu, R., Kataoka, Y., Tanaka, T. and Kawai, S. (1975). Field emission pattern of Lab_6-single crystal tip. Japan Journal of Applied Physics, 14(7), 1089-1090.

Smith, A., Al-Brithen, H., Ingram, D. & Gall, D. (2001). Molecular beam epitaxy control of the structural, optical, and electronic properties of ScN(001). Journal of Applied Physics, 90(4), 1809-1816.

Spears, K.E. (1976). Phase Diagram, Vol. IV. New York: Academic Press.

Storms, E. K. & Mueller, B. A. (1981). Thermionic emission and atom vaporization of the Gd-B system. Journal of Applied Physics, 52(4), 2966-2970.

Swanson, L. W., Gesley, M. A., & Davis, P. R. (1981). Crystallographyic dependence of the work function and volatility of LaB_6. Surface Science, 107, 263.

Swanson, L.W., McNeely, D.R. (1979). Work functions of the (001) face of the hexaborides of BA, LA, CE and SM. Surface Science, 83(1), 11-28.

Takigawa, T., Sasaki, I., Meguro, T. & Motoyama, K. (1982). Emission characteristics of single-crystal Lab_6 electron gun. Journal of Applied Physics, 53(8), 5891-5897.

Tanaka, T., Nishitani, R., Oshima, C., Bannai, E. & Kawai, S. (1980) The preparation and properties of CeB_6, SmB_6, and GdB_6. Journal of applied Physics, 51(7), 3877-3883.

Tanaka, T., Okada, S. & Ishizawa, Y. (1994). A new yttrium higher boride - YB50. Journal of Alloyed Compounds, 205(1-2), 281-284.

Tanaka, T., Okada, S., Yu, Y. & Ishizawa, Y. (1997). A new yttrium boride: YB25. Journal of Solid State Chemistry, 133(1), 122-124.

Tennant, D. M. & Swanson, L. W. (1989). The effect of LaB_6 cathode shape on its performance in a JBX 5DII electron beam lithography system. Journal of Vacuum Science and Technology B, 7(1), 93-97.

Vissokov, G. & Pirgov P. (1996). Preparation of ultradispersed magnesium nitride by the electric-arc low-temperature plasma technique. Journal of Material Science, 31 (14), 3685-3690.

Wagner, R. S. & Ellis, W. C. (1964). Vapor-liquid-solid mechanism of single crystal growth. Applied Physics Letters, 4(5), 89-90.

Williams, D. B. & Carter, C. B. (1996). Transmission electron microscopy. New York: Plenum Press.

Wong, K. W., Zhou, X. T., Frederick, C. K., Lai, H. L., Lee, C. S. & Lee, T. (1999). Field-emission characteristics of SiC nanowires prepared by chemical-vapor deposition. Applied Physics Letters, 75(19), 2918-2920.

Wu, Y. Y., Messer, B., & Yang, P. D. (2001). Superconducting MgB_2 nanowires. Advanced Materials, 13(19), 1487-1489.

Xia, Y., Yang, P., Sun, Y., Wu, Y., Mayers, B., Gates, B., Yin, Y., Kim, F., & Yan, H. (2003). One-dimensional nanostrucutures: synthesis, characterization, and applications. Advanced Materials, 15(5), 353-389.

Xu, T.T., Zheng, J.G., Nicholls, A.W., Stankovich, S., Piner, R.D. & Ruoff, R.S. (2004). Single-crystal calcium hexaboride nanowires: Synthesis and characterization. Nano Letters, 4(10), 2051-2055.

Yamabe, M., Furukawa, Y. and Inagaki, T. (1984). Electron-emission from (100) LaB_6 cathodes with large cone angles and flat tips. Journal of Vacuum Science & Technology A-Vacuum Surfaces and Films, 2(3), 1361-1364.

Yang, H., Al-Brithen, H., Smith, A., Borchers, J., Cappelletti, R. & Vaudin, M. (2001). Structural and magnetic properties of eta-phase manganese nitride films grown by molecular-beam epitaxy Applied Physics Letters, 78(24), 3860-3862.

Yang, P. & Lieber, C. (1996). Nanorod-superconductor composites : a pathway to materials with high critical current densities. Science, 273(5283), 1836.

Yin, Y. B., Bando, Y., Golberg, D. and Kurashima, K. (2005). Growth and field emission of hierarchical single-crystalline wurtzite AIN nanoarchitectures. Advanced Materials, 17(1), 110.

Yin, Y., Zhang, G. & Xia, Y. (2002). Synthesis and characterization of MgO nanowires through a vapor-phase precursor method. Advanced functional materials, 12(4), 293-298.

Zaima, S., Sase, M., Adachi, H., Shibata, Y., Ohshima, C., Tanaka, T., & Kawai, S. (1980). Spread of total energy distribution of thermal field-emitted electrons from LaB_6 single crystal needles. Journal of Physics D: Applied Physics, 13, L47-9.

Zeng, X., Pogrebnyakov, A. V., Kotcharov, A., Jones, J. E., Xi, X. X., Lysczek, E. M., Redwing, J. M., Xu, S., Li, Q., Lettiere, J., Schlom, D. G., Tian, W., Pan, X., & Liu, Z. K. (2002). In situ epitaxial MgB_2 thin films for superconducting electronics. Nature Materials, 1(1), 1-4.

Zhang, D., Liu, Z., Han, S., Li, C., Lei, B., Stewart, M., Tour, J. & Zhou, C. (2004). Magnetite (Fe_3O_4) core-shell nanowires: synthesis and magnetorisisteance. Nano Letters, 4(11), 2151-2155.

Zhang, H., Tang, J., Zhang, Q., Zhao, G.P., Yang, G., Zhang, J., Zhou, O. & Qin, L.C. (2006). Field emission of electrons from single LaB6 nanowires. Advanced Materials, 18(1), 87-91.

Zhang, H., Zhang, Q., Tang, J. & Qin, L.C. (2005 I). Single-crystal line CeB6 nanowires. Journal of the American Chemical Society, 127(22), 8002-8003.

Zhang, H., Zhang, Q., Tang, J. & Qin, L.C. (2005 II). Single-crystalline LaB6 nanowires. Journal of the American Chemical Society, 127(9), 2862-2863.

Zhang, H., Zhang, Q., Zhao, G.P., Tang, J.; Zhou, O. & Qin, L.C. (2005 III). Single-crystal line GdB6 nanowire field emitters. Journal of the American Chemical Society, 127(38), 13120-13121.

Zhang, J. Tang, J., Yang, G., Qiu, Q., Qin, L.C. Zhou, O. (2004). Efficient fabrication of carbon nanotube point electron sources by dielectrophoresis. Advanced Materrials, 16(14), 1219-+

Zhang, J., Zhang, L., Peng, X. & Wang, X. (2001). Fabrication of MgO nanobelts using a halide source and their structural characterization. Applied Physics A, 73, 773-775.

Zhao, M., Chen, X., Zhang, X., Dai, L., Jian, J. & Xu, Y. (2004). Growth and morphologies of one- and three-dimensional MgO nanostructures. Applied Physics A, 79(2004), 429-431.

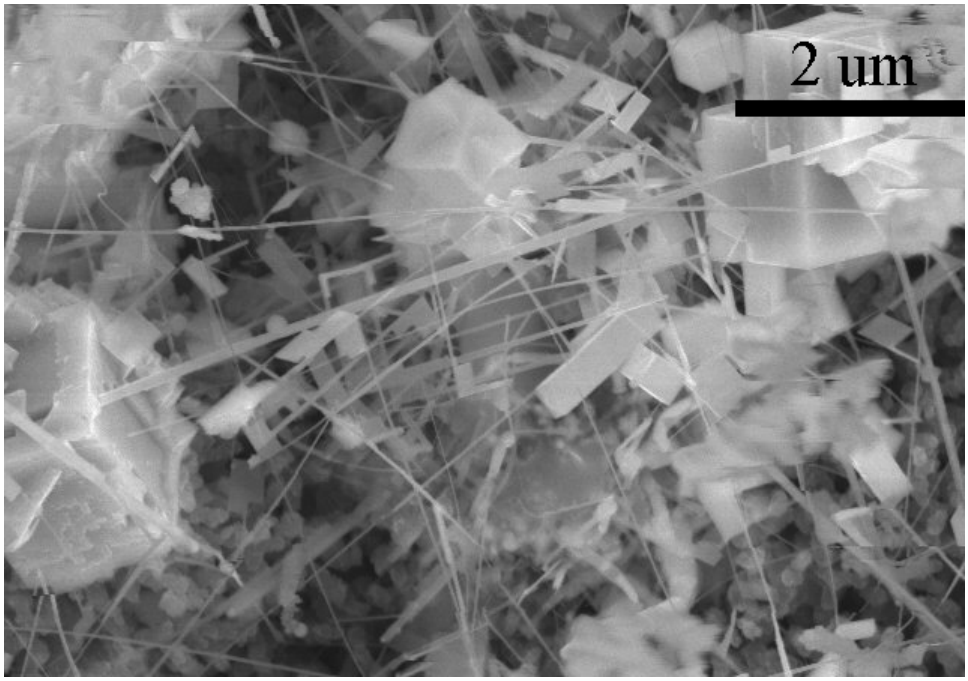

Figure 2.1. SEM image of single-crystalline LaB6 nanowires synthesized on silicon substrate. Some cubes and platelets are also grown along with the nanowires. The arrow indicates a cube grown on a nanowire.

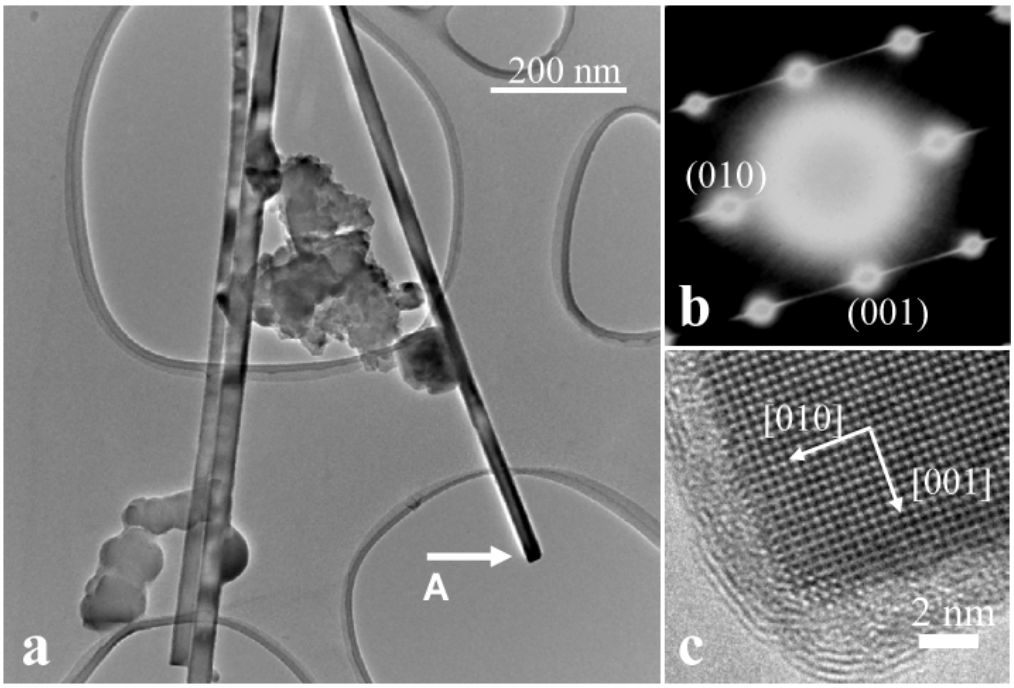

Figure 2.2. a) Low-magnification TEM image of LaB_6 nanowires. Arrows point to the tips terminated with a flat surface. b) Electron diffraction pattern of the LaB_6 nanowire displayed a) indicated by letter A showing [100] zone axis geometry. Streaks are perpendicular to the axial direction of the nanowire. c) High-resolution image showing the tip of the same LaB_6 nanowire, revealing the flat tip surface (001).

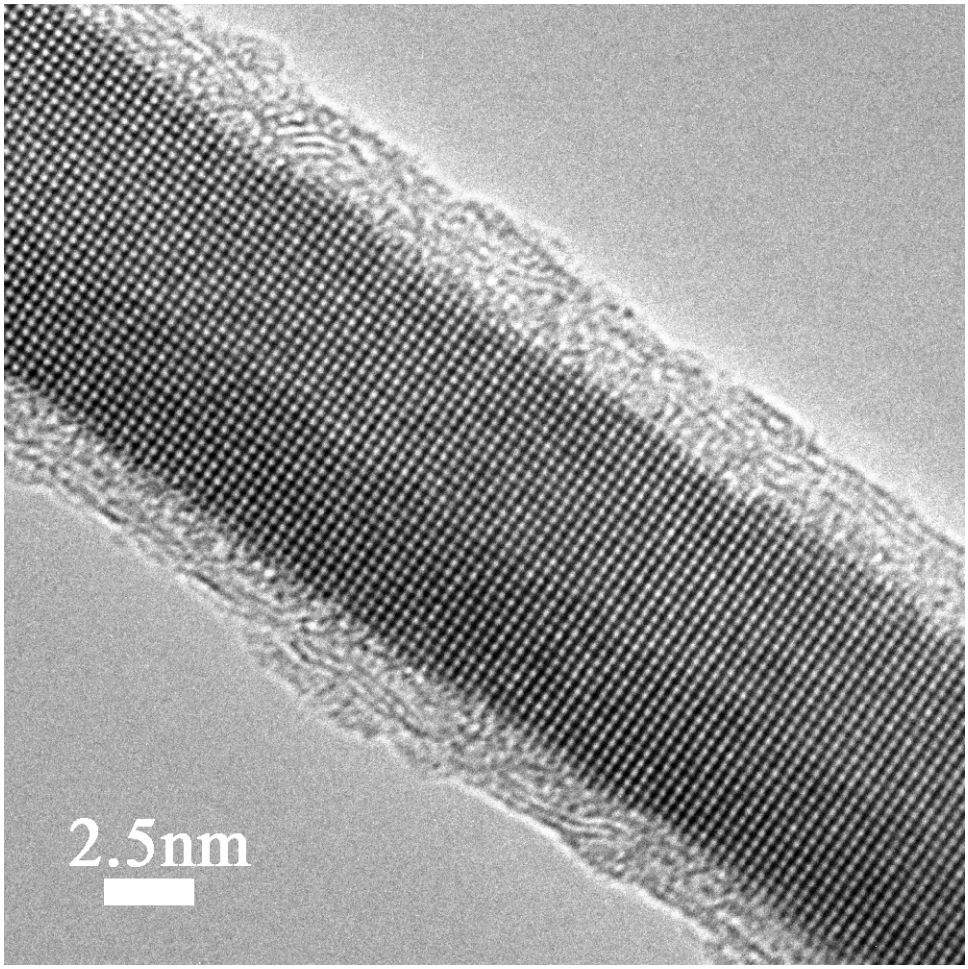

Figure 2.3. High-resolution TEM image of a thin LaB_6 nanowire of 15 nm in width. The nanowire is single-crystalline and grown in the [001] direction.

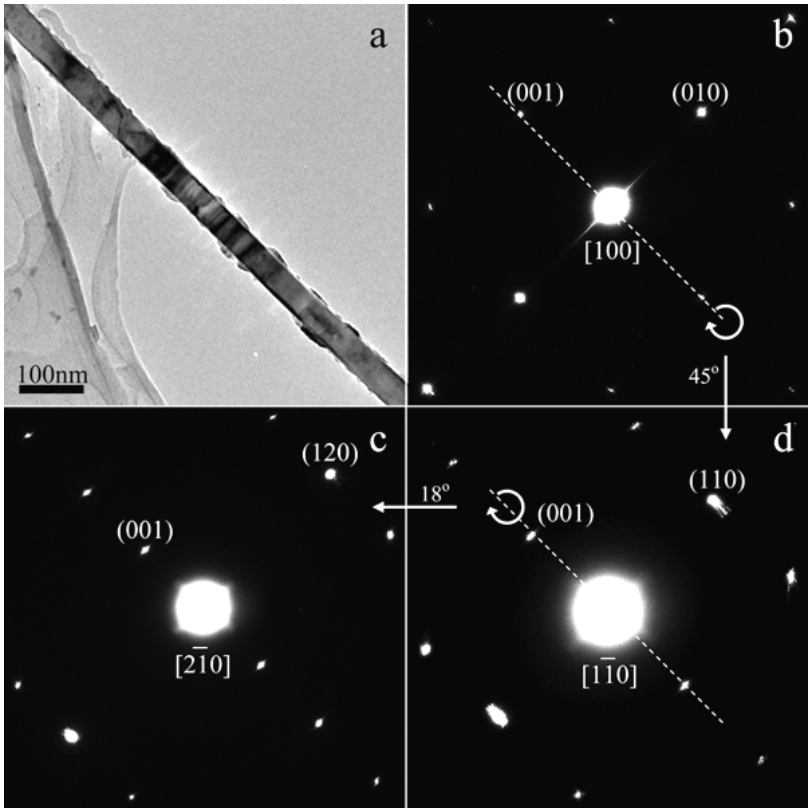

Figure 2.4. (a) Low-magnification TEM image of a CeB6 nanowire. (b-d) Electron diffraction patterns of the same CeB6 nanowire tilted to zone axes [100], [1-10], and [2-10], respectively. Dashed lines indicate the tilting axes about which the nanowire is rotated to the desired orientation. Circular arrows indicate the tilting angles and the straight arrows point to the tilting sequence in experiment.

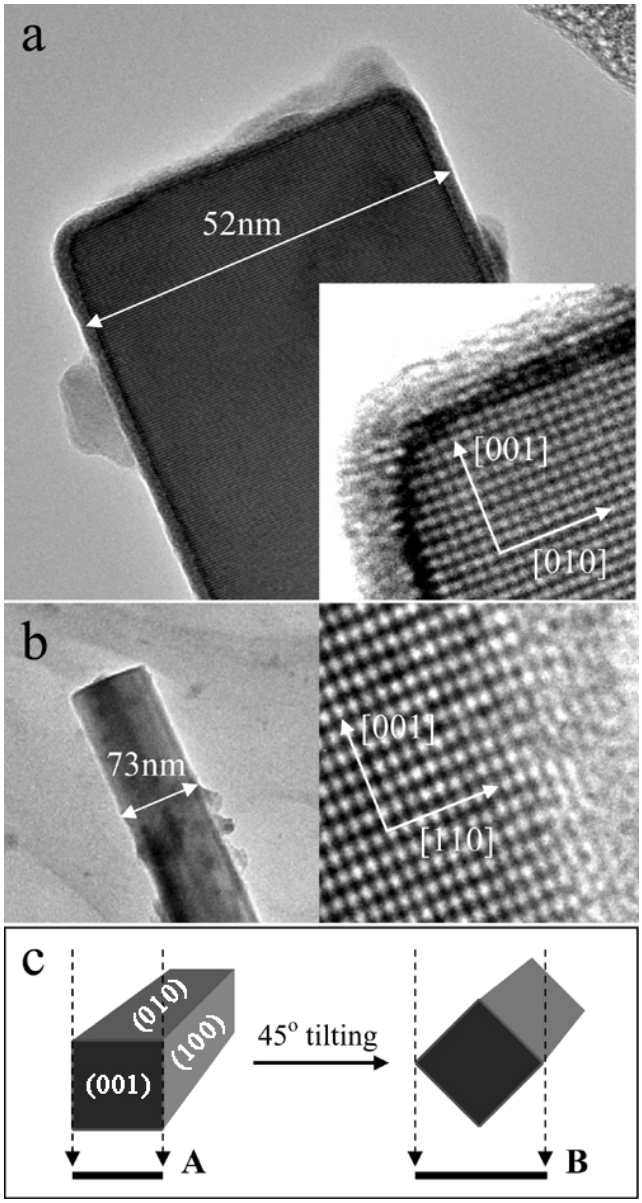

Figure 2.5. (a) [100] direction TEM image of the CeB6 nanowire tip. Inset is a high-resolution lattice image of the tip's top left corner. (b) [1-10] direction TEM image of the same nanowire together with a high-resolution lattice image showing its right-side wall. (c) Illustration of the 45° tilting process to reconstruct the morphology of the nanowire.

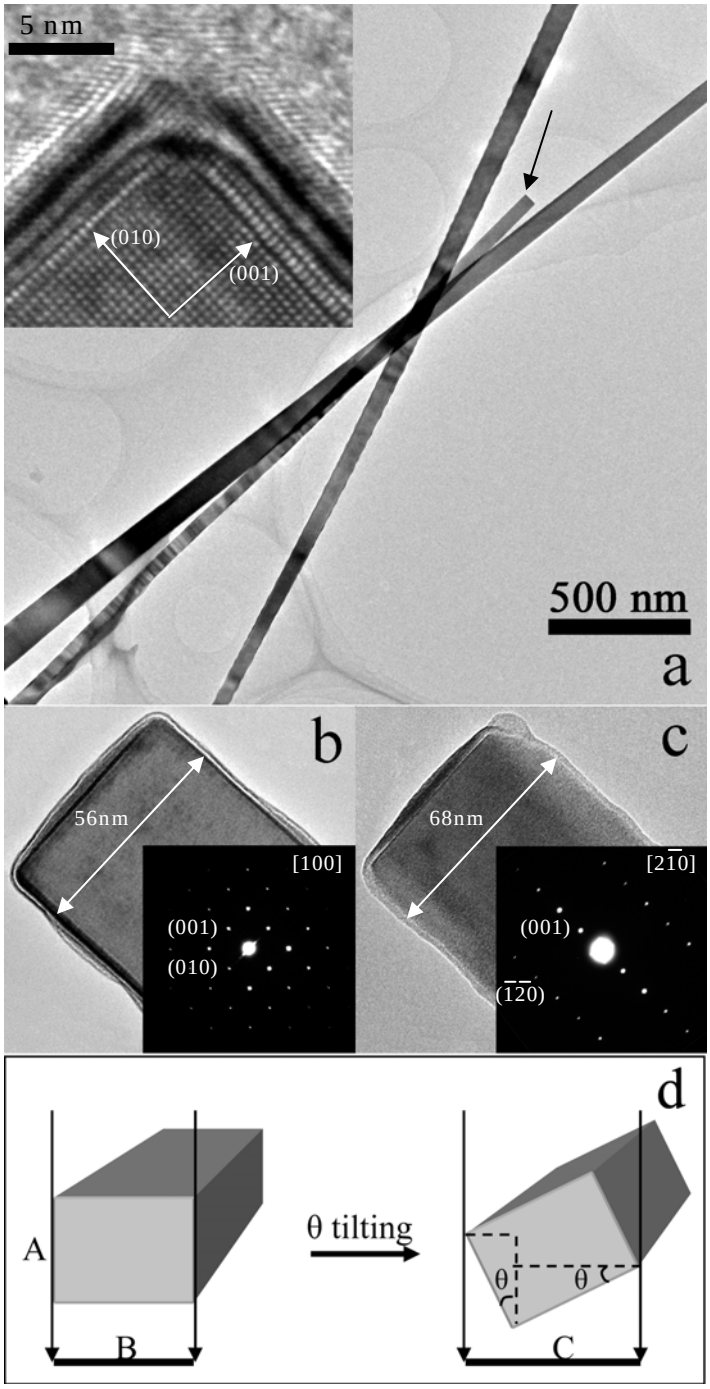

Figure 2.6. (a) TEM image of GdB_6 nanowires. Inset is a high-resolution lattice image of the tip's top-left corner of the nanowire marked by a dark arrow. (b-c) TEM images and selected area diffraction patterns taken from the same nanowire along its [100] and [2-10] lattice directions, respectively. (d) Illustration of the tilting process to reconstruct the morphology of the nanowire tip.

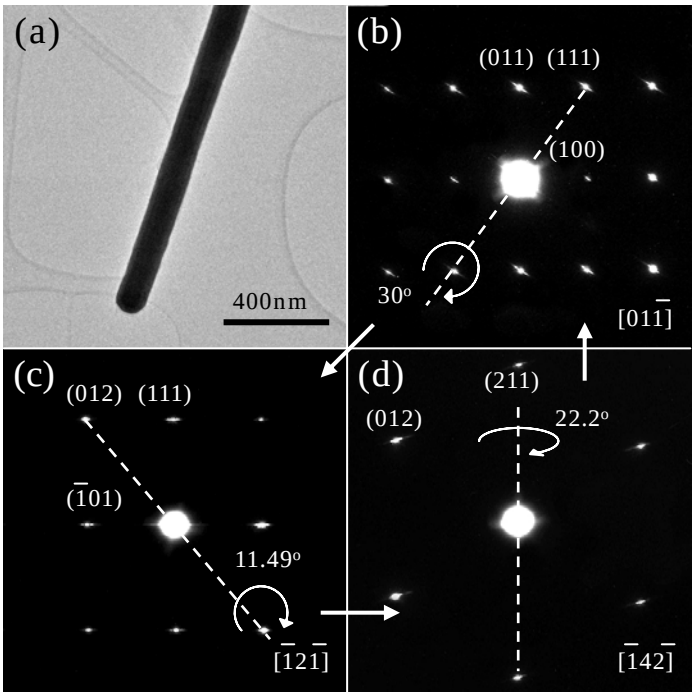

Figure 2.7. a) Low-magnification TEM image of LaB_6 nanowires. b-d) Electron diffraction patterns of the same LaB_6 nanowire tilted to zone axes [0 1 -1], [-1 2 -1], and [-1 4 -2], respectively. Dash lines indicate the tilting axes about which the nanowires were rotated to obtain the needed orientation. Circular arrows give the tilting angles and the straight arrows point to the tilting sequence.

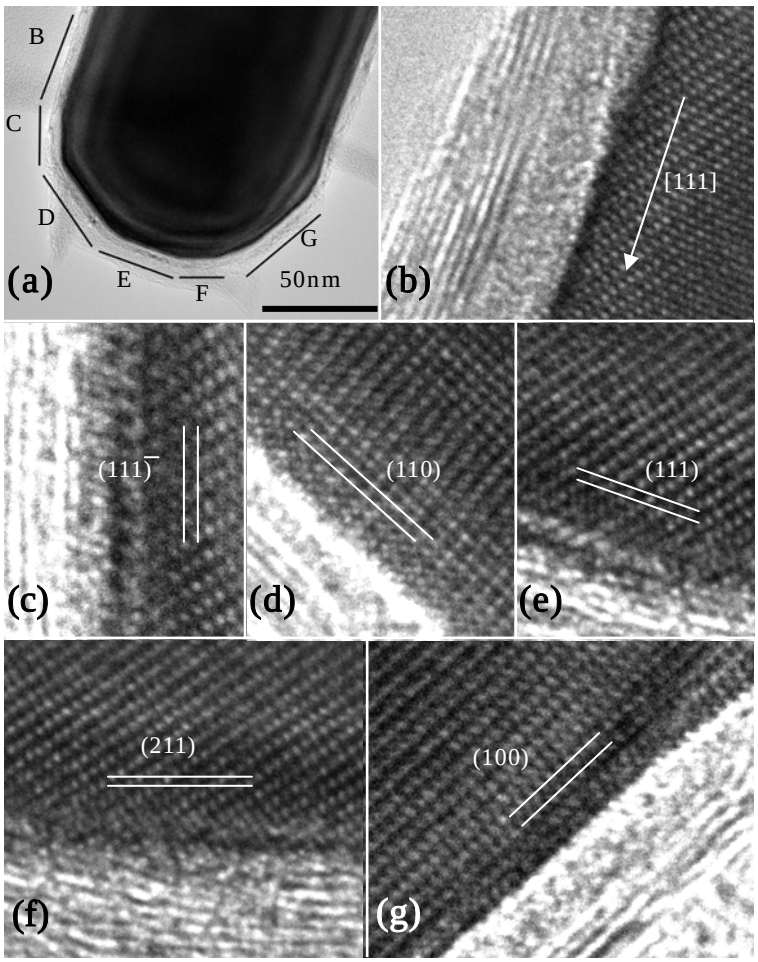

Figure 2.8. a) High-resolution image of the LaB_6 nanowire tip with terminating facets labeled with letters B through G. b-g) Lattice images of the nanowire stem (B) and facets C to G as indicated in (a). The terminating facets are lattice planes of low indices, such as {100} (G), {110} (D) and {111} (C and E).

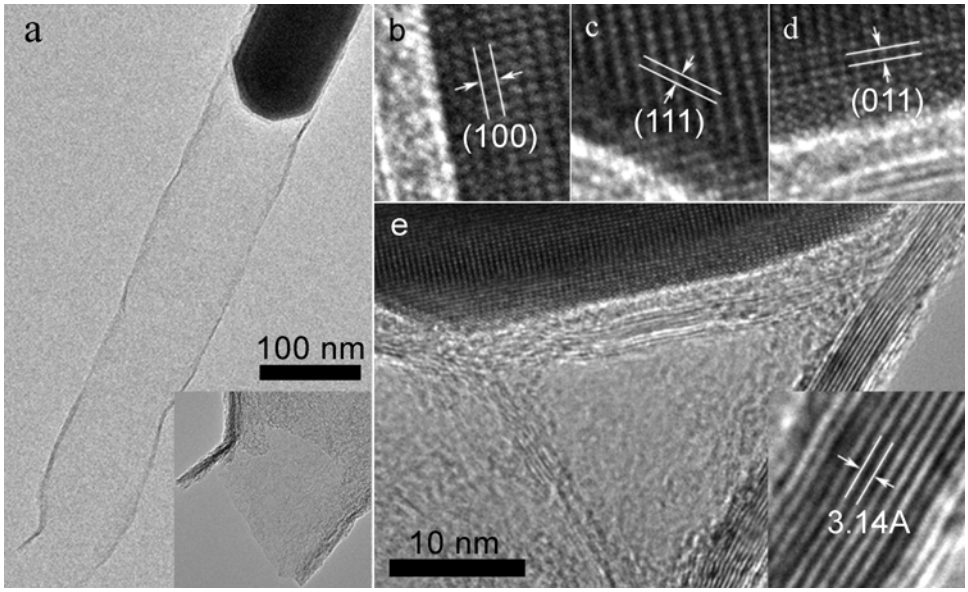

Figure 2.9. a) low magnification image of a LaB_6-in-CNT nanocable structure, inset: magnified image at the open end of the CNT; b)-d) high resolution image of the tip area of the LaB_6 core; e) A triangle formed by graphitic layers near the tip of the LaB_6 core tip. Inset: high resolution image showing the graphite layer spacing.

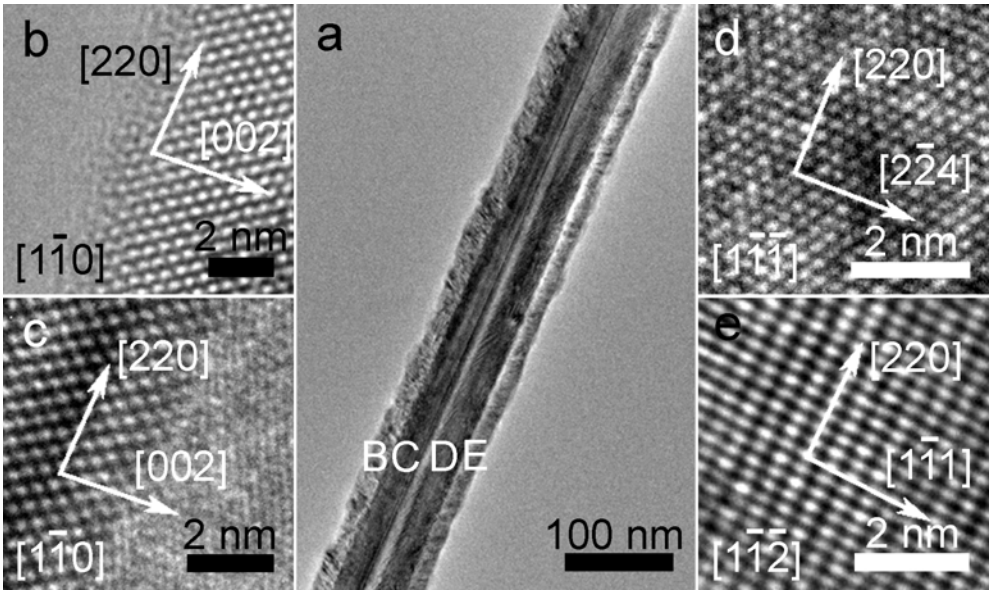

Figure 2.10. a) low magnification image showing the body of a YB_{12} nanowire which is composed of four co-axial grains labeled as B, C, D and E; b)-e) corresponding high reolution images of grains labeled in a.

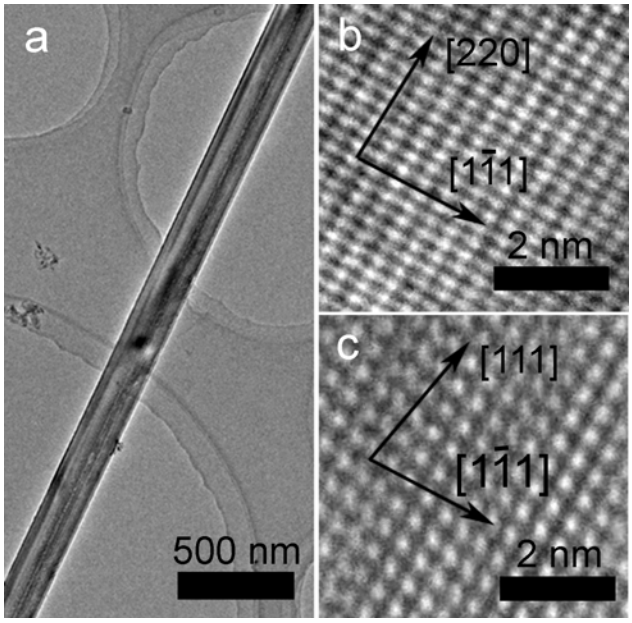

Figure 2.11. a) low magnification image of a LaB_{12} nanowire; b) high resolution image taken before the nanowire is tilted; c) high resolution of the nanowire after the sample is tilted with 35^{o} angle.

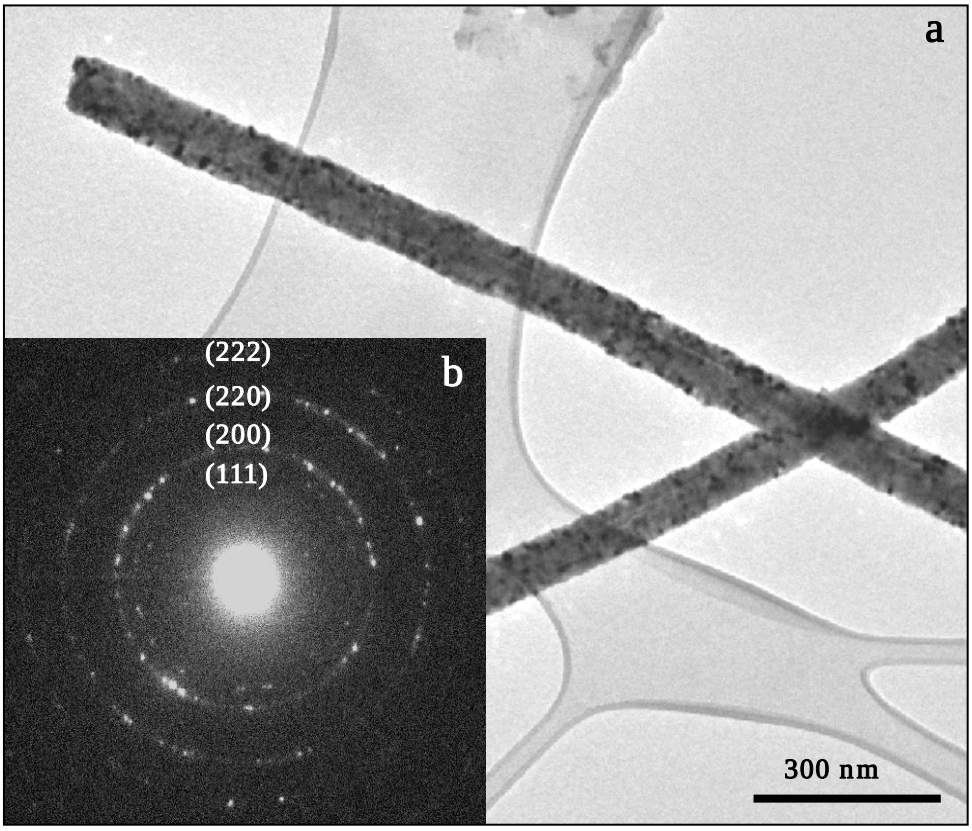

Figure 2.12. (a) TEM image of MgO nanowires. The MgO nanowires' diameter is approximately 80 nm; (b) Selected-area electron diffraction pattern taken from a single nanowire. The reflection rings are only from the polycrystalline MgO crystal.

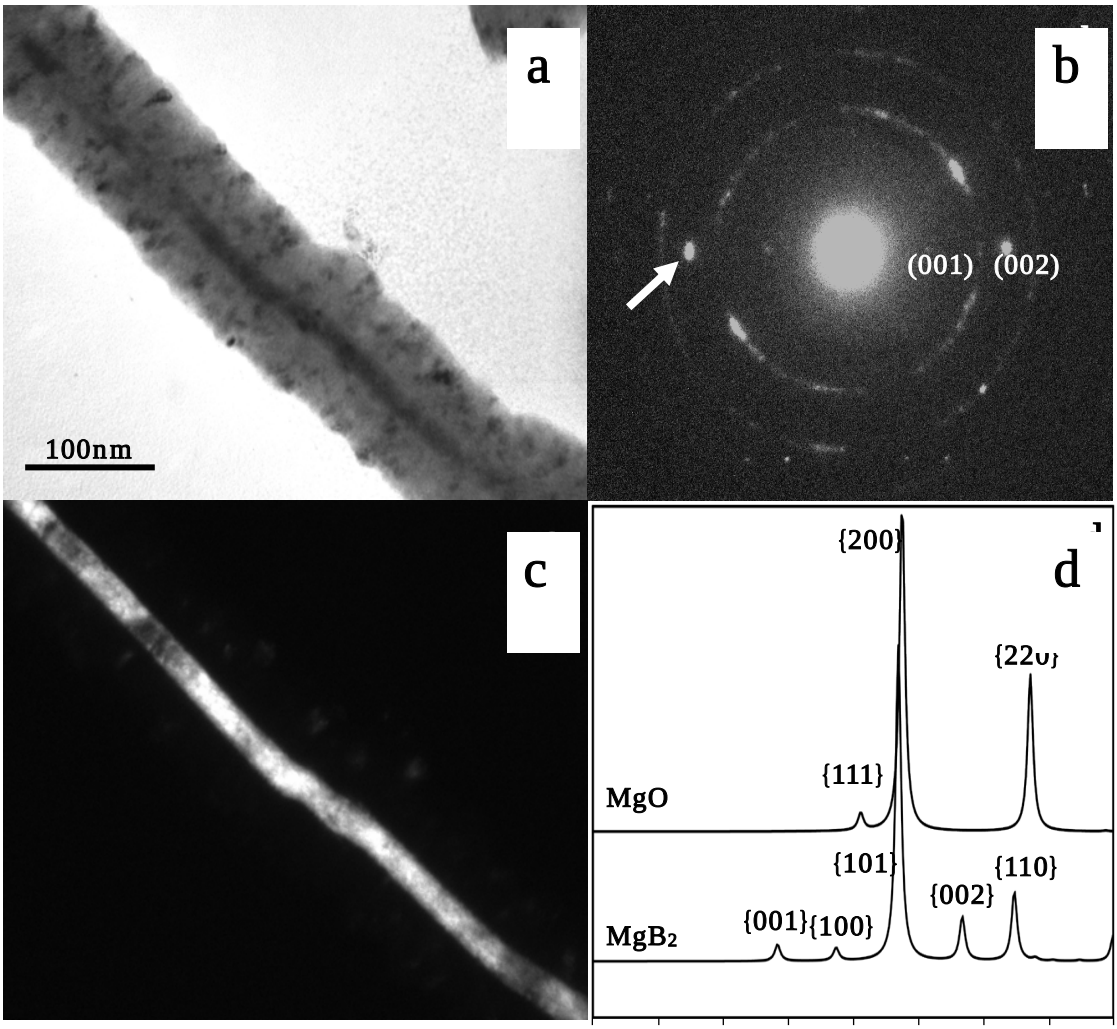

Figure 2.13. (a) Bright-field TEM image of an MgB_2/MgO nanocable structure. The darker core is a single crystal of MgB_2 covered with a polycrystalline MgO shell showing lighter contrast. The whole nanowire is about 100 nm in diameter and the MgB_2 core is about 10 nm in diameter; (b) Selected-area electron diffraction pattern taken from the nanocable, showing MgO diffraction rings together with a set of single crystalline reflections of MgB_2; (c) Dark-field image taken by selecting the (002) reflection marked by an arrow in (b). Only the core inside the nanocable shows bright contrast, indicating that the core is MgB_2 and it is single crystalline; (d) Electron diffraction profiles simulated for MgB_2 and MgO powders (grain size set to be 10X10X10nm) with y-axis as intensity and x-axis as reciprocal d^*. The first five MgB_2 lattice reflections together with the first five MgO lattice reflections are indexed.

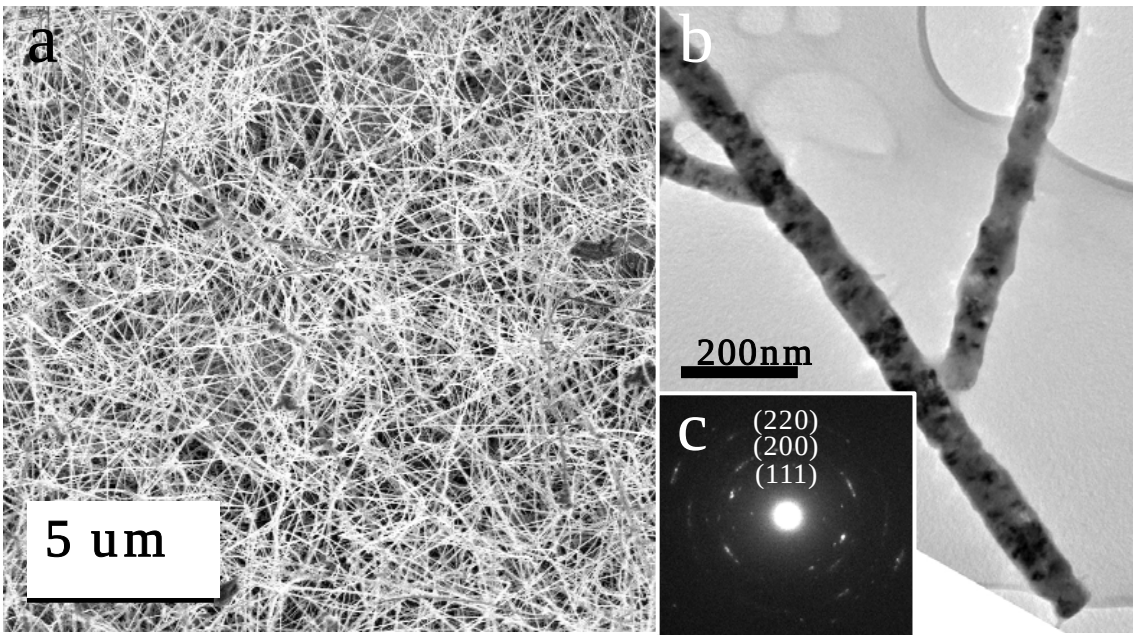

Figure 2.14. a) SEM image of MgO nanowires grown on Platinum catalyst wires. Thick film of nanowires were found evenly cover the whole catalyst wire surface. Their average length is about 20um; b) TEM image of such MgO nanowires shows an average diameter of 80nm. Dark contrast grains are visible along the nanowire body; c) Selected area diffraction pattern reveals the polycrystalline structure of the MgO nanowres; Diffraction rings are indexed as (220), (200) and (111) planes of the crystal.

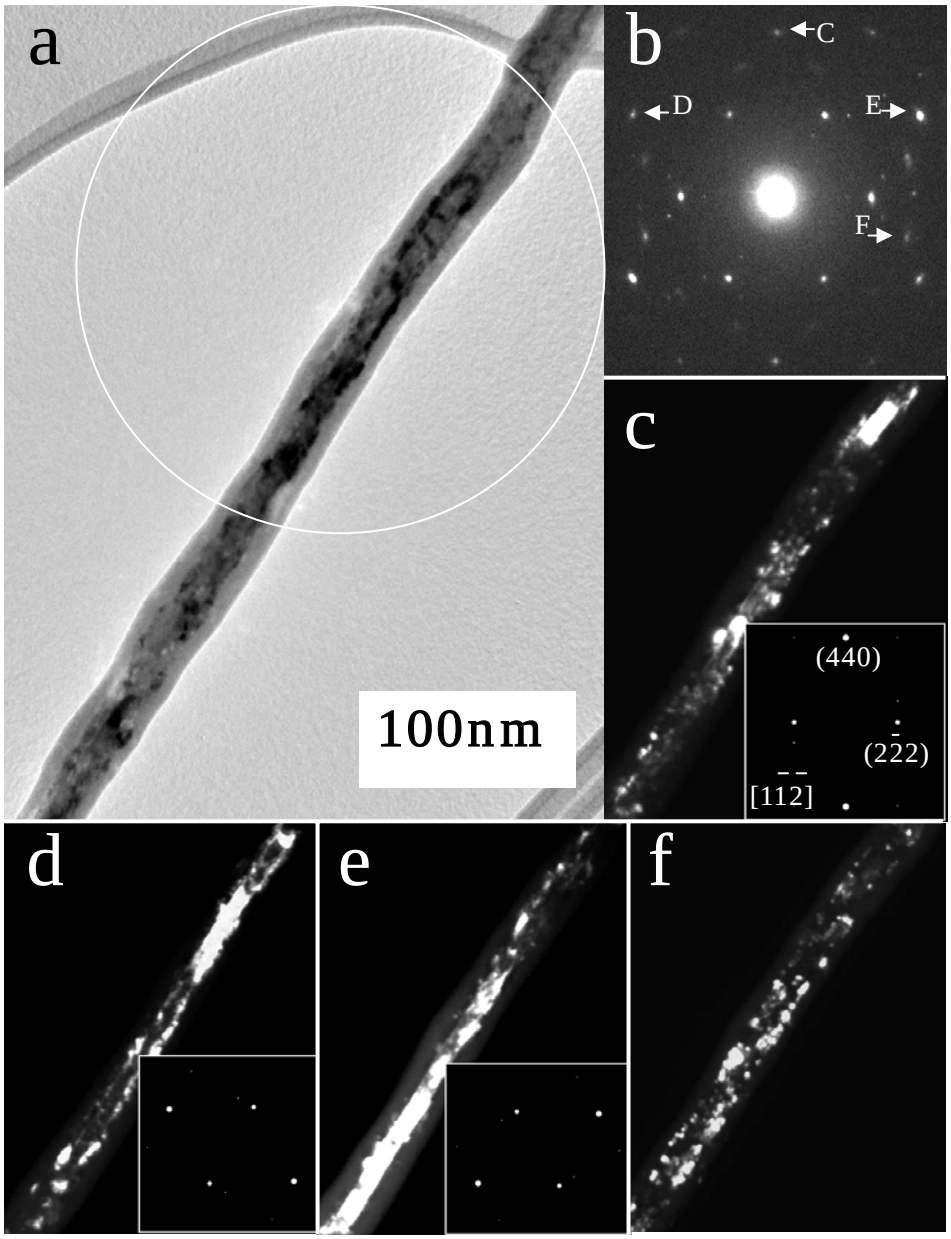

Figure 2.15. a) Bright field image of a composite MgO/Mg_3N_2 nanowire with a diameter of about 30nm. A dark contrast core composed of many grains is shown with a lighter contrast layer wrapping from outside; b) Selected area diffraction pattern taken from the region marked by a white circle in a. A set of seemingly 6-fold symmetric diffraction spots presents with diffraction discrete rings. c) to f) are corresponding dark field images taken with the diffraction spots marked through C to F in b. The insets in c, d and e are simulated full diffraction pattern of Mg_3N_2 with respect to the lightened grains. Diffraction rings are indexed with MgO structure.

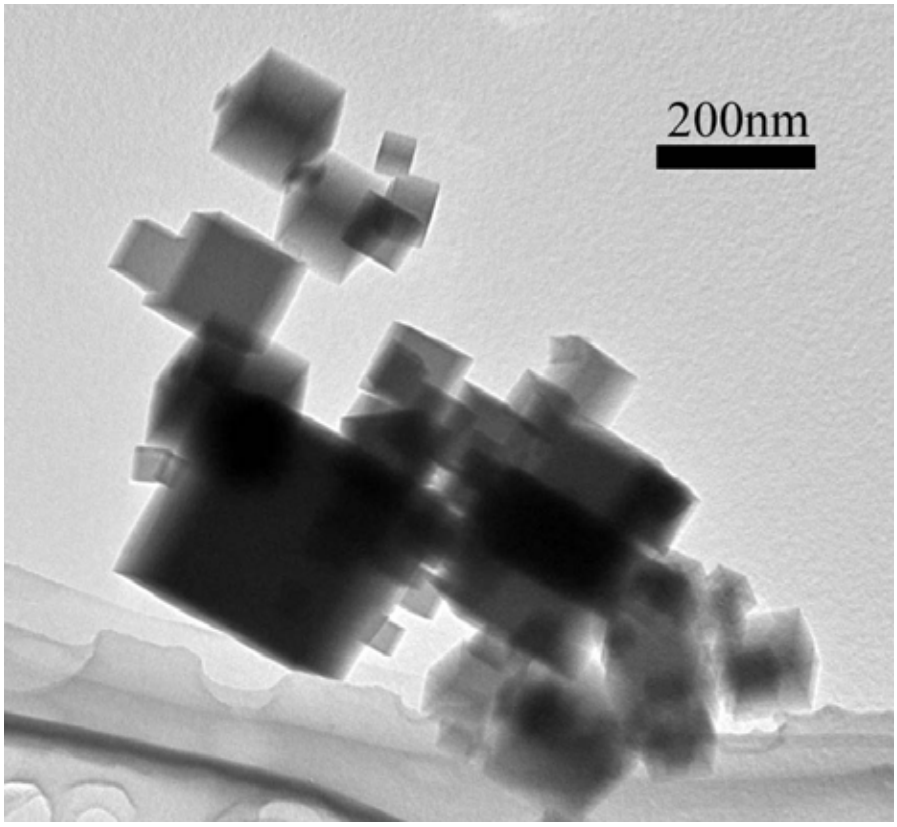

Figure 2.16. MgO powder in the form of single crystalline cubes are observed when air was added into the reaction chamber to oxidize Mg.

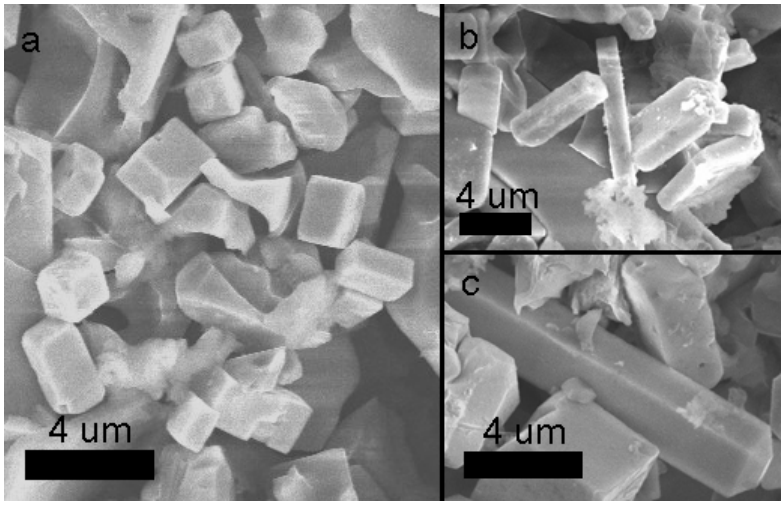

Figure 2.17. LaB_6 single crystals produced by aluminum flux method. a) LaB_6 cubes produced under 1200^{o}C for 30 minutes. b) and c) LaB_6 rods produced under 1200^{o}C for 30 minutes followed by 1100^{o}C for 30 minutes.

Chapter 3 Formation and Growth of One-Dimensional Nanowires

3.1. Introduction

3.1.1. Background

One-dimensional single crystal growth from the vapor phase was initially studied in the 1950's (Levitt, 1970). Two categories of growth mechanisms were proposed for the formation of whisker structures: an impurity assisted "vapor-liquid-solid (V-L-S)" mechanism and a screw dislocation induced "vapor-solid (V-S)" mechanism. V-L-S mechanism was first proposed by Wagner et al. in 1964 to explain the whisker growth of Si on an Au coated substrate (Wagner & Ellis, 1964; Wagner & Treuting, 1961). In their model, a low freezing point Si-Au alloy liquid droplet was first formed on the substrate surface. This liquid droplet serves as a sink for the further adsorption of Si atoms from the gas phase. After the droplet reaches supersaturation, the Si nuclei solidify on the droplet surface. As the droplet continuously traps more Si atoms from the gas phase, more Si atoms deposit at the interface between the previously formed Si nuclei and the droplet. By this manner, one-dimensional single crystal growth of Si is realized. The presence of a catalyst ball at the tip of the grown whisker was found to be a sign for such a growth mechanism. The catalyst can be a foreign metal that forms eutectic solid solution with the whisker material or one of the metal components of a compound that grows into the whisker structure. The V-S mechanism was established to explain the whisker growth on non-catalyst surfaces (Sears, 1955; Brenner & Sears, 1956). Screw dislocations on the initial substrate are believed to be the higher energy sites that favor the deposition of atoms from the gaseous phase. Therefore, the deposited single crystal grows

perpendicular to the substrate surface. The screw dislocation develops with the grown crystal and always remains at the tip top surface. On one hand, this mechanism succeeded in explaining the quite often observed non-catalyst growth of whisker structures, but on the other hand, the necessary existence of the screw dislocation at the top surface was rarely observed. For some compound nanowires, though the catalyst balls were not found at the tips, it was believed that the VLS mechanism still accounts for the growth (Xia et al., 2003; Yao et al., 2002). One element from the compound could serve as the catalyst ball or a layer at the tip. Eventually, this catalyst layer reacts with the other components and disappears at the end of the growth. However, the growth of pure metal whiskers without catalyst is still hard to explain by the VLS mechanism, though the VS mechanism doesn't seem to be valid either, since no screw dislocation has been found.

The discovery of carbon nanotubes in 1991 brought tremendous research interests into this type of one-dimensional nano-scale system (Iijima, 1991). Though being similar to graphite, made out of carbon element with SP^2 bondings, the nanotube exhibits very different properties originated from its unique morphology and dimensionality. Many new device concepts and applications based on these new properties have been proposed for solving some important real-life issues, from building a ladder to the moon to curing of cancer. The benefits are not restricted to carbon. A large variety of nanowires have been synthesized through the past 15 years (Rao et al., 2003; Xia et al., 2003), including: elemental metals, semiconductors, binary metal oxides, nitrides, carbides, chalcogenides, borides and some ternary compound metal salts. Quaternary copper oxides based superconducting nanowires have also been synthesized. The combinations of the intrinsic and size-induced properties of the materials have enabled a wide range of device applications using these nanowires as their functioning parts, which for examples are, electronic transistors, computing logic gates, chemical and bio-sensors, photodetectors,

high efficiency solar cells, colorimetric markers, laser device, wave guides, and field emitters.

To make these functional nanowires and nantubes, different strategies have been developed. These can be divided into four categories. The first type is to use directly the high anisotropy of the material. Some crystals are made of chain-shaped molecules or have layered structure. For such structures, only one direction is favored when crystallize, therefore produce one dimensional nanotubes/nanowires naturally. For the synthesis, little has to be done to restrict the growth in one dimension. One just has to prepare the molecules in a dilute form, either solutions or vapors, and then let them crystallize. Type two is to use a template material as the host, and then physically confine the desired material in the nanometer-sized pores available in the template. This could be done by electrochemical plating, vapor phase deposition or liquid phase filling. After that, the template should be removed by certain reactant that does not etch away the wanted material. The third type is to use the principle of VLS mechanism: forming catalyst particles followed by introducing a vapor phase of the desired materials. The last type is VS growth of nanotubes/nanowires. This type of growth is as generally applicable as the VLS mechanism, though its exact mechanism still remains unknown (Dai et al., 2003). In a typical VS procedure to produce metal oxide nanowires, the gas phase of the metal is brought into a furnace tube to react with the oxygen gas. Nanowires growth is often found on the wall of the furnace tube, where temperature is slightly lower than the reaction zone.

Regarding the progress in nanowire growth mechanism study, more work has been focused on the VLS mechanism than others (Tan et al., 2003 & 2004; Liu et al., 2005; Westwater et al., 1997; Zhang et al., 2001; Yang et al., 2004; Kikkawa et al., 2005). It is because: firstly, the mechanism is the most generable and usually produces nanowires

with good crystalinity; secondly, the growing picture is relatively clearer. The effects of operation parameters, such as the catalyst type, catalyst size, temperature, and vapor density have been understood basing on a thermodynamic model. The mechanism has been intensively studied ever since it was first proposed by Wagner et al. in 1964. However, though the trend of how these parameters affect the nanowires growth can be roughly predicted, there is little good match between predictions and actual observation on a quantitative level. The reason for that is the lack of accurate measurements of most of the thermodynamic and kinetic quantities involved in the theory, even though these quantities could be well defined. Another reason is the poorly controlled experimental environment used in synthesis. Unpredictable factors such as turbulence, temperature fluctuations, and gas flow fluctuations, for example, are very hard to take into consideration quantitatively.

3.1.2. Motivations:

In Chapter 2, using the same chemical vapor deposition system, we synthesized successfully nanowires of LaB_6, CeB_6, GdB_6, YB_{12} and LaB_{12}. Oxide nanowires of MgO together with nitride nanowires Mg_3N_2 were also obtained. For the LaB_6 nanowire growth alone, different phenomena were observed when experimental conditions changed. These phenomena all indicate different growth history and mechanisms. It was found by using an iron catalyst, <001> oriented LaB_6 nanowires can be changed into <111>. Carbon graphitic layers were always observed on the <111> LaB_6 nanowires and sometimes even extended out as nanotubes. While in some other batches, carbon balls were always observed on the nanowires and the nanowires seemd to have a flower-like pattern, where more than 100 nanowires rooted from the same spot on the substrate. In some runs, more than 50% of the LaB_6 nanowires have sub-branches which form a right angle with main

stems, while in other runs, all nanowires are perfectly free of sub-structures. Since our synthesis was the first report on rare-earth hexaboride nanowires, no studies have been done about their growth mechanism. At the same time, these growth mechanisms should be generally applicable to other nanotube/nanowire growth studies. We will develop three growth models in this chapter using thermodynamic theories. Experimental data are also used as a reference to justify the proposed models in a quantitative way.

3.1.3. Over view of Chapter 3:

In the nanowires we produced from vapor phase using our CVD system, altogether 3 types of growth mechasnims were observed. They are the vapor-solid mechanism, the vapor-liquid-solid mechanism and the carbon nanotube template assisted mechanism. They will be detailed with experimental examples of LaB_6 nanowire growth in the following three sections. In each section, thermodynamic models will be established first, and then experimental parameters will be input to predict the growth results. These will be compared with actual electron microscope observation to justify the models. Lastly, summary will be briefly provided and conclusions will be drawn at the end.

3.2. Vapor-Solid Growth

The reaction was conducted as following: after evacuating the furnace tube to remove the oxygen, the hydrogen gas was allowed in. Hydrogen flow rate and pumping rate were set to a certain ratio so that in the chamber hydrogen partial pressure was kept at 10^4 Pa. The furnace temperature was then raised to 1400 K. The $LaCl_3$ powders placed in a quartz boat start to melt and the vapor pressure at the temperature is 186 Pa (Chervonnyi & Chervonnaya, 2004). The BCl_3 gas was then let into the reaction zone

through a quartz conduction tube. BCl_3 is a gas at room temperature. At 1400K, it would have higher pressure than atmosphere. However, considering the environmental pressure of 10^4 Pa created by the vacuum pump, its partial pressure is taken as 10^5 Pa in the calculations. The chemical reaction is:

$$LaCl_3(g) + 6BCl_3(g) + \frac{21}{2}H_2(g) = LaB_6(g) + 21HCl(g)$$

Here, the LaB_6 product on the right hand side is treated as a gas phase first, its condensation into the solid phase will be taken as a second step.

Since there is no additional LaB_6 or HCl sources, their partial pressure should follow the ratio of $P_{LaCl6} : P_{HCl} = 1:21$. At equilibrium, the reaction constant K is

$$K = \frac{P_{LaB6} \cdot P_{HCl}^{21}}{P_{LaCl3} \cdot P_{BCl3}^{6} \cdot P_{H2}^{21/2}} = \frac{21^{21} \cdot P_{LaB6}^{22}}{P_{LaCl3} \cdot P_{BCl3}^{6} \cdot P_{H2}^{21/2}} \quad (3.1)$$

where K is a function of the reaction Gibbs free energy ΔG_r and temperature T:

$$K = \exp(-\frac{\Delta G_r}{RT}) \qquad (3.2)$$

where R is the gas constant, R=8.314J/K•mol; According to Peshev, ΔG_r is equal to 420 kJ/mol at 1400 K (Peshev, 2000). After substituting the partial pressure values P_{LaCl3}=186 Pa, $P_{BCl3}=10^5$ Pa and $P_{H2}=10^4$ Pa, we obtain P_{LaB6}=25 Pa;

Since there is no direct measurement on the vapor pressure of LaB_6 at 1400 K, the following treatment is used to obtain this value for our calculations. The melting point of LaB_6 is 2485 K, its sublimation energy, L_s, is 564.8 kJ/mol (Nordine et al., 1991), and these values are very close to those of boron, which are 2349 K and 565.6 kJ/mol, respectively. Therefore, it is reasonable to assume that the equilibrium vapor pressure of LaB_6, P_{ELaB6}, equals that of boron, P_B at the temperature of about 1400 K. To find the vapor pressure of boron, the following formula could be used, if we assume that the sublimation energy is independent of temperature change (Swalin, 1972):

$$P = A\exp(-\frac{L_s}{RT}) \qquad (3.3)$$

There are two unknown parameters in this equation; P and A. Therefore, we need another set of data to evaluate A for P=10^5 Pa at T=4200 K, which is the boiling point for boron. This gives us the equilibrium vapor pressure of LaB_6, P_{ELaB6}, to be 9×10^{-10}Pa at 1400 K.

We now can define the supersaturation α(Hook, 1963):

$$\alpha = \frac{P_{LaB6}}{P_{ELaB6}} = 2.7\times10^{10} \qquad (3.4)$$

As for nucleation, we consider that the nucleus is a cube cubic terminated with {100} planes. This is due to several reasons: first, most LaB_6 nanowires grown are observed to have {100} planes as their terminating facets; Second, a recent calculation by Uijttewaal et al. indicates that the {100} plane has the lowest surface energy σ of about 8 ev/nm^2=1 J/m^3, when the chemical potential of La gets close to its value of bulk form (Uijittewaal et al., 2006). The nucleation energy ΔG_N can be expressed as:

$$\Delta G_N = \Delta g_B l^3 v + 6l^2\sigma \qquad (3.5)$$

$$\Delta G_N = \Delta g_N l^3 v \qquad (3.6)$$

where, Δg_B is the condensation energy of bulk form, Δg_N is the nucleation energy density, l is the nucleus side length, v is volume density in the unit of mol/m^3. The critical cube length l^* is thus:

$$l^* = -\frac{4\sigma}{\Delta g_B \cdot v} \qquad (3.7)$$

Substitute it back to equation 3.5, we obtain the relation between critical nucleation energy density Δg_N and the condensation bulk energy density Δg_B:

$$\Delta g_N{}^* - \Delta g_B = \frac{6\sigma}{l^* v} \qquad (3.8)$$

On the other hand, if P is the vapor pressure in equilibrium with $\Delta g_N{}^*$ and P_E is the vapor

pressure in equilibrium with Δg_B, we have

$$\Delta g_N{}^* - \Delta g_B = RT \ln(\frac{P}{P_E}) = RT \ln(\alpha). \qquad (3.9)$$

Therefore, the critical length l^* and nucleation energy $\Delta G_N{}^*$ are

$$l^* = \frac{6\sigma}{vRT \ln \alpha}, \quad (3.10)$$

$$\Delta G_N{}^* = \frac{72\sigma^3}{v^2 R^2 T^2 \ln^2 \alpha}. \quad (3.11)$$

By taking the volume density of LaB_6 v=2.35X10^{4}mol/m^3, at the current supersaturation, we obtain l^*=9.1×10^{-10}m, $\Delta G_N{}^*$=1.67×10^{-18}J.

The impingement rate of an ideal gas, N, can be expressed as:

$$N = P\sqrt{\frac{3}{mRT}}. \quad (3.12)$$

For a nucleus of volume l^3, its mole number is l^3/v, therefore, the impingement rate for such a nucleus is:

$$K = \frac{N}{l^3 v} = \frac{P}{l^3 v}\sqrt{\frac{3}{mRT}}, \quad (3.13)$$

where m is the mass density of LaB_6, m=0.205 kg/mol. The overall rate of nucleation is:

$$V = K \exp(-\frac{\Delta G_N}{kT}), \qquad (3.14)$$

where k is the Boltzmann constant. At the current nucleus size and temperature, V=1.58X10^{-15} /m^{2}s. As Figure 3.1a shows, the number of nanowires grown in an area of 400 μm×400μm is about 50 in 300 s of time span. If each individual nanowire grows from a single nucleus, the corresponding nucleation rate is at least 10^7/m^{2}s. A supersaturation of 2.7×10^{15} will be required, which is 10^5 higher than our experimental value. Therefore, homogenous nucleation is impossible for our experimental supersaturation condition!

If the nucleation is 2-D, which means one layer of LaB_6 atoms are formed on the

substrate, the energy needed to form a new surface is significantly less. We can still use the same derivation as above, except the change of a few expressions. The shape of the nucleus is considered as a square with length l and thickness a, which is lattice constant of LaB_6, a=4.15×10^{-10}m. For such a scenario, forms of the critical length l^* and the critical nucleation energy ΔG_N^* are changed into:

$$l^* = \frac{4\sigma}{vRT\ln\alpha}, \quad (3.15)$$

and $$\Delta G_N^* = \frac{8a\sigma^2}{vRT\ln\alpha}. \quad (3.16)$$

Due to the change of the shape of the nucleus, the nucleus impingement rate K needs to be modified as such:

$$K = \frac{N}{a\cdot l^2 v} = \frac{P}{a\cdot l^2 v}\sqrt{\frac{3}{mRT}}. \qquad (3.17)$$

With other equations being the same, we obtained the critical nucleus length l^*= 6X10^{-10}m, the critical nucleation energy ΔG^*_N=5X10^{-19} J and the nucleation rate 1.07X10^{12}/m^2s. Noting that this rate of nucleation also accounts for the growth of nanowires into one-dimension.

A model of 2D nucleation and growth is therefore able to explain the VL growth of the LaB_6 nanowires. Figure 3.2 illustrates the procedures In step i, a single layer of LaB_6 atoms are formed on the substrate surface, with its side equal to the critical length. After the nucleus is formed, it grows in two dimensions as shown in step ii, until a second nucleus forms on top of it, as shown in step iii. This 2D growth rate is much higher than the nucleation rate, since the energy it cost to add one more atom to the previously formed nucleus is much smaller. The second nucleus grows in 2D as well till it reaches the edge of the first layer. By this layer after layer manner, the crystal grows eventually in the direction perpendicular to the substrate surface. The reason that no nucleus is formed on

the side of the nanowire is that, since the LaB_6 vapor phase is away from the substrate, it forms a natural pressure gradient from top to bottom, as shown in step v. Note that the vapor impingement rate K is proportional to vapor pressure P, the nucleation will be much faster on the top than on its side surfaces. Practically, the growth will only occur on the top of the nanowire.

This layer by layer growth is supported by the SEM observations given as the inset to Figure 3.1a. In the image, it is clearly revealed that the nanowires have growth perpendicular to its axis. The nanowire on the right hand side stopped growing vertically due to a white particle landed on its top surface. Such particles are marked with black arrows in the image. Only after the top surface growth was suppressed by the particle did side surface nucleation start. The LaB_6 vapor pressure is still higher where it is close to the tip, therefore branching occurred only at the top area as shown in the image. It is very interesting to notice that, after the branch grew for a short length, it turned its way back to vertical. It further shows that the pressure gradient is the driving force for the one-dimensional growth of these nanowires.

In the above described model, it is possible to estimate the growth rate by accumulating the thickness of each layer throughout the entire experiment duration. For example, in Figure 3.1a, if we take an area of 400 μm×400 μm, and a total growth time of 300 s, a total of 5.14×10^7 nuclei are expected. There are roughly 50 nanowires, so about 10^6 nuclei for each nanowire, which corresponds to $4.15\times10^{-10}\times10^6$ m axial growth for each nanowire. This value agrees well with the actual length of the nanowire, as measured from Figure 3.1a, which is about 400 μm. Another area from the same sample was imaged and the result is shown in Figure 3.1b. In this area, all nanowires are coated with a layer of particles, which are believed to be the condensation of $LaCl_3$ approaching the end of the growth. As shown in the inset, a fine straight core is seen and this core is a single

crystalline LaB_6 nanowire. The area presented in the image is about 50 μm×50 μm, containing about 30 nanowires with an average length about 40 μm. Using the nucleation rate deduced from these observations, we obtain a supersaturation value of 9×10^7, which is higher than our pre-set of $2.7X10^7$. This difference could be caused by the vapor pressure fluctuations over the substrate surface. The reason that the number of nanowires in Figure 3.1a is less than that in Figure 3.1b might be that the former substrate area had fewer flat clean sites for nucleation. This can be seen in the inset of Figure 3.1a, where particle-looking debris is seen covering the entire surface.

3.3. Vapor-Liquid-Solid Growth

In our other runs to synthesize the rare-earth hexaboride nanowires, different morphologies were also observed. An SEM image of the CeB_6 nanowires is shown in Figure 3.3a, where we find the CeB_6 nanowires are either buried inside as a core for melt-looking substance or interconnect several round ball-shaped particles. TEM image of such nanowires is shown in Figure 3.3b. Two nanowires are found to have grown from a large particle. At the root of each nanowire, thickening is also observed. The presence of such particles suggests a VLS growth mechanism, in which the particle is a catalyst and the nanowires nucleate inside these liquid catalysts. Figure 3.3c is an SEM image of the LaB_6 nanowires with a similar morphology. About 300 nanowires are formed in a radiation-shaped pattern, suggesting that they all grow from the same spot, which could be a catalyst underneath. These experiments are performed using the same parameters as those in Figure 3.1.

To investigate the composition of these catalyst particles, TEM samples were made and they were studied by electron energy loss spectroscopy (EELS) in the scanning transmission electron microscopy (STEM) mode. Figure 3.4a is an STEM image acquired

in the area where a catalyst is seen attached to a LaB_6 nanowire. From the image contrast, we can see that the nanowire passes through the catalyst, so the particle might not be the original catalyst ball where the nanowire nucleates. However, it is very likely to be a drop of catalyst liquid that happens to stick to the nanowire when it grows out of the catalyst surface. Therefore, its chemical composition should be the same as the original catalyst. An EELS spectrum was taken at the particle. The actual acquisition spot forms a black hole as shown in Figure 3.4a, which is caused by radiation damage from the electron beam. The spectrum shows that three elements are presented in the particle: La, B and C. Because of the small size of particle', the spectrum is often affected by the LaB_6 nanowire. We took another STEM picture on the nanowire and acquired another EELS spectrum from it. The results are shown in Figure 3.4c and d. In the spectrum, we can see that all the three elements are revealed again. However, the relative intensities from La and B got higher compared to C signal. The lowest La and B signals from the particle suggest that it might mainly contain C with much less contents of LaB_6. Although we did not find ternary phase diagram with La, B and C elements, La and C do form an alloy at temperature below 1200 K (Massalski et al., 1986). Therefore there might be a certain solubility of LaB_6 in C around our experimental temperature.

Based on the above discussion, a VLS growth model is proposed and the process is shown in Figure 3.5. In step i, a catalyst ball is formed with a certain mixture of C and LaB_6. Then the LaB_6 vapors continue to arrive and dissolve in the liquid catalyst. After the concentration of LaB_6 exceeds the equilibrium concentration of the alloy, LaB_6 starts to nucleate in the liquid catalyst, as steip ii shows. Half of the nucleus stays outside of the catalyst and half of it stays inside to serve as the growth sites. In step iii, the 2D nucleation takes place on the preformed nucleus bottom surface and thus realizes the one-dimensional nanowire growth by a layer-by-layer manner.

Such a process can be evaluated by the thermodynamic theory based on a 3D homogenous nucleation and a 2D crystal growth. Since all other parameters are the same as the VS growth, except the introduction of the C catalyst, the vapor pressure of LaB_6 is still 25 Pa. The supersaturation in the catalyst liquid is not known without the knowledge of the exact shape of phase diagram. However, if we consider a supersaturated liquid has the same energy as its counterpart in equilibrium temperature of the same concentration, the supersaturation value αcan be estimated. For example, in the extreme case, the liquid mixture is so supersaturated that it has almost the same concentration as pure LaB_6. Since we know that the equilibrium temperature for liquid LaB_6 is 2400 K, the supersaturation can be treated as a value close to this up-limit, which is:

$$\alpha_{Max} = \frac{P_{2400K}}{P_{1400K}} = 5.8 \times 10^{9}. \qquad (3.18)$$

On the other hand, the gas impingement rate K_l should have a different form with that of the gas phase K, because in the catalyst droplet, conductance of the material is by diffusion in the solution. This quantity is dependent on the specific alloy and therefore is not known for our case. A rough estimation could be made this way: first, normally the diffusion rate in gas is 10^5 times that in liquid phase; second, at 25 Pa, the density of vapor is 10^{-8} of that of liquid. Therefore the impingement rate K_l is about 10^{-3} times that of K_g. The surface energy σ_l must be reduced as well. This is because in solid-gas interface, the surface dangling bonds should be more than that at the solid-liquid interface. Since there are no values for the interfacial energy is available, we take the interfacial energy of solid-liquid to be less than half of that of the solid-gas interface. Taking into consideration that only half of the nucleus is exposed to gas, the overall effect leads to more than 25% deduction of the original σ. We therefore will use 0.73 J/m^3 for in this case.

With these parameters, we obtained that 280 nuclei are formed during an

experiment duration of 300 s and a catalyst area of 20 μm×20 μm. The catalyst area is considered as the whole area for LaB_6 source impingement. This value agrees well with the observed roughly 300 nanowires grown from the same spot of the size 20 μm×20 μm as observed in Figure 3.4c. The growth rate from the 2D nucleation model, however, brings only 2 μm for the length of each nanowire. This is much shorter than the observed 100 μm length on average for the nanowire length in Figure 3.4c. The reason for the discrepancy could come from the fact that a much larger area should also be accounted for the LaB_6 impingement.

The much higher homogenous nucleation rate is mainly due to the lowering of the surface energy of the formed nucleus. The increase in impingement rate K also helps, but contributes only to a lesser extent. During the 2D growth, however, the increase in surface area with each addition of layer happens at the solid-gas interface. Therefore, the benefit of reducing the surface energy is not at by the 2D growth compared to the 3D homogenous nucleation. We should notice fully utilized that the actual nucleation driving force, the supersaturation α, actually gets lower in the VLS scenario. However, in the VLS case, the homogenous nucleation rate is about 10^{24} faster than that in the VS case. This proves again the importance in reducing the surface energy in the nanowire growth process. Therefore, the use of a metal catalyst should be preferred if it reduces the most of the surface energy of wanted nanowires.

3.4. Nanotube-Assisted Template Growth

By choosing 316-stainless steel as a catalyst, a special type of LaB_6 nanowire-inside-CNT nanocable structure was obtained. The obtained structure has been studied in the TEM and the results are shown in Figure 3.6. As Figure 3.6a shows, this type of nanowires are usually consisted of a dark LaB_6 crystalline core and a carbon

nanotube wrapping around it. The nanotube lots of times extends out as a hollow tube of micron meter long. Most of the times, they are open tubes as shown in the lower image in Figure 3.6a. The terminating faces of the LaB_6 core are all low index planes, which are (100), (111) and (110) as shown in Figure 3.6b-d. It is quite interesting to see that some small humps on the stem of the nanowire. These humps have {100} planes as their terminating facets even though the overall growth direction of the stem is along the <111> direction. Knowing that the {100} has a lower surface energy than {111}, this leads us to believe that the surface energy is still the driving force in forming such a unique nanocable structure. In Figure 3.6f, we found that rather than having dangling bonds at the solid-gas interface, the LaB_6 nanowire core is covered with graphitic layer as well. This is believed to reduce the surface energy σ.

The [111] oriented LaB_6-in-CNT nanocables, however, have a different growth mechanism and this is indicated by two facts: first, the [111] growth of the LaB_6-in-CNT nanocables only occurs on 316-stainless steel pieces with carbon contents, but not on the iron/silicon substrate, which does not contain carbon; second, the [111] oriented LaB_6 nanowires are always observed inside a CNT shell, no naked LaB_6 nanowires were ever observed with [111] orientation. We propose a CNT-assisted growth mechanism for this type of nanocable structure, which is illustrated as a five-step process in Figure 6. In step i, when the temperature reaches above 800^oC, liquid droplets of Fe/C are formed on the stainless steel substrate. In step ii, the solubility of C in Fe decreases, leading to C precipitations to form a CNT on the droplet surface. The drop of the solubility of C could be due to the absorption of La/B elements in the Fe/C droplets. In step iii, more LaB_6 molecules are absorbed and start to nucleate. The initial nuclei are more likely to be cubic shaped due to its primitive cubic structure and randomly oriented in the catalyst droplets. In step iv, the continuous supply of LaB_6 molecules into the droplets causes nuclei to

grow into a single crystal. In order to reduce the surface energy, the surface of the crystal prefers to end against the pre-formed CNT walls. In order to most closely match the circular cross-section of CNT, the LaB_6 crystal orient itself with its [111] direction parallel to the CNT axis so that it forms a hexagon with the (110) planes as the terminating surfaces. The lattice orientation of the crystal is also shown in the figure. Lastly, as shown in step v, with the continuous supply of LaB_6 molecules from the atmosphere and C molecules diffused from the stainless steel substrate, this LaB_6-in-CNT nanocable structure keeps growing till either of the material supplies is terminated. When C is absent in the catalyst, there will be no CNT formed and therefore will not provide a template to guide the [111] orientation of the LaB_6 crystal. In this case, [001] will still be the more favored growth direction to achieve surface energy minimization.

The quantitative thermodynamic analysis is difficult due to the lack of measurement of the parameters. The equations developed in the VLS section should be still applicable in this model. The only modification that has to be made is the surface energy of the LaB_6 nucleus. In this case, since the crystal is wrapped with a graphitic layer, no solid-gas interface exists. We should expect a even lower surface energy than the already reduced one in the VLS case. This reduction in surface energy is also valid in the 2D growth. Therefore, not only would we expect a higher nucleation rate, but also a much higher growth rate. Nucleation in this case, both in the initial nucleation period and in the subsequent 2-D growth period, is heterogeneous. Had been terminated with its (100) planes, the LaB_6 core could have had more solid-gas interface due to the morphology mismatch. The fact that the LaB_6 nanowires terminate their surface with (110) planes which have surface energy double that of (100) suggests that the interfacial energy between LaB_6 core and C coating should be less than half of that between solid-gas interface. This observation justified our surface energy reduction value of more than 50%

in the estimation of the VLS nucleation estimation.

3.5. Summary and Conclusions

In this chapter, we used a thermodynamic theory to analyze semi-quantitively the growth process of the LaB_6 nanowires. Three mechanisms have been proposed for three different types of growth: the vapor-solid (VS) growth model, the vapor-liquid-solid (VLS) model and the VLS-carbon nanotube-assisted growth model. Experimental parameters were used to find the vapor pressure of LaB_6. Then this vapor pressure was used to compare with the equilibrium vapor pressure at the reaction temperature, in order to find the supersaturation value. After knowing the driving force, supersaturation, homogenous nucleation and 2-D heterogeneous nucleation were evaluated separately to match with the experimental observations. It was found that the 2D nucleation accounts for both nucleus formation and growth in the VS model. In the other two models, however, the presence of catalyst droplets was found to reduce the surface energy for nucleation, therefore homogeneous nucleation is highly possible in the VLS model even its final supersaturation is at least one order of magnitude lower. In the VLS-CNT assisted growth, the surface energy was further reduced due to the presence of the carbon wrapping layer. The pre-formed CNT also serves as the nucleation substrate for the LaB_6 precipitation and thus indures heterogeneous nucleation.

An important conclusion is that the employed parameters in our experiment provide a sufficient driving force to grow LaB_6 nanowires without the assistance of catalysts. However, the presence of C or Fe as a catalyst will enhance the growth by orders of magnitude in growth rate. This is mainly due to the reduction of surface energy due to catalyst.

REFERENCES

Brenner, S. S. & Sears, G. W. (1956). Mechanism of whisker growth-III Nature of growth sites. Acta metallurgica, 4(x), 268-270.

Chervonnyi, A. D. & Chervonnaya, N. A. (2004). Thermodynamic properties of lanthanum chlorides. Inorganic Materials, 40(10), 1249-1257.

Dai, Z. R., Pan, Z. W., & Wang, Z. L. (2003). Novel nanostructures of functional oxides synthesized by thermal evaporation. Advanced Functional Materials, 13(1), 9-24.

Hook, A. V. (1963). Crystallization theory and practice. New York: Reinhold Publishing Corporation.

Iijima, S. (1991). Helical microtubules of graphitic carbon. Nature, 354(6348), 56-5.

Kikkawa, J., Ohno, Y., & Takeda, S. (2005). Growth rate of silicon nanowires. Applied Physics Letters, 86, 123109.

Levitt, A. P. (1970). Whisker technology. New York: Wiley-Interscience.

Liu, Q. X., Wang, C. X., Xu, N. S., & Yang, G. W. (2005). Nanowire formation during catalyst assisted chemical vapor deposition. Physical Review B, 72, 085417.

Massalski, T. B., Murray, J. L., Bennett, L. H., & Baker, H. (1986). Binary alloy phase Diagrams. Ohio: American Society for Metals**.**

Nordine, P., Weber, J. K. R., Krishnan, S., & Schiffman, A. (1991). The vapor pressure and sublimation enthalpy of pure boron. High Temperature Science, 30(x), 163-171.

Peshev, P. (2000). A thermodynamic estimation of the chemical vapor deposition of some borides. Journal of Solid State Chemistry, 154, 157-161.

Rao, C. N. R., Deepak, F. L., Gundiah, G., & Govindaraj, A. (2003). Inorganic nanowires. Progress in Solid State Chemistry, 31, 5-147.

Sears, G. W. (1955). A growth mechanism for mercury whiskers. Acta Metallurgica, 3(x), 361-369.

Swalin, R. A. (1972). Thermodynamics of solids. New York: Wiley-Interscience.

Tan, T. Y., Li, N., & Gosele, U. (2003). Is there a thermodynamic size limit of nanowires grown by the vapor-liquid-solid process? Applied Physics Letters, 83(6), 1199-1201.

Tan, T. Y., Li, N., & Gosele, U. (2004). On the thermodynamic size limit of nanowires grown by the vapor-liquid-solid process. Applied Physics A, 78, 519-526.

Uijttewaal, M. A., de Wijs, G. A., & de Groot, R. A. (2006). Ab initio and work function and surface energy anisotropy of LaB_6. Journal of Physical Chemistry B, 110, 18459-18465.

Wagner, R. S. & Ellis, W. C. (1964). Vapor-liquid-solid mechanism of single crystal growth. Applied Physics Letters, 4(5), 89-90.

Wagner, R. S. & Treuting, R. G. (1961). Morphology and growth mechanism of silicon ribbons. Journal of Applied Physics, 32, 2490-2491.

Westwater, J., Gosain, D. P., Tomiya, S., Usui, S., & Ruda, H. (1997). Growth of silicon nanowires via gold/silane vapor-liquid-solid reaction. Journal of Vacuum Science and Technology B, 15(3), 554-557.

Xia, Y., Yang, P., Sun, Y., Wu, Y., Mayers, B., Gates, B., Yin, Y., Kim, F., & Yan, H. (2003). One-dimensional nanostrucutures: synthesis, characterization, and applications. Advanced Materials, 15(5), 353-389.

Yang, Y. H., Wu, S. J., Chiu, H. S., Lin, P. I., & Chen, Y. T. (2004). Catalytic growth of silicon nanowires assisted by laser ablation. Journal of Physical Chemistry B, 108, 846-852.

Yao, B. D., Chan, Y. F., & Wang, N. (2002). Formation of ZnO nanostructures by a simple way of thermal evaporation. Applied Physics Letters, 81(4), 757-759.

Zhang, H., Li, J. X., Jin, A. Z., & Zhang, Z. (2001). Dependence of morphology of SiO_x nanowires on the supersaturation of Au-Si alloy liquid droplets formed on the Au-coated Si Substrate. Chinese Physics Letters, 18(11), 1529-1834.

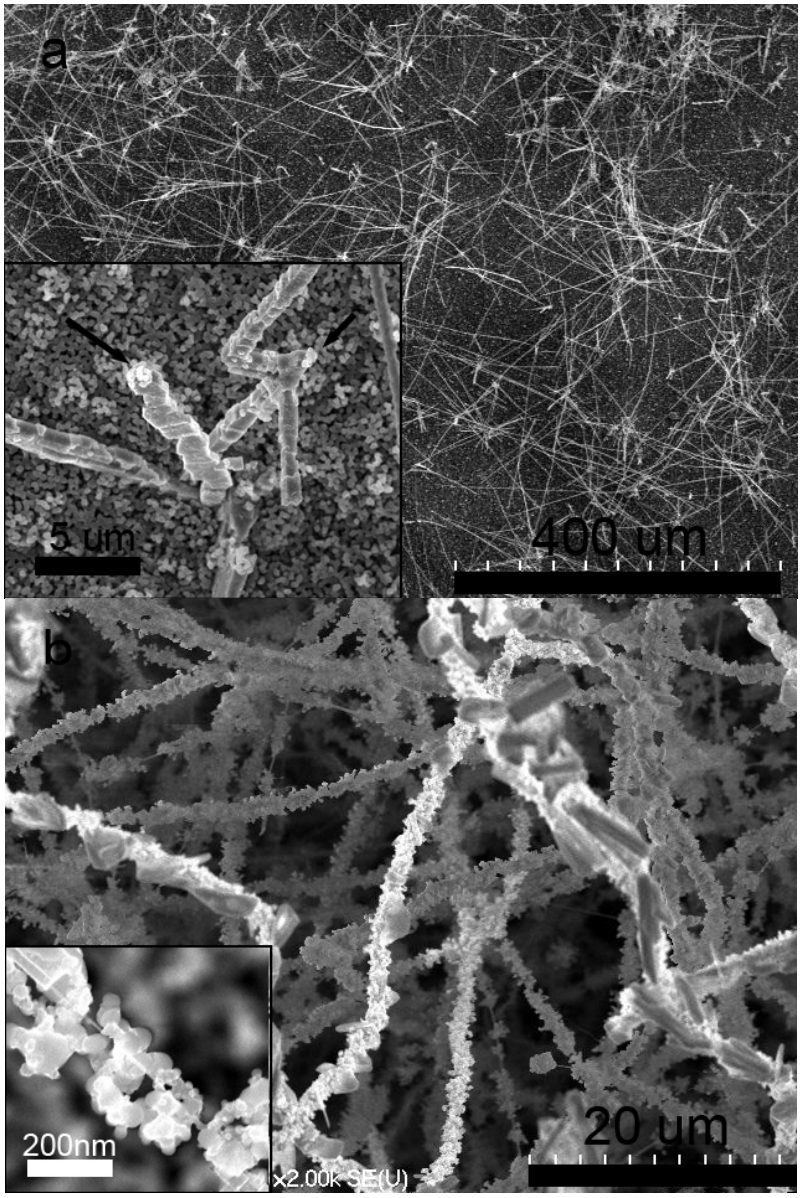

Figure 3.1. a) SEM image at lower part of a Pt coated silicon substrate, on which LaB_6 whiskers were found evenly distributed. Lengths of the whiskers are around 400 μm and diameters are around 1 μm. Change of growth direction of one whisker is shown in the inset; b) Particle wrapped LaB_6 nanowires on the upper part of the substrate. With an average length about 50 nm, the 20 nm-thin nanowires can be seen through the particle layer as shown in the inset.

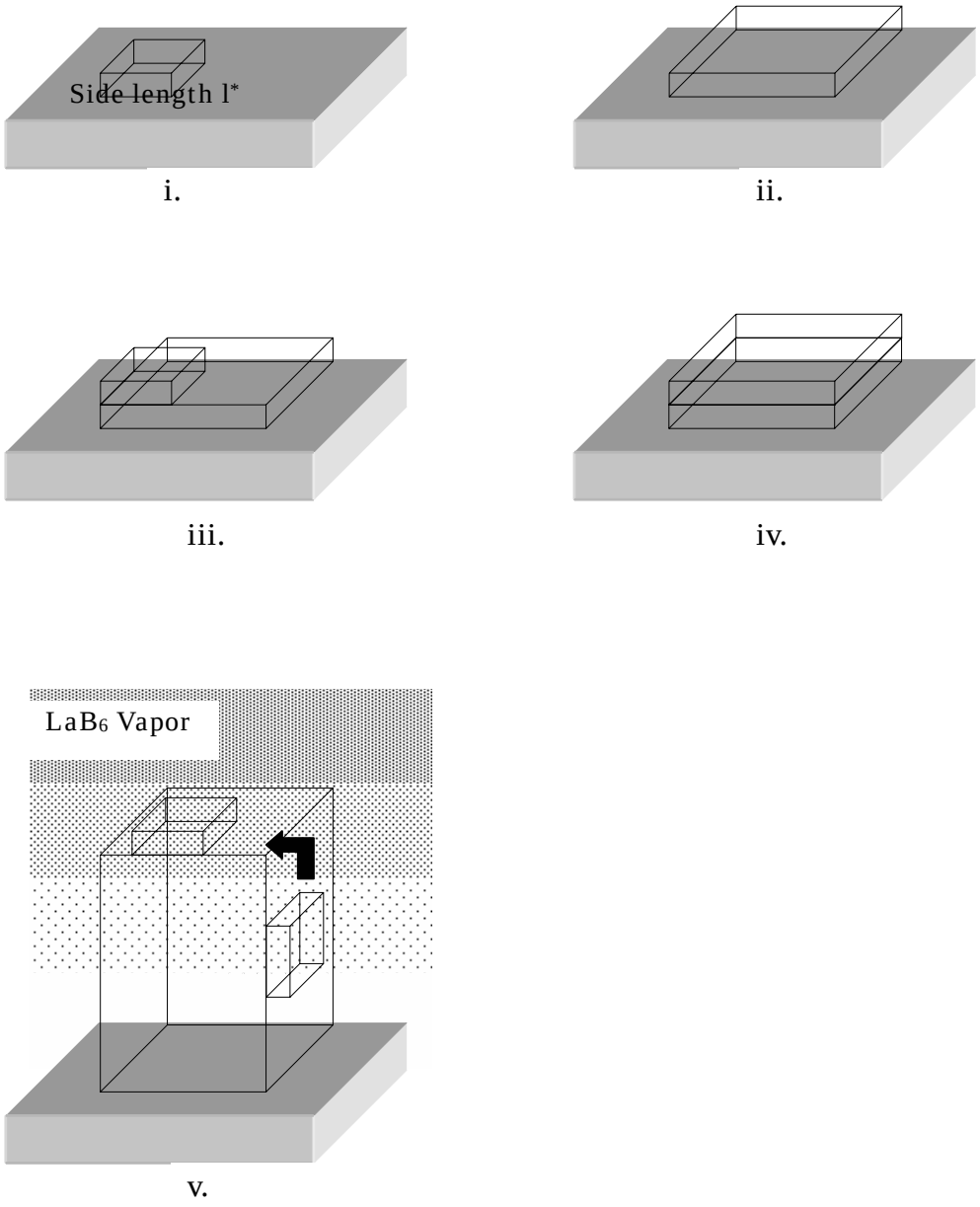

Figure 3.2. Illustration showing the vapor-solid growth process of LaB_6 nanowires. Step i, a monolayer of LaB_6 with critical side length l^* nucleates on the substrate; step ii, the nucleus grows into 2 dimensions till it reaches a certain size; step iii, second monolayer nucleates on top of the grown layer. Its side length is also l^*; step iv, the second nucleus undergoes 2-D growth till it reaches the size of the layer underneath; v, vertical LaB_6 vapor gradient drives the 1-D growth of the nanowire. Growth on the side walls is suppressed of its lower vapor density, which results in a lower nucleation rate.

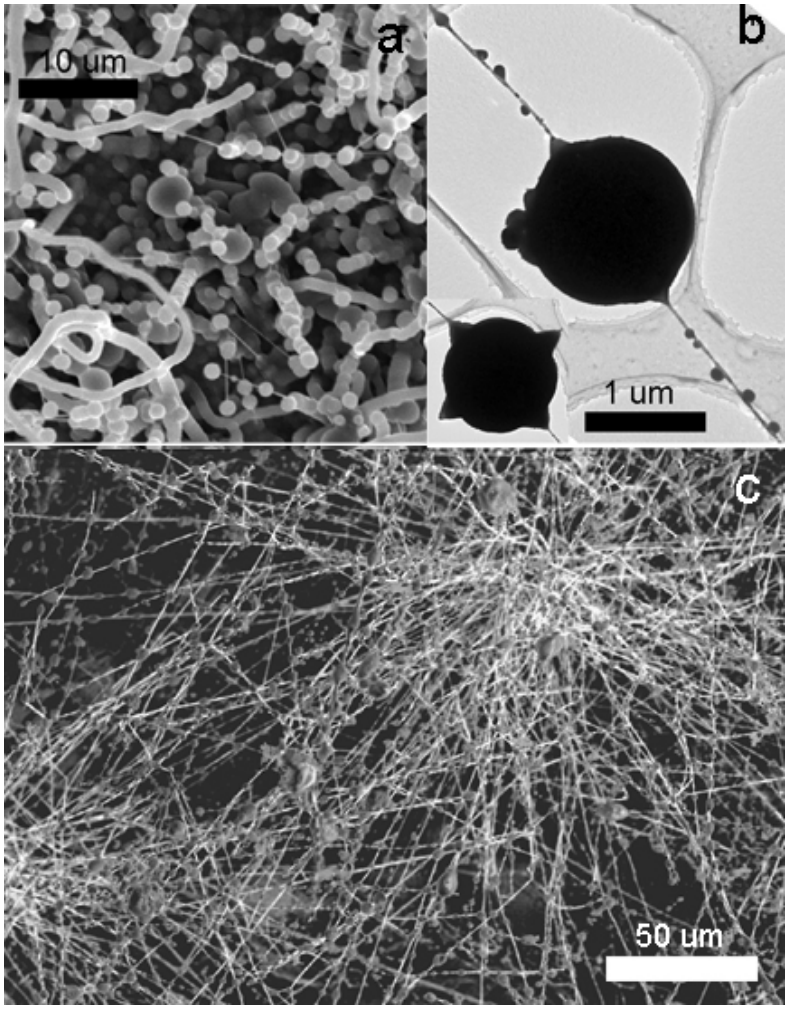

Figure 3.3. a) SEM image of CeB_6 nanowires grown on Pt coated Si substrate. Smooth surfaced melt-looking substance and spherical particles are seen around the nanowires; b) TEM image of the CeB_6 nanowires. Diameter increase at the nanowire/catalyst ball intercept area indicates it is the growth sites; c) Over 200 μm long LaB_6 nanowires with similar morphology grown on Pt coated Si substrate. Over 300 nanowires are grown from the same center in radial directions.

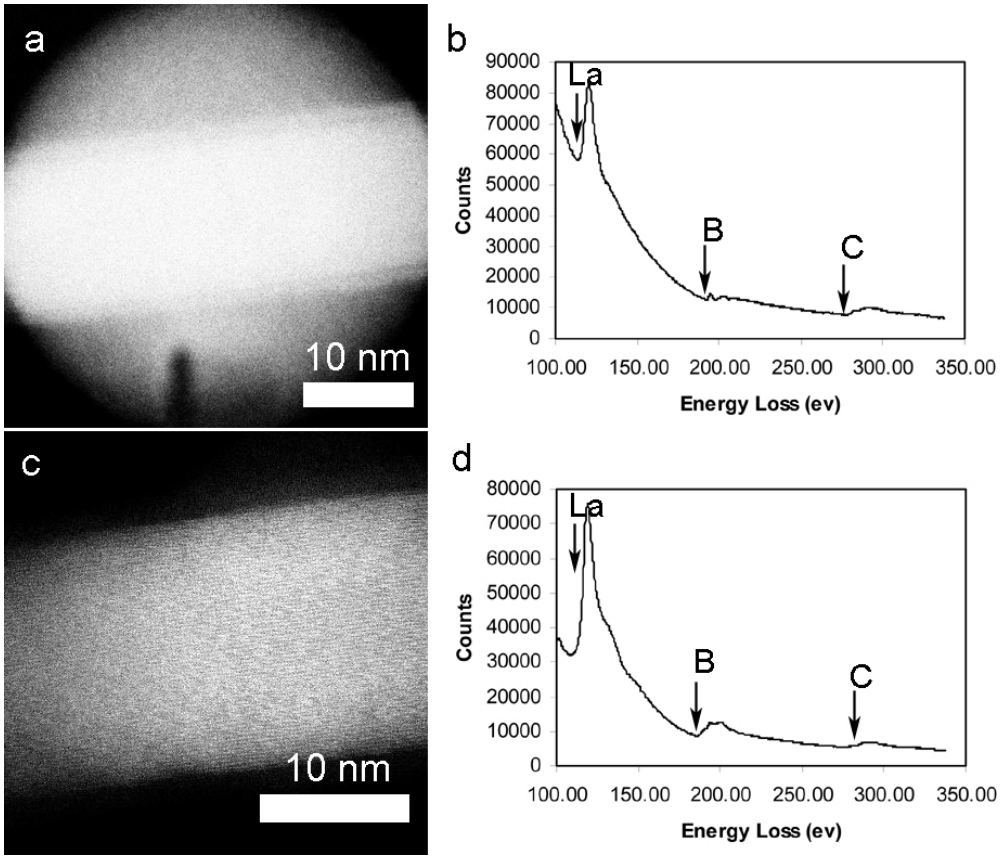

Figure 3.4. a) STEM image of a catalyst ball with LaB_6 nanowire passing through. The nanowire is about 200 nm in diameter and the catalyst particle is about 400 nm in diameter; b) EELS spectrum taken from the catalyst ball shown in a, at the site left with a hole caused by radiation damage. La, B and C elements are detected; c) STEM image of the body of a LaB_6 nanowire. Very light contrast shell can be seen at the edges; d) EELS spectrum taken from the nanowire body shown in c. Much higher La and B peaks are obtained with reduced intensity from C.

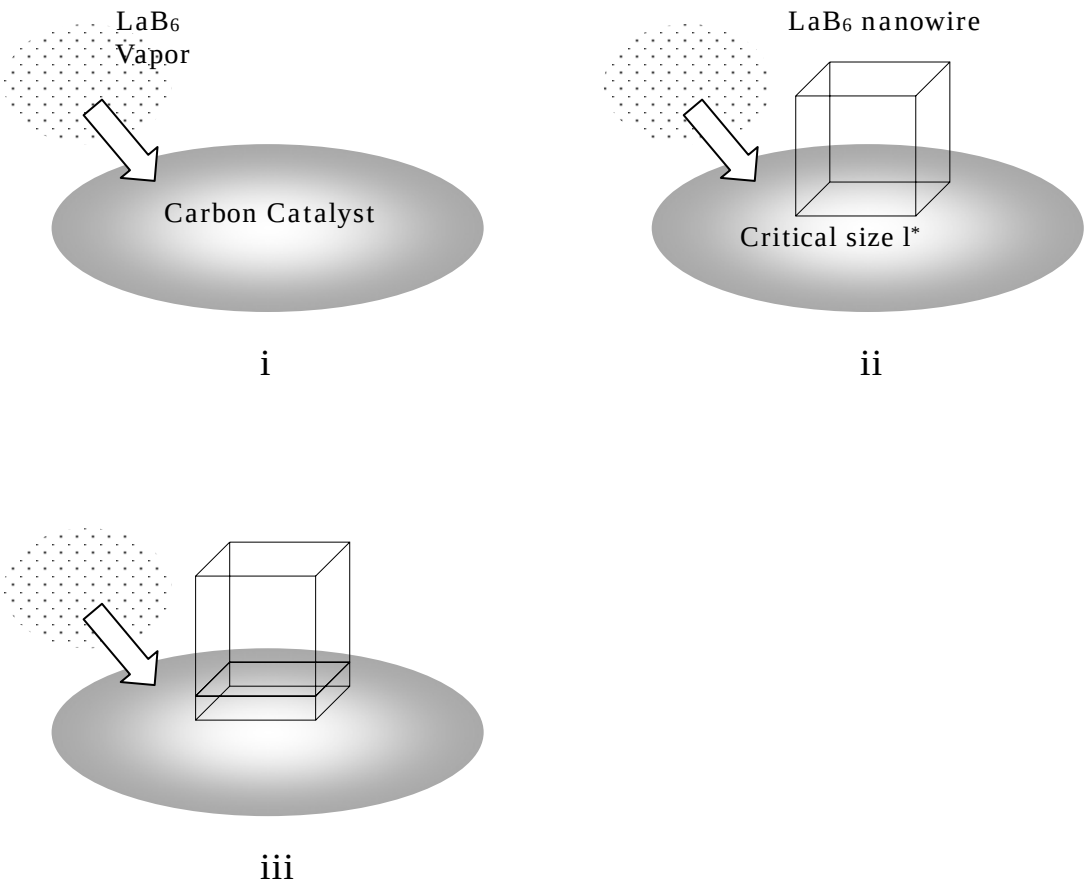

Figure 3.5. Illustration showing vapor-liquid-solid growth mechanism of LaB_6 nanowires. Step i, C and LaB_6 form alloy liquid at temperature above 1400 K. LaB_6 vapor keeps dissolving into the catalyst droplet; step ii, after the LaB_6 concentration inside the alloy liquid reaches certain supersaturation, homogeneous nucleation occurs with a critical side length l^*; step iii, 2-D monolayer nucleation and growth take place at the nucleus/liquid interface. With the continuous LaB_6 supply from vapor and the monolayer-by-monolayer growth, 1-D nanowire growth is achieved.

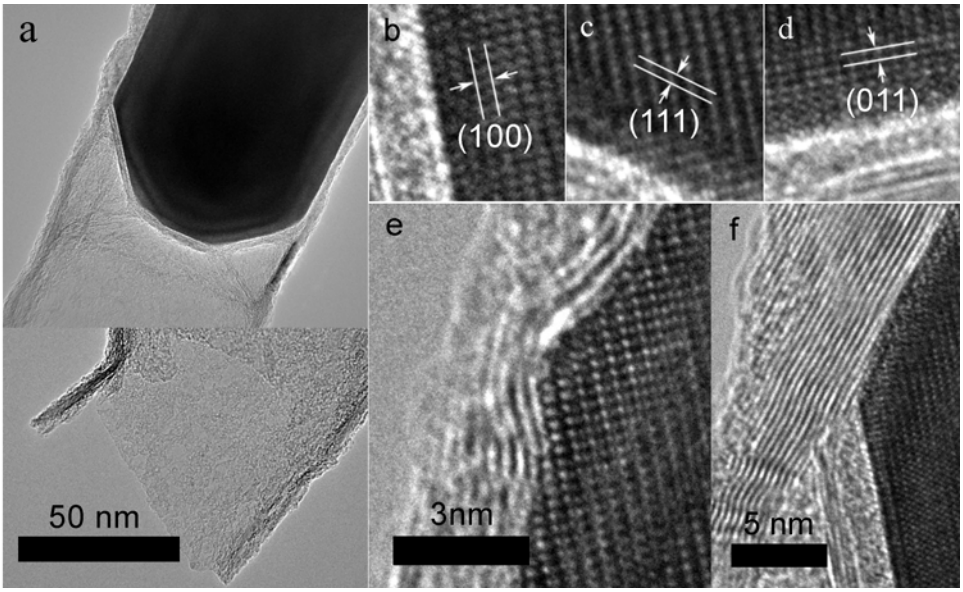

Figure 3.6. a) Low magnification TEM image showing the crystalline LaB_6 core and an open-ended MWCNT wrapping outside. The hollow part of the tube is about 5 μm long. Only the end of it is presented in the lower part of a; b) to d) The three facets terminating the LaB_6 core in a. They are low index planes of (100), (111) and (011) respectively; e) a hump on the nanowire wall showing the actual terminating facet of (100) plane, though the nanowire axial direction is <111> in this case; f) splitting of the MWCNT at the tip of the LaB_6 single crystal core.

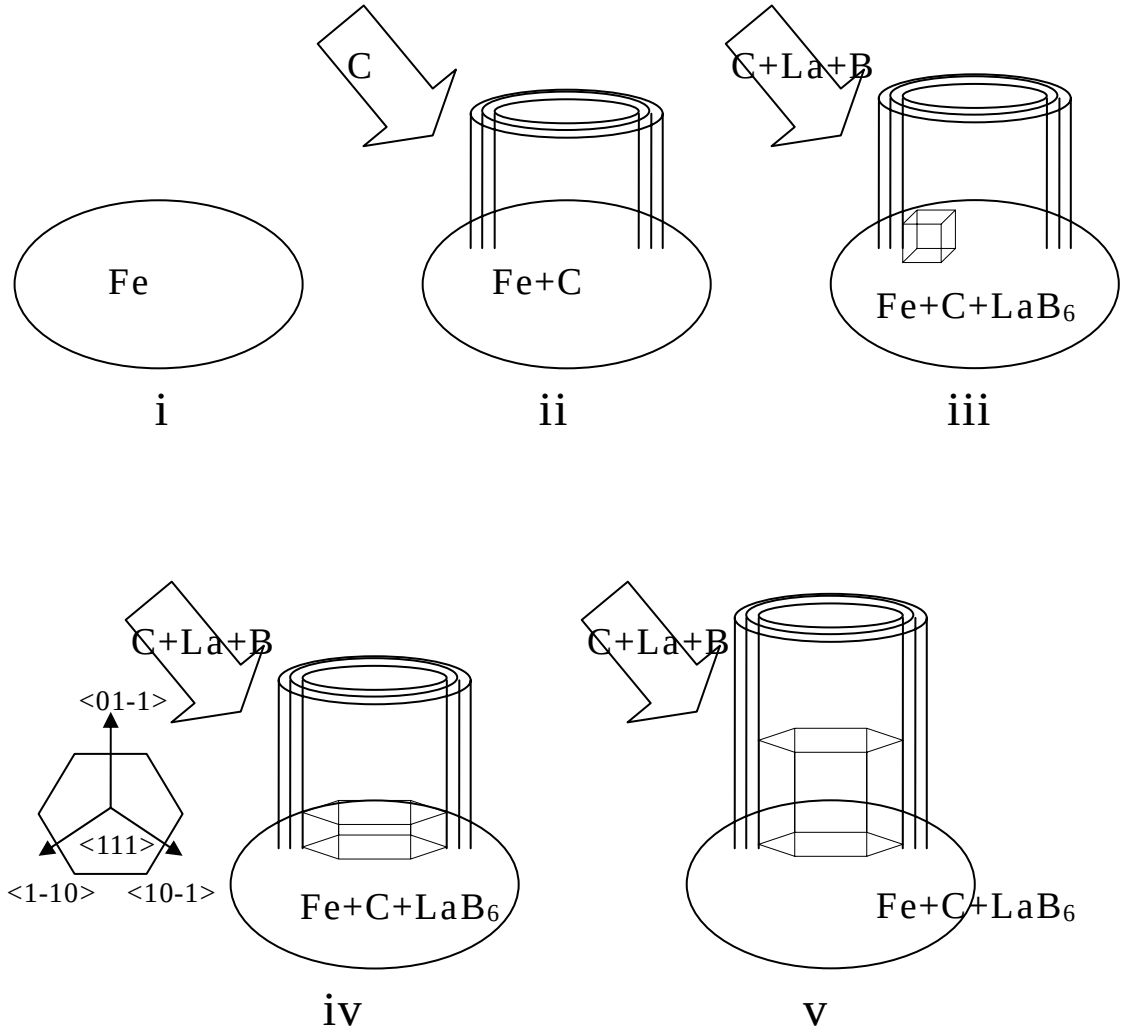

Figure 3.7. Illustration showing the VLS-CNT assisted template growth of LaB_6/CNT nanocable. Step i, Fe catalyst ball is formed on the substrate surface; step ii, diffusion of C into the Fe catalyst ball induces supersaturation and eventually leads to the growth of MWCNT; step iii, LaB_6 vapor dissolves into the Fe/C catalyst droplet. After reaching supersaturation, LaB_6 3D heterogeneous nucleus forms on the wall of MWCNT at the liquid-solid interface; step iv, to closely match the circular shape of the MWCNT template, the LaB_6 single crystal reorient itself into <111> direction vertically and has {110} planes as terminating faces; step v, continuous supply of LaB_6 from vapor phase maintains a 2D nucleation and growth process. The nanowire grows along with the growth of MWCNT with continuous C deposition.

Chapter 4 Nanotube/Nanowire Field Emission

4.1. Introduction

4.1.1. Background

4.1.1.1. NT/NW Field Emission Theory

Emission of electrons is essentially a process of free electrons in a solid escaping from the surface to enter the vacuum. Therefore, the electronic structure of the solid determines the processes. When groups of atoms condensed into solids, their electron cloud overlaps with each other and forms a series of electron energy bands. Electrons located in a band which is not fully occupied are free electrons and those free electrons are the cause of electric current related phenomena, including electron emission. We call the average energy of these free electrons the Fermi energy and the corresponding energy level, the Fermi level. In a metal, we always have bands that are partially occupied while in an insulator, all energy bands are fully occupied. In semiconductors, all energy bands are originally fully occupied. However, excitations by thermal power or the insertions of an impurity energy level, always cause some electrons to upgrade their band locations and create partially occupied bands, thus also, free electrons. Fermi level of Metal is usually 2-5 eV lower than the vacuum level, we call this energy difference the work function. Though an insulator does not have free electrons, the bottom of the energy band next to its last full band is very close to vacuum level and sometimes even higher. We call that energy distance, electron affinity, which is an analog to work function in the case of metal and semiconductor.

For a metal, the above mentioned energy difference between the Fermi level and

the vacuum level forms the energy barrier that a free electron has to overcome so as to escape from the metal surface. Figure 4.1 is electron energy diagram of a metal/vacuum interface. As Figure 4.1a shows, before applying any external potential, the interface between the metal and vacuum is abrupt and the work function is denoted as Φ. After a negative external potential is added on the metal side, a linear potential drop is formed and thus forms as well an energy barrier with a sharp corner, as Figure 4.1b shows. The barrier height is Φ and its width x equals Φ/Ee, where E is the external field strength and e is the electron charge. At the same time, another energy term, V_{img}, the image potential, is caused by polarization of the metal surface due to the external field and this can be expressed as $V_{img} = -e^2/4x$. Its effect is the rounding of the sharp corner of the original potential barrier and reducing its width as well. The effect is only minor and the exact reduction in barrier height and width is hard to give as exact. This is shown graphically in Figure 4.1c. (Gomer, 1961)

Based on the picture described above, Fowler and Nordheim derived the classical Fowler-Nordheim (F-N) formula, which describes the determination of field emission current density J at a local electric field strength E and emitter work function $\boldsymbol{\Phi}$. (Fowler & Nordheim, 1928) When taking the units of J, E and Φ conventionally in A/cm^2, V/cm and eV respectively, the formula is written as

$$J = 6.2\times10^{-6}\frac{\sqrt{\mu}}{(\mu+\phi)\sqrt{\phi}}E^2\cdot\exp(-6.8\times10^7\frac{\phi^{1.5}}{E})A/cm^2 \qquad (4.1)$$

with μ being the Fermi energy of the free electrons. For metals we commonly deal with, μ is around 5 eV, $\boldsymbol{\Phi}$is around 5 eV. A rough estimation from the F-N formula shows that a field with strength at the order of 3-6X10^7 V/cm will extract a current density of 10^2-10^3 A/cm^2. This result agrees with the experimental data. A big uncertainty here is the determination of the local field strength, which could vary a lot due to complexities in

geometric factors such as the surface roughness. The value of work function value could also be tricky to use in this formula, since the value could be different even from the same emission area due to adsorptions. A more commonly used way to judge if the set of field emission data agree with the F-N formula is to compare with F-N plot. Before doing that, the external applied voltage V and the field enhancement factor β are used to substitute the electric field strength E with the relation E = βV. The formula can then be written as:

$$\frac{I}{V^2} = A \cdot 6.2 \times 10^{-6} \frac{\sqrt{\mu}}{(\mu+\phi)\sqrt{\phi}} \beta^2 \cdot \exp(-6.8 \times 10^7 \frac{\phi^{1.5}}{V\beta}). \qquad (4.2)$$

After taking a natural logarithm on both sides, we obtain

$$\ln(\frac{I}{V^2}) = \ln[A \cdot 6.2 \times 10^{-6} \frac{\sqrt{\mu}}{(\mu+\phi)\sqrt{\phi}} \beta^2] - 6.8 \times 10^7 \frac{\phi^{1.5}}{\beta} \cdot \frac{1}{V} \quad (4.3)$$

Therefore a linear relation between the quantities $ln(I/V^2)$ and 1/V are expected. From the slope, one quantity between β and $\boldsymbol{\Phi}$ is also extractable after knowing the other from different measurements. Eventually, the emission area A can also be deduced from the y-intercept of the F-N plot. The above formula does not take into account the image effect on the current density, since the effect is minor.

The formula neglects the influence of temperature, so it should be only valid at T=0 strictly speaking. However, as long as T is within a normal range, which is to say μ>>kT, it works as well for field emission under moderate temperatures. From the F-N formula, the energy distribution in the applied field direction can also be calculated. Let E be the kinetic energy of the electron, △ be the energy difference between the Fermi energy and the kinetic energy of the electron, the energy distribution density, I(E)dE is then

$$I(E)dE = 16P \cdot im\{\Delta \frac{\sqrt{E(\phi+\Delta)}}{h^3(\phi+\mu)} \cdot \exp(-\frac{b(\phi+\Delta)^{1.5}}{F})\}dE \quad (\text{for E}<\boldsymbol{\mu}) \qquad (4.4)$$

$$I(E)dE = 16P \cdot im\{kT \frac{\sqrt{E(\phi+\Delta)} \cdot e^{\Delta/kT}}{h^3(\phi+\mu)} \cdot \exp(-\frac{b(\phi+\Delta)^{1.5}}{F})\}dE \quad (\text{for E} > \boldsymbol{\mu}) \qquad (4.5)$$

Where h is plank constant and b is a constant. From the above formula, it is clearly seen that as F (electric field strength) becomes stronger, the energy distribution is broadened. The absolute value of the Fermi level μ only slightly affects the distribution. However, the width of the distribution broadening is strongly dependent on the values of Δ and $\boldsymbol{\phi}$, which both decide the tunneling barrier dimensions.

Applying a negative potential at the semiconductor surface results in the whole band structure being bent down and this effect is illustrated in Figure 4.2. The Fermi level which is originally located between the conduction band bottom and the valence band top therefore has a chance to sit above the conduction band now or still sits below it, if the bending is not strong enough. In the former case, as shown in Figure 4.2, the emission is just like in case of metal field emission and is independent from the temperature. In the latter case, however, thermal energy will still be needed to pump electrons from valence band into the conduction band to provide the 'electron pool' for field tunneling. The distribution of such electrons obeys Boltzman statistics and therefore strongly depends on temperature.

In order to achieve a current sufficiently large to be used in electron optical applications, the local electric field strength in the order of 10^7 V/cm is usually required. In reality, such a field strength is impractical to achieve just by applying an electric potential to a normal flat surface. Therefore, a sharp needle shaped metal is usually used to generate an intensified local electric field at its tip apex when an electric potential at the order of 3000 V is applied. If we define an external field $E_{external}$ as a spatial average of the applied potential, V/d, with d being the distance between the emitter tip to the anode, β, the enhancement factor is then the ratio of actual local electric field divided by

this average applied field, $E_{local}/E_{external}$. For normal metal emitters, the value of β is usually considered as a constant and is only determined by the geometry of its tip apex, such as the radius of curvature. A commonly accepted empirical form is $\beta = 1/kr$, with k being a number around 5 (Brodie & Spindt, 1992). Therefore, using nanometric sized emitter tips is of great advantage to obtain a higher emission current density under the same applied field. The recent discovery of carbon nanotubes and one-dimensional nanowires of other materials make people believe that their extremely sharp tips and long aspect ratios are advantageous in field emission applications. The most extensively studied subject is the cold field emission from carbon nanotubes.

Carbon nanotubes can be as small as about 1 nm in diameter. A single walled carbon nanotube (SWCNT) is only composed of one single layer of carbon atoms. It is hollow in the middle and can be either terminated with a closed cap or open tube structure. In either case, there are only a few atoms at the tip apex and they contribute the most to field emission current. However, the general F-N theory was formulated to describe electron tunneling from bulk metal surfaces, in a relatively much more uniform electric field. Experimental results do show that some emission features from CNT, especially SWCNTs can not be explained by the F-N theory. These deviations include the non-linearity of F-N plot and an emission current saturation under high electric field (Han, Lee, & Ihm, 2002). Though there is no generally applicable theory to describe the detail emission from CNTs, in other words, the picture is still unclear, there has a considerable amount of theoretical work been done to address this issue. The following points have been proposed: Buldum and Lu proposed that the local electric field is distributed with a large variation on the nanotube cap and this distribution also changes with externally applied electric field (Buldum & Lu, 2003); Zheng et al. suggested that the strong field penetration at the CNT cap region is responsible for the lowering of tunneling barrier

(Zheng, Chen, Li, Deng, & Xu, 2004); Liang *et al*. compared the behavior of metallic and semiconducting CNTs and concluded that, due to the band structure changes, the emission current density of a semiconducting CNT actually increases with the increase of tube diameter. This is opposite to what the F-N theory predicts (Liang, Huang, Deng, & Xu, 2004); Han *et al*. proposed that the CNT has some localized states at the cap region which contributes 10 times more electron current than the extended graphite states (Han & Ihm, 2002).

For multi-walled nanotubes (MWCNT) or nanowires of relatively larger diameters (>10 nm), the emission current characteristics usually agree quite well with the F-N formula, due to their similarities to bulk crystals. This type of consistency is usually evidenced by the good linearity of the F-N plot. Though in such cases, the field enhancement factor β seems to be constant being given a certain experimental set-up, its exact value and dependence on the specific geometry parameters still remain unclear. Some formulas have been determined empirically through experiments where a set of F-N plots was recorded while changing parameters like the cathode-anode distance, nanotube length and diameters (Bonard, Dean, Coll, & Klinke, 2002; Xu, Bai, & Wang, 2006). However, these formulas seem to be limited within a small range of cathode-anode configurations and parameters. A more commonly applied approach to determine β is to use numerical simulations according to a certain experimental set-up and nanowire emitter geometry.

4.1.1.2. Previous Studies

Aside from theoretical studies of NT/NW field emission, experimental examinations have been carried out to offer a large amount of knowledge about using NT/NW as field electron emitters. Nanowires including Si, SiC, ZnO, Co, TiO_2, W, MoO_3

and many others have been demonstrated to have good field emission properties under low extraction voltages (Chueh et al., 2005; Wong et al., 1999; Li et al. 2004; Vila et al.,, 2004; Wu et al., 2005; Lee et al., 2002; Li et al., 2002). Noting that a lot of these materials, especially oxides, are not considered as good candidate for field electron emission in their bulk forms, however, do give surprisingly good I-V curves when the size comes down to the nano-scale. The huge field enhancement at the sharp tip could be the reason to overcome its high work function barrier and surface states could contribute more to the electron conductance, which compensates the insulating nature of its body. Among all the one-dimensional field emission structures tested so far, CNT still attracted the most attention in the field. Its field emission properties have been systematically studied (Bonard et al., 1999; de Jonge & Bonard, 2004). The following issues have been carefully addressed: the field enhancement factor (Peng *et al*., 2006), shape of the emission beam (Dean *et al*., 1999I), emission stability (Dean & Chalamala, 1999II), emitter failure (Bonard & Klinke, 2003) and energy spread (Groning *et al*., 2000).

CNT has many forms that differed both in size and in its cap structure. A SWCNT can be as thin as below 1 nm, while a MWCNT can be grown in the range of tens of nanometers. SWCNT has only a few atoms at its apex and is a natural atomically sharp needle. Its enormous field enhancement effect is the very reason to attract people into the field emission studies of this kind of material. Closed-capped MWCNTs are found to start emission at a much lower voltage than expected from an enhancement factor calculated directly from its geometry. It is proposed that adsorbates or local small protrusions may always exist on its cap surface and therefore enhance the field more than a clean smooth cap. Open-capped MWCNTs are expected to have more efficiency in field induced emission compared to their closed-capped counterpart. This is expected because the open edges of the nanotube have more local protrusions for field amplification. However,

opposite phenomena are always observed in experiments: twice as much extraction voltage is usually needed for open tubes than for closed ones. It again indicates that the actual emitting sites are not atoms on a smooth hemisphere surface as would be expected in an ideal model.

By recording the field emission patterns with a multi-channel plate and phosphor screen, the deviation of the emission from an ideal perfect structure is more clearly shown. For open-capped tubes, multiple bright spots in the field emission pattern are usually observed. These spots sometimes appear as rings as expected from the dangling atoms on the edge of an open tube structure. However, patterns of other structures were also observed quite often. For a closed-capped tube, though the presence of only one bright spot is observed, the spot changes with time and eventually becomes much dimmer and flattened out when the tube is heated to desorb surface molecules. Emission current dropped four times compared to when it started. The speculation is that the emission is an adsorbate-type, though the local protrusions are also a possible mechanism. The results in part explained the lower turn-on voltage of CNTs than the calculated value directly through the F-N formula and emphasized the importance in obtaining clean emitter tube surface for good stability.

Field emission stability is always a most important factor in determining if the emitter can be used in a practical field emission device. It can be directly measured by recording the emission current with the elapse of time or recording the applied voltage to keep a certain value of emission current. Stability studies under a high vacuum, 10^{-7} mbar, show the following chracteristics: emission from SWCNT films is not stable and loses its emission current gradually as emission continues. SEM examinations before and after the emission test shows a significant reduction in film density. It is likely due to the ion bombardment damage on the layer of carbon atoms of SWCNTs at such a vacuum level.

Closed-capped MWCNT films are better option to offer stable emission. For the same type of CNT, either single nanotube form or film, it is always observed that the emission current density also affects the stability of the emitter. At low current densities, emission is stable with some low amplitude noise. When emission current density is raised to the medium range, current steps which fluctuate more than 10% are observed. The best stability is obtained after the current goes to high values, although catastrophic breakdowns usually follow after a short span of time, depending on the specific emitter structure. The phenomena could be explained as follows: under a low current density, it is an adsorbate-emission type. Field emission is actually from the local absorbed molecules on the nanotube top surface. Under the median emission, desorption and absorption occur at the same time. Absorption leads to localized large field amplification and as a result, higher emission current. Desorption on the other hand, causes a loss of local protrusions and damping of emission current. The switching between these two mechanisms causes large current fluctuations. When the emitter is operated at high current, however, the joule heating caused by the emission current keeps the emitter tip clean so that a stable emission is obtained. The catastrophic breakdown of the emitter is likely due to the ion bombardment damage to the emitter body. Good stability is also observed when an emitter temperature of about 600 ^{o}C is maintained by a heating unit during emission. Operating the emitter at a ultra high vacuum with base pressure less than 10^{-9} torr, is helpful in getting stable emission current (de Jonge *et al*., 2003). Current drifts lower than 0.5% were observed for a single CNT during an hour of continuous emission. The emission current was set at 190 nA, the emitter temperature was set at 500 ^{o}C and the vacuum level was 10^{-10} torr.

Generally speaking, field emitters running at poor vacuum environment and high emission current are subjected to more damage from chemical *et al*hing or sputtering,

thus usually have a shorter service life. The limit of a safe operation current is different from emitter to emitter. It is found that the type of gas residues has very different effects on the emitters' destruction. For example, a CNT emitter keeps an emission current of 1 uA without much degradation when working under H_2O gas for any pressure lower than 10^{-6} torr. The H_2O gas is also believed to restore a certain surface state which is the origin of CNT field emission. H_2 gas of 10^{-6} torr seems to have little effect on the operation of the same nanotube emitter. No obvious degradation was observed after running the same emitter for more than 40 hours under 10^{-7} torr of Ar. However, the same pressure of O_2 gas made the emission current drop by more than 75% at a time span of 48 hours. Rapid non-recoverable decrease in emission current still occurs even running the same emitter under 10^{-8} torr of O_2 residue gas. The conclusion is that the CNT emitter behaves differently from the regular W metal based emitters. For W metal emitters, bombardment from light ions such as hydrogen, usually causes ion enhanced protrusion growth on the emitter apex; bombardment from heavy ions like Ar, usually causes blunting of the tip. Neither of these two was observed with the CNT emitter and it is very likely due to the stronger co-valence bonds between C atoms than the metallic bonds in W. Oxygen ion bombardment could cause chemical *et al*hing on the surface and eventually destruct the CNT emitter.

Energy spread of the emitted electrons is an important quantity. For applications in high resolution electron optical instruments, energy spread causes chromatic aberrations, and therefore limits the ultimate resolution. For energy resolved spectrometry, the narrower distribution of the electron probe energy is directly desired. Highly coherent electron beam with narrower energy spread is the basis of phase interference techniques, such as electron holography. Energy spread can be deduced from F-N theory. By combining the energy spectrum and I-V curves, one can obtain the true work function of

the emitter. For such a study, a value around 5ev was extrapolated for CNT field emitters. The energy spread of the CNT emitter is found to be only half of the value of typical metal emitters. The origin of this low energy spread is believed to be that electrons tunneled from a localized surface state on the CNT apex, not directly from the body states. Similar lowering of the energy spread was also found in W nanotip emitters, where the surface state is dominant.

Though these studies were all based on the CNT emitters, several of the key issues are generally applicable to the nanostructure field emitters. The results and properties obtained are to some extent shared with other refractory non-metal NT/NW emitters, such as the response to ion bombardment, lower energy spread and contamination induced current fluctuations.

4.1.2. Motivation

4.1.2.1. Fundamental Properties and Device Applications

The phenomenon of electric field induced electron emission has been known to the world for almost a century. The emission mechanism is well understood and established for most of the encountered situations in real life. Device applications in microelectronics industry hold an unshakable position for its unique advantages over other electron emission mechanism (Fursey, 2005). However, the advancement in the emitter materials preparation always brings up new scenarios in which the old theories fail to explain or seem inadequate. On the other hand, the immergence of new emitters offers chances not only to enable better use of the present applications but also further its application in new areas of our life, which a lot of times are more significant. These opportunities demand better understanding of the mechanism and more knowledge about the properties of the new emitter materials' characteristics.

Conventional emitters are divided into two types. Type one is usually metal or semiconductor needles sharpened from their bulk forms through chemical *et al*hing. To further localize the electron emission site in order to get a more stable, angular confined and coherent beam, either a field build-up or low work function adsorbates are utilized to produce point emission. Its advantage is the ability to make atomically sharp tips and to produce a highly confined electron beam. The disadvantage is the difficulty in controlling the needle shape and therefore can only be used to construct single emitter structures. Type two is pyramid shaped emitter arrays fabricated through semiconductor processes. The materials can be a metal or semiconductor with dielectric material coatings. This type enables the application of field emission on a relatively large scale. But the sharpness of individual tips is hard to improve. Recent development in the chemical synthesis of one-dimensional nano-structures has offered new opportunities in search of nanowire emitter materials. Nanotubes and nanowires, grown through chemical methods on a large scale, naturally have nano-scale sharpness at their tip end. By making a nanotube/nanowire film, one can easily obtain field emitter arrays with individual tip sharpness comparable to or even better than the state-of-the-art type one emitter. Therefore, in principle, it combines the advantages from both type one and type two field emitters.

Current stability and emitter lifetime are the most important characteristics for a practical field emitter. Fundamental properties that affect the emitter stability and life time include: joule heating, ion sputtering, emission site, vacuum stringency, and surface absorption. The electric field enhancement factor β is also important since it determines the ease of operation in terms of the applied voltage (Gomer, 1961). However, the above listed properties are all material sensitive and emitter-geometry sensitive. Since nanotubes/nanowires have very different dimensions and geometry from the conventional

field emitters, their fundamental properties as field emitters must be studied in detail.

Joule heating is caused by the passing of emission current through the emitter body. Field emission usually generates a current density at the order of 10^7 A/cm^2. Because of small cross section of nanotubes/nanowires, joule heating could be very severe. Though the field emission itself is fairly stable with temperature variations, the emitter material might fail when temperature approaches its melting point. As the temperature increases, the mobility of the emitter tip goes up. Under a high electric field, atoms will start to build up into even sharper protrusions. The protrusion leads to an even higher localized electric field and higher emission current density, which in turn generates more joule heating. Eventually this accumulated effect results in the destruction of the emitter. Therefore, it is crucial to know the heat transportation property of the nanotube/nanowire emitter material, strength of bonding, its response to field build-up and electric resistivity. Ion bombardment is another cause of emission instability. The emitted electrons ionize the gas residues around the tip area and those ionized gas molecules could bombard the emitter tip due to static forces. The bonding strength of the emitter materials is therefore crucial in response to the ion bombardment. The consistency of emission sites on the tip top surface is also important, because current fluctuations and changes in electron coherence will occur if more than one spot on the tip top surface is emitting electrons. Field built-up and adsorbates both could be the cause of changing emission sites. The influences of the adsorbates on the emission properties are from two aspects. Some adsorbates can the lower work function of the emitter material on certain crystal planes. Zr absorped on W (100) plane is one of such examples. Adsorbates also form a localized protrusion, which greatly enhances the local electric field. In both cases, electron emissions are localized to the sites of adsorbate. Sometimes, two mechanisms work at the same time when field build-up occurs underneath the adsorbates due to

localized emission originally induced by the lowering of work function. The reactivity of the emitter materials with gas residues is especially important in determining the emission stability and life time. The emission crystal planes usually have the lowest work function and at the same time the highest reactivity with active gas residues, such as oxygen. Different materials therefore have different stringency for vacuum conditions. These are the determining factors for the manufacturing cost and put a limit on applications. Nanotubes/nanowires usually grow along their crystallographic axis and terminated with crystal planes determined by specific crystallographic features. Therefore, the geometries of different types of nanotubes/nanowires are quite different. This difference results in different electric field enhancement. Since the field enhancement affects directly the emission current density, this property should be addressed as well.

The unique features of field emission include: extremely high current density, instantaneous emission almost without any time delay, high temperature tolerance, compactness, high coherence and sensitive to vacuum conditions. Based on these features, the applications of field emission devices fall into two categories: single emitter point source and field emitter arrays. Point electron source is mainly used in electron optical and surface analysis instruments, which includes TEM, SEM, electron lithography system, and surface analyzer for example. In these applications, in order to achieve high spatial resolution, the brightness of the emission source is crucial. Field emission source can reach a brightness in the order of 10^9 A/cm^2*sr, which is two orders of magnitude higher than the thermionic LaB^6 source and 3 orders of magnitude higher than the thermionic W source. Such a high brightness enables the operator to achieve very a small electron probe, below 10 nm in diameter, but still with a sufficient beam intensity both for imaging and chemical composition analysis. The theoretical brightness limit of an electron source is defined by the Langmuir equation (Fursey, 2005):

$$B_{\max} = \frac{jeV}{\pi kT}, \qquad (4.6)$$

where j is the emission current density of the emitter. As shown by the F-N formula, j is dependent on the emitter tip geometry and its emission surface work function. Therefore, nanotubes/nanowires out of low work function material, such as LaB_6 will be highly suitable for such applications. Another use in electron optical systems is to use a highly coherent electron beam to form holograms of the object under observation. Electron holography can retrieve phase information about the object, which reflects magnetic field or electric field distribution around the object. For such applications and electron energy resolved analyzer, such as electron energy loss spectrometry (EELS), low energy spread, or in other word, high coherence of the emission source is required. The energy spread of field emission source is around 0.2-0.3 eV, which is only a tenth of that of a thermionic source. Recently, Dejonge has built a field emission point projection microscope with a single SWCNT as the field emitter and obtained a magnified image of a holey carbon film without the help of any lens (de Jonge, 2002). It is from this work that the field emission characteristics of the carbon nanotube were evaluated and were shown to be even better than the commercial field emission source based on tungsten needles. In a subsequent work, he also pointed out the importance in using nanotubes/nanowires of low work function in achieving a higher coherence of the electron beam (de Jonge, 2005). LaB_6 nanowires are therefore an excellent candidate for the purpose.

Besides electron optical applications, field emission is very useful in vacuum microelectronics. In these fields, more than one field emitter is needed to work with many others. So field emitter arrays are usually the desired configuration. Each emitter unit has a triode structure, where a well shaped control gate is used to extract electrons out of the cathode emitter and those electrons are accelerated and collected at an anode. Some examples are listed below.

Field emission flat panel display utilizes arrays of field emitters as the electron sources. Each emitter is individually addressable through a control matrix. By applying a negative potential between the emitter tip and its control anode gate, electrons are extracted out of the emitter and its trajectories strike a phosphor screen put in the front, thus produce images. Because of the compactness of the emitter structure, a high density packing is attainable. Each display pixel usually contains more than 1000 emitters. Such a layout is necessary not only to produce a high current, but also to get an overall even current between different pixels. Conventionally, the emitters are pyramid shaped Si or Mo tips fabricated through semiconductor processes. Vertically grown nanotubes/nanowires on a metal surface or nanotube/nanowire pasted films are also promising candidates as field emission arrays. Their advantage is having much sharper tips, capability of producing large area arrays and the low cost to manufacture. Recently, Choi, *et al*. have reported a full color field emission display based on pasted carbon nanotube film (Choi *et al*., 1999). Same type of nanotube/nanowire films can also be used as a cathode for x-ray generation in a micro-CT device (Yue *et al*., 2002). The advantage of such a micro-CT is its large area of coverage, which enables 3-D imaging of large living object, such as the human body. The triode structure of the field emission arrays can be easily used as field emission transistors and amplifiers. Space concerned, field emission transistors only occupy a very small vacuum tunneling gap in the range of microns, thus enabling higher density packing compared to solid-state transistors. The biggest advantage of using field emission transistors is that the event of field emission is instantaneous without any delay time, electrons fly in a ballistic manner without inertia, so it allows fast switching between on and off. The switching frequencies are ranged from a few GHz to thousands GHz. These unique features can be used in building all types of microwave devices and energy converters. Since field emission does not have any energy consumption, light source

utilizing this feature could save much energy. A field emission lamp using CNT pasted films have been built (Croci et al., 2003).

4.1.2.3. Experimental Goals

The above mentioned application potentials are for one-dimensional nanotubes/nanowires in general. Recently, systematic studies and large amount of experimental data have been collected for carbon nanotube field emitters. Nanowires out of rare-earth hexaboride family, though possessing better properties in terms of their lower work functions, more robust structure, have received less attention. Such negligence is due to the lack of synthesis method for these materials. Our recent successful growth of rare-earth hexaboride nanowires now makes the evaluation on their field emission properties possible (Zhang et al., 2005I, 2005II, 2005III, 2006). To achieve an ultimate goal of realizing a product out of single rare-earth hexaboride nanowire field emitter, we plan to achieve the following results at this stage. The first goal is to develop a reliable route to fabricate single nanowire field emitters. Special attention will be paid on the bonding nature between the nanowire and the supporting object, such as a tungsten wire. A mechanically robust, electrically and thermally conductive bonding is expected. The second goal is to make a thorough structural characterization of the single nanowire emitter. High resolution TEM equipped with chemical analysis spectrometer will be the major tool for this purpose. Special attention will also be paid to the surface structure and compositions, which contribute the most to the emission properties. The third goal is to measure the field emission characteristics of the so made nanowire field emitters. The I-V curves will be collected and field emission patterns will be recorded. Emission characteristics such as the work function, field enhancement factor, emission area, current density will all be extrapolated from the data. Finally, our goal is to correlate the

structural and compositional information with the real-time field emission properties. One approach is to perform ex-situ experiment by measuring the same structure separately in TEM and in emission measurement chamber; another approach is to utilize in-situ microscopy method to perform field emission measurement inside a TEM. Both of these two approaches will be executed in this research.

4.1.3. Overview of Chapter 4

The rest of the contents of Chapter 4 will be organized in the following manner. Fabrication of single nanotube/nanowire emitters will first be described. Four methods, namely, the direct contact method, dielectrophoresis method, focused ion beam method and electron beam lithographic method will be introduced in sequence. Since the electron beam lithographic method is what we found the most efficient at the current stage, it will be discussed in more details. In the following part, high vacuum chamber, the ex-situ, measurement of three types of single nanowire field emitters will be reported in such order: first, carbon glue bonded LaB_6 emitters; second, EBL bonded LaB_6 emitters and lastly, carbon glue bonded GdB_6 emitter. In the third part of the Chapter, details about the in-situ field emission measurement will be introduced. It will start with the field emission in-situ holder design in general and the studies that have been done, followed by the details of our own design of an in-situ holder for JEOL 2010F TEM and the description of the experiment procedure. Then results and discussion will be presented on two major experiments we performed by this method: the emission current density study and a study over the charge of distribution using TEM imaging as a tool. Concluding remarks will be given at the end. Finally, summary and conclusionss of the Chapter shall be presented, followed by a reference list.

4.2. Fabrication of Single Nanowire Electron Field Emitters

To use nanotubes/nanowires as a electron point source, the first step is to make a single nanotube/nanowire field emitter strucuture, which usually consists of a free-standing nanotube/nanowire attached to the tip of a needle. Electrochemically et alhed tungsten needle is a popular choice for this purpose. Its sharp tip is usually below tens of nanometers, providing a comparable size for the nanowire attachment, while its shaft can be as thick as a third of a millimeter, offering convenience in handling and manipulation. There are four major ways to attach a nanotube/nanowire onto the tungsten needle.

4.2.1. Direct Contact Method

The simplest way is the direct contact method. It usually involves a manipulator with micron precision. The tungsten needle is first bound to the manipulator and then is directed towards a selected nanotube/nanowire previously grown on a deposition substrate. For a carbon nanotube, after the tungsten tip is brought into contact with the desired nanotube/nanowire, a large current density is passed through the CNT. The current introduces severe joule heating and will eventually break the CNT in the middle. The half of CNT left attaches to the tungsten tip and completes a single nanotube emitter structure (Nishijima et al., 1999). Due to the small size of CNT (<10 nm), it is beyond the resolution of an optical microscope. This type of experiment is usually done inside an SEM using an in-situ manipulator. Stronger bonding between the CNT and tungsten tip can be achieved by focusing the electron beam on the joint area for some time under a rather poor vacuum (Nakayama et al., 2000). In this way, the electron beam induced deposition of amorphous carbon will serve as a binding glue to enforce the joint. An

alternative way is to prepare a soot of nanotubes/nanowires so that there is no strong bonding between them and the growth substrate (Rinzler et al., 1995). In that case, the van der Waals interactions between the tungsten tip and the nanowire/nanotube are sufficient to pull it out of the bunch.

The operation could be done under an optical microscope without the help of SEM. Even though the individual nanotube/nanowire can not be seen during tip approaching, one can still tell if the tip is in contact with the bunch. Chances are that there are always some nanotubes/nanowires attached to the tip after retraction of the tungsten needle. Single nanowire/nanotube attachment is possible to obtain after multiple tries. To secure the single nanowire/nanotube attachment and reduce the bonding strength of it to the supporting substance, it is preferred to disperse the nanotubes/nanowires on the edge of the substrate or on holey carbon films. It should be noted that, though it is a cost-efficient way to attach a single nanotube/nanowire to the tungsten needles through the direct contact method, the bonding strength is rather poor. This usually leads to a loss of the nanotube/nanowire during transportation or field emission process. A recent work done by Fan's group used an AFM to measure the force born by the apex of a single CNT field emitter during field emission (Wei et al., 2006). A pulling force in the range of tens of nano newtons is obtained, which corresponds to a pressure of $5X10^8$ Pa. Some groups reported the use of ''carbon glue'' in helping to improve the bonding strength between the CNT and the tungsten tip. In their experiments, a tungsten tip first pierced into a carbon tape and then was brought into contact with the CNT sample. However, the sticky substance on carbon tape is acrylic, which is insulating and also has a low melting point (about 300^o C). The lack of reliability of the direct contact method is still inevitable.

4.2.2. Dielectrophoresis Method

It is well-known that under a non-uniform electric field, particles suspended in dielectric media is subject to a force due to polarization. The force exerted on a field aligned cylinder is expressed as (Pohl, 1978):

$$F = \frac{\pi a^2 b}{3} \varepsilon_m \,\mathrm{Re}\left(\frac{\varepsilon_p^{*} - \varepsilon_m^{*}}{\varepsilon_m^{*}}\right) \cdot \nabla \left|E\right|^2, \qquad (4.7)$$

where *a* is the radius, *b* is the length in axial direction, ε_p and ε_m are the dielectric constant for the cylinder and the media, respectively, and E is the electric field. The formula tells us that by applying a non-uniform field in the suspension of nanotubes/nanowires, we can drive them to the place where a higher electric field is present. The force can be negative if $\varepsilon_p < \varepsilon_m$. Tang et al. uses a sharp tungsten tip piecing into a water suspension of CNT (Tang et al., 2003). A non-uniform electric field which is greatly intensified at the tip region was thus produced. As a consequence, CNT bundles are attracted to the apex of the tungsten tip and formed a fibril as the tip was drawn out of the suspension. The length of the fibril can be controlled by the concentration, frequency used and the speed of the tip in leaving the suspension surface. Entangled nanotube bundles are found to wrap the tungsten tip, providing a strong binding. Field emission measurement by Zhang et al. showed a good structural stability (Zhang et al., 2004). The strength of the binding is also exhibited by the unchanged tip structure after testing the structure for AFM probe applications. The reliability of the technique is fairly good. However, the number of nanotubes/nanowires attached is hard to control. Since this method involves the use of suspension, it is also hard to guarantee the cleanness of the nanotube/nanowire surface, which is on the other hand a determining factor for current stability of the field emitter.

4.2.3. Focused Ion Beam (FIB) Method

An improvement over the above mentioned direct contact method is to use

focused ion beam (FIB) technique to deposit a tungsten metal bond at the nanotube/nanowire joint with the supporting tip. The procedure is to use the direct contact method to attach more than one nanotube/nanowire on the tungsten tip. Then put the structure into an FIB chamber, where the milling mode will be first used to cut off the excessive nanotube/nanowires, and then deposition mode will be used for the tungsten binding formation. A demonstration of this procedure is given in Figure 4.3. In Figure 4.3a, two nanowires of about 10 μm long and 100 nm wide were attached to the surface of a tungsten tip. They are marked by white arrows. Then the top nanowire was cut off by the focused ion beam. After introducing tungsten vapors into the FIB chamber at a pressure of about $5X10^{-6}$ torr, ion induced deposition was performed at the root area for 30 minutes. The FIB image taken after these steps is shown in Figure 4.3b. The inserted images show the magnified details of the cutting and deposition sites, respectively. The technique offers high resolution imaging and precise tailoring capability. The bonding between the nanowire and the tungsten tip has fairly good mechanical strength and conductivity. The two drawbacks of this technique are that firstly, the FIB imaging process is destructive. If the nanotube/nanowire is too small, for example a few nanometers wide or even less, damage to the structures could become severe. Secondly, the use of Ga ion in the process could introduce surface contaminations, which could affect the work function of the so made nanotube/nanowire field emitters.

4.2.4. Electron Beam Lithography Method

4.2.4.1. Introduction

One-dimensional nanotube/nanowire (NT/NW) has raised tremendous scientific interests for the past 15 years. One of the most intensively studied applications is the use of nanotube/nanowire as electron field emission sources which directly take advantage of

the extremely small tip size and long aspect of the ratio to generate a high brightness in the highly coherent electron beam, yet with a low fabrication cost (de Jonge & Bonard, 2004; Bonard et al., 1999). One promising example of this application is the electron field emission point source for electron optical instruments such as the transmission electron microscope (TEM), scanning electron microscope (SEM) and electron beam lithography system (de Jonge, 2002).

While fabrication of flat panel displays usually desires a continuous film out of NTs/NWs, a point electron source, on the other hand, demands a single free-standing NT/NW structure attached to a supporting object through a robust, thermally and electrically conductive contact. Current methods of fabricating single NT/NW emitters include direct growth (She et al., 2003), dielectrophoresis (Zhang et al., 2004), or simply putting a supporting object in contact with the NT/NW and hold it by the van der Waals forces (Rinzler et al., 1995), acrylic based glue (de Jonge et al., 2003) or electron irradiation induced C contamination bonding (Akita et al., 1999). While these attempts were proven useful in making structures for the purpose of laboratory measurements and have indeed demonstrated the excellent properties of the NT/NW field emitters, they are all somehow lack of reliability and therefore might not be suitable for making a practical electron emitter product. For example, the direct growth method is very hard to control the length and number of the NTs/NWs grown on the desired sites. It is also not applicable to NTs/NWs formed through non-catalyst reactions. Electrophoresis usually attaches a bundle of NTs/NWs instead of a single unit and it inevitably introduces serious contamination due to the nature of the liquid-based process. C contamination bonding restricts the post contaminants cleaning procedures that are necessary to obtain a stable electron emission. At the same time, both theoretical and experimental studies have shown that, during field emission, the NT/NW field emitter body is under a high out pull

electrostatic force and a self joule heating, which easily raises the emitter body temperature to over 1000^{o} C (Bonard et al., 2003; Vincent et al., 2002; Huang et al., 2004). This harsh environment always causes falling-offs of the NTs/NWs from the van der Waals bonding and the acrylic glue bonding, which has a temperature tolerance of only 60^{o} C (Wang et al., 2005; Zhang et al., 2005). Another frequent cause of failure of the NT/NW emitters fabricated by these methods, including the direct growth, is that the supporting substrate melts even before the breakdown of the NT/NW body. This is due to the poor thermal conductivity at the emitter/substrate contact (She et al., 2003; Wang et al., 2005; Zhang et al., 2005; Nilsson et al., 2003). Therefore, a better fabrication method must be established in order to make a reliable NT/NW field emitter, because after all, for an ultra-high vacuum field emission gun system, it costs much more replacing the electron emitter than the actual cost of the emitter material itself.

Photo and electron beam lithography (EBL) techniques are well-established fabrication process used in modern microelectronic industry. The wirings and connections made by this masked metal deposition approach offer excellent electrical and thermal conductions which make possible the reliable performance of every piece of daily electronics. The nano-scale precision and manipulation flexibility of the technique have been utilized to make various kinds of NT/NW based electronic devices such as field effect transistors (Tans et al., 1998), logic gates (Huang et al., 2001; Bachtold et al., 2001), laser emitters (Duan et al., 2003), random access memories (Rueckes et al., 2000) and nano-scale electromechanical devices such as the torsional pendulums (Meyer et al., 2005; Williams et al., 2003; Papakakis et al., 2004). The lithography-made contacts between the NT/NW and its supporting substrate have excellent thermal, electrical conductivities and robust mechanical strength. It enabled passing through a large current to break the carbon nanotube shells layer by layer and can provide robust anchoring

attachments for nanotube torsional springs (Collins, 2001). In thesis, we also used EBL in making a reliable and practical single LaB_6 nanowire electron field emitter. High resolution transmission microscope (HRTEM) was employed to study the field emitter structure before and after the emission measurements. While this method is generally applicable to all single NT/NW field emitter structures, we chose LaB_6 nanowire because it has the greatest chance to be the optimum field emission nanowire material as promised by the compound's low work function, high melting point, high chemical resistance at high temperature and high electrical conductivity (Zhang et al., 2006).

4.2.4.2. Experimental

A silicon substrate was covered with CVD synthesized single crystalline [001] oriented LaB_6 nanowires and the CVD method is described somewhere else. A copper foil (0.1 mm thick, McMaster-Carr, Inc.) is cut into a rectangle with dimensions of 2 mmX10 mm to be used as a supporting object for the emitter body. The foil tip was dipped into contact with the silicon substrate so that it has randomly distributed nanowires dangling out of its tip top edge. The foil was then put onto a clean silicon substrate with the nanowire-covering side facing upwards. The structure was examined by an SEM (Hitachi S4700, equipped with a cold field emission gun) to select and locate the desired LaB_6 nanowire. A drop of PMMA (10% in chlorobenzene) was then applied on top of the structure to cover the nanowire area after drying in air. The structure was then transferred back to the SEM where a home developed computer EBL program, Seegerizer, was used to drive the electron beam to expose the selected root area of the nanowire at an acceleration voltage of 30 kv and a dose of 1.4 nC/cm. The exposed area was then developed in a 1:3 mixture of methylisobutylketon (MiBK) and isopropyl alcohol (IPA) for 1 minute. The structure was then loaded into a thermal evaporator where 10 nm thick

Cr was first deposited onto the sample followed by a 100 nm thick Au deposition. Lift-off was done by immersing the sample in acetone for 10 minutes before the excessive Au layer was peeled off from the PMMA resist protected area. The single nanowire field emitter was then dried in air.

The copper foil was further cut short in order to fit a TEM (JEOL2010F, equipped with a Schotky field emission gun) double-tilting sample holder and then it was put into the TEM chamber for characterization. EELS analysis was performed with the same type of TEM with a Gatan imaging filter.

4.2.4.3. Results and Discussions

Figure 4.4 illustrates the procedure for the EBL fabrication of a single LaB_6 nanowire electron field emitter. A copper foil cut into a slim rectangle was used as support for a LaB_6 nanowire in order to achieve optimum thermal conductance (Akita et al., 1999). The foil tip was then brought into contact with a silicon substrate covered with single crystalline [001] oriented LaB_6 nanowires grown by a chemical vapor deposition (CVD) method (Zhang et al., 2006) (Figure 4.4a, step i). the LaB_6 nanowires with random diameters and lengths are consequently attached to the foil tip with random orientation through van der Waals interactions (Figure 4.4a, step ii). One nanowire with preferred diameter, length and orientation can then be selected and its relative location can be recorded with reference to the foil edge topographic features. It is found helpful to put a substrate on the back of the structure in order to provide a support for the following polymethylmethacrylate (PMMA) resist coating (Figure 4.4a, step iii). After the PMMA coating, it turned out that, although the nanowires were all buried underneath the resist, topographic features at the foil edge were still recognizable and with their help we were able to locate the desired “welding” spot on the selected nanowire. A hole through the

resist was drilled to expose the root of the selected LaB_6 nanowire after electron beam exposure and developing procedures. 10 nm thick Cr layer was thermally deposited into the hole to ensure a good adhesion and the best mechanical strength between the nanowire and the deposited 100 nm Au layer. After lift-off, as shown in Figure 4.4b, the foil tip was found clean with only the presence of the selected nanowire with its root buried underneath a layer of Cr/Au metal. The presence of the Au layer can be verified by seeing a golden colored spot near the copper foil tip edge under the optical microscope.

A single LaB_6 nanowire emitter fabricated by the method described above was studied by TEM before field emission measurements. Figure 4.5a is a low magnification image showing the morphology of the emitter structure. A single LaB_6 nanowire with diameter of 90 nm extends out of the copper foil tip with a length of 2.5 μm. The film-looking substance near the root of the nanowire is suspected to be the PMMA resist residue which was not completely removed by acetone rinsing. A magnified image, Figure 4.5b, shows that the root of the LaB_6 nanowire is buried in metal particles of diameters ranging from 10 nm to 50 nm. Figure 4.5c is an HRTEM image of one of the particles marked by a black arrow in Fig. 2b. It clearly shows the face-entered cubic lattice of Au with a lattice constant of 4.08 Å. Figure 4.5d is also an HRTEM image characterizing the side wall of the LaB_6 nanowire. We confirmed that the nanowire is grown along its [001] lattice direction and both its side surfaces and top surface are terminated with the (100) lattice planes. The wall of the nanowire is found wrapped with a 5 nm thick layer which is composed of amorphous substance and a crystalline phase which we identified us graphite. These graphitic layers are believed to have formed during the CVD synthesis of the LaB_6 nanowires. In order to identify the chemical composition of the amorphous substance, electron energy loss spectroscopy (EELS) was applied to study a single LaB_6 nanowire. In order to avoid influence from sample drifting

during data collection, we acquired the spectrum in the scanning transmission electron microscopy (STEM) mode so that we can simultaneously observe the image when acquiring the EELS spectrum. The STEM image is presented in Figure 4.5e. The two marked circles i and ii represent two spots on the main body and wrapping layer, respectively, where we set the electron beam to collect the EELS spectra. The beam size is about 3 nm in diameter. The cubic lattice image indicates that the nanowire is tilted to [100] lattice direction, which ensures the same thickness along the electron beam direction where the two spots were set. It is based on the knowledge that the nanowire has a rectangular cross-section with (100) lattice planes as the terminating surfaces. In Figure 4.5f, we can see that spectrum i and ii both have La, B and C peaks. However, noting the fact that both the B peak and the La peak are lower in spectrum ii than in spectrum i and that the C peak is ranked reversely, we deduce that the amorphous substance is more likely to be amorphous C. This is because if the amorphous substance is La or B, their signal intensities should be the same in the main body as in the wrapping layer, since both parts have the same thickness. However, since C does not exist in the main body, its only existence in the wrapping layer makes the C signal much stronger when the electron beam was set on the wrapping layer than on the main body. The presence of La and B in spectrum ii is speculated to be from the electron scattering effect due to the relatively large beam size we used.

4.2.4.4. Conclusions

As a conclusion, an electron beam lithography method has been established to make single NT/NW based field electron emitter structures with robust, electrically and thermally conductive contacts.

4.3. High Vacuum Chamber Measurement:

4.3.1. Carbon Glue Bonded LaB_6 Emitter:

For field emission measurement, the tungsten wire was used as the cathode and a piece of ITO glass plate was used as the anode. A layer of phosphor was also painted on the ITO glass to enable observation of electron emission pattern when field emission electrons from the cathode reach the anode. The FE measurement was carried out in a high-vacuum chamber of pressure 10^{-7} torr.

Figure 4.6a shows a TEM image of a single LaB_6 nanowire of 140 nm in width and about 1 μm in length, fixed to the top of a 0.5 mm thick tungsten wire. Field emission measurement on this structure was performed in at pressure of 10^{-7} torr inside a high-vacuum chamber. While an increasing voltage was applied, the electron fluorescent pattern observed on a phosphor screen was recorded by a CCD camera. An observable bright emission pattern started to appear on the phosphor screen when the applied voltage reached 650 V and the emission pattern is presented in the inserted image of Figure 4.6a. The elliptical shape of the emission pattern is likely due to the fact that the emitter was not well aligned with respect to the applied electric field and therefore caused the cylindrical electron beam to intercept the phosphor screen with an angle from a direction normal to the viewing screen. The emission *I–V* curve is displayed in Figure 4.6b. A measurable field emission current of 0.5 pA was obtained at 450 V, which corresponds to average electric field strength of 1.5 V/μm obtained by dividing the applied voltage by the cathode-anode separation of about 300 μm. Also inserted is the F-N plot from the data $ln(I/V^2)$ vs. $1/V$. The good linearity of the plot suggests that the field emission from the LaB_6 nanowire emitter agrees with a metal-vacuum field emission model as described by the F-N equation. In addition, by knowing the work function of the LaB_6 emitter (2.6 eV

for the {001} planes), the slope of the F-N plot

$$k = -6.44 \times 10^7 \phi^{3/2} / \beta \qquad (4.8)$$

can be used to estimate the lateral dimension of the emitter with enhancement factor $\beta \approx 1/5r$. For this structure, we obtained D = 2*r* ≈ 152 nm. This value falls between the edge length and the diagonal of the cross-section of the square LaB_6 nanowire measured from the TEM image shown in Figure 4.6a. The good consistency again revealed the validity of applying F-N equation in describing the field emission from our LaB_6 nanowire emitter. Effective emission area A was derived to be 6.4nm^2 after substituting β and ϕ into the F-N plot y-intercept

$$b = \mathrm{Ln}\left(\frac{1.5 \times 10^{-6} A\beta^2}{\phi}\right) + \frac{10.4}{\phi^{1/2}}. \qquad (4.9)$$

Although the reason why only a small spot from the relatively large area of the whole tip (about 2000nm^2) was activated for emission is still unclear, the small emitting area is a desired feature for high resolution electron optical applications, since it promises low energy spread which in turn low down chromatic abrasion and enhance resolution. The emission current density at 800v was estimated to be about 5x10^5 A/cm^2 by dividing the total emission current by the effective emission area. Comparing to the state-of-art W/ZrO thermal assisted field emitter working at 1800^{o}C with 3000v extraction voltage, the LaB_6 nanowire emitter offers a current density one order of magnitude higher while working at room temperature with 800v extraction voltage. The current density of the LaB_6 nanowire emitter was also compared with that of a carbon nanotube field emitter, which was believed to be the most promising field emitter material among all other nanotubes/nanowires emitters. Result obtained from a single-walled carbon nanotube bundle emitter under the same experimental configuration shows that the current density is at the same order of magnitude as the tested LaB_6 nanowire emitter. Four other I-V

curves were also obtained from the same LaB_6 nanowire emitter with continuous emitting time duration of 30 minutes. The good consistency among the curves indicates a good stability of field emission from the LaB_6 single nanowire emitter.

To study the influence of the amorphous boron layer on LaB_6 nanowires' field emission property, an amorphous boron nanowire of about 170 nm in diameter was attached to a tungsten tip and arranged in the similar field emission measurement set-up as the LaB_6 nanowire emitter. Emission current never exceeded 1 nA before the applied voltage went over 800 V in contrast to the 30nA stable emission from the LaB_6 nanowire emitter of the similar size and under the same applied voltage. This might be due to the high work function of boron (4.5 eV) while that of LaB_6 is much lower (2.6 eV). This suggests that the field emission from LaB_6 nanowires should be mainly contributed from the crystalline part of the nanowire rather than the amorphous boron layer though some partial impact still can not be excluded at this point. This point of view is also supported by the field emission data from the single GdB_6 nanowire emitter with a similar geometry. While having the same thickness of amorphous boron layer and a GdB_6 crystalline part of lower work function (1.5 eV), the GdB_6 nanowire emitter had higher emission current than LaB_6 nanowire emitter at the same applied voltage, which should not occur if it is the amorphous boron layer that played the key role in the field emission property.

4.3.2. EBL Bonded LaB_6 Emitter

Before the measurement, a copper foil was taped to a micrometer and connected as cathode. A phosphor pasted ITO glass was put 300 μm in front of the copper foil to serve as both the anode and an imaging screen, from which, the emission pattern can be observed and recorded with a CCD camera. The set was then put into a high vacuum chamber with a pressure of $5X10^{-7}$ torr and I-V, I-t curves were subsequently recorded by

a highly sensitive amp meter connected to a control computer.

After TEM characterization, the same single LaB_6 nanowire field emitter was transferred to a high vacuum chamber where field emission property was measured. Altogether 18 field emission I-V curves were recorded from 700 volts to 1400 volts at a vacuum level of 10^{-7} torr. The emission current went as high as several micro amperes, after which the emission from the copper foil starts. Figure 4.7a is a representative I-V curve from the LaB_6 nanowire emitter and its inset panel is the field emission pattern taken at 950 V, recorded on a phosphor screen which also serves as anode. The single round bright spot at the center screen verifies that the emission is indeed from the single LaB_6 nanowire. By plotting $Ln(I/V^2)$ versus 1/V, one can obtain the F-N plot, from the slope of which, work function of the emission surface can be extrapolated by using the formula of $\varphi= (-0.031*m/r)^{2/3}$ (eV) with m being the F-N plot slope and r (nm) being the nanowire tip radius. We found that the F-N curve plotted from the emission data in Fig. 3a, instead of forming a straight line, actually consists of two straight lines with different slope values and those are presented in Figure 4.7b and Figure 4.7c respectively. The splitting point is marked by a black arrow in Figure 4.7a. Figure 4.7b presents a less steep slope at high current and high voltage end, which corresponds to a work function value of 2.67 eV+_0.06 eV. Figure 4.7c presents a steeper slope at low current and low voltage end, which gives a work function value of 5.2 eV+-0.11 eV. Noting that 2.67 eV agrees with the reported work function value of 2.6 eV for LaB_6 and 5.2 eV is very close to the work function value of 5.1 eV for C, we proposed the following emission mechanism of the LaB_6 nanowire field emitter. When the extraction voltage is low, it is an adsorbates emission type from the high work function C layer on the LaB_6 nanowire surface. When the extraction voltage gets higher, the wrapping C is “burned away” through current induced defects forming and it allows the emission from true LaB_6 surface with a low

work function. The observation of the similar emission characteristic in the I-V curve taken immediately after this run suggests that, however, the newly exposed LaB_6 gets covered again with C contaminants from the chamber through electrostatic attraction, and the two emission mechanisms follow each other in this switching manner. We calculated the work function values for each of the 18 runs and plotted the profile in Figure 4.7d. The work function values are found to fluctuate between 2.1ev and 5.5ev throughout the whole emission test period and this indicates that the emissions are from C contamination layer, true LaB_6 surface and sometimes a mixture of both. A poor vacuum condition is believed to be accounted for the large C presence in the emission testing chamber. The emitter current is also recorded under a fixed extraction voltage of 1000 V with respect to time duration and the data is presented in Figure 4.7e. Since work function exponentially affects the emission current density, as a direct consequence, the emission current also exhibits a large fluctuation over the whole testing period. The fact that emission current over 400 nA still constantly recovers after damping off even towards the end of the testing period suggests that neither of the emitter structure nor the LaB_6 nanowire gets damaged throughout this 3 hours continuous emission test.

After the field emission measurement, the same single LaB_6 nanowire field emitter was transferred back to the TEM sample holder again for imaging characterization. We found that the nanowire's thickness and length remained unchanged after the emission test and the gold contact area also stayed the same way, without signs of melting or mechanical failure. Figure 4.8a and Figure 4.8b are respectively the TEM image about the emitter's tip left corner before and after the field emission measurement. After field emission test, the emitter top surface is still atomically smooth without the presence of any oxide phase, proving the properties of LaB_6 nanowire, such as the high resistance against oxidation, field evaporation and ion bombardment under a high electric field.

However, obvious changes were observed on the C wrapping layer, as can be seen from the graphitic layers' position change marked by arrows in Figure 4.8a and Figure 4.8b. The disappearance of the graphitic layer from the emitter top surface after the emission supports the current induced damaging mechanism as often be accounted for the failure of Carbon nanotube emitter. The fact that only amorphous carbon formed on the top surface suggests that the temperature at the emitter top surface raised by joule heating is not high enough for the formation of graphite.

4.3.3. Carbon Glue Bonded GdB_6 Emitter

For field emission property study, a GdB_6 nanowire with lateral dimension of about 200nm was picked up by an optical microscope assisted manipulator and attached onto an electrically *et al*hed 0.5mm W tip with carbon adhesive. The set was then put into a high vacuum chamber working at 10^{-7} torr for field emission measurement. With the W tip as cathode, a piece of P coated ITO glass as anode with a separation of 250um in between, an increasing electric voltage was then applied and in the meantime, emission current was recorded by a high sensitive ampere meter and emission pattern was recorded by a CCD camera simultaneously.

Figure 4.9a shows the I-V curve of the field emission from the GdB_6 single nanowire emitter. An emission current of 10 nA was able to be achieved at a voltage of 650v and eventually reached an emission current over 200 nA before an abrupt shut off occurred. After the experiment, the nanowire was found lost from the W tip and this was believed to cause the abrupt shut off of the emission. The poor attaching between the GdB_6 nanowire and the W tip might also count for the current fluctuation in the emission I-V curve. An F-N plot with $Ln(I/V^2)$ versus $1/V$ was graphed as displayed in Figure 4.9b. Even with some spreading in the high voltage range, we can still see the straight line tendency

which indicates a metallic field emission characteristic. Figure 4.9c is a low magnification TEM image of the GdB_6 nanowire emitter and the insertion is the emission pattern recorded from the P screen at an applied voltage of 750 V. The ring feature of the emission pattern might be due to the fact that local electric field was more enhanced at the edges and corners of the tip top surface and therefore induced emission from this circle of sites. We then performed a computer simulation (FEMLAB) with a model based on experimental conditions and obtained a local electric field enhancement factor β of $3.3X10^4$ cm^{-1} at the edges of the top surface. By substituting β into the F-N plot slope $k=-6.44X10^7X\phi^{3/2}/\beta$, we got a work function value for the GdB_6 nanowire as about 1.5ev, which agrees with the Russian researcher 's result. The lower work function of the GdB_6 can also be seen by directly comparing its emission current value with that of LaB_6 nanowire emitter. For example, at 750 V, GdB_6 nanowire emitter offers more than 50 nA emission current which is more than 5 times the current drawn from the LaB_6 nanowire emitter working under the same condition.

4.4. TEM in-situ Measurement

4.4.1. Introduction

4.4.1.1. Field Emission In-situ Holder Designs

TEM has very small pole piece gap where specimen is allowed (about 3 mm in height) in order to obtain high resolution. The sample holder head piece can only be about 1mm in thickness to still allow tilting operation. Width concerned, the holder head for conventional side-entry TEM is normally about 10mm wide. So every manipulating part including the sample to be studied has to be built within this limited space. To enable general 2 probe conductivity measurement, field emission I-V curve recording or electric

field induced bending/vibration, the wiring of the holder design isn't too complicated. Only two wires needed to be carried out side of the vacuum using proper feedthroughs. The biggest challenge in the holder design is the movement of a manipulating tip. To ensure the safe handling and in the same time have the capability of approaching the specimen, the manipulating tip must be able to move in the axial direction with both coarse and fine modes. The movement in the TEM z direction is also crucial if one want to align the tip with the specimen under study. Such alignment is for both imaging purpose and accurate measuring of their distance, which is very important in field emission experiment. The movement in lateral direction is desirable, for it will allow the access of the manipulating tip to the whole specimen area. The nanotubes/nanowires under study are nanometric in size, but spacially located in the range of millimeters. This nature of the specimen demands that both coarse and fine movements are incorporated in all 3 dimensions. There are roughly 3 types of moving mechanisms utilized among the available in-situ holder designs for a conventional medium voltage side-entry TEM.

Type one is the simplest design as the one used in Wang's work. (Wang *et al*., 2003; Xu *et al*., 2006; Dong *et al*., 2002) Only axial direction move is built. Coarse move is realized by a step motor which translates the linear movement to the head piece area through a solid rod. A piezo ceramic is either put at the tip of the translation rod or on the other electrodes to perform fine movement down to sub-nanometer scale. This design is cost efficient. But the lack of movement in the other two directions restricts the tips accessibility and also introduces error in measuring the distance between two electrodes. The second type is a 3-D moving holder using step motors for coarse movements and piezo ceramics for fine tuning (Oshima *et al*., 2003; Wall *et al*., 1998; Stach *et al*., 2001). The holder is similar to the structure of the first type, except that the translation rod is coupled to 3 step motors or micrometer screws at the rear of the holder. A below structure

is used to separate the motors from the vacuum parts but still enable motion translation. Such holder design enables its tip to access much larger area of the specimen. The price to pay is the heavy weight of the motors and rather complicated translation mechanic system. The last type of the holder utilizes the frontier inertial sliding technique to realize coarse move just by a piece of piezo ceramic (Svensson *et al*., 2003; Bobji *et al*., 2006). The basic idea is to controllably switch between static friction and sliding at the interface between the piezo ceramic and the moving part. When the piezo is accelerated at certain speed, the moving part of the holder in contact moves with its motion. In other acceleration, the moving part goes on a sliding motion on the surface of the piezo ceramic. A full cycle of the above described motion moves the moving part forward once at a time. Such mechanism saves much space in the design by removing the necessity for step motors. An oxford group uses three such inertial sliding motors in three directions respectively, while a more compact design is proposed by Svensson where only one piezo tube is used for all. In his design, a sapphire ball is rigidly fixed to the top of piezo cerami tube. A tip holder embraces the sapphire ball with six metal spring legs. By applying waves with different shape to the piezo tube, the tip holder can slide on the surface of the sapphire ball in three dimensions. The directions and magnitude of the movments all depend on the vibration modes of the sapphire ball driven by the piezo tube. This is to perform coarse move. Fine movement is simply by bending and str*et al*hing of the piezo tube. This design bears no translation rod and no additional motors out side of the vacuum. It is commercialized now through Nanofactory Inc. distributed by Gatan Inc.

4.4.1.2. Studies Been Done by in-situ Method

Considerable amount of work has been done with these TEM in-situ holders and special attention was paid to mechanical properties, field emission and conductivity study

of carbon nanotubes. For mechanic property studies, Wang *et al*. applied an oscillating potential between a single standing nano entity and an electrode placed by its side (Poncharal *et al*., 1999; Wang *et al*., 2003). When the frequency of the oscillating potential matches with the resonance frequency of the nano entity, maximum amplitude in vibration is expected. The resonance frequency:

$$f = \frac{\beta_i^{\,2} T}{4\pi L}\sqrt{\frac{E}{3\rho}}, \quad (4.10)$$

where T is the thickness of the nanoentity in the bending direction, β_i is a constant related to the *i*th harmonic, L is its length, E is the bending modulus and ρ is the mass density of the nano-emitters. Therefore, by finding the resonance frequency, the bending modulus of the nano entity can be extracted out. As an extension of this method is the mass measurement of small particles attached to a carbon nanotube. Since the change in resonance frequency is related to the inertia of moment of the structure, its mass is therefore extractable after knowing the geometry information obtained from direct TEM image. Other studies about mechanical properties of 1 D nano entity include using electrostatic force to bend them and in the same time imaging the deformation area.

A recent interesting conductance measurement of CNT was done by Peng's group (Wang *et al*., 2006I). They use a STM-TEM holder to bend a CNT inside TEM and then utilize the electron beam to induce amorphous carbon deposition at the bending site. The bending was found to keep its shape even after the initial bending force was removed. Another CNT/CNT joint structure was also created by the same means. Electrical conductance measurement showed that all these in-situ fabricated joints have good electric contact. The total structure has the same electric conductance as the original CNT. The results provide the hope to shape circuit interconnects with high current density carrying CNT.

A lot of attention has been paid to the field emission property of CNT in recent years. It is believed that the small size of CNT greatly localizes the electron emission sites and therefore provides a better coherent source and a large emission current density. More importantly, CNT has a very good emission current stability. In the same time, emission current from CNT was observed to drop when the emission current exceeds a certain limit. Current steps are also quite common during field emission study. These phenomena all found answers in the in-situ field emission study of CNT under TEM. It is found that when current go over tens of micron amperes, CNT tends to split or shorten. A gradual modification on the tip cap structure was also observed (Wang *et al*., 2006II; Wang *et al*., 2005). Inner tubes inside a nano bell structures can sometimes fly off during high electric field condition.

A recent experiment done by K. Svensson demonstrates the possibility of using CNT as a nano pipette to pick up and transfer iron particles (Svensson *et al*., 2004). The pick-up and transportation of the iron particles is done by applying negative bias on the nanotube to repel and applying positive potential to attract the particles.

A CNT biprism was also proposed for an application of the TEM in-situ holder, where they try to use the positively charged CNT as a biprism to form holography of the sample under study (Cummings *et al*., 2002 & 2004).

4.4.2. Experimental

4.4.2.1. 2010F HRTEM in-situ Holder Design and Fabrication

The general instrumental design for the in-situ field emission measurement is presented in Figure 4.10. The 2010F holder will be constituted of 3 major parts: actuator chamber, transmission chamber and head piece. Inside the actuator chamber will sit the PI actuator with a linear resolution of 50 nm. The motion of the actuator is then transmitted

to the final nanowire emitter through an alumina rod which goes through the transmission chamber. The nanowire will be attached to a tungsten tip which is clamped to the alumina rod. In the head piece region, the anode and the nanowire emitter cathode will be connected with a copper wire respectively, which eventually connected to external circuits through a vacuum feedthrough. Since there is no y-tilting mechanism, the holder is a single-tilt type. A voltage power supply and a high sensitivity ampere meter are connected in series with the anode and cathode in order to measure field emission current. The anode end is grounded in this case. For computerized control, the actuator, power supply and ampere meter are all connected to computers.

Detailed design of the holder is presented in Figure 4.11. Altogether 7 major components constitute the holder body and they are labeled through a to g in the illustration. Part a is the head frame, which is also the field emission anode. Its material is chosen to be aluminum for conductance purpose and in the same time, because no magnetism is allowed inside the objective lens pole piece to prevent its interference with the projection electron beam. Several screw holes are prepared on the top beam to hold some special shaped anode metal. Part b is a Teflon disk. Its function is to insulate the anode frame from the main body. Insulating Teflon screws are used to fix it together with part a to part c. Part c and part d are the same shape as the original JEOL 2010F holder in order to match the vacuum sealing system. Part c is partially anodized for insulating purpose. Two small holes are drilled through in order to support an alumina sheath for wiring and to confine the move of the alumina transmission rod respectively. It is made a separate part from part d because the difficulty in drilling the two holes through the whole length with required precision. Part e is electrode chamber. It is made of stainless steel to enable welding with the electrode feedthroughs. Wirings are silver soldered onto the feedthroughs before part e is assembled with part f. Part f and Part g consist the actuator

chamber. The PI 50 nm resolution actuator sits inside and it transmits the motion to the nanowire emitter through the transmission rod. The actuator chamber is the biggest space consuming part and also the heaviest, due to the big size of the actuator with the desired resolution and moving range combination.

The final product of the field emission holder is shown in Figure 4.12. Four photographs are taken at the whole holder, head piece, actuator chamber and electrode chamber respectively and they are labeled as a, b, c and d in Figure 4.12. The whole holder measures about 31 inches long without the connecting cables and its relative size to a ball-pen is revealed in Figure 4.12a. Figure 4.12b is the photo of the head piece. A tungsten tip is clamped to the alumina transmission rod and it is connected as cathode. A thin copper foil is clamped to the frame and it's connected as anode. Figure 4.12c is the actuator computer interface and Figure 4.12d is the feedthroughs for the cathode/anode connection.

Figure 4.13a is an optical microscope image taken during tip alignment. LaB_6 nanowire is attached to the tip of the tungsten wire. The object opposing the tungsten sharp tip is the thickness of the copper foil, which measures about 100 μm. Before putting into the electron microscope, the foil is aligned with the tungsten tip so that when the tip approaches the anode foil, it is within the thickness range. Since in electron microscope, the image we obtain is only a projection shadow. So if the tip is out of the anode foil thickness range, determination of the anode/cathode distance will be impossible. However, since this is no mechanism designed to align the edge of the anode foil parallel to projection electron beam, the angle deviation still introduces considerable errors in determining the exact anode-cathode distance. This effect is depicted in Figure 4.13b. If we take the projection direction of electron beam as normal direction, one degree off of the anode foil surface will introduce about 1.7 μm difference between the

measurement distance and the actual distance. Reducing the thickness of the anode foil will help in reducing this measurement difference, but in the same time, make the alignment of the tungsten tip harder. In the actual experiment, we use larger anode-cathode distance to reduce the relative error in order to minimize the effect from this angular misalignment.

4.4.2.2. TEM in-situ Measurement and Imaging

A single LaB_6 nanowire is first attached to the tip of a tungsten wire. The tungsten tip is then clamped onto the head piece of 2010F field emission holder. The tip vertical position is then adjusted under an optical microscope so that it is within the anode foil thickness range when approaching it. After the alignment, the holder is inserted into the sample chamber of our JEOL 2010F HRTEM. It takes about 2 hours for pre-pumping before the holder is completely allowed into the objective lens pole piece. A high voltage power supply and a high sensitivity ampere meter are connected in series with the cathode of the holder and anode feedthroughs. Both electronic equipments are connected with a computer for controlling and recording. The actuator is then used to push the nanowire emitter towards the anode to obtain the desired cathode-anode distance. Before applying extraction voltage, the projection electron beam is shut off to eliminate its contribution to the measured current. A series of I-V curves are recorded with different cathode-anode separations.

To study the charge distribution on the cathode tip during field emission, the microscope is set at focus and under-focus conditions respectively while a series of voltage is applied on the nanowire emitter. A series of images are taken at 75 V, 100 V and 160 V bias when using under-focus imaging condition. After that, another thicker LaB_6 nanowire emitter is used to study the contrast shrinkage when different negative

bias is applied on the emitter. A series of images are taken at -2200 nm under-focus while 9 V, 16 V and 24 V negative bias is applied on the nanowire.

Numerical simulations about the charge distribution are done with FEMLAB software. The image contrast difference is used to trace back the charge distribution and the results are compared with the numerical simulations.

4.4.3. Results and Discussion

4.4.3.1. Emission Current Density Study

A low magnification image showing the experiment set-up is presented in Figure 4.14a. A LaB_6 nanowire previously welded to a copper foil edge is connected as cathode. The nanowire is about 10 μm long and 250 nm wde, perpendicularly sticking out of the foil edge. The in-situ anode is another copper foil edge. The cathode-anode distance can be adjusted by an actuator with a resolution of 50 nm. A dc voltage supply and a high sensitivity ampmeter with a minimum reading of 1 Pico ampere are connected in series with the cathode and anode. Since the actual anode could be some humps loosely attached to the copper surface, and the strong electric static force can move the hump or nanowire, which cause the change of cathode-anode distance. Such change is in the range of one to two micron meters. Therefore, if small cathode to anode distance is used, the large relative distance change could induce large field enhancement change and as a consequence, cause instability of the emission current. In our experiment, the cathode to anode distance was first set at 10 μm. The field emission I-V curve obtained at this condition is shown in Figure 4.14b. A detectable emission current of about 1 pico ampere was recorded when the voltage reached 350 V. The voltage was increased till 500 V and no current saturation was observed. We didn't go to higher voltage for the equipment safety reason. During field emission measurement, electron beam from the microscope

was turned off to remove its influence on the current reading. A current with opposite sign to the field emission current is still detected when the applied voltage is zero if we keep the imaging beam on and it is usually in the magnitude of a few pico amperes.

F-N fitting of $Ln(I/V^2)$ versus 1/V was plotted with results shown in the inserted panel of Figure 4.14b. From the F-N formula, the slope of the plot $m = -\frac{6.8\times10^7 \phi^{1.5}}{\beta}$, with $\boldsymbol{\Phi}$ in the unit of ev and β in the unit of cm^{-1}; The y intercept equals $b = \ln[\frac{A\cdot 6.2\times10^{-6}\cdot 1.45\cdot\beta^2}{\sqrt{\phi}(2.12+\phi)}]$ with A being emission area in the unit of cm^2. Therefore, if we know the value of $\boldsymbol{\Phi}$ or β, all other emission parameters can be accordingly deduced. β, the field enhancement factor can be numerically calculated with the knowledge of the exact geometry information about the emitter. However, field emission is usually localized by very tiny surface extrusions or local spot with lower work function. Those emission sites are usually in the order of a few nanometers or even atomic. Therefore, knowing the exact emission spot is almost impossible. The deviation of β value from calculated can be off by orders of magnitude. On the other hand, for most metals, the work function $\boldsymbol{\Phi}$ is usually in the range of 2-5 eV. In the LaB_6 nanowire system, the possible contaminants, carbon or boron are all with work function around 5 eV and LaB_6 with 2.3 eV for its (100) plane. Emission area, A, value is very sensitive to that of work function. So it could be used as a good reference to tell which work function value should be used from a certain F-N plot. In this case, we use a value of 5 eV, which results in an emission area diameter of 182 nm. By putting LaB_6 work function value 2.3 eV, we got an emission area much larger than the actual nanowire diameter, so it was excluded. Using the actual emission area diameter, we can trace back β by the simple empirical relation of 1/5r to compare with the fitted value. In this case, they all fall in the

same magnitude. The measurement result matches with our previous high resolution image showing the amorphous carbon layer covering the LaB_6 nanowires. This indicates that the contamination layer greatly reduces the emitter emission current density.

The distance was then adjusted to 6 μm and another I-V curve was obtained, the result of which is shown in Figure 4.15a. This time the current goes above 1 μA at 200 V. When applied voltage reaches 260 V, the emission current is almost 20 μA without showing any sign of saturation. The current fluctuation is also very small. F-N plot was presented in Figure 4.15b and this time, same method was used to extract work function value Φ and emission area A by fitting field enhancement value β. As a result, the work function 2.3 eV of the LaB_6 (100) plane was found to match the curve the best and its corresponding emission site diameter was determined to be 6.6 nm. Field enhancement factor β is consistent in the same magnitude as predicted from the emission diameter. It's much larger than the value obtained by a direct evaluation based on the cathode-anode distance. It proved again that in nanotube/nanowire field emissions, field enhancement is determined by detailed tip top surface geometry, which could be off by one order of magnitude if only cathode-anode distance and simple model were used for numerical calculation. The small emission area might be due to a local LaB_6 (100) surface extrusion just been formed after the burnt off of the contamination layer above it. After that, the voltage was kept at 260 V and stable current at 20 μA was obtained with fluctuation less than 10%. The stability was much improved compared to our ex-situ measurement with glue attached or gold attached nanowire emitters. This is probably in account for the good attachment through the FIB method.

A high resolution image about the LaB_6 nanowire emitter tip was taken before and after the emission measurement. They are presented in Figure 4.16a and b, respectively. Because the nanowire crystal axis forms an angle away from the perpendicular direction

with the projection electron beam, we were unable to get lattice contrast image. However, a thin layer of lighter contrast contamination layer is shown outside the emitter body in figure 4.16a, which proved the existence of higher work function surface. Though through such 2D projection image, local protrusions as emission sites are hard to identify, we do see some rough features on the tip surface. Such geometry details affect the field enhancement factor value, thus making simple model calculation deviated from its true value. Figure 4.16b looks almost the same as figure 4.16a except that the upper right side of the tip seems to be a little sharper, but this is very likely due to the tilting of the tip caused by slight sample movement during emission experiment. The similarity between the two images taken before and after emission indicates that the emitter structure remains quite stable during approximately 20 minutes high current density electron emission.

The in-situ emission measurement confirmed that the LaB_6 field emitter is indeed composed of one single nanowire. Its field emission current was initially from large area covered with high work function contamination layer and then from localized protrusions of real LaB_6 surface with a lower work function. The emission current can go up to tens of micron amperes without showing much current fluctuation or sign for saturation. A current density as high as 10^8 A/cm^2 can be achieved with good stability. High resolution image shows no sign of destruction to the tip after the emission measurement.

4.4.3.2. Charge Distribution Study

Another LaB_6 single nanowire field emitter was used to study the charge distribution on the nanowire tip using in-situ microscopy when a voltage is applied between cathode and anode. The original projection image without applying extraction voltage is shown in Figure 4.17c. In previous studies, we have already confirmed that the

LaB_6 nanowires all have a flat tip top with rectangular cross-section. The reason this nanowire appears to have triangle tip is that the nanowire is not perpendicular to the projection electron beam and therefore has one of its four corners sticking out in the front. A numerical simulation about the charge density distribution was performed using FEMLAB software. The model is presented in Figure 4.17a, in which the geometry of the nanowire and relative angle to the projection direction were chosen so as to match the microscope image in Figure 4.17c. The white contrast represents areas with higher electron charge density. A series of images were taken under different focus conditions and different voltages applied between cathode and anode. It is noticed that when the image is at focus, the change in applied field has little affect on the image contrast. However, when it is under-focused, the nanowire image starts to shrink as we apply higher voltage. The shrinkage is also non-linear. It tends to narrower the nanowire more on the top than bottom. Figure 4.17e is an image taken at an under-focus value of 2.2 μm when 9 V is applied between cathode and anode. Figure 4.17f is an image taken at the same focus value when 24 V is applied. The shrinking of the nanowire is obviously shown through the whole nanowire body and more shrinkage is at its top.

We adopted a charge density approximation theory in order to interpret the observed phenomena (Lynch *et al*., 1975; Amelincks *et al*., 1997). From the charge density approximation theory point of view, the image contrast is from two aspects: one is the absorption of electron by sample thickness and the other is the charge density of the crystal. Here, we consider a reverse dependence of absorption contrast on sample thickness as: $I_{ab} = 1- A/t$, with A as an imaging coefficient and t as sample thickness. We assume here that when t approaches A, the image contrast is white, which means the sample being transparent. According to above assumptions, I_{ab} is simulated as shown in Figure 4b. The gray scale gradient represents the thickness variation of the sample along

projection electron beam direction. Based on charge density approximation theory, the image contrast caused by charge density is presented as $I_{charge} = 1 + 2\varepsilon\lambda\sigma\rho$, where ε is the focus value, λ is electron wavelength, σ is a electron wavelength and electrostatic potential related constant and finally, ρ is the charge density projected along the electron beam direction. From the expression, we can see that when the beam is under-focused which corresponds to a negative ε value, image will lose its contrast more where electron charge density is higher. The charge density simulation image of Figure 4.17a reflects exactly this effect and therefore Figure 4.17a is also a simulation of I_{charge}. Finally, in order to combine the two types of contrast together, we assume the final contrast to be $I_{final} = I_{ab} * I_{charge}$. In order to simulate the final contrast image, we first simulated two charge density distribution images like the one shown in Figure 4.17a, but with different applied voltages. Secondly, we multiplied those images with Figure 4.17b by using Adobe Photoshop software to generate the final images as shown in Figure 4.17f and Figure 4.17h. The images were leveled to choose the absorption coefficient value A in order to match with the observed contrast in Figure 4.17e and Figure 4.17g. We can clearly see that, the shrinkage trend is indeed revealed. With higher applied voltage, shrinkage becomes more severe and nanowire is not only narrowed, but also sharpened on the tip top. However, the above method fails to explain the lighten-up on the tip when voltage exceeds a certain value. Also the shrinkage at the bottom is less developed compared to the actual observation in Figure 4.17e and h. The limitation could be rooted from the fact that the charge density approximation theory is originally developed for small defocus value, while in our system, the defocus is in the range of micron meters, which is too large for the theory to still hold valid.

In Figure 4.18, the single nanowire field emitter was also applied with a series of different voltages. The original image taken at focus before applying voltage is shown in

Figure 4.18a. Then the imaging was set at under-focus condition. 75 V, 100 V and 160 V are applied one at a time to the emitter and the corresponding images are presented in Figure 4.18b, c and d respectively. The original dark contrast nanowire becomes a bright contrast reverse triangle. The triangle is wider when higher voltage is applied. To note in Figure 4.18b that the stem of the nanowire still have some dark contrast left and that contrast is lost when higher voltage is applied. Another interesting thing to notice by comparing Figure 4.18a and b is that the right edge of the bright triangle is the same shape as the left edge of the original nanowire and vice versa. Such phenomena are believed to be a continuing effect of those observed in Figure 4.17, only at higher potential bias or deeper under-focus values.

The charged effect in imaging field emission carbon nanotubes was initially mentioned in the work by Wang's group and briefly discussed in Cummings' work about CNT bi-prisms (Wang *et al*., 2002; Cummings *et al*., 2004). It can also well explain the observed image contrast change along with voltage in our case. Figure 4.19 is a series of ray diagram illustrating the effect of negative charges on the image formation in an electron microscope when the imaging condition is set at under-focus. As shown in Figure 4.19a, the object is negatively charged, so the incident electron beams in the vicinity of its edge are repelled. The scattering angle increases as the voltage applied gets higher. The beam passing at the edge of the object goes through the objective lens and always intercepts the image plane at the same location for a given magnification. This location is independent from the applied bias voltage. This is the reason why no shrinkage or expanding is observed when the imaging condition is set at focus. However, when the actual image plane is set at under-focus, the dark projection contrast area reduces when scattering angle increases. This is depicted from Figure 4.19a to b. As the angle goes larger, the beams from both side of the object start to overlap and cause the contrast to flip

from dark to bright, as shown in Figure 4.19c. A further increase of the bias, thus the scattering angle, leads to the expanding of the overlap area and this is shown in Figure 4.19d.

The overall effect of the negative charge is depicted in Figure 4.20. The dark square represents the nanowire. The two dents on each side mark the right and left side respectively. The two areas within the dash line are the projection beams that will be moved during charging. As seen from the under-focus imaging plane in Figure 4.19, as the nanowire is applied with increasing voltage, the two beams will come towards each other. However, the beam closer to the nanowire tip will move faster, because of the higher charge density on the emitter tip. Therefore, the two beams are tilted with an angle while moving closer to each other, as shown in Figure 4.20b. This scenario represents what has been observed in Figure 4.17e. As voltage increases, the beams come closer, with only a dark triangle left in the middle, as shown in Figure 4.20c and this is the case in Figure 4.17f. Figure 4.20d is the case when top parts of the beam already overlap while the bottom parts still separate. Therefore, half bright contrast and half dark contrast are shown in the same image and this is observed in Figure 4.18b. As the two beams come towards each other even more as voltage increases, the original dark contrast triangle completely changes into a bright contrast reverse triangle. It can be easily seen that if the movement continues, the bright region will get wider. These scenarios match with our observation in Figure 4.18c and d respectively.

As a conclusion remark, the above charge effect study offers an opportunity to directly observe charge distribution on the nanowire emitter tip through off-focus imaging technique. Similar effects are expected if positive bias is applied and imaging is done under over-focus condition. The triangle shape of the contrast image proves the higher density at the emitter tip region, which agrees with the simulation results. Provided with

the detailed information about the imaging ray diagram and under-focus value, one could extract out the exact scattering angle of the electron beam by measuring the shrinkage. Since the scattering angle is related to the charge density, it is possible to quantify the charge density distribution with such procedures. The charge density distribution will help us to find the accurate field enhancement factor, which is hard to obtain using other methods. It is also interesting to notice that the above described brightening effect of charged nanowires is a common phenomenon in field emission microscopy, where focusing is not performed (Prigent and Morin, 2001). However, the brightening in those occasions are caused by the attraction force due to positive charging on the nanowire, while in our case, opposite effect was observed. This is because the different image forming process between transmission microscope and field emission microscope, though both techniques use electron beam as projection tool.

4.4.4. Conclusions

The simple design of the field emission in-situ holder for JEOL2010F TEM proves to be successful. It allows the clamping of a single nanowire field emitter as cathode and the use of anode of any shaped materials, as long as the dimension coincides with that of the TEM pole piece. In this study, an FIB attached LaB_6 single nanowire emitter was installed onto the holder as cathode and a copper foil was used as anode. With the help of the PI linear actuator, one can adjust the cathode/anode distance with a resolution of 50 nm. Voltage up to 1000 V can be applied between the cathode and anode from external power supply outside the vacuum. The holder allows recording of field emission I-V curve and imaging its emission tip at the same time.

I-V curve measurement on the single LaB_6 nanowire emitter revealed fair stability at low current level (a few nano amperes), compared to a better stability achieved at high

current level (a few tens of micron amperes). The results probably correlate to an adsorbates emission and true LaB_6 surface emission respectively. Emission area is used to help estimate the work function of emission sites in each case, which support the existence of two emission types.

Image contrast shrinkage was observed for LaB_6 nanowire during field emission, using an under-focus image mode. Charged density approximation theory was used to simulate the effect and successfully obtain similar shrinkage when imaging conditions are set to be under-focus. Further increasing of the bias voltage or degree of under-focus results in reversing of the image contrast and subsequent expanding of the overlap shadow. A projection beam bending model was established and qualitatively explained these charge distribution induced phenomena.

4.5. Summary and Conclusions

In the beginning of the chapter, classical field emission theory was first briefly reviewed. The Fowler-Nordheim electron tunneling model was developed originally for emitter structures with flat surface and uniform electric field distribution. In many experiments, field emission from nanotubes/nanowires still followed the model well, as shown by the good linearity in the F-N plots. Deviations from the theory are also commonly observed. Corrections to the theory were made in the literatures in recent years, studying the emission from very thin single walled carbon nanotubes, which only have a few atoms at its apex. For nanotubes/nanowires with bigger dimensions, F-N theory is still a good phenomenological basis to extrapolate the various parameters of the nanowire. Towards the goal of utilizing nanotubes/nanowires in field emission devices, considerable amount of works in the field are directed to study the field enhancement factor, field emission sites, field emission stability, emitter failure and emission energy spread.

Rare-earth hexaboride nanowires are a new family of nanostructures that just been produced by us. Therefore, both of its field emission mechanism and accurate parameters remain blank in literature. Our motivation of the current work is partially set to fill this blank in knowledge. Another part of the motivation is drawn by the huge application potential that field emission devices in general posses. Aside from its most immediate application as high brightness point electron source, the nanotube/nanowire field emitters are also promising switching devices in microelectronics. Some of its unique features, such as instantaneous response and extremely low consumption of energy can greatly promote the current microelectronic technology. Motivated by the above two aspects, our work is set at the direction of developing a method of fabricating and obtaining some key characteristics of single rare-earth hexaboride field emitters.

Four methods were introduced to make single nanotube/nanowire field emitter structure, which is usually a single nanotube/nanowire bonded to an electrochemically *et al*hed tungsten tip. The relative pros and cons of these methods are compared. The nanotube/nanowire emitters made from these methods are used in our field emission measurements.

Ex-situ measurement is to characterize the detailed structure and chemical composition of the NT/NW emitter in HRTEM and then carefully transferred to high vacuum chamber for field emission measurements. Comparing to in-situ method, one can fully utilize the capability of the HRTEM, such as tilting and the use of vibration proof holder. Also the filed emission measurement can be done in a freer environment. Two types of LaB_6 nanowire emitters, one by EBL method and one by direct contact method, are studied thoroughly. It was found that the emitter has a low work function close to reported value for LaB_6 crystal. The emission current density is comparable to CNT emitter tested under the same circuitry. No apparent destruction was observed after the

emission test, revealing robustness of the emitter material. Current fluctuations are fairly large and it is believed to originate from carbon contaminants' adsorption and desorption process, which is inevitable at vacuum levels used. GdB_6 emitter was tested also using the same ex-situ method. A lower work function value of 1.5 eV was convinced with the reported bulk value. The emitter failed during emission due to the melting of bonding glue when joule heating causes the emitter temperature to reach over 300 ^{o}C.

In-situ experiment was also conducted with a home-made field emission holder for JEOL2010F HRTEM. Simultaneous emission measurement and image recording are achieved. The single nanowire emitter was confirmed to be quite stable during emission even high current of more than 20 μA was drawn from the tip. High resolution images taken before and after the emission show similar morphology, indicating no destruction occurred. Different emission types are observed when changing the cathode/anode distance with the built actuator. A qualitative projection bending model was built to explain a series of image shrinking, contrast flip and image expanding observed when imagine the charged single nanowire field emitter at under-focus conditions.

REFERENCES

Akita, S., Nishijima, H., Nakayama, Y., Tokumasu, F. & Takeyasu, K. (1999). Carbon nanotube tips for a scanning probe microscope: their fabrication and properties. Journal of Physics D-Applied Physics, 32(9), 1044-1048.

Amelinckx, S., Van Dyck, D., Van Landuyt, J., & Van Tendeloo, G. (1997). Electron microscopy: principles and fundamentals. Weinheim: VCH.

Bachtold, A., Hadley, P., Nakanishi, T. & Dekker, C. (2001). Logic circuits with carbon nanotube transistors. Science, 294(5545), 1317-1320.

Bobji, M. S., Ramanujan, C. S., Pethica, J. B., & Inkson, B. J. (2006). A miniaturized TEM nanoindenter for studying material deformation in situ. Measurement Science and Technology, 17, 1324-1329.

Bonard, J. M., Dean, K. A., Coll, B. F., & Klinke, C. (2002). Field emission of individual carbon nanotubes in the scanning electron microscope. Physical Review Letters, 89(19), 197602.

Bonard, J.M. & Klinke, C. (2003). Degradation and failure of carbon nanotube field emitters. Physical Review B, 67(11), 115406.

Bonard, J.M., Salvetat, J.P., Stoeckli, T., Forro, L. & Chatelain, A. (1999). Field emission from carbon nanotubes: perspectives for applications and clues to the emission mechanism. Applied Physics A-Materials Science & Processing, 69(3), 245-254.

Brodie, I. & Spindt, C. A. (1992). Advances in electronics and electron physics Vol.83. San Diego: Academic.

Buldum, A., & Lu, J. P. (2003). Electron field emission properties of closed carbon nanotubes. Physics Review Letters, 91(23), 236801.

Choi, W. B., Chung, D. S., Kang, J. H., Kim, H. Y., Jin, Y. W., Han, I. T., Lee, Y. H., Jung, J. E., Lee, N. S., Park, G. S., Kim, J. M. (1999). Fully sealed, high-brightness carbon-nanotube field-emission display. Applied Physics Letters, 75(20), 3129-3131.

Chueh, Y. L., Chou, L. J., Cheng, S. L., He, J. H., Wu, W. W., & Chen, L, J. (2005). Synthesis of taperlike Si nanowires with strong field emission. Applied Physics Letters, 86(13), 133112.

Collins, P.G., Arnold, M.S. & Avouris, P. (2001). Engineering carbon nanotubes and nanotube circuits using electrical breakdown. Science, 292(5517), 706-709.

Croci, M., Arfaoui, I., Stoeckli, T., Chatelain, A. & Bonard, J. M. (2003). A fully sealed luminescent tube based on carbon nanotube field emission. Microelectronics Journal, 35, 329–336.

Cumings, J., Zettl, A., & McCartney, M. R. (2004). Carbon nanotube electrostatic biprism : Principle of operation and proof of concept. Microscopy and Microanalysis, 10, 420-424.

Cumings, J., Zettl, A., McCartney, M. R., & Spence, J. C. H. (2002). Electron holography of field-emitting carbon nanotubes. Physical Review letters, 88(5), 056804.

de Jonge, N. & Bonard, J.M. (2004). Carbon nanotube electron sources and applications. Philosophical Transactions of the Royal Society of London Series A-Mathematical and Physical and Engineering Sciences, 362(1823), 2239-2266.

de Jonge, N., Allioux, M., Oostveen, J. T., Teo, K. B. K. & Milne, W. I. (2005). Optical performance of carbon-nanotube electron sources. Physical Review Letters, 94(x), 186807.

de Jonge, N., Lamy, Y. & Kaiser, M. (2003). Controlled mounting of individual multiwalled carbon nanotubes on support tips. Nano Letters, 3(12), 1621-1624.

de Jonge, N., Lamy, Y., Schoots, K. & Oosterkamp, T.H. (2002). High brightness electron beam from a multi-walled carbon nanotube. Nature, 420 (6914), 393-395.

Dean, K. A. & Chalamala, B. R. (1999)I. Field emission microscopy of carbon nanotube caps. Journal of Applied Physics, 85(7), 3832-3836.

Dean, K. A. & Chalamala, B. R. (1999)II. The environmental stability of field emission from single-walled carbon nanotubes. Applied Physics Letters, 75(19), 3017-3019.

Dong, L.Arai, F., & Fukuda, T. (2002). Electron-beam-induced deposition with carbon nanotube emitters. Applied Physics Letters, 81(10), 1919-1921.

Duan, X.F., Huang, Y., Aganwai, R. & Lieber, C.M. (2003). Single-nanowire electrically driven lasers. Nature, 421(6920), 241-245.

Fowler, R. H., & Nordheim, L. (1928). Electron emission in intense electric field. Proceedings of Royal Society of London, 119(x), 173-181.

Fursey, G. (2005). Field emission in vacuum microelectronics. New York: Kluwer Academic.

Gomer, R. (1961). Field emission and field ionization. Cambridge: Harvard University Press.

Groning, O., Kuttel, O. M., Emmenegger, Ch., Groning, P., & Schlapbach, L. (2000). Field emission properties of carbon nanotubes. Journal of Vacuum Science and Technology B, 18(2), 665-678.

H. Zhang, J. Tang, Q. Zhang, G. P. Zhao, G. Yang, J. Zhang, O. Zhou, L. C. Qin, Adv. Mater. 2006, 18, 87.

H. Zhang, Q. Zhang, G. P. Zhao, J. Tang, O. Zhou, L. C. Qin, J. Am. Chem. Soc. 2005, 127, 13120.

Han, S. & Ihm, J. (2002). First-principles study of field emission of carbon nanotubes. Physical Review B, 66(x), 241402.

Han, S., Lee, M. H., & Ihm, J. (2002). Dynamical simulation of field emission in nanostructures. Physical Review B, 65(x), 085405.

Huang, N.Y., She, J.C., Chen, J., Deng, S.Z., Xu, N.S., Bishop, H., Huq, S.E., Wang, L., Zhong, D.Y., Wang, E.G. & Chen, D.M. (2004). Mechanism responsible for initiating carbon nanotube vacuum breakdown. Physical Review Letters, 93(7), 075501.

Huang, Y., Duan, X.F., Cui, Y., Lauhon, L.J., Kim, K.H., Lieber, C.M. (2001). Logic gates and computation from assembled nanowire building blocks. Science, 294(5545), 1313-1317.

Lee, Y. H. Choi, C. H., Jang, Y. T., Kim, E. K., Ju, B. K., Min, N. K., Ahn, J. H. (2002). Tungsten nanowires and their field electron emission properties. Applied Physics Letters, 81(4), 745-747.

Li, S. Y., Lin, P., Lee, C. Y., & Tseng, T. Y. (2004). Field emission and photofluorescent characteristics of zinc oxide nanowires synthesized by by a metal catalyzed vapor-liquid-solid process. Journal of Applied Physics, 95(7), 3711-3716.

Li, Y. B., Bando, Y., Golberg, D., Kurashima, K. (2002). Field emission from MoO3 nanobelts. Applied Physics Letters, 81(26), 5048-5050.

Liang, S. D., Huang, N. Y., Deng, S. Z., & Xu, N. S. (2004). Chiral and quantum size effects of single-wall carbon nanotubes on field emission. Applied Physics Letters, 85(5), 813-815.

Lynch, D. F., Moodie, A. F., & O'Keefe, M. A. (1975). n-Beam lattice images .V. The use of the charge-density approximation in the interpretation of lattice images. Acta Crystallography A, 31, 300.

Meyer, J.C., Paillet, M. & Roth, S. (2005). Single-molecule torsional pendulum. Science, 309(5740), 1539-1541.

Nakayama, Y., Nishijima, H., Akita, S., Hohmura, K. I., Yoshimura, S. H. & Takeyasu, K. (2000). Microprocess for fabricating carbon-nanotube probes of a scanning probe microscope. Journal Vacuum Science and Technology B, 18, 661–664.

Nilsson, L., Groening, O., Groening, P. & Schlapbach, L. (2001). Collective emission degradation behavior of carbon nanotube thin-film electron emitters. Applied Physics Letters, 79(7), 1036-1038.

Nishijima, H., Akita, S. & Nakayama, Y. (1999). Novel process for fabricating nanodevices consisting of carbon nanotubes. Japanese Journal of Applied Physics, 38, 7247–7252.

Oshima, Y., Mouri, K., Hirayama, H., & Takayanagi, K. (2003). Development of a miniature STM holder for study of electronic conductance of metal nanowires in UHV-TEM. Surface Science, 531, 209-216.

Papadakis, S.J., Hall, A.R., Williams, P.A., Vicci, L., Falvo, M.R., Superfine, R., Washburn, S. (2004). Resonant Oscillators with Carbon-Nanotube Torsion Springs. Physical Review Letters, 93(14), 146101.

Peng, L. M., Wang, M. S., & Wang, J. Y. (2006). On the phenomenological nature of the work function as determined from electron field-emission experiments on nanotubes and nanowires. Surface and Interface Analysis, 38, 1073-1077.

Pohl, H. A. (1978). Dielectrophoresis. Cambridge: Cambridge University Press.

Poncharal, P., Wang, Z. L., Ugarte, D., & Deheer, W. A. (1999). Eletrostatic deflections and electromechanical resonances of carbon nanotubes. Science, 283, 1513-1516.

Prigent, M. & Morin, P. (2001). Charge effect in point projection images of Ni nanowires and I collagen fibres. Journal of Physics D: Applied Physics, 34, 1167-1177.

Rinzler, A.G., Hafner, J.H., Nikolaev, P., Lou, L., Kim, S.G., Tamanek, D., Nordiander, P., Colbert, D.T. & Smalley, R.E. (1995). Unraveling nanotubes–field-emission from an atomic wire. Science, 269(5230), 1550-1553.

Rueckes, T., Kim, K., Joselevich, E., Tseng, G.Y., Cheung, C.L., Lieber, C.M. (2000). Carbon nanotube-based nonvolatile random access memory for molecular computing. Science, 289(5476), 94-97.

She, J.C., Xu, N.S., Deng, S.Z., Chen, J., Bishop, H., Huq, S.E., Wang, L., Zhong, D.Y. & Wang, E.G. (2003). Vacuum breakdown of carbon-nanotube field emitters on a silicon tip. Applied Physics Letters, 83 (13), 2671-2673.

Stach, E. A., Freeman, T., Minor, A. M., Owen, D. K., Cumings, J., Wall, M. A., Chraska, T., Hull, R., Morris, J. W. Jr., Zettl, A., & Dahmen, U. (2001). Development of a nanoindenter for in situ transmission electron microscopy. Microscopy and Microanalysis, 7, 507-517.

Svensson, K., Jompol, Y., Olin, H., & Olsson, E. (2003). Compact design of a transmission electron microscope-scanning tunneling microscope holder with three-dimensional coarse motion. Review of Scientific Instruments, 74(11), 4945-4947.

Svensson, K., Olin, H., & Olsson, E. (2004). Nanopipettes for Metal Transport. Physical Review Letters, 93(14), 145901.

Tang, J., Gao, B., Geng, H., Velev, O. D., Qin, L. C., & Zhou, O. (2003). Assembly of 1D nanostructures into sub-micrometer diameter fibrils with controlled and variable length by dielectrophoresis. Advanced Materials, 15(15), 1352-1355.

Tans, S.J., Verschueren, A.R.M. & Dekker, C. (1998). Room-temperature transistor based on a single carbon nanotube. Nature, 393(6680), 49-52.

Vila, L., Vincent, P., Dauginet-De Pra, L., Pirio, G., Minoux, E., Gangloff, L., Demoustier-Champagne, S., Sarazin, N., Ferain, E., Legras, R., Piraux, L., & Legagneux, P. (2004). Growth and field-emission properties of vertically aligned cobalt nanowire arrays. Nano Letters, 4(3), 521-524.

Vincent, P., Purcell, S.T., Journet, C. & Binh, V.T. (2002). Modelization of resistive heating of carbon nanotubes during field emission. Physical Review B, 66(7), 075406.

Wall, M. A. & Dahmen, U. (1998). An in situ nanoindentation specimen holder for a high voltage transmission electron microscope. Microscopy Research and Technique, 42, 248-254.

Wang, M. S., Peng, L. M., Wang, J. Y., & Chen, Q. (2006I). Shaping carbon nanotubes and the effects on their electrical and mechanical properties. Advanced Functional Materials, 16, 1462-146.

Wang, M. S., Wang, J. Y., & Peng, L. M. (2006II). Engineering the cap structure of individual carbon nanotubes and corresponding electron field emission characteristics. Applied Physics Letters, 8, 243108.

Wang, M.S., Wang, J.Y., Jin, C.H., Chen, Q. & Peng, L.M. (2005). Observations of carbon nanotube field emission failure in the transmission electron microscope. Materials Science Forum, 475-479, 4071-4076.

Wang, Z. L. (2003). New developments in transmission electron microscopy for nanotechnology. Advanced Materials, 15(18), 1497-1514.

Wang, Z. L., Gao, R. P., de Heer, W. A., & Poncharal, P. (2002). In situ imaging of field emission from individual carbon nanotubes and their structural damage. Applied Physics Letters, 80(5), 856-858.

Wang, Z. L., Poncharal, P. & de Heer W. A. (2000). Nanomeasurements of individual carbon nanotubes by in situ TEM. Pure and Applied Chemistry, 72(1-2), 209-219.

Wei, W., Jiang, K., Wei, Y., Liu, M., Yang, H., Zhang, L., Li, Q., Liu, L., & Fan, S. S. (2006). Measuring the stress in field-emitting carbon nanotubes. Nanotechnology, 17, 1994-1998.

Williams, P.A., Papadakis, S.J., Patel, A.M., Falvo, M.R., Washburn, S. and Superfine, R. (2003). Fabrication of nanometer-scale mechanical devices incorporating

individual multiwalled carbon nanotubes as torsional springs. Applied Physics Letters, 82(5), 805-807.

Wong, K. W., Zhou, X. T., Au, F. C. K., Lai, H. L., Lee, C. S., & Lee, S. T. (1999). Field-emission characteristics of SiC nanowires prepared by chemical-vapor deposition. Applied Physics Letters, 75(19), 2918-2920.

Wu, J. M., Shih, H. C., & Wu, W. T. (2005). Electron field emission from single crystalline TiO_2 nanowires prepared by thermal evaporation. Chemical Physics Letters, 413(4-6), 490-494.

Xu, Z., Bai, X. D., & Wang, E. G. (2006). Geometrical enhancement of field emission of individual nanotubes studied by in situ transmission electron microscopy. Applied Physics Letters, 88(x), 133107.

Yue, G. Z., Qiu, Q., Gao, B., Cheng, Y., Zhang, J., Shimoda, H., Chang, S., Lu, J. P. & Zhou, O. (2002) Generation of continuous and pulsed diagnostic imaging X-ray radiation using a carbon-nanotube-based field-emission cathod. Applied Physics Letters, 81, 355–357.

Zhang, H., Tang, J., Zhang, Q., Zhao, G.P., Yang, G., Zhang, J., Zhou, O. & Qin, L.C. (2006). Field emission of electrons from single LaB6 nanowires. Advanced Materials, 18(1), 87-91.

Zhang, H., Zhang, Q., Tang, J. & Qin, L.C. (2005I). Single-crystal line CeB6 nanowires. Journal of the American Chemical Society, 127(22), 8002-8003.

Zhang, H., Zhang, Q., Tang, J. & Qin, L.C. (2005II). Single-crystalline LaB6 nanowires. Journal of the American Chemical Society, 127(9), 2862-2863.

Zhang, H., Zhang, Q., Zhao, G.P., Tang, J.; Zhou, O. & Qin, L.C. (2005III). Single-crystal line GdB6 nanowire field emitters. Journal of the American Chemical Society, 127(38), 13120-13121.

Zhang, J. Tang, J., Yang, G., Qiu, Q., Qin, L.C. Zhou, O. (2004). Efficient fabrication of carbon nanotube point electron sources by dielectrophoresis. Advanced Materrials, 16(14), 1219.

Zhang, J. Tang, J., Yang, G., Qiu, Q., Qin, L.C. Zhou, O. (2004). Efficient fabrication of carbon nanotube point electron sources by dielectrophoresis. Advanced Materrials, 16(14), 1219-+

Zheng, X., Chen, G. H., Li, Z. B., Deng, S. Z., & Xu, N. S. (2004). Quantum-mechanical investigation of field-emission mechanism of a micrometer-long single-walled carbon nanotube. 92(10). 106803.

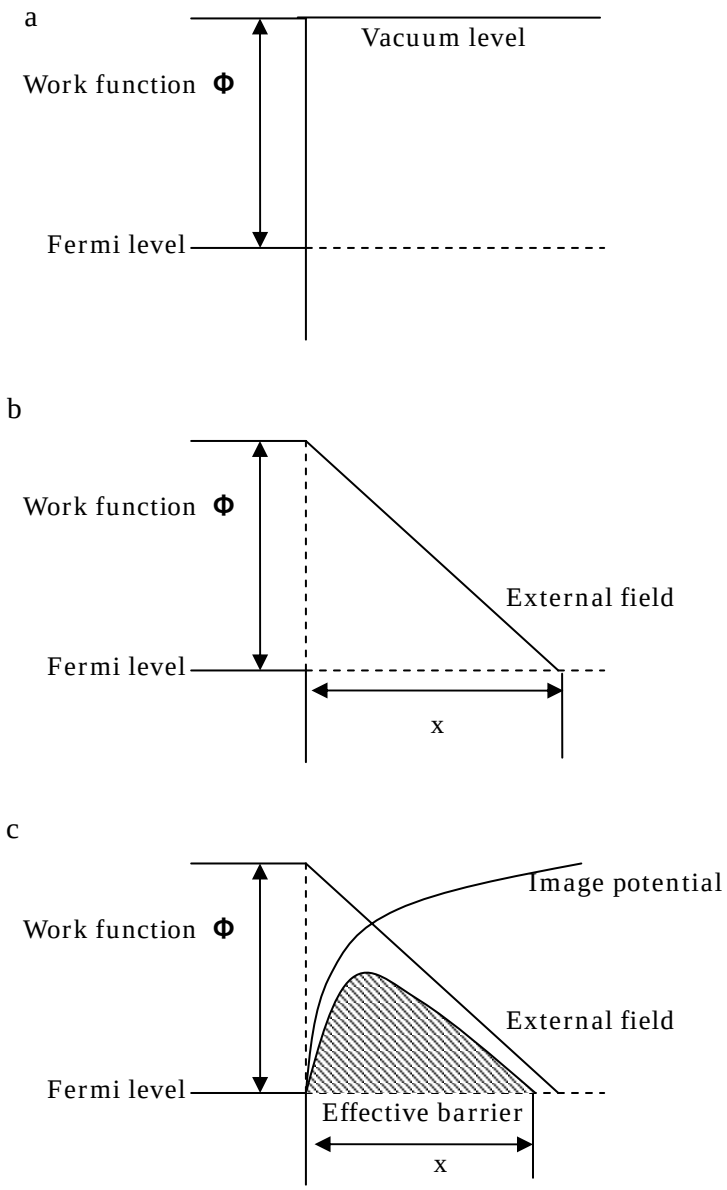

Figure 4.1. a) Interface between metal and vacuum before applying potential. Energy step height is φ; b) Metal/vacuum interface after an external field is applied. A energy barrier with height φ and width x is formed; c) Modification of the barrier shape due to image potential. Reduction in both height and width occurs due to image correction.

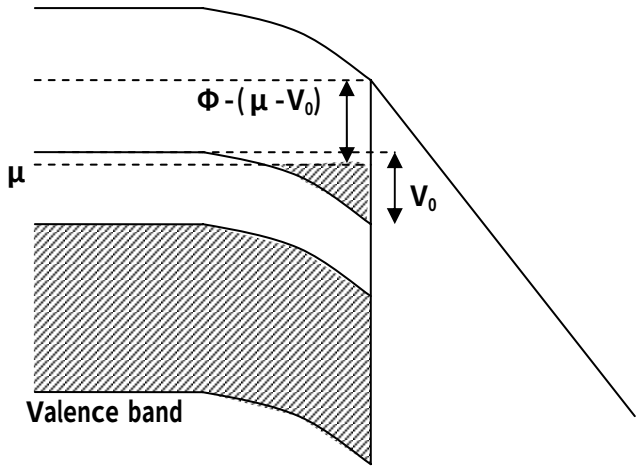

Figure 4.2. Energy diagram of semiconductor/vacuum interface. Electron pool formed by band structure bending of V_0. Actual potential barrier height is $\varphi-(\mu-V_0)$.

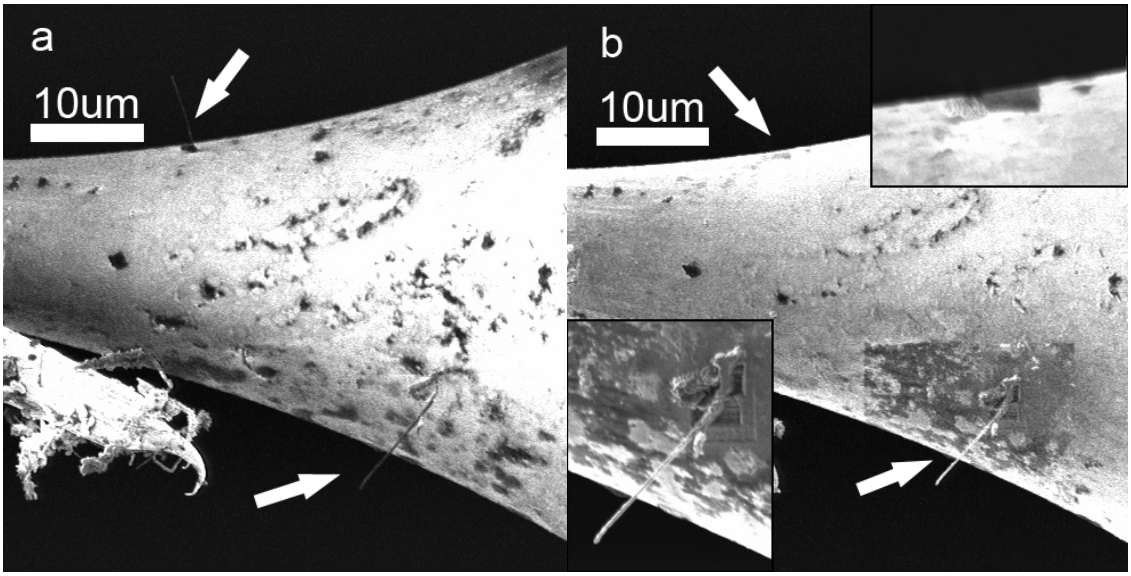

Figure 4.3. a) FIB image of a tungsten tip attached with two free-standing nanowires, which are marked by two white arrows on the graph; b) The upper nanowire is removed by Ga ion beam milling and the lower nanowire is welded to the tungsten body through deposition of W metal. Insets are magnified view of where arrows point to.

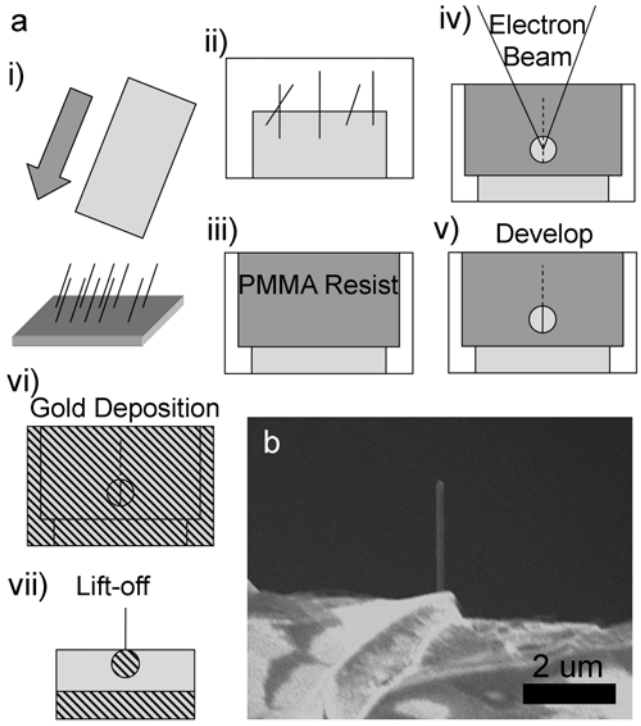

Figure 4.4. a) Procedures for the EBL fabrication of sinlge LaB_6 nanowire field emitters. Bring a rectangular copper foil in contact with a silicon substrate covered with pre-grown LaB_6 nanowires (i); lay the copper foil against a supporting substrate with nanowire-covering side facing up. Select a desired nanowire and record its relative position with reference to foil edge topographic features (ii); apply a PMMA resist on top of the foil covering the nanowires area (iii); Expose electron beam at the root area of the selected nanowire (iv); Develop the drawn pattern with MiBK solution to expose the selected nanowire's root (v); deposit 10nm thick of Cr and 100nm thick of Au into the hole sing thermal evaporation (vi); Resist lift-off by rinsing the sample with acetone to remove excessive Au metal and LaB_6 nanowires. b) An SEM image of a fabricated single LaB_6 nanowire field emitter.

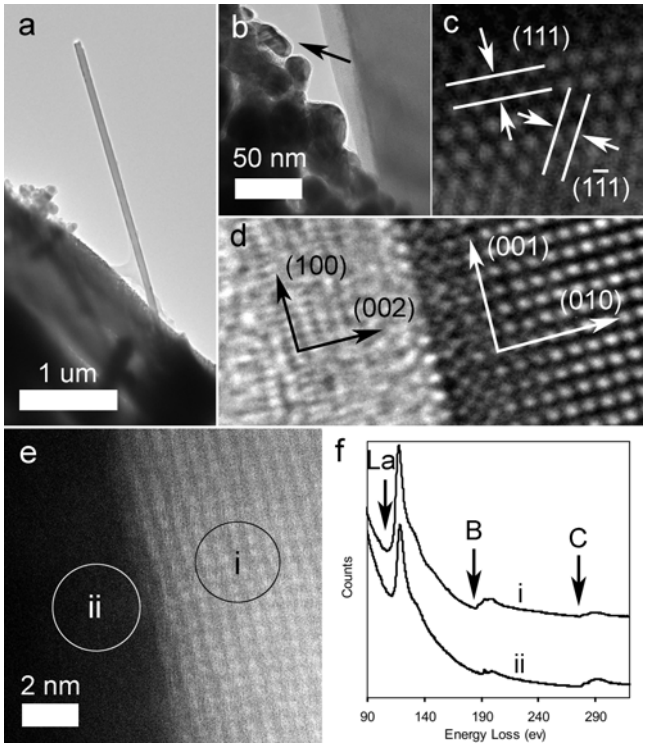

Figure 4.5. a) A low magnification TEM image of a single LaB_6 nanowire emitter fabricated by EBL. b) Au nano-particles covering the nanowire's root area. c) An HRTEM image showing the (20-2) lattice plane of a gold nano-particle. d) An HRTEM image about the side wall of the nanowire, showing the LaB_6 crystal's (-100) lattice plane (darker contrast region) and the (-210) lattice plane of graphite (lighter contrast region). e) STEM image taken on the side wall of a LaB_6 nanowire with (100) lattice direction parallel to electron beam. Two circles i and ii mark the spot where we collect the EELS spectra. f) EELS spectra i and ii, taken from marked cirlcles i and ii in fig. 2e. The La, B peaks' intensities are higher in spectrum i than in spectrum ii, C peak is ranked reversely.

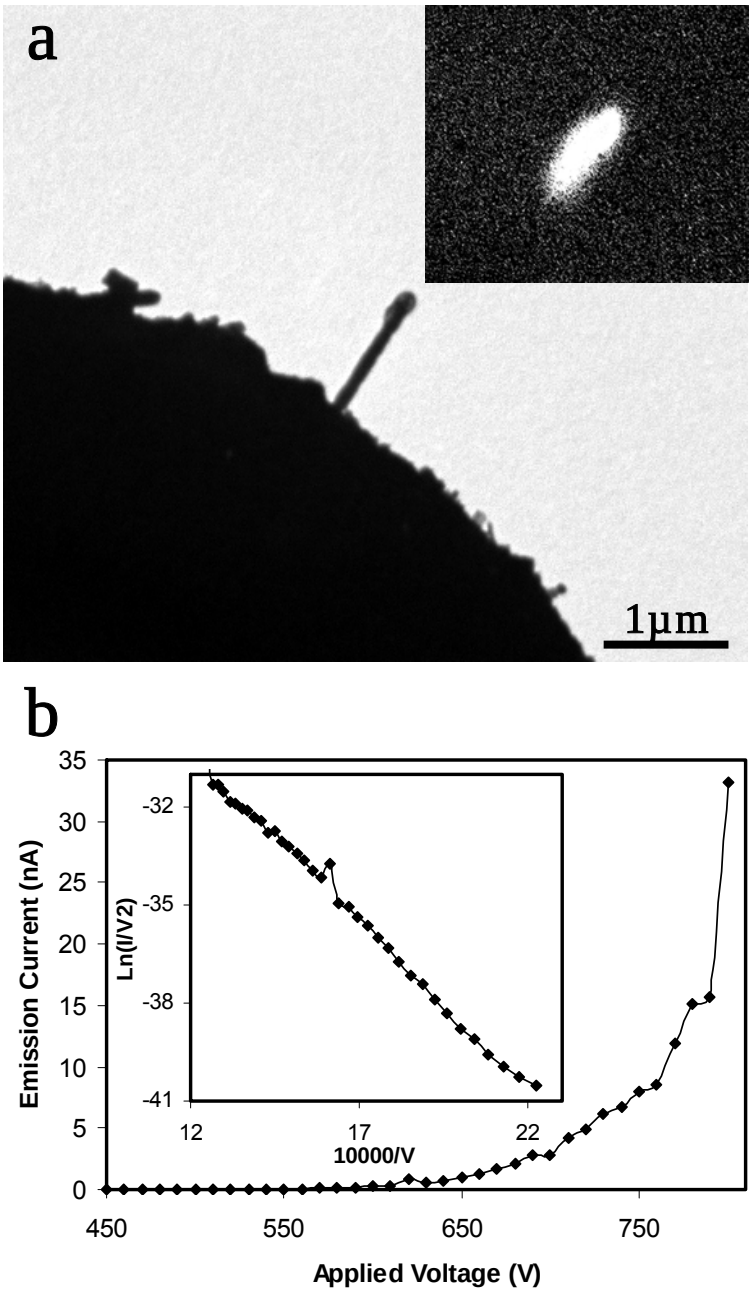

Figure 4.6. a) Low-magnification TEM image of a single LaB_6 nanowire field electron emitter. Inset: Fluorescent electron emission image of the emitter recorded on the phosphor viewing screen. b) I-V curve of the field emission from the single LaB_6 nanowire emitter with F-N plot $ln(I/V^2)$ vs. $1/V$ inserted. Excellent agreement with the F-N theory of field emission is observed.

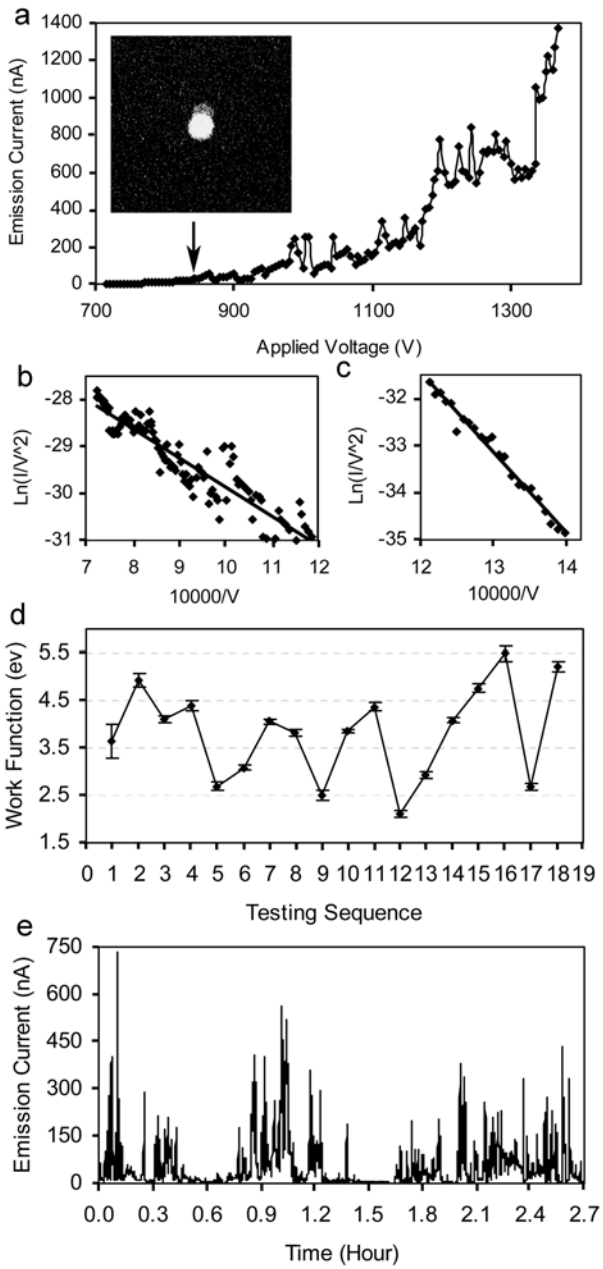

Figure 4.7. a) Field emission I-V curve of the single LaB_6 nanowire electron field emitter. The arrow marks the splitting point of two sets of emission characteristics. Inset is the field emission pattern taken from a phosphor screen at 950v. b) F-N plot of the I-V curve after splitting point, suggesting emission from a low work function surface. c) F-N plot of the I-V curve before splitting point, suggesting emission from a high work function surface. d) Work function profile throughout the 18 I-V curves recorded from the same LaB_6 emitter. e) Field emission stability profile with duration of 2.7 hours.

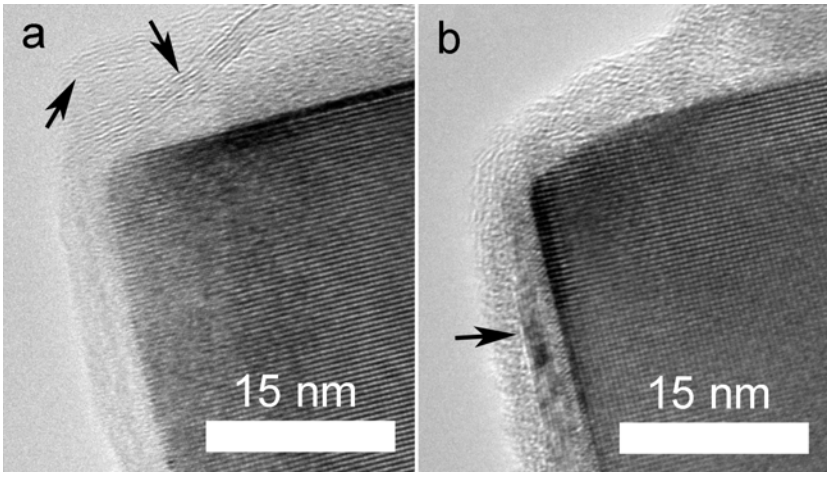

Figure 4.8. a) TEM image taken at the left corner of the LaB_6 nanowire field emitter tip before field emission measurement. b) TEM image taken at the same spot of the same nanowire after the 5-hour field emission measurement. arrows mark the wrapping graphitic layers.

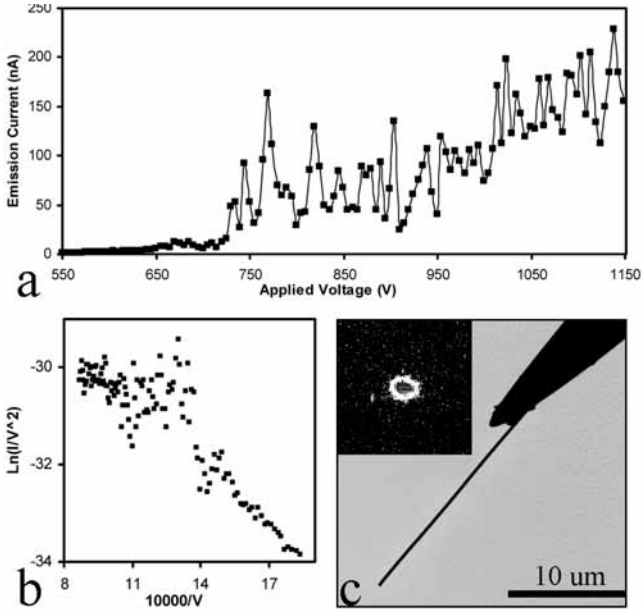

Figure 4.9. (a) field emission I-V curve from a GdB_6 single nanowire field emitter (b) F-N plot of the field emission I-V curve (c) low magnification TEM image of the single nanowire field emitter. Inset is the field emission pattern recorded from a P screen.

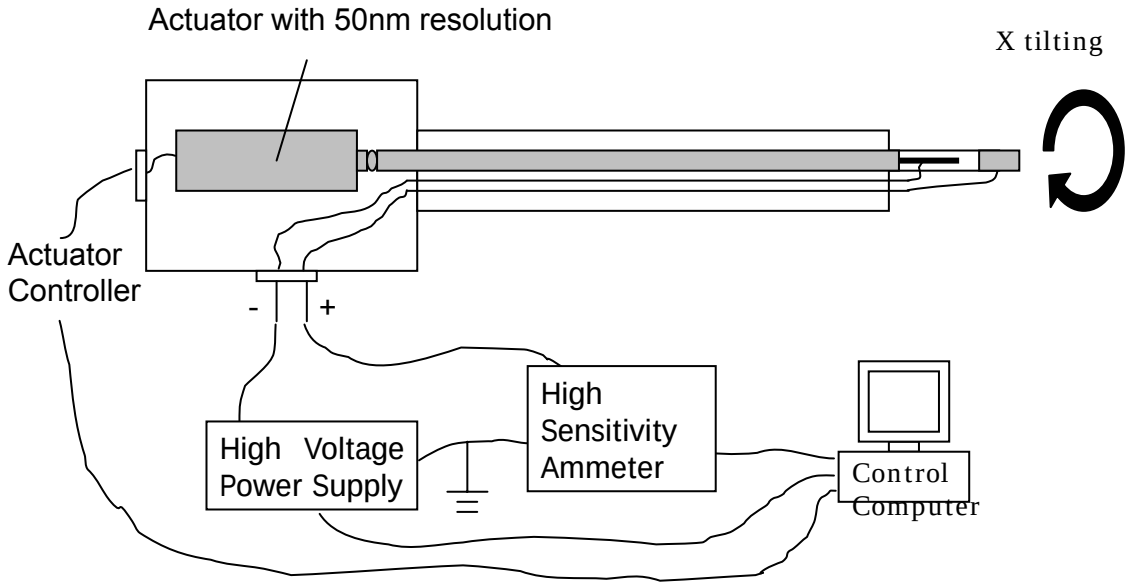

Figure 4.10. Diagram showing the general design for field emission in-situ holder for 2010F HRTEM.

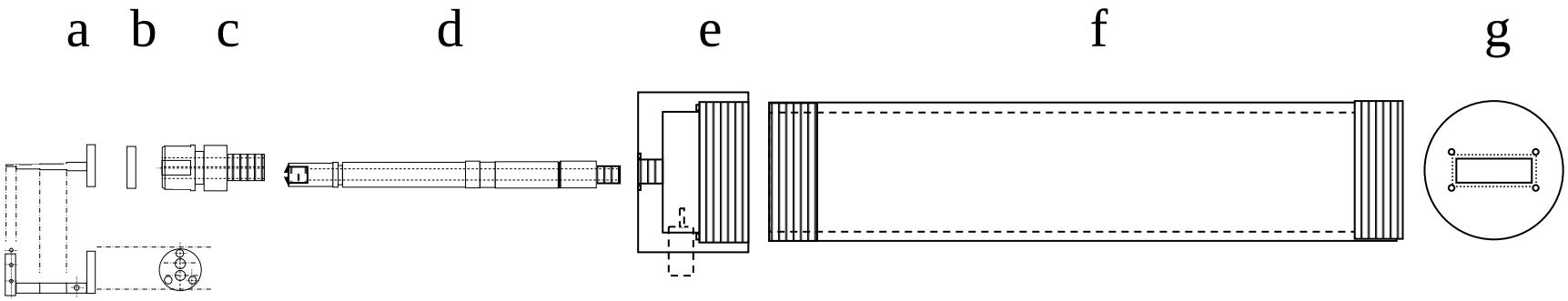

Figure 4.11. Designer drawing for the entire 2010F HRTEM field emission in-situ holder. Parts labeled as through a to g are: head frame, Teflon disk, supporting head, rod chamber, electrode chamber, actuator chamber and actuator chamber lid respectively.

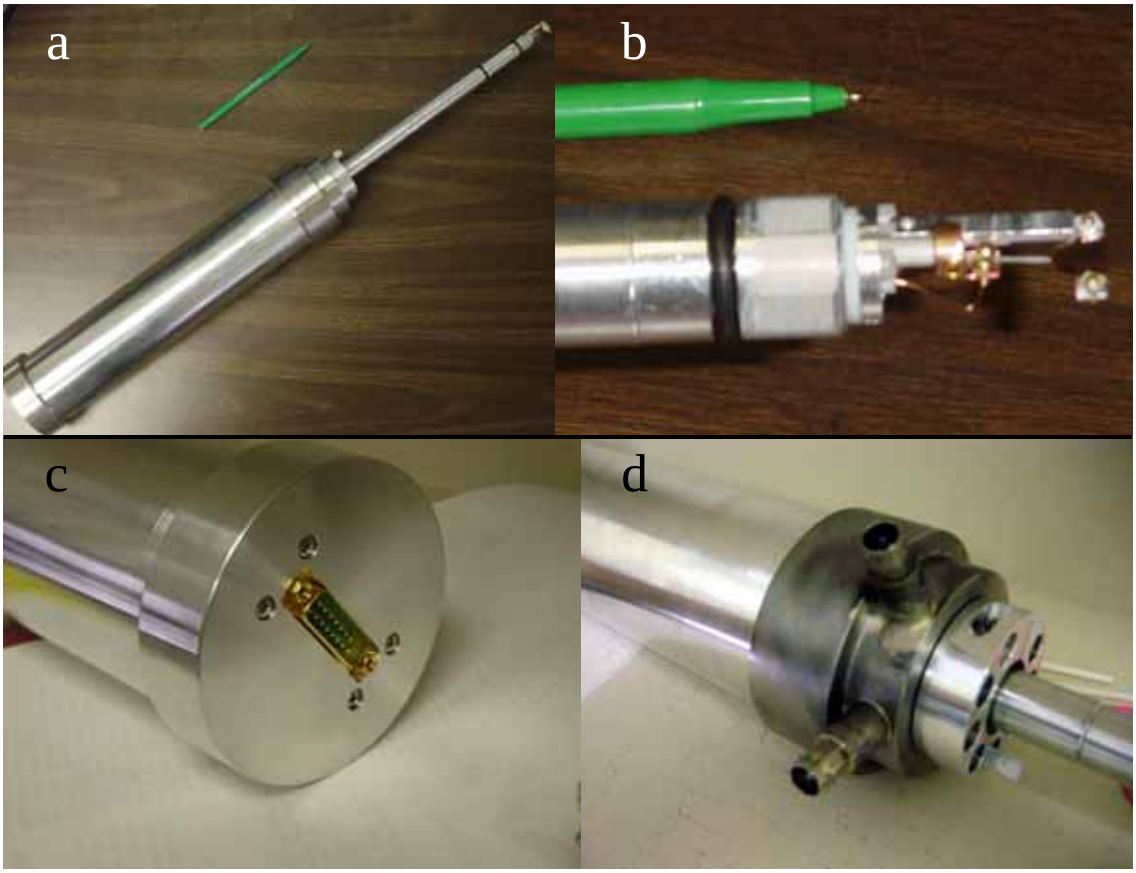

Figure 4.12. a) Top view of the entire 2010F field emission in-situ holder body with a ball-pen beside as reference; b) Holder head with two copper pieces as cathode and anode. A tungsten needle is attached to the cathode to hold nanowire to be studied; c) Rear of the holder where computer interface for the linear actuator is shown; d) high voltage feedthroughs for cathode and anode connection.

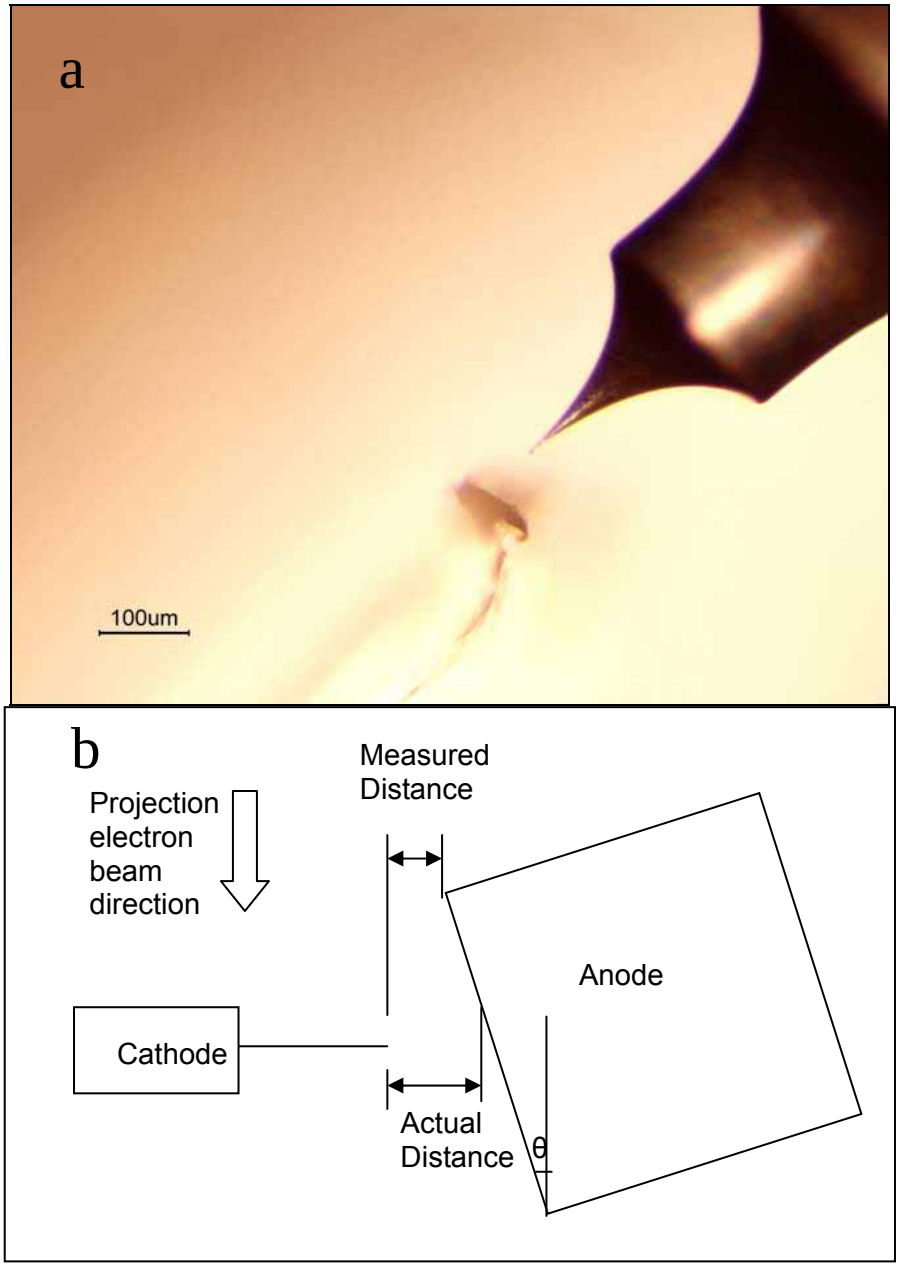

Figure 4.13. a) A photograph taken with optical microscope showing the alignment of tungsten needle to the anode copper foil (side view); b) Drawing illustrating the blocking effect caused by the thickness of anode foil. Measured distance is shorter than actual distance as shown.

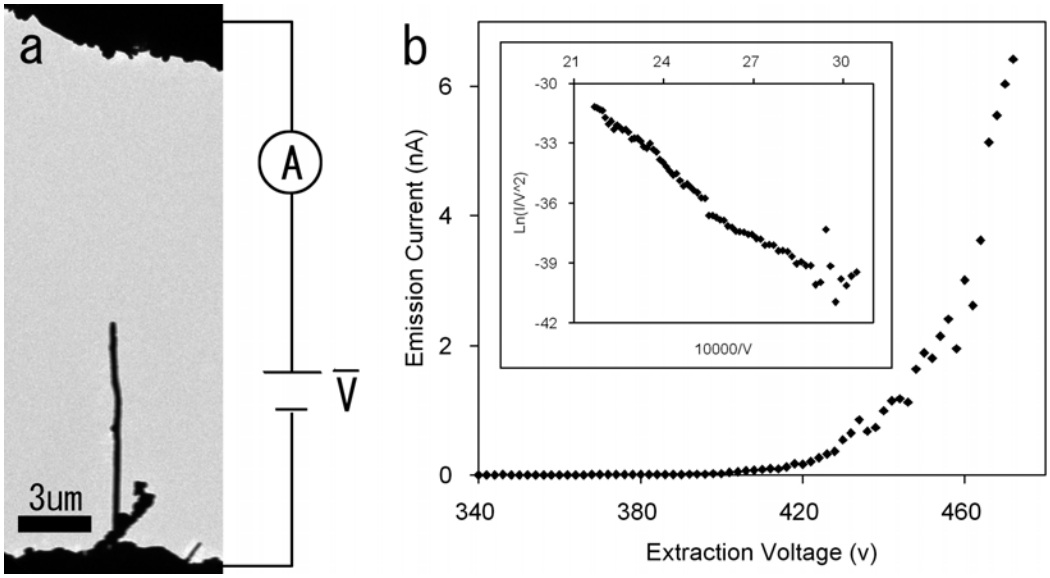

Figure 4.14. a) Low magnification TEM image about a LaB_6 single nanowire field emitter connected in series to the counter electrode with a DC power supply and an amp meter; b) field emission I-V curve recorded during low current in-situ field emission. Inset is the corresponding F-N plot showing good linearity.

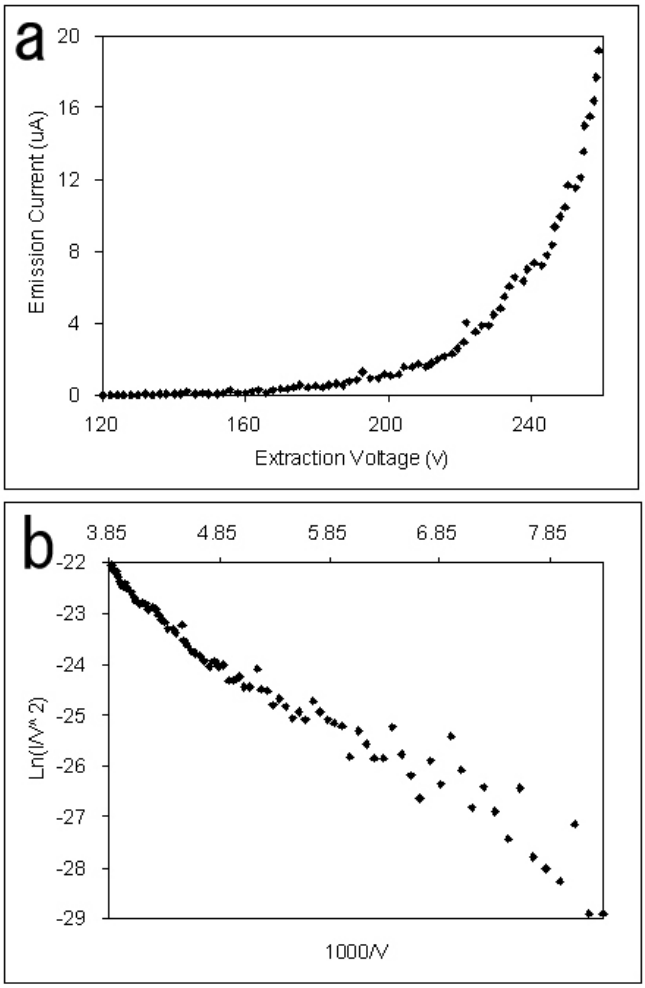

Figure 4.14. a) Emission I-V curve with higher emission current and lower onset voltage after changing cathode/anode distance; b) F-N plot from the I-V curve in a, revealing a steeper slope which corresponds to a lower work function.

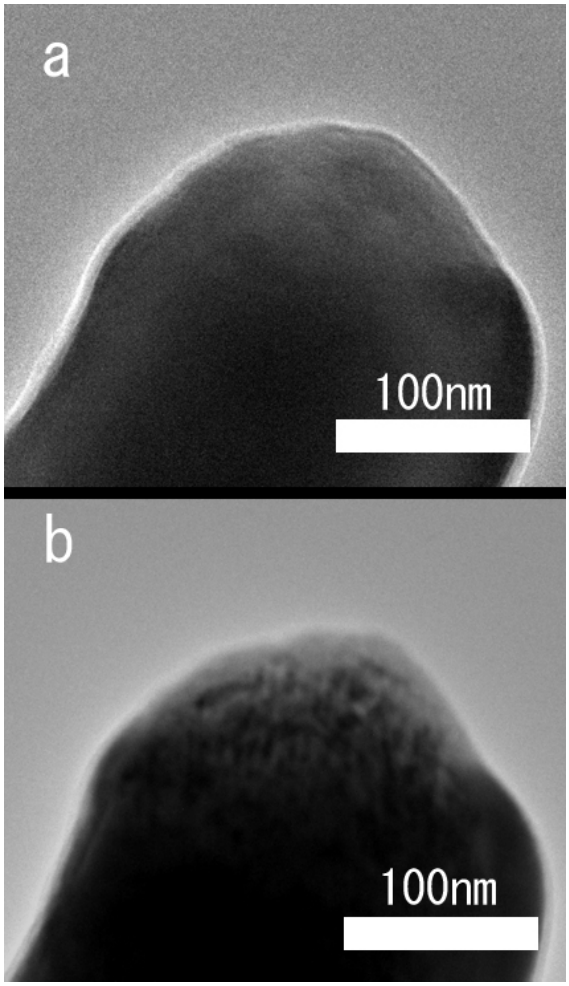

Figure 4.16. a) High resolution image taken at the LaB_6 nanowire field emitter tip before field emission measurement; b) image about the same area after 20 minutes high current density emission experiment.

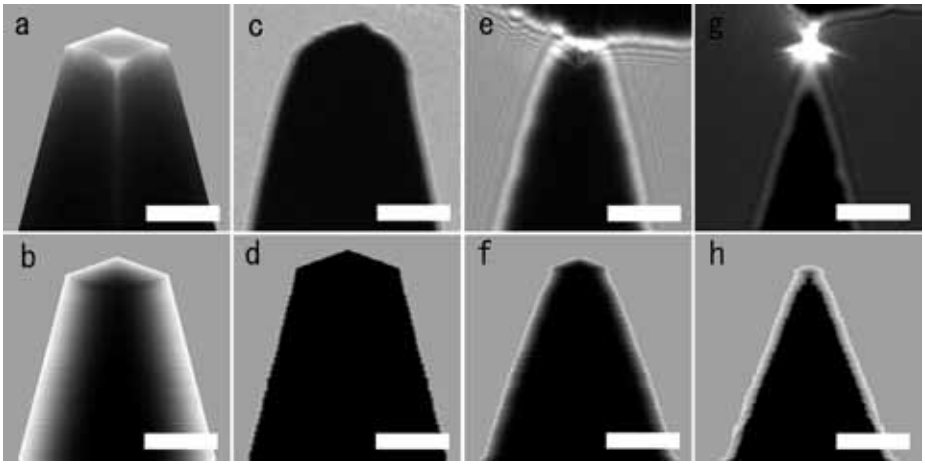

Figure 4.17. a) charge density simulation distribution on a LaB_6 nanowire's tip with bright contrast representing higher density; b) thickness profile of the nanowire emitter along the direction of projection electron beam; c), e) and g) TEM projection images taken at a LaB_6 nanowire emitter's tip area at under-focus condition when 0v, -9v and -24v are applied respectively; d), f) and h) simulation projection images by multiplying a with b. For each conditions, different voltages as of those in c, e and f are used to simulate a.

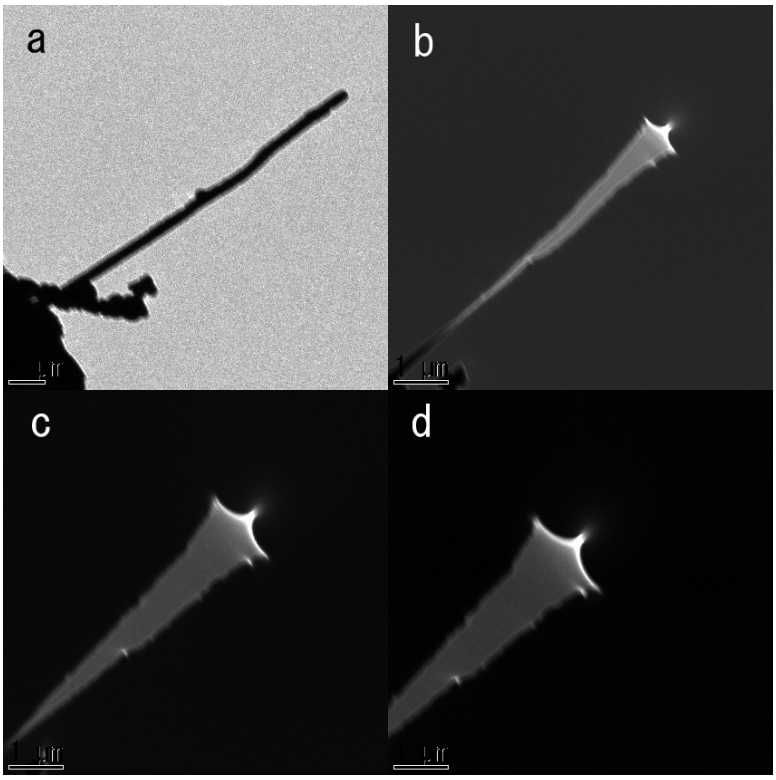

Figure 4.18. A series of TEM images taken at under-focus condition about a LaB_6 nanowire field emitter. The negative biases applied to the nanowire are 0v, -75v, -100v and -160v, respectively presented through a to d.

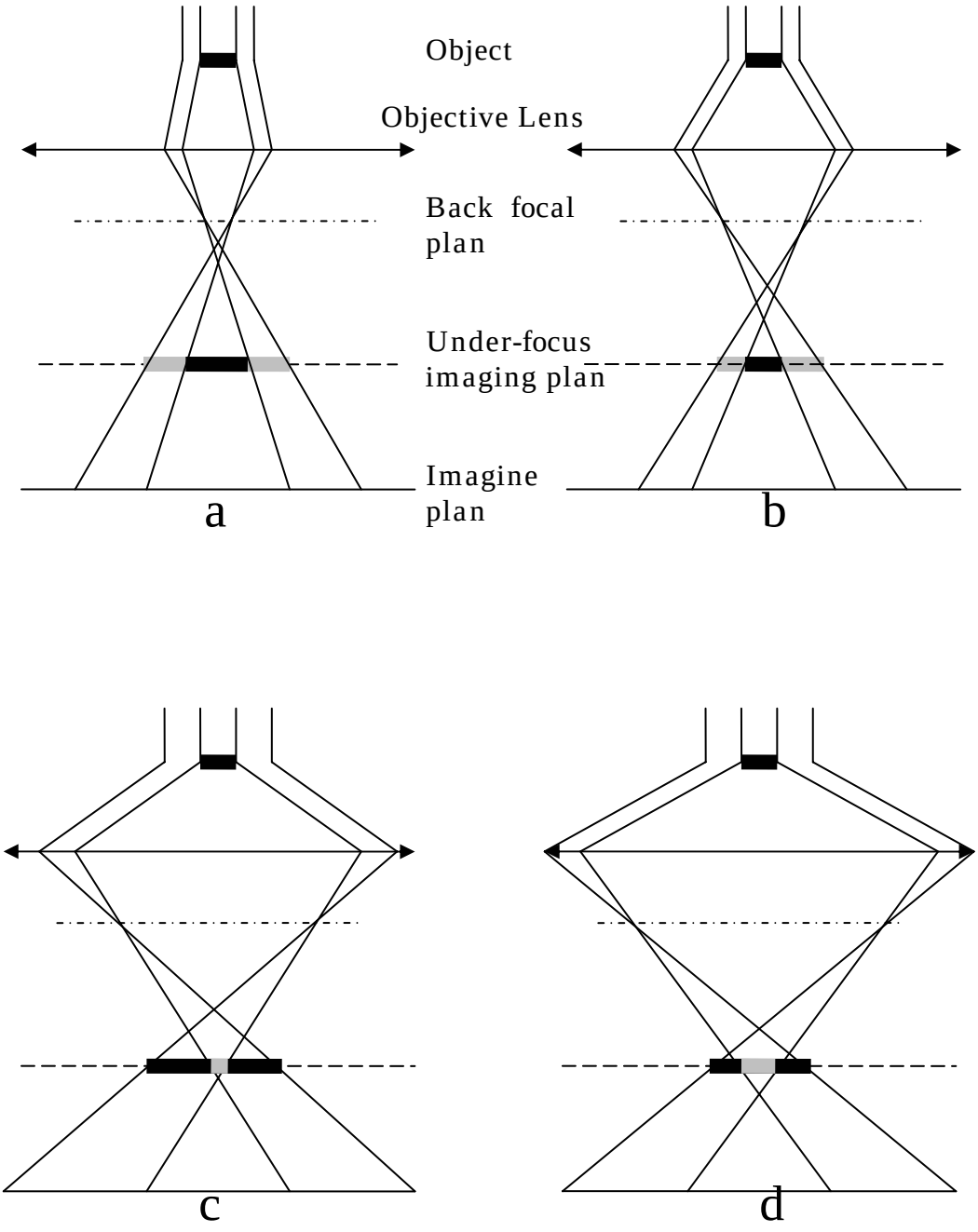

Figure 4.19. Ray diagrams showing the effect of negative charge on size of image when taken at under-focus conditions. Through a to d, sequence is followed by from weak to stronger bias. Grey line at the image plane represents bright contrast and black line represents dark contrast.

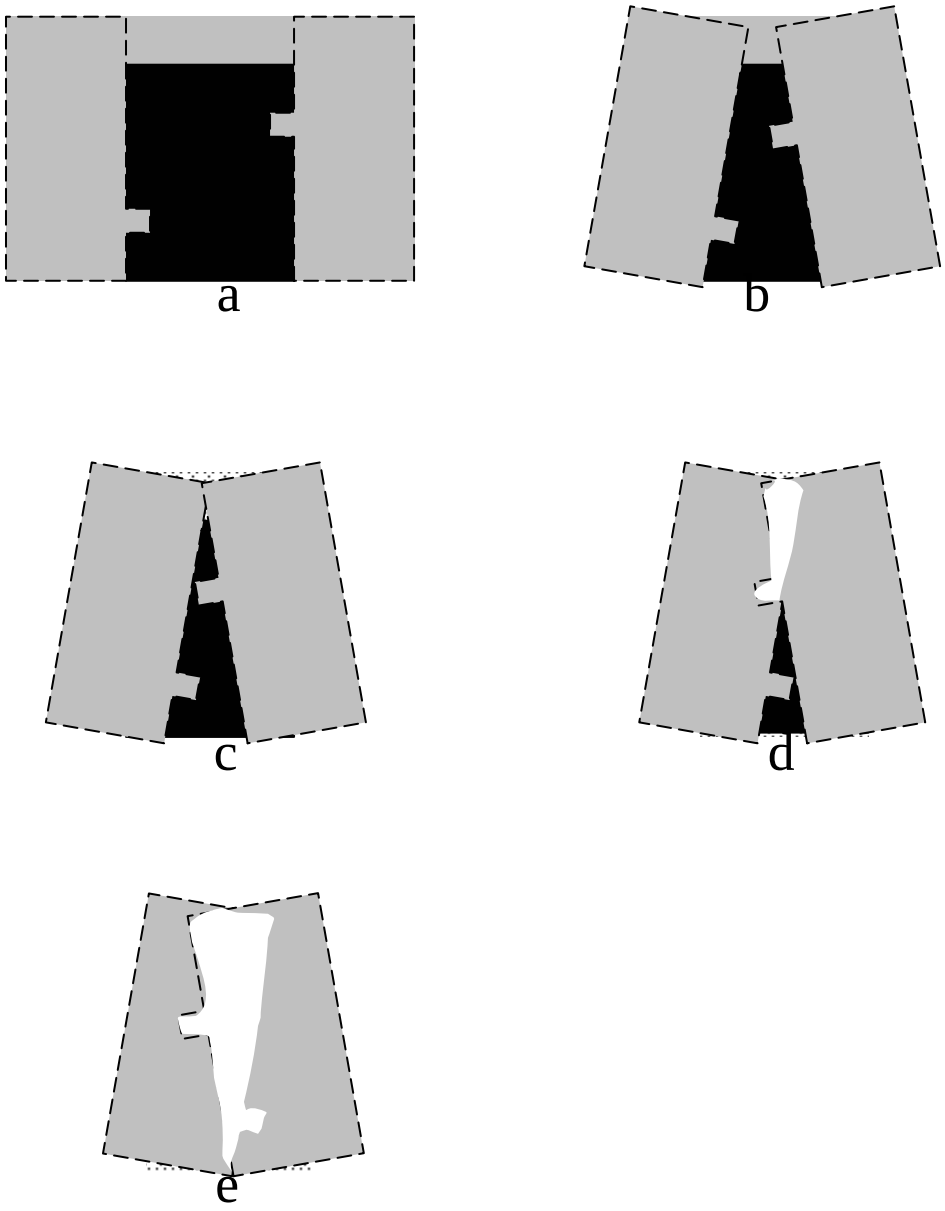

Figure 4.20. Effect of negative charge distribution on the shape of object image when taken at under-focus conditions. Dark area in panel a is the objects original projection image with 0 charge and grey areas inside dashed rectangles are the beams to be bent by charge. Panel b to e show the movement of the two beams and its effect on the image contrast development of the original object.

Appendix

A. Zhang, H., Zhang, Q., Tang, J. & Qin, L.C. (2005). Single-crystalline LaB6 nanowires. Journal of the American Chemical Society, 127(9), 2862-2863.

B. Zhang, H., Zhang, Q., Tang, J. & Qin, L.C. (2005). Single-crystal line CeB6 nanowires. Journal of the American Chemical Society, 127(22), 8002-8003.

C. Zhang, H., Zhang, Q., Zhao, G.P., Tang, J.; Zhou, O. & Qin, L.C. (2005). Single-crystal line GdB6 nanowire field emitters. Journal of the American Chemical Society, 127(38), 13120-13121.

D. Zhang, H., Tang, J., Zhang, Q., Zhao, G.P., Yang, G., Zhang, J., Zhou, O. & Qin, L.C. (2006). Field emission of electrons from single LaB6 nanowires. Advanced Materials, 18(1), 87-91.

J|A|C|S
COMMUNICATIONS

Published on Web 02/11/2005

Single-Crystalline LaB_6 Nanowires

Han Zhang,[†] Qi Zhang,[‡] Jie Tang,[‡,§] and Lu-Chang Qin*[,†,‡]

Curriculum in Applied and Materials Sciences and Department of Physics and Astronomy, University of North Carolina at Chapel Hill, Chapel Hill, North Carolina 27599-3255, and National Institute for Materials Science, Tsukuba, Japan

Received October 26, 2004; E-mail: lcqin@physics.unc.edu

Lanthanum hexaboride (LaB_6) is widely used in modern technology as an excellent thermionic electron emission source which offers high brightness and long service life. The advantages are originated from its low work function and nature of low volatility.[1,2] Extensive thermal field-emission tests have also been performed with LaB_6.[3−5] These studies revealed that, compared to the LaB_6 thermionic electron emitters, a brightness of at least 2 orders of magnitude higher could be achieved with the LaB_6 thermal field emitter. The required local electric field is only half of that needed by the typical commercial thermal field emitters made with zirconiated tungsten sharp tips.

For a LaB_6 thermionic electron emitter, a smaller emitter tip diameter results in a brighter electron beam and a smaller minimum electron beam spot size, which will in turn improve greatly the resolution and performance of electron optical instruments such as the transmission electron microscope (TEM) and the scanning electron microscope (SEM) that are often equipped with a thermionic LaB_6 electron emission cathode.[6−8] The tip diameter of commercial LaB_6 thermionic electron guns is typically in the range of $\sim$5−100 μm. The emitter tip size plays an even more important role in the thermal field-emission applications such as the Shottky electron gun, which at present is considered as the best high-resolution electron filament. With a low work function as one factor, a strong local electric field is the other factor to determine the electric field-induced emission for a given applied voltage and cathode gun geometry. For a rod-shaped field-induced electron emitter, the local electric field F which extracts electrons from the emitter tip can be expressed as a function of the applied voltage V, the emitter tip radius r, its longitudinal length h, and the distance d between the anode and the substrate where the emitter stands: [9]

$$F = 1.2V(2.5 + h/r)^{0.9}\,[1 + 0.013d/(d - h) - 0.033(d - h)/d]/d$$

The above relationship indicates that the smaller the emitter tip radius r and the higher its aspect ratio h/r, the greater the local electric field F will become, which in turn will enable field-induced electron emission to occur at a lower applied voltage compared to emitters of the same material but of larger dimensions. This lowered turn-on voltage for field-induced electron emission has been observed in many nanoscale structures including carbon nanotubes and nanowires of SiC, W, CuS, and MoO_3 materials.[10−14] The small diameter and large aspect ratio of such one-dimensional nanostructures magnify enormously the local electric field at the emitter's free end and give greatly enhanced electric field-induced emission from these materials whose work functions are even considered high compared to that of LaB_6. Therefore, it is of both great scientific and practical significance to fabricate and investigate nanoscale LaB_6, the compound being considered as the best electron emitter material thus far.

We herein report the synthesis and structural characterization of LaB_6 nanowires with diameter smaller than 100 nm and length more than a few tens of micrometers. We have developed and applied a chemical vapor deposition (CVD) method that produces single-crystalline LaB_6 nanowires of uniform diameter and well-defined growth direction. The synthesis is based on the following chemical reaction:[15−17]

$$2LaCl_3(g) + 12BCl_3(g) + 21H_2(g) = 2LaB_6(s) + 42HCl(g)$$

The reaction was conducted in a tube furnace operated at 1150 °C where the BCl_3 gas was introduced to the reaction zone in a stainless steel tube and $LaCl_3$ powders were vaporized in a tantalum bowl placed inside the tube furnace. The reaction was conducted in an atmosphere at 1 atm pressure of hydrogen and nitrogen ($5\%H_2 + N_2$) gases. Single-crystalline nanowires were grown on gold metal films coated on silicon substrates. Single-crystalline whiskers can also be produced under similar conditions.

For electron diffraction and microscopy observations, the LaB_6 nanowires were first dispersed in ethanol and then collected onto a copper grid that was coated with a thin holey carbon film. The TEM (JEM-2010F equipped with a Shottky field-emission gun) was operated at 200 kV during structural characterization.

A representative morphological study of the nanowires is presented in Figure 1. The nanowires with smooth surfaces of diameter around 100 nm and length extending to more than a few tens of micrometers were observed and measured using both electron imaging and selected-area electron diffraction. Figure 1a is a typical TEM image at low magnification where the dimensional morphology is displayed. Figures 1b−d show three electron diffraction patterns taken from three different crystal zone axes of the same nanowire to identify the LaB_6 crystal lattice, which has a primitive cubic structure of space group $Pm3m$ and has lattice constant $a = 0.4153$ nm. The three zone axes are [0 1 −1] (Figure 1b), [−1 2 −1] (Figure 1c), and [−1 4 −2] (Figure 1d). The relative orientational relationship between the three electron diffraction patterns is also given in the figures. For example, the [−1 2 −1] zone axis electron diffraction pattern (Figure 1c) was obtained by rotating the nanowire 30° about its [111] direction (illustrated in Figure 1b). It can also be seen from the diffraction patterns that all reflection spots are elongated to become streaks and these streaks are always perpendicular to the [111] lattice direction, indicating that the nanowire axis is parallel to the [111] direction of the LaB_6 crystal. This result was further confirmed by high-resolution transmission electron microscopy (HRTEM).

HRTEM was applied to analyze the detailed atomic structure around the nanowire tip. Figure 2a is an electron microscope image

[†] Curriculum in Applied and Materials Sciences, University of North Carolina at Chapel Hill.
[‡] Department of Physics and Astronomy, University of North Carolina at Chapel Hill.
[§] National Institute for Materials Science.

10.1021/ja043512c CCC: $30.25

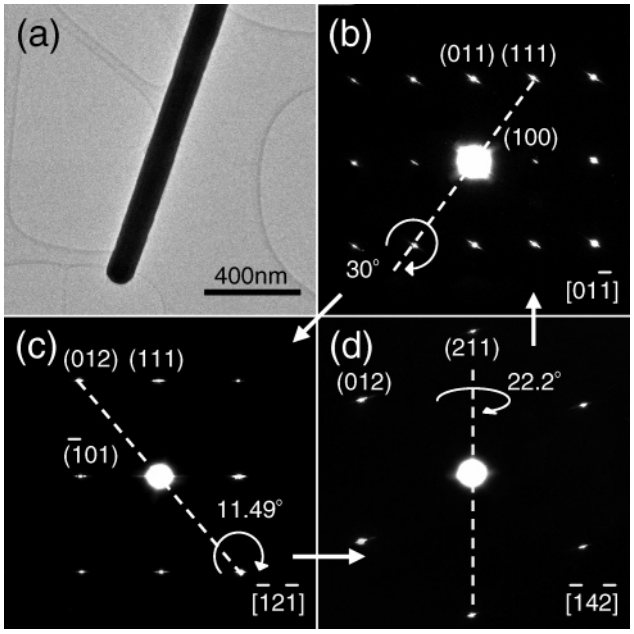

Figure 1. (a) Low-magnification TEM image of a LaB_6 nanowire. (b−d) Electron diffraction patterns of the same LaB_6 nanowire tilted to zone axes [0 1 −1], [−1 2 −1], and [−1 4 −2], respectively. Dash lines indicate the tilting axes about which the nanowire was rotated to obtain the needed orientation. Circular arrows give the tilting angles, and the straight arrows point to the tilting sequence.

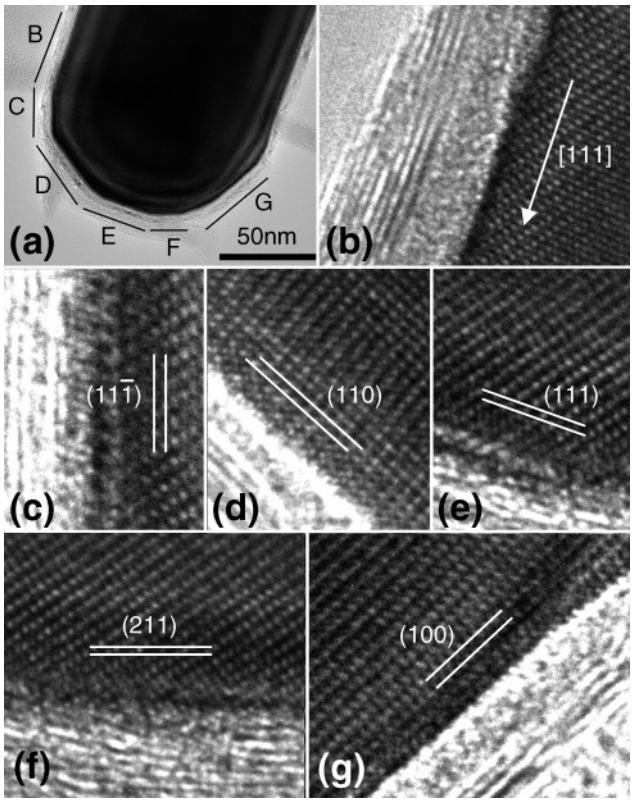

Figure 2. (a) High-resolution image of the LaB_6 nanowire tip with terminating facets labeled with letters B−G. (b−g) Lattice images of the nanowire stem (B) and facets C−G as indicated in (a). The terminating facets are lattice planes of low indices, such as {100} (G), {110} (D), and {111} (C and E).

of the nanowire tip. The tip is hemispherical, and it is terminated by several different lattice planes that are labeled with letters B through G on the image. The HRTEM images characterizing these faceted lattice planes are displayed in Figures 2b−g in corresponding sequence. Figure 2b shows the lattice image of the stem area (marked B in Figure 2a) of the LaB_6 nanowire. The axial direction, [111], which is the same of the growth direction, of the nanowire has also been indicated in the figure. Figure 2c shows the lattice image near facet C of Figure 2a, whose surface is terminated with the (1 1 −1) lattice plane. Figure 2d shows the area marked with letter D in Figure 2a, which has a (110) facet. Figure 2e shows a (111) facet, which is equivalent to Figure 2c in atomic structure with the same surface energy and is perpendicular to the nanowire axis [111]. Figure 2f shows (211) facet corresponding to the area marked with F in Figure 2a. It is interesting to note that facet F is the smallest compared with others shown in Figure 2a. Area G, shown in Figure 2g, is a facet of (100) which is a low index lattice plane. By examining the areas covered by the various facets characterized, we found that the (100), (110), and (111) planes are the dominant terminating facets. Lattice planes of higher indices appeared only as transitions between the above dominant facet planes of low indices. This result agrees with the lowest surface energy principle in crystal growth.

Though commercial LaB_6 electron gun filaments are usually made along the ⟨100⟩ direction of the crystal lattice due to the {100} plane's lower work function and higher symmetry,[1] it has been suggested that the ⟨111⟩ oriented LaB_6 single-crystalline tips might be an even better alternative since they offer better stability.[18] Electric field-induced electron emission measurements on the LaB_6 nanowires are in progress.

In conclusion, we have developed a CVD method that has been able to produce successfully LaB_6 nanowires of well-characterized morphology. The nanowires have a diameter around and smaller than 100 nm and length extending to a few tens of micrometers. The growth direction of the nanowires is its ⟨111⟩ lattice direction, and they have hemispherical tips that are terminated by lattice planes of low indices such as {100}, {110}, and {111}. The LaB_6 nanowires' potential applications include providing thermionic emission, field-induced emission, and thermal field-induced emission of electrons for TEM, SEM, flat panel displays, as well as other electronic devices that require high-performance electron sources.

References

(1) Gesley, M.; Swanson, L. W. *Surf. Sci.* **1984**, *146*, 583.
(2) Swanson, L. W.; Gesley, M.; Davis, P. *Surf. Sci.* **1981**, *107*, 263.
(3) Harada, K.; Nagata, H.; Shimizu, R. *J. Electron. Microsc.* **1991**, *40*, 1.
(4) Nagata, H.; Harada, K.; Shimizu, R. *J. Appl. Phys.* **1990**, *68*, 3614.
(5) Nakamoto, M.; Furuda, K. *Appl. Surf. Sci.* **2002**, *202*, 289.
(6) Yamabe, M.; Furukawa, Y.; Inagaki, T. *J. Vac. Sci. Technol., A* **1984**, *2*, 1361.
(7) Doy, T. K.; Kasai, T.; Ohmori, H. *J. Ceram. Soc. Jpn.* **1999**, *107*, 502.
(8) Tennant, D. M.; Swanson, L. W. *J. Vac. Sci. Technol., B* **1989**, *7*, 93.
(9) Bonard, J. M.; Dean, K. A.; Coll, B. F.; Klinke, C. *Phys. Rev. Lett.* **2002**, *89*, 197602.
(10) Rinzler, G.; Hafner, J. H.; Nikolaev, P.; Lou, L.; Kim, S. G.; Tomanek, D.; Nordlander, P.; Colbert, D. T.; Smalley, R. E. *Science* **1995**, *269*, 1550.
(11) Wong, K. W.; Zhou, X. T.; Au, F. C. K.; Lai, H. L.; Lee, C. S.; Lee, S. T. *Appl. Phys. Lett.* **1999**, *75*, 2918.
(12) Lee, Y. H.; Choi, C. H.; Jang, Y. T.; Kim, E. K.; Ju, B. K.; Min, N. K.; Ahn, J. H. *Appl. Phys. Lett.* **2002**, *81*, 745.
(13) Chen, J.; Deng, S. Z.; Xu, N. S.; Wang, S.; Wen, X.; Yang, S.; Yang, C.; Wang, J.; Ge, W. *Appl. Phys. Lett.* **2002**, *80*, 3620.
(14) Li, Y. B.; Bando, Y.; Golberg, D.; Kurashima, K. *Appl. Phys. Lett.* **2002**, *81*, 5048.
(15) Motojima, S.; Takahashi, Y.; Sugiyama, K. *J. Cryst. Growth* **1978**, *44*, 106.
(16) Givargizov, E. I.; Obolenskaya, L. N. *J. Cryst. Growth* **1981**, *51*, 190.
(17) Givargizov, E. I.; Obolenskaya, L. N. *J. Less-Common Met.* **1986**, *117*, 97.
(18) Takigawa, T.; Sasaki, I.; Meguro, T.; Motoyama, K. *J. Appl. Phys.* **1982**, *53*, 5891.

JA043512C

J|A|C|S
COMMUNICATIONS

Published on Web 05/12/2005

Single-Crystalline CeB_6 Nanowires

Han Zhang,[†] Qi Zhang,[‡] Jie Tang,[‡,§] and Lu-Chang Qin*[,†,‡]

Curriculum in Applied and Materials Sciences and Department of Physics and Astronomy, University of North Carolina at Chapel Hill Chapel Hill, North Carolina 27599-3255, and National Institute for Materials Science, Tsukuba, Japan

Received March 3, 2005; E-mail: lcqin@physics.unc.edu

Single-crystalline rare-earth hexaborides, especially lanthanum hexaboride (LaB_6) and cerium hexaboride (CeB_6), are thermionic cathode materials widely used in a broad range of electron beam applications where a high brightness electron source with long service life is required. The advantage of using rare-earth hexaboride originated from its crystal structure, which is composed of rare-earth metal atoms embedded inside a stable boron octahedron network.[1] This arrangement allows a unique combination of all the desired properties for an excellent cathode material, such as low work function, low volatility, low electrical resistivity, high mechanical strength, and high chemical resistance, while these properties seldom coexist in any other materials. Compared to LaB_6, CeB_6 is believed to have even lower work function (~2.5 eV) and lower volatility, which mean lower operation temperature and longer service life when used as a thermionic electron emitter.[2,3] The low work function is even more crucial a criterion when a cathode material is designed for field-induced electron emission applications, which offer a brightness 100 or more times higher than a thermionic electron source. Field emission current density J can be expressed by the Fowler−Nordheim equation:[4]

$$J = 1.5 \times 10^{-6}(E^2/\phi)\exp(10.4/\phi^{1/2} - 6.44 \times 10^7\phi^{3/2}/E)\mathrm{A/cm}^2$$

where E is the local electric field produced at the tip and ϕ is the work function of the emitting surface of the tip. It can be inferred that the emission current density J is enhanced almost exponentially with the decrease of work function ϕ. However, to achieve a high emission current density J, high local electric field E is another important factor and can be expressed as $E = V/5r$, with V being the voltage applied on the emitter tip and r being the tip radius. The difficulty in making single-crystalline rare-earth hexaboride sharp tips has impeded the development of field emission cathode from this low work function material. Several attempts were made to fabricate electrolytically sharpened LaB_6 and CeB_6 needle-shaped field emitters from bulk single crystals, but no satisfactory field emission results have been reported, in contrast to the highly expected low turn-on voltage and high emission current promised by the low work function that these hexaborides possess.[5−9] On the other hand, sharper tips and higher aspect ratio will also enhance field emission for a given material. In a recent communication, we reported a successful synthesis of ⟨111⟩ oriented LaB_6 nanowires with diameter below 100 nm.[10] In a subsequent article, we reported the fabrication of ⟨001⟩ oriented LaB_6 nanowires and measurement of their field emission characteristics where a field emission current density of about 5×10^5 A/cm^2 was obtained at a driving voltage of 800 V.[11] In this communication, we present the successful synthesis of single-crystalline CeB_6 nanowires with lateral dimension around 50 nm, length more than several micrometers, and a well-defined ⟨001⟩ crystal growth direction.

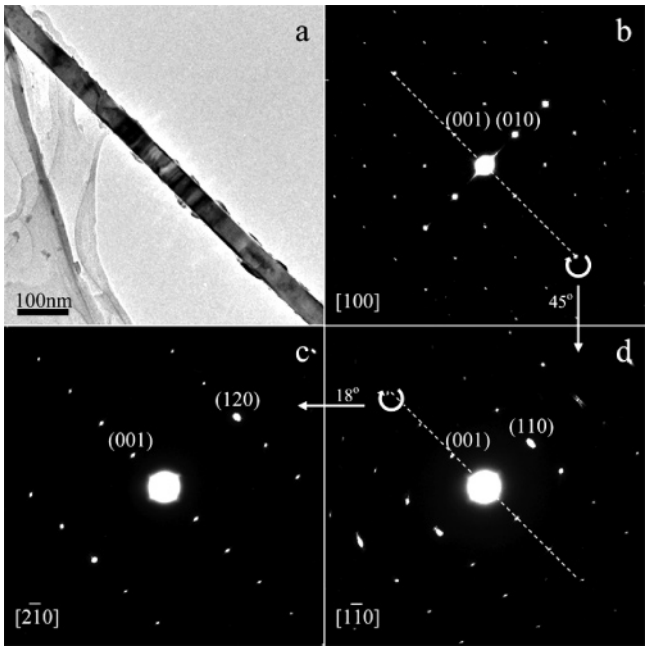

Figure 1. (a) Low-magnification TEM image of a CeB_6 nanowire. (b−d) Electron diffraction patterns of the same CeB_6 nanowire tilted to zone axes [100], [1$\bar{1}$0], and [2$\bar{1}$0], respectively. Dashed lines indicate the tilting axes about which the nanowire is rotated to the desired orientation. Circular arrows indicate the tilting angles, and the straight arrows point to the tilting sequence in experiment.

The synthesis is based on the following chemical reaction:

$$2CeCl_3(g) + 12BCl_3(g) + 21H_2(g) = 2CeB_6(s) + 42HCl(g)$$

The reaction was conducted in a tube furnace operated at 1125 °C where the BCl_3 gas (Aldrich, 99.9%) was introduced to the reaction zone in a quartz tube and $CeCl_3$ powders (Aldrich, 99.9%) were vaporized in a quartz boat placed inside the same tube furnace. A silicon substrate coated with platinum was placed at a position downstream of the quartz boat for CeB_6 nanowire deposition.

After the reaction, CeB_6 nanowires with lateral dimensions ranging from below 50 nm to more than 1 μm were grown on the substrate surface. The nanowires were examined in both scanning electron microscope (SEM, JEM-6300) equipped with an energy-dispersive X-ray spectrometer (EDX, KevexSigma3) and transmission electron microscope (JEM-2010F operated at 200 kV). EDX analysis indicates that these nanowires are composed of B and Ce elements.

A representative morphological study and structure determination of the nanowires are presented in Figure 1. Figure 1a is a typical

[†] Curriculum in Applied and Materials Sciences, University of North Carolina.
[‡] Department of Physics and Astronomy, University of North Carolina.
[§] National Institute for Materials Science.

10.1021/ja051340t CCC: $30.25

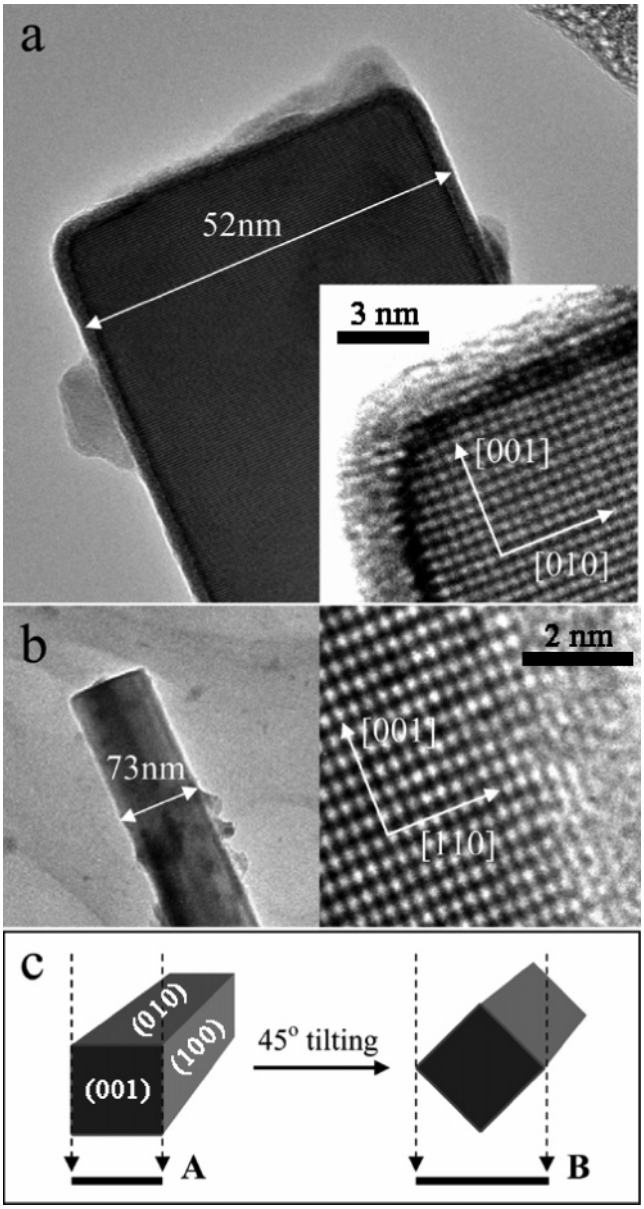

Figure 2. (a) [100] direction TEM image of the CeB_6 nanowire tip. Inset is a high-resolution lattice image of the tip's top left corner. (b) [$1\bar{1}0$] direction TEM image of the same nanowire together with a high-resolution lattice image showing its right-side wall. (c) Illustration of the 45° tilting process to reconstruct the morphology of the nanowire.

TEM image at low magnification showing a straight nanowire with smooth surfaces of lateral dimension around 50 nm and length extending more than 10 μm. Parts b−d of Figure 1 show three electron diffraction patterns taken along three different crystal zone axes of the same nanowire to identify the CeB_6 crystal lattice, which has a primitive cubic structure of space group *Pm*3*m* and has lattice constant $a = 0.4129$ nm. The three zone axes are [100] (Figure 1b), [$2\bar{1}0$] (Figure 1c), and [$1\bar{1}0$] (Figure 1d). The relative orientational relationship between the three electron diffraction patterns are also given in the figures. For example, the [$1\bar{1}0$] zone axis electron diffraction pattern (Figure 1d) was obtained by tilting the nanowire 45° about its [001] direction (illustrated in Figure 1b).

Due to the important role of the emitter tip in the emission properties, a morphological study of the tip area of a typical CeB_6 nanowire was also conducted as shown in Figure 2. Figure 2a is a TEM image showing that the CeB_6 nanowire has a flat tip top, and its lateral dimension is measured to be 52 nm in this orientation. A high-resolution electron microscopy (HRTEM) image of the top left corner the CeB_6 nanowire is displayed in the inset. We found that, similar to the LaB_6 nanowires,[11] the growth direction is the [001] axis of the crystal and both the flat tip top and the nanowire side surfaces are terminated with the {100} lattice planes. Figure 2b is a TEM image of the same tip after a 45° tilting about the axial direction of the nanowire. As expected, the electron diffraction pattern confirmed that the nanowire was oriented in the [$1\bar{1}0$] zone axis, as also shown in the HRTEM image in Figure 2b. Moreover, since now the projected width of the nanowire at this angle is 73 nm, which makes a ratio of $\sqrt{2}$ with that obtained in Figure 2a, it suggests that the nanowire has a square cross section. This morphology of the nanowire is also indicated in the left image of Figure 2b, where a darker contrast line appears in the middle of the nanowire due to the largest thickness in the diagonal direction of the nanowire of a square cross section. A schematic summary of the nanowire morphology is illustrated in Figure 2c: both the tip of the nanowire and the side surfaces are terminated with the {100} crystallographic lattice planes as labeled in the illustration; the dashed arrows represent the direction in which the electron beam is incident with the projections labeled underneath using letters A and B, which correspond to the images given in Figure 2a and Figure 2b, respectively. After checking several other nanowires among the same sample, we obtained similar results except that some nanowires have cross sections that are rectangular rather than square. The fact that catalyst particles were sometimes seen at the end of the nanowires suggests that the formation of the CeB_6 nanowires is likely a vapor−liquid−solid process.

In conclusion, we have developed a chemical vapor deposition method that is able to produce successfully CeB_6 nanowires of well-defined morphology. The nanowires have a square cross section with width of about 50 nm and have lengths extending more than 10 μm. The growth direction of the nanowires is the ⟨001⟩ lattice direction, and they have flat tips and walls that are all terminated by the {100} lattice planes. These CeB_6 nanowires are of potential use as point electron emitters for applications including providing thermionic emission, field-induced emission, and thermal field-induced emission of electrons for TEM, SEM, flat panel displays, as well as other electronic devices that require high-performance electron sources.

Acknowledgment. We wish to thank the UNC Research Council for financial support and J.T. is also partially supported by Japan-U.S. Collaborative Scientific Research Program of JSPS.

References

(1) Lafferty, J. M. *J. Appl. Phys.* **1951**, *22*, 299.
(2) Swanson, L. W.; McNeely, D. R. *Surf. Sci.* **1979**, *83*, 11.
(3) Davis, P. R.; Gesley, M. A.; Schwind, G. A.; Swanson, L. W. *Appl. Surf. Sci.* **1989**, *37*, 381.
(4) Brodie, I.; Spindt, C. A. In *Advances in Electronics and Electron Physics*; Hawkes, P. W., Ed.; Academic Press: San Diego, CA, 1992; Vol. 83, Ch. 2.
(5) Shimizu, R.; Kataoka, Y.; Tanaka, T.; Kawai, S. *Jpn. J. Appl. Phys.* **1975**, *14*, 1089.
(6) Futamoto, M.; Hosoki, S.; Okano, H.; Kawabe, U. *J. Appl. Phys.* **1977**, *48*, 3541.
(7) Nagata, H.; Harada, K.; Shimizu, R. *J. Appl. Phys.* **1990**, *68*, 3614.
(8) Harada, K.; Nagata, H.; Shimizu, R. *J. Electron Microsc.* **1991**, *40*, 1.
(9) Okano, H.; Futamoto, M.; Hosoki, S.; Kawabe, U. *Shinkai* **1977**, *20*, 127.
(10) Zhang, H.; Zhang, Q.; Tang, J.; Qin, L.-C. *J. Am. Chem. Soc.* **2005**, *127*, 2862.
(11) Zhang, H.; Zhang, Q.; Zhao, G., Yang, G.; Zhang, J.; Tang, J.; Zhou, O.; Qin, L.-C. In press.

JA051340T

J|A|C|S
COMMUNICATIONS

Published on Web 09/03/2005

Single-Crystalline GdB_6 Nanowire Field Emitters

Han Zhang,[†] Qi Zhang,[‡] Gongpu Zhao,[‡] Jie Tang,[‡,§] Otto Zhou,[†,‡] and Lu−Chang Qin*[,†,‡]

Curriculum in Applied and Materials Sciences, Department of Physics and Astronomy, University of North Carolina at Chapel Hill, Chapel Hill, North Carolina 27599-3255, and National Institute for Materials Science, Tsukuba, Japan

Received June 28, 2005; E-mail: lcqin@physics.unc.edu

Rare-earth hexaborides are the best thermionic electron sources due to their low work function, low volatility at high temperature, high conductivity, high chemical resistance, and high mechanical strength.[1] Single-crystalline LaB_6 and CeB_6 (with work functions of about 2.5 eV) have shown this advantage in thermionic electron emission applications during the past 50 years. In the rare-earth hexaboride family, GdB_6 is believed to have the lowest work function (~1.5 eV).[2] However, satisfactory thermionic emission has not been achieved with this material, likely due to the relatively poor stability of GdB_6 at high working temperature around 1500 °C.[2−4] Nevertheless, GdB_6's extremely low work function offers a great opportunity for making this material room temperature field emitters that put less stringency on the high-temperature stability. A field emission electron source offers a brightness more than 100 times higher than the conventional thermionic electron sources, and its current density J can be expressed by the Fowler−Nordheim equation (in SI units):[5,6]

$$J = 2.23 \times 10^{-25}(E^2/\phi)\exp(4.12 \times 10^{-9}/\phi^{1/2} - 1.02 \times 10^{38}\,\phi^{3/2}/E)\ \mathrm{A/m^2}$$

where E is the local field produced at the tip, and ϕ is the work function of the emitting surface of the tip. It can be inferred that the emission current density J increases rapidly with an increasing electric field E, which can be expressed as $E = \beta V$, with V being the voltage applied on the emitter tip and β a geometry-dependent enhancement factor that becomes larger as the emitter tip is sharper. It can also be seen that the emission current density J is enhanced almost exponentially with the decrease of work function, ϕ. A recent study also indicates that, in electron optical applications, reducing the emitter's work function is the only way to achieve high brightness without increasing the electron energy spread, which causes chromatic aberrations.[6] Therefore, to obtain a high emission current with small energy spread at a convenient working voltage, sharp field emitters out of low work function materials, for example, rare-earth hexaboride nanowires, are desired. In our previous work, we have demonstrated the synthesis of ⟨111⟩ oriented LaB_6 nanowires, ⟨001⟩ oriented LaB_6 nanowires, and ⟨001⟩ oriented CeB_6 nanowires and also demonstrated field emission from a single LaB_6 nanowire emitter with a current density as high as 5×10^5 A/cm^2 at a working voltage of 800 V.[7−9] In this communication, we present for the first time a successful synthesis of single-crystalline GdB_6 nanowires and a measurement of their field electron emission.

The synthesis is based on the following chemical reaction:

$$2GdCl_3(g) + 12BCl_3(g) + 21H_2(g) = 2GdB_6(s) + 42HCl(g)$$

The reaction was conducted in a similar chemical vapor deposition (CVD) system described before,[7] except that $GdCl_3$ powders (99.99%, Aldrich) were used as the evaporation source and a clean silicon wafer was used as the deposition substrate.

After the reaction, a scanning electron microscope (SEM, JEM-6300) equipped with an energy-dispersive X-ray spectrometer (EDX, KevexSigma3) was used to examine the nanowires. The lateral dimensions of the nanowires range from below 100 nm to more than 1 μm. EDX analysis indicates the nanowires are composed of B and Gd elements.

The GdB_6 nanowires were also examined in a transmission electron microscope (TEM, JEM-2010F) operated at 200 kV. Figure 1a is a morphological image of the grown GdB_6 nanowires. They are typically 50−60 nm in lateral dimensions and are more than several microns in length. The nanowires' tip-top surfaces are flat and form a right angle with the side surfaces, as can be clearly seen in the inserted high-resolution image of the area marked by an arrow. The nanowires were found to grow along their ⟨001⟩ lattice directions, and both the tip-top and the side surfaces are terminated with the {100} lattice planes. Panels b and c of Figure 1 are the TEM images together with their corresponding selected area electron diffraction patterns taken from a single GdB_6 nanowire along its [100] and [2$\bar{1}$0] lattice directions, respectively. A simple geometric calculation was performed, as illustrated in Figure 1d, in order to obtain the morphology of the nanowire tip. By using $B = 56$ nm measured from Figure 1b, $C = 68$ nm from Figure 1c, and $\theta = 26.6°$ determined from the two diffraction patterns, we obtained the nanowire's other side length A from the equation $A = (C - B\cos\theta)/\sin\theta = 40$ nm.

To study its field emission properties, a GdB_6 nanowire with lateral dimension of about 200 nm was picked up under an optical microscope assisted with a manipulator, and the nanowire was then attached onto an etched 0.5 mm tungsten (W) tip with an acrylic adhesive. Field emission was measured in a high vacuum chamber of 10^{-7} Torr. With the W tip as the cathode and a phosphor-coated ITO glass as the anode spaced at 250 μm, an increasing electric voltage was then applied and, in the meantime, the emission current was measured and the emission patterns were recorded with a CCD camera simultaneously.

Figure 2a shows the $I-V$ curve of the field emission from the GdB_6 single nanowire. An emission current of 10 nA was obtained at a voltage of 650 V, and the emission current reached 200 nA before the emitter broke down. During the entire emission process, the emitter's surface is estimated to reach a maximum temperature of about 400 °C, which is much lower than the melting point (2510 °C) of GdB_6, but is much higher than the acrylic adhesive's tolerance temperature of 60 °C. The large current fluctuations observed in the $I-V$ curve are therefore suggested to be caused by the melting of the adhesive attaching the GdB_6 nanowire to the W tip. A Fowler−Nordheim plot ($\ln(I/V^2)$ vs $1/V$) is depicted in Figure 2b, revealing characteristics of metallic field emission. Figure 2c is a low-magnification TEM image of the GdB_6 nanowire emitter,

[†] Curriculum in Applied and Materials Sciences, University of North Carolina.
[‡] Department of Physics and Astronomy, University of North Carolina.
[§] National Institute for Materials Science.

10.1021/ja054251p CCC: $30.25

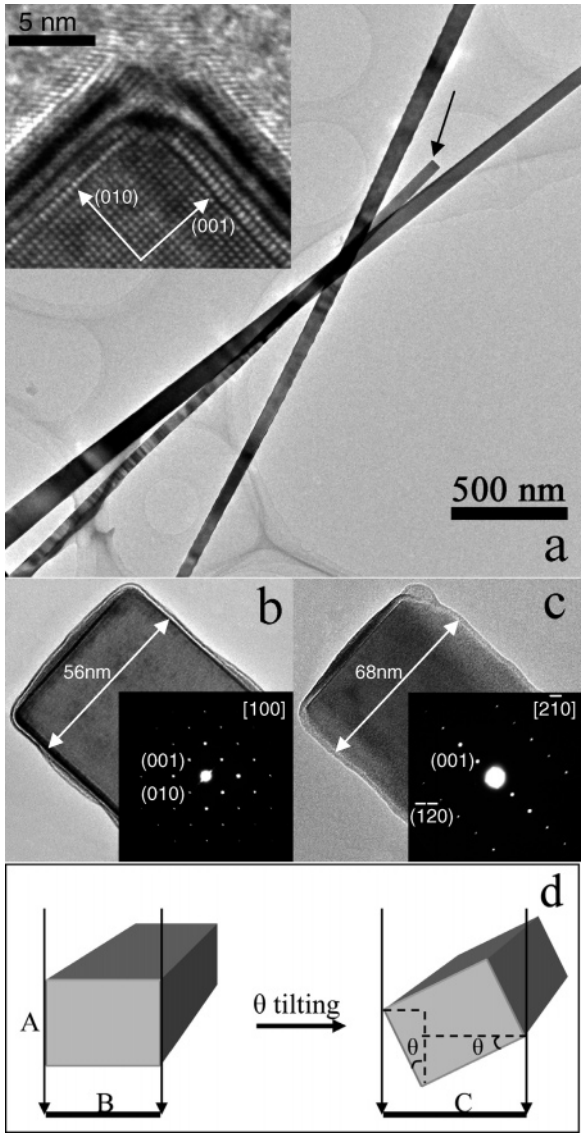

Figure 1. (a) TEM image of GdB_6 nanowires. Inset is a high-resolution lattice image of the tip's top-left corner of the nanowire marked by a dark arrow. (b−c) TEM images and selected area diffraction patterns taken from the same nanowire along its [100] and [2$\bar{1}$0] lattice directions, respectively. (d) Illustration of the tilting process in reconstructing the morphology of the nanowire.

and the inset is an emission pattern recorded at an applied voltage of 750 V. The ring-like feature in the emission pattern is attributed to the fact that the local electric field was more enhanced at the edges and corners of the tip-top surface and therefore induced more emission from a circle of emission sites. We also performed a numerical simulation (FEMLAB) using a model based on the experimental conditions and obtained a local electric field enhancement factor $\beta = 3.3 \times 10^6\ m^{-1}$ at the edges of the top surface. By substituting β into the Fowler−Nordheim plot with slope $k = -1.02 \times 10^{38}\ \phi^{3/2}/\beta$, we obtained the value of work function for the GdB_6 nanowire to be about 1.53 ± 0.2 eV, which agrees well with the reported value.[2] The lower work function of the GdB_6 can also be seen by directly comparing its emission current with that of a LaB_6 nanowire emitter. For example, at 750 V, the GdB_6 nanowire emitter produces more than 50 nA emission current, which is more than 5 times larger than the current drawn from the LaB_6 nanowire emitter working under same conditions.[8]

In conclusion, we have developed a CVD process that is able to produce GdB_6 nanowires of well characterized morphology. The

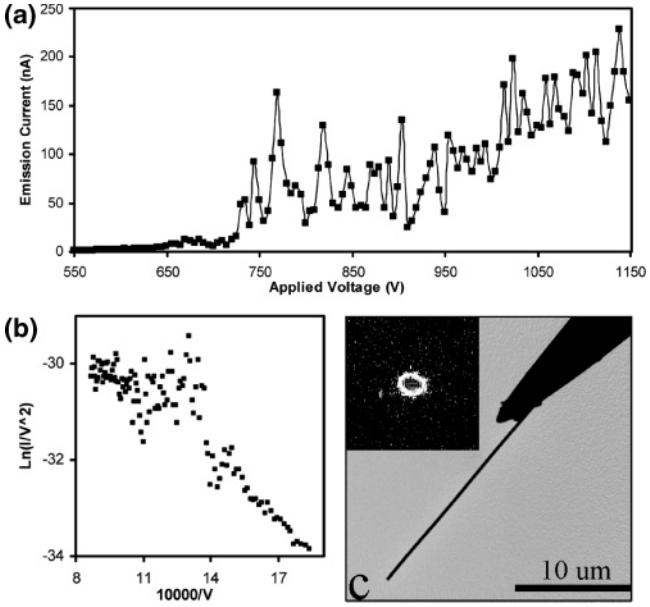

Figure 2. (a) Field emission $I-V$ curve from a GdB_6 single nanowire. (b) Fowler−Nordheim plot of the field emission $I-V$ curve. (c) Low-magnification TEM image of the single nanowire field emitter. Inset is the field emission pattern recorded on a phosphor screen.

nanowires have a rectangular cross-section with a width of about 50 nm and have a length extending to more than several microns. The growth direction of the nanowires is its ⟨001⟩ lattice direction, and they have flat tips and walls which are all terminated by the {100} lattice planes. A GdB_6 single nanowire field emitter produced emission current of more than 150 nA at an average applied field under 3.2 V/μm. The work function of the GdB_6 nanowires was determined to be about 1.5 eV, which is lower than that of LaB_6 nanowire emitters. These GdB_6 nanowires have great potential use as point electron emitters for applications including providing point emission sources for TEM, SEM, flat panel displays, as well as other electronic devices that require high-performance electron sources.

Acknowledgment. We thank H. Jing and Dr. R. Superfine for assistance in the simulations and use of SEM, and Dr. J. Zhang for assistance in field emission measurement. J.T. is partially supported by the Japan-U.S. Collaborative Scientific Research Program of JSPS.

Supporting Information Available: SEM image, EDX spectrum, computer simulation, and procedure descriptions. This material is available free of charge via the Internet at http://pubs.acs.org.

References

(1) Lafferty, J. M. *J. Appl. Phys.* **1951**, *22*, 299.
(2) Kudintseva, G. A.; Kuznetsova, G. M.; Bondarenko, V. P.; Selivanova, N. F.; Shlyuko, V. Ya. *Poroshkovaya Metallurgiya* **1967**, *2*, 45.
(3) Tanaka, T.; Nishitani, R.; Oshima, C.; Bannai, E.; Kawai, S. *J. Appl. Phys.* **1980**, *51*, 3877.
(4) Storms, E. K.; Mueller, B. A. *J. Appl. Phys.* **1981**, *52*, 2966.
(5) (a) Fowler, R. H.; Nordheim, L. *Proc. R. Soc. London* **1928**, *119*, 173. (b) Brodie, I.; Spindt, C. A. In *Advances in Electronics and Electron Physics*; Hawkes, P. W., Ed.; Academic Press: San Diego, 1992; Vol. 83, Chapter 2.
(6) Jonge, N. D.; Allioux, M.; Oostveen, J. T.; Teo, K. B. K.; Milne, W. I. *Phys. Rev. Lett.* **2005**, *94*, 186807.
(7) Zhang, H.; Zhang, Q.; Tang, J.; Qin, L.-C. *J. Am. Chem. Soc.* **2005**, *127*, 2862.
(8) Zhang, H.; Zhang, Q.; Tang, J.; Qin, L.-C. *J. Am. Chem. Soc.* **2005**, *127*, 8002.
(9) Zhang, H.; Zhang, Q.; Zhao, G.-P., Yang, G.; Zhang, J.; Tang, J.; Zhou, O.; Qin, L.-C. *Adv. Mater*. **2005**, in press.

JA054251P

ing in a bending of the AFM cantilever and an increase in the shear stress at the interface. The cantilever bending increased until the force applied to the nanotube was sufficient to pull the nanotube from the polymer (Fig. 1) owing to interfacial failure in shear. This test was repeated using larger nanotube embedded lengths by pushing the nanotube at different depths into the liquid. The embedded lengths were evaluated from SEM images of the nanotube before and during embedment within the epoxy. Further experiments were performed using carbon nanotubes that had been previously chemically modified with carboxylic groups [12] to improve the adhesion with the epoxy matrix.

Received: May 20, 2005
Final version: July 6, 2005
Published online: December 5, 2005

[1] M-F. Yu, O. Lourie, M. J. Dyer, K. Moloni, T. F. Kelly, R. S. Ruoff, *Science* **2000**, *287*, 637.
[2] M-F. Yu, B. S. Files, S. Arepalli, R. S. Ruoff, *Phys. Rev. Lett.* **2000**, *84*, 5552.
[3] B. G. Demczyk, Y. M. Wang, J. Cumings, M. Hetman, W. Han, A. Zettl, R. O. Ritchie, *Mater. Sci. Eng. A* **2002**, *334*, 173.
[4] M. M. J. Treacy, T. W. Ebbesen, J. M. Gibson, *Nature* **1996**, *381*, 678.
[5] A. Krishnan, E. Dujardin, T. W. Ebbesen, P. N. Yianilos, M. M. J. Treacy, *Phys. Rev. B.* **1998**, *58*, 14 013.
[6] W. Wong, P. E. Sheehan, C. M. Lieber, *Science* **1997**, *277*, 1971.
[7] C. A. Cooper, S. R. Cohen, A. H. Barber, H. D. Wagner, *Appl. Phys. Lett.* **2002**, *81*, 3873.
[8] A. H. Barber, S. R. Cohen, H. D. Wagner, *Appl. Phys. Lett.* **2003**, *82*, 4140.
[9] A. H. Barber, S. R. Cohen, S. Kenig, H. D. Wagner, *Compos. Sci. Tech.* **2004**, *64*, 2283.
[10] R. Z. Li, L. Ye, Y. W. Mai, *Compos. A* **1997**, *28*, 73.
[11] J. Chen, M. A. Hamon, H. Hu, Y. S. Chen, A. M. Rao, P. C. Eklund, R. C. Haddon, *Science* **1998**, *282*, 95.
[12] A. Eitan, K. Jiang, D. Dukes, R. Andrews, L. S. Schadler, *Chem. Mater.* **2003**, *15*, 3198.
[13] A. Bukuwska, W. Bukowski, *Org. Process Res. Devel.* **1990**, *3*, 432.
[14] L. Shechter, J. Wynstra, *Industr. Eng. Chem.* **1956**, *48*, 86.
[15] J. Cumming, A. Zettl, *Science* **2000**, *289*, 602.
[16] A. Kelly, W. R. Tyson, *J. Mech. Phys. Solids* **1965**, *13*, 329.
[17] H. L. Cox, *Brit. J. Appl. Phys.* **1952**, *3*, 72.
[18] S. J. V. Frankland, A. Caglar, D. W. Brenner, M. Griebel, *J. Phys. Chem. B.* **2002**, *106*, 3046.
[19] L. Liu, A. H. Barber, S. Nuriel, H. D. Wagner, *Adv. Funct. Mater.* **2005**, *15*, 975.
[20] Z.-F. Li, D. T. Grubb, *J. Mater. Sci.* **1994**, *29*, 189.
[21] H. Nishijima, S. Kamo, S. Akita, Y. Nakayama, K. I. Hohmura, S. H. Yoshimura, K. Takeyasu, *Appl. Phys. Lett.* **1999**, *74*, 4061.
[22] A. H. Barber, S. R. Cohen, H. D. Wagner, *Phys. Rev. Lett.* **2004**, *92*, 186 103.
[23] J. E. Sader, J. W. M. Chon, P. Mulvaney, *Rev. Sci. Instr.* **1999**, *70*, 3967.

DOI: 10.1002/adma.200500508

Field Emission of Electrons from Single LaB_6 Nanowires**

By *Han Zhang*, *Jie Tang*, *Qi Zhang*, *Gongpu Zhao*, *Guang Yang*, *Jian Zhang*, *Otto Zhou*, and *Lu-Chang Qin**

Lanthanum hexaboride (LaB_6) single crystals have been one of the most widely used thermionic electron sources in a large variety of devices requiring electron emission. The low work function (~2.6 eV)[1] together with low vapor pressure at high temperature[2] makes LaB_6 a thermionic electron cathode material superior to conventional filamentous tungsten in electron optical instruments such as the transmission electron microscope and the scanning electron microscope. To pursue higher performance in these microscopy applications, field-emission (FE) electron sources have been introduced to achieve an even higher brightness and lower energy spread. W or W/ZrO based field-emission guns (FEG) are now commercially available and can offer a brightness two orders of magnitude higher than the LaB_6 thermionic electron gun.[3] The brightness of an FEG is proportional to the current density J of electrons emitted from the cathode surface, which can be described by the zero-temperature Fowler–Nordheim (F–N) equation (in $A\,cm^{-2}$) as[4]

$$J = 1.5 \times 10^{-6} \frac{E^2}{\phi} \exp\left(\frac{10.4}{\phi^{1/2}} - \frac{6.44 \times 10^7 \phi^{3/2}}{E}\right) \quad (1)$$

where ϕ is the cathode material's work function and E is the local electric field applied on the cathode tip, which can be expressed as $E = V/5r$ with V being the applied voltage and r the radius of the cathode tip.

The above relations show that a lower work function and a smaller tip radius of the cathode result in a higher emission current density. Stimulated by the fact that LaB_6 has a much lower work function than W or W/ZrO and that it offers ex-

[*] Prof. L.-C. Qin, H. Zhang, Prof. O. Zhou
Curriculum in Applied and Materials Sciences
University of North Carolina at Chapel Hill
Chapel Hill, NC 27599-3255 (USA)
E-mail: lcqin@physics.unc.edu
Prof. L.-C. Qin, Dr. J. Tang, Dr. Q. Zhang, G. Zhao, G. Yang, Dr. J. Zhang, Prof. O. Zhou
Department of Physics and Astronomy
University of North Carolina at Chapel Hill
Chapel Hill, NC 27599-3255 (USA)
Dr. J. Tang
National Institute for Materials Science
Tsukuba, Ibaraki 305-0047 (Japan)

[**] We thank Dr. Minghui Song for EELS analysis and the W. M. Keck Foundation for financial support. J. Tang is partially supported by the Japan–US Collaborative Scientific Program.

ADVANCED MATERIALS

cellent performance as a thermionic electron source, extensive field-emission studies have been carried out on electro-etched LaB_6 needles with tip radii ranging from 100 nm to 300 nm in the search of a brighter field-emission electron source.[5–9] High temperature field-emission studies showed that a brightness at least two orders of magnitude higher than that of a LaB_6 thermionic emitter could be achieved with good stability and that only half of the local electric field was necessary to draw substantial current from the LaB_6 needles compared to a thermal-assisted W/ZrO FEG, which was attributed to the lower work function of LaB_6. However, when the electron emission is operated at high temperature, it requires a higher vacuum and has a larger energy spread in the electron beam, resulting in a larger chromatic aberration in electron coherence. In cold field-emission studies, a high-temperature flashing procedure and a high vacuum of at least 10^{-9} torr (1 torr ~ 133 Pa) were required throughout the measurement in order to obtain field emission. These limitations have made FE electron source applications impractical for this type of electro-etched LaB_6 needles.

One-dimensional nanotube/nanowires have very sharp tips with diameters ranging from more than a hundred to just a few nanometers. Their properties in field emission were first demonstrated in carbon nanotubes.[10–12] The nanometer-scale tip geometry of carbon nanotubes greatly enhances the local electric field and allows stable field emission of high current density under much more practical experimental conditions, such as low applied voltage, low vacuum, and room temperature, and even without the need for the flashing procedure. These attractive features have aroused a tremendous amount of scientific interest in this field, and today its advantage over conventional field-emission electron sources has been well demonstrated.[13–15] In the meantime, nanowires of many other materials have also been reported to show low turn-on voltage field-emission phenomena which are believed to originate from their small tip dimensions.[16–20] However, the large work functions of these materials, including carbon nanotubes, still require tough working conditions for the utilization of these materials. To find a high-performance nanowire/nanotube field-emission cathode material, LaB_6 nanowires, which have a low work function and good electrical conductance, offer a better possibility that has not been well explored. Among all the crystal lattice planes of LaB_6, the {001} planes have both low work function and low volatility, and therefore they are usually preferred as the emission planes for commercialized LaB_6 thermionic electron guns.[1,2] In this article, we report the synthesis by chemical vapor deposition (CVD) of <001> oriented single-crystalline LaB_6 nanowires and the measurement of their excellent FE characteristics.

Figure 1 is a typical scanning electron microscopy (SEM) image of the synthesized LaB_6 nanowires on a silicon substrate. The nanowires have lateral dimensions from a few tens of nanometers to more than 100 nm, and lengths extending to more than a few micrometers. Nanometer- and micrometer-sized cubes and rectangular platelets were also found to have grown on the substrate along with the nanowires, whose geometries reveal the crystallographic symmetries of cubic LaB_6 single crystals. These cubes and platelets sometimes form a right angle connecting two nanowires, as indicated by the arrow in Figure 1.

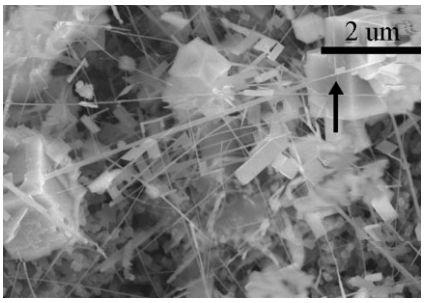

Figure 1. SEM image of single-crystalline LaB_6 nanowires synthesized on silicon substrate. Some cubes and platelets are also grown along with the nanowires. The arrow indicates a cube grown on a nanowire.

A typical low-magnification transmission electron microscopy (TEM) image of the produced LaB_6 nanowires is shown in Figure 2a. The nanowires are about 40 nm in lateral dimensions and more than several micrometers in length. The nanowires have smooth surfaces and their tips, indicated by the arrows in the image, are always terminated with a flat surface and form right angles with their side surfaces. Selected-area electron diffraction (SAED) was used to determine the lattice structure of the nanowires. An electron diffraction pattern of the nanowire labeled A in Figure 2a is shown in Figure 2b, showing that this nanowire was grown in the [001] crystallographic direction of the cubic LaB_6 with lattice constant $a = 4.153$ Å. It was also noticed that all the diffraction spots are elongated into streaks perpendicular to the [001] lattice direction, indicating that the nanowire axis is parallel to the [001] direction of the LaB_6 crystal. The diffraction pattern ap-

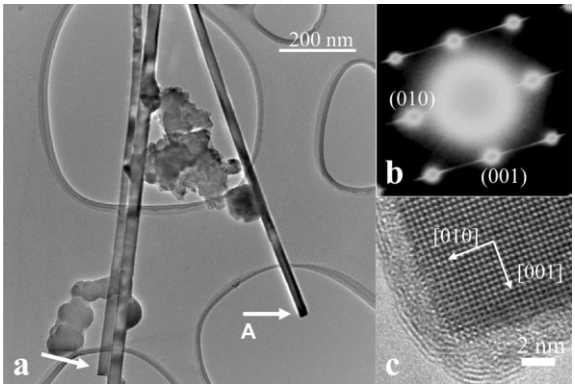

Figure 2. a) Low-magnification TEM image of LaB_6 nanowires. Arrows point to the tips terminated with a flat surface. b) Electron-diffraction pattern of the LaB_6 nanowire displayed in (a) labeled A showing [001] zone axis geometry. Streaks are perpendicular to the axial direction of the nanowire. c) High-resolution image showing the tip of the same LaB_6 nanowire, revealing the flat tip surface (001).

peared identical as we moved the SAED aperture along the entire nanowire, suggesting that the LaB_6 nanowire is single crystalline. To elucidate more details of the atomic structure of the LaB_6 nanowires, high-resolution transmission electron microscopy (HRTEM) was also employed, as shown in Figure 2c. The atomic-resolution image confirms that the nanowire is parallel to the [001] crystallographic direction of the LaB_6 crystal and also reveals that a right angle was formed between the side surfaces and the tip, even at the atomic scale. It should also be pointed out that the HRTEM image contrast near the edge of the nanowire is uniform, unlike the diminishing image contrast observed in cylindrical nanowires, suggesting that the cross-section of the LaB_6 nanowire were more likely to be square, which was also observed in the case of LaB_6 micrometer-sized whiskers,[21,22] as well as CeB_6 and GdB_6 nanowires of the same type of crystal structure.[23,24] To determine the chemical composition of the amorphous layer covering the nanowire, a small electron-beam probe was focused on the amorphous layer and electron energy-loss spectra (EELS) were acquired. The fact that only boron and lanthanum elements were detected suggests that the layer is composed of amorphous boron, since it is the only feasible amorphous phase among the combinations of the two elements, and the lanthanum signals were due to the electron scattering from the crystalline part of the nanowire.

LaB_6 nanowires with lateral dimensions below 20 nm were also fabricated. Figure 3 shows an HRTEM image of a LaB_6 nanowire about 15 nm in width. The growth direction of the nanowire is also parallel to its <001> lattice direction, and its surfaces are all terminated with {001} lattice planes. This thin

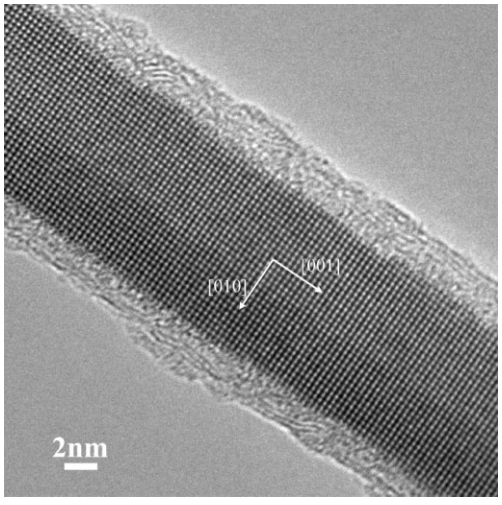

Figure 3. High-resolution TEM image of a thin LaB_6 nanowire 15 nm in width. The nanowire is single crystalline and has grown in the [001] direction.

LaB_6 nanowire is also single crystalline. The <001> growth of these LaB_6 nanowires is attributed to the fact that the {001} lattice planes of LaB_6 have the highest atomic density, and therefore, it would minimize the total energy for the crystal to grow in this lattice direction. However, the causes of the thickness and length variations among the nanowires are still unknown, and a detailed growth mechanism still needs further investigation.

Figure 4a shows a TEM image of a single LaB_6 nanowire of 140 nm in width and about 1 μm in length attached to the tip of a 0.5 mm thick tungsten wire. Field-emission measurements of this structure were performed at a pressure of 10^{-7} torr in-

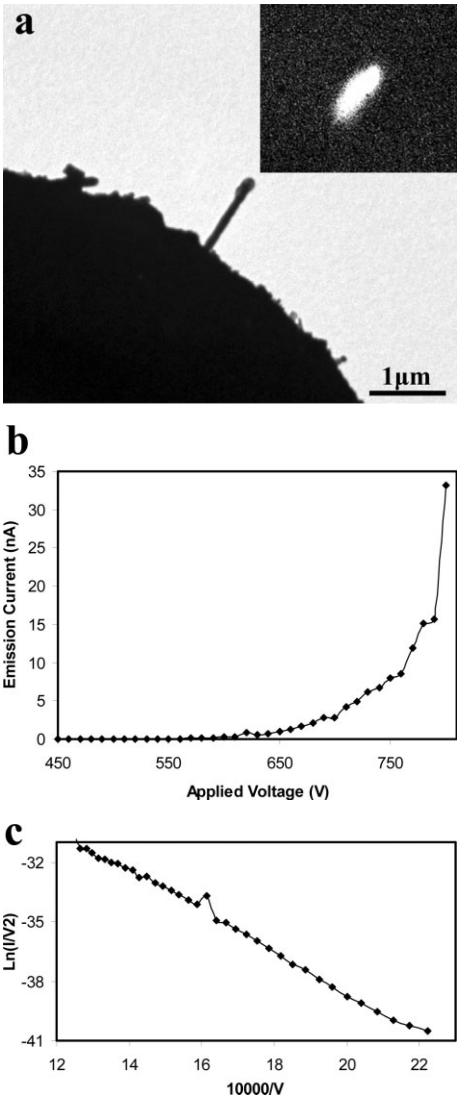

Figure 4. a) Low-magnification TEM image of a single LaB_6 nanowire field-electron emitter. Inset: Fluorescent electron emission image of the emitter recorded on the phosphor viewing screen. b) Current–voltage (I–V) curve of the field emission from the single LaB_6 nanowire emitter. c) F–N plot of $\ln(I/V^2)$ vs. $1/V$. Excellent agreement with the F–N theory of field emission is observed.

side a high-vacuum chamber. While an increasing voltage was applied, the electron fluorescent pattern observed on a phosphor screen was recorded by a charge-coupled device (CCD) camera. An observable, bright emission pattern started to ap-

ADVANCED MATERIALS

pear on the phosphor screen when the applied voltage reached 650 V, and the emission pattern is shown in the inset of Figure 4a. The elliptical shape of the emission pattern is likely due to the fact that the emitter was not well aligned with respect to the applied electric field, therefore causing the cylindrical electron beam to intercept the phosphor screen at an acute angle. The emission current–voltage (I–V) curve is displayed in Figure 4b. A measurable field-emission current of 0.5 pA was obtained at 450 V, which corresponds to an average electric field of 1.5 V μm^{-1}, obtained by dividing the applied voltage by the cathode–anode separation of about 300 μm. Figure 4c shows the F–N plot, $\ln(I/V^2)$ vs. $1/V$. The good linearity of the plot suggests that the field emission from the LaB_6 nanowire emitter agrees with a metal–vacuum field-emission model as described by the F–N equation. In addition, by knowing the work function of the LaB_6 emitter (2.6 eV for the {001} planes[1]), the slope k of the F–N plot, where $k = -6.44 \times 10^7 \phi^{3/2}/\beta$, can be used to estimate the lateral dimensions of the emitter with an enhancement factor $\beta \approx 1/5r$. For this structure, we obtained $D = 2r \approx 152$ nm. This value falls between the edge length and the diagonal of the cross-section of the square LaB_6 nanowire measured from the TEM image shown in Figure 4a. The effective emission area A was derived to be 6.4 nm^2 after substituting β and ϕ into the y-intercept b of the F–N plot as

$$b = \ln\left(\frac{1.5 \times 10^{-6} A\beta^2}{\phi}\right) + \frac{10.4}{\phi^{1/2}} \quad (2)$$

Although the reason why only a small spot of the relatively large area of the whole tip (about 2000 nm^2) was activated to emit electrons is still unclear, the small emitting area is a desired feature for high-resolution electron optical applications where point electron sources are needed. The emission current density at 800 V was estimated to be about 5×10^5 A cm^{-2} by dividing the total emission current by the effective emission area. In comparison with the state-of-the-art W/ZrO thermal field emitter working at 1800 °C with a 3000 V extraction voltage, the LaB_6 nanowire emitter offers a current density one order of magnitude higher while working at room temperature with an 800 V extraction voltage. The current density of the LaB_6 nanowire emitter was also compared with that of a carbon nanotube field emitter, which was believed to be the most promising field-emitter material of all nanotube/nanowire emitters. Results obtained from a single-walled carbon nanotube bundle emitter under the same experimental configuration show that the current density is at the same order of magnitude as the tested LaB_6 nanowire emitter.[15] Four other I–V curves were also obtained from the same LaB_6 nanowire emitter with a continuous emitting time duration of 30 min.

To study the influence of the amorphous boron layer on the field-emission properties of the LaB_6 nanowires, an amorphous boron nanowire about 170 nm in diameter was attached to a tungsten tip and arranged similarly to the LaB_6 nanowire emitter field-emission measurement setup. The emission current never exceeded 1 nA before the applied voltage rose higher than 800 V, in contrast to the 30 nA stable emission from the LaB_6 nanowire emitter of similar size and under the same applied voltage. This might be due to the high work function of boron (4.5 eV). On the other hand, it also suggests that the field emission from the LaB_6 nanowires should mainly result from the crystalline part of the nanowire rather than the amorphous boron layer. This point of view is also supported by the field-emission data from single-crystalline GdB_6 nanowires with a similar geometry.[24] With the same amorphous boron layer on a GdB_6 single-crystalline nanowire of work function 1.5 eV, the GdB_6 nanowire emitter has a higher emission current than the LaB_6 nanowire emitter at the same applied voltage. This should not have occurred if it were the amorphous boron layer that played the key role in the field emission.

In summary, straight single-crystalline <001>-oriented LaB_6 nanowires with widths ranging from 15 nm to more than 100 nm have been successfully synthesized by a CVD method. These nanowires are terminated with {001} surfaces and offer a promising structure as point electron sources. Field-emission measurements on a single LaB_6 nanowire showed that a high emission current density of 5×10^5 A cm^{-2} was achieved at a voltage below 800 V with an effective emission area as small as 6.4 nm^2. With an even thinner emitter, LaB_6 nanowires offer the prospect to make the best point electron sources as a consequence of the low work function and low dimensionality of this unique material.

Experimental

The synthesis of the LaB_6 nanowires is based on the chemical reaction

$$2LaCl_3(g) + 12BCl_3(g) + 21H_2(g) \rightarrow 2LaB_6(s) + 42HCl(g) \quad (3)$$

The reaction was conducted in a tube furnace operated at 1150 °C where BCl_3 gas and $LaCl_3$ powders were brought together in an atmosphere of hydrogen and nitrogen gases. Single-crystalline nanowires were grown on metal substrates with a good yield and a small amount of amorphous boron impurity, similar to the CVD approaches that have also been used to produce LaB_6 whiskers with diameters over 1 μm [21,22,25–27].

For electron-microscopy observations, the LaB_6 nanowires were first dispersed in ethanol and then collected onto a TEM grid coated with a holey carbon film. A transmission electron microscope (JEM-2010F equipped with a field-emission gun) operated at 200 kV was used in the electron-diffraction and electron-microscopy examinations, as well as for electron energy-loss spectroscopic analysis.

For field-emission measurements, the tungsten wire was used as the cathode and a piece of indium tin oxide (ITO) glass plate was used as the anode. A layer of phosphor was also painted on the ITO glass to enable observation of the electron-emission pattern when field-emission electrons from the cathode reached the anode. The FE measurement was carried out in a high-vacuum chamber at a pressure of 10^{-7} torr.

Received: March 11, 2005
Final version: August 17, 2005
Published online: December 5, 2005

[1] M. Gesley, L. W. Swanson, *Surf. Sci.* **1984**, *146*, 583.
[2] L. W. Swanson, M. A. Gesley, P. R. Davis, *Surf. Sci.* **1981**, *107*, 263.
[3] D. B. Williams, C. B. Carter, *Transmission Electron Microscopy*, Plenum, New York **1996**.
[4] I. Brodie, C. A. Spindt, in *Advances in Electronics and Electron Physics*, Vol. 83 (Ed: P. W. Hawkes), Academic, San Diego, CA **1992**, Ch. 2.
[5] R. Shimizu, Y. Kataoka, T. Tanaka, S. Kawai, *Jpn. J. Appl. Phys.* **1975**, *14*, 1089.
[6] M. Futamoto, S. Hosoki, H. Okano, U. Kawabe, *J. Appl. Phys.* **1977**, *48*, 3541.
[7] H. Nagata, K. Harada, R. Shimizu, *J. Appl. Phys.* **1990**, *68*, 3614.
[8] K. Harada, H. Nagata, R. Shimizu, *J. Electron Microsc.* **1991**, *40*, 1.
[9] S. Zaima, M. Sase, H. Adachi, Y. Shibata, C. Ohshima, T. Tanaka, S. Kawai, *J. Phys. D: Appl. Phys.* **1980**, *13*, L47.
[10] L. A. Chernozatonskii, Y. V. Gulyaev, Z. J. Kosakovskaja, N. I. Sinitsyn, G. V. Torgashov, Y. F. Zakharchenko, E. A. Fedorov, V. P. Val'chuk, *Chem. Phys. Lett.* **1995**, *233*, 63.
[11] A. G. Rinzler, J. H. Hafner, P. Nikolaev, L. Lou, S. G. Kim, D. Tomanek, P. Nordlander, D. T. Colbert, R. E. Smalley, *Science* **1995**, *269*, 1550.
[12] W. A. D. Heer, A. Chatelain, D. Ugarte, *Science* **1995**, *270*, 1179.
[13] J. M. Bonard, H. Kind, T. Stockli, L. O. Nilsson, *Solid-State Electron.* **2001**, *45*, 893.
[14] N. de Jonge, Y. Lamy, K. Schoots, T. H. Oosterkamp, *Nature* **2002**, *420*, 393.
[15] J. Zhang, J. Tang, G. Yang, Q. Qiu, L.-C. Qin, O. Zhou, *Adv. Mater.* **2004**, *16*, 1219.
[16] K. W. Wong, X. T. Zhou, C. K. Frederick, H. L. Lai, C. S. Lee, S. T. Lee, *Appl. Phys. Lett.* **1999**, *75*, 2918.
[17] J. Chen, S. Z. Deng, N. S. Xu, S. Wang, X. Wen, S. Yang, C. Yang, J. Wang, W. Ge, *Appl. Phys. Lett.* **2002**, *80*, 3620.
[18] Y. Lee, C. Choi, Y. Jang, E. Kim, B. Ju, N. Min, J. Ahn, *Appl. Phys. Lett.* **2002**, *81*, 745.
[19] Y. B. Li, Y. Bando, D. Golberg, K. Kurashima, *Appl. Phys. Lett.* **2002**, *81*, 5048.
[20] L.-W. Yin, Y. Bando, Y.-C. Zhu, M.-S. Li, Y.-B. Li, D. Golberg, *Adv. Mater.* **2005**, *17*, 110.
[21] A. Hagimura, A. Kato, *Nippon Kagaku Kaishi* **1980**, *7*, 1108.
[22] E. I. Givargizov, L. N. Obolenskaya, *J. Less-Common Met.* **1986**, *117*, 97.
[23] H. Zhang, Q. Zhang, J. Tang, L.-C. Qin, *J. Am. Chem. Soc.* **2005**, *127*, 8002.
[24] H. Zhang, Q. Zhang, G. Zhao, J. Tang, O. Zhou, L.-C. Qin, *J. Am. Chem. Soc.* **2005**, *127*, 13 120.
[25] S. Motojima, Y. Takahashi, K. Sugiyama, *J. Cryst. Growth* **1978**, *44*, 106.
[26] E. I. Givargizov, L. N. Obolenskaya, *J. Cryst. Growth* **1981**, *51*, 190.
[27] S. S. Kher, J. T. Spencer, *J. Phys. Chem. Solids* **1998**, *59*, 1343.

DOI: 10.1002/adma.200500451

Fluorescence Enhancement by Metal-Core/Silica-Shell Nanoparticles**

By *Oleg G. Tovmachenko*, *Christina Graf*, *Dave J. van den Heuvel*, *Alfons van Blaaderen*, and *Hans C. Gerritsen**

The fundamental and applied physics of noble-metal nanoparticles is currently attracting much attention. To a great extent this is due to promising new applications of noble-metal colloidal nanoparticles in fields such as materials science,[1] biophysics,[2] molecular electronics, and fluorescence-spectral engineering based on surface-enhancement effects.[3] In particular the nanoparticles have promising applications as bright fluorescent markers with enhanced photostability in fluorescence microscopy, sensor technology, and microarrays. The enhancement of the fluorescence emission of molecules near a metal surface arises from interactions with surface plasmon (SP) resonances in the metal particles.[4–6] These interactions may also result in shortening of the excited-state lifetime thus improving the photostability of the dye.[7]

The optical properties of a fluorescent molecule located near a metal nanoparticle are affected by the near-field electrodynamical environment.[4–6] This can cause an enhancement or quenching of the fluorescence depending on the distance between the molecule and the metal surface. In the case of fluorescent molecules located at very short distances from a metal surface, non-radiative energy transfer to SPs in the metal takes place.[8,9] Electromagnetic-field enhancement due to SPs, however, still occurs at longer distances from the metal core. As a result, there is an optimal fluorescent molecule to metal-core distance for fluorescence enhancement.

Important factors affecting the strength of the fluorescence enhancement are the size and shape of the nanoparticle, the orientation of the dye dipole moments relative to the nanoparticle surface normal, the overlap of the absorption and emission bands of the dye with the plasmon band of the metal, and the radiative decay rate and quantum yield (Q) of the fluorescent molecules.

[*] Prof. H. C. Gerritsen, Dr. O. G. Tovmachenko, Dr. C. Graf,[+] D. J. van den Heuvel, Prof. A. van Blaaderen
Soft Condensed Matter & Molecular Biophysics Department
Debye Institute, Utrecht University
Princetonplein 1, NL-3584 CC Utrecht (The Netherlands)
E-mail: H.C.Gerritsen@phys.uu.nl

[+] Present address: Institut für Physikalische Chemie, Universität Würzburg, Sanderring 2, 97070 Würzburg, Germany.

[**] This work is part of the research programme of the Stichting voor Fundamenteel Onderzoek der Materie (FOM), financially supported by the Nederlandse Organisatie voor Wetenschappelijk Onderzoek (NWO).